Universiteit
Leiden
The Netherlands

Don't blink : detecting transiting exoplanets with MASCARA

Talens, G.J.J.

Citation
Talens, G. J. J. (2018, December 19). *Don't blink : detecting transiting exoplanets with MASCARA*. Retrieved from https://hdl.handle.net/1887/67535

Version:	Not Applicable (or Unknown)
License:	Licence agreement concerning inclusion of doctoral thesis in the Institutional Repository of the University of Leiden
Downloaded from:	https://hdl.handle.net/1887/67535

Note: To cite this publication please use the final published version (if applicable).

Cover Page

Universiteit Leiden

The handle http://hdl.handle.net/1887/67535 holds various files of this Leiden University dissertation.

Author: Talens, G.J.J.
Title: Don't blink : detecting transiting exoplanets with MASCARA
Issue Date: 2018-12-19

Don't Blink

Detecting transiting exoplanets with MASCARA

ISBN : 9789463233774
A digital copy of this thesis is available at https://openaccess.leidenuniv.nl

Don't Blink

Detecting transiting exoplanets with MASCARA

Proefschrift

ter verkrijging van
de graad van Doctor aan de Universiteit Leiden,
op gezag van Rector Magnificus prof. mr. C. J. J. M. Stolker,
volgens besluit van het College voor Promoties
te verdedigen op woensdag 19 december 2018
klokke 13:45 uur

door

Geert Jan Jacob Talens
geboren te Alkmaar
in 1991

Promotiecommissie

Promotor:	Prof. dr. Ignas A.G. Snellen	
Co-promoters:	Dr. Matthew A. Kenworthy	
Overige leden:	Prof. dr. H. J. A. Röttgering	
	Prof. dr. C. U. Keller	
	Prof. dr. M. Fridlund	
	Dr. J. L. Birkby	(University of Amsterdam)
	Dr. S. Albrecht	(Aarhus University)

Dedicated to my mother.

Contents

1 Introduction **3**
- 1.1 Detecting planets . . . 4
  - 1.1.1 Radial velocities and transits . . . 4
  - 1.1.2 Direct imaging and other methods . . . 6
- 1.2 Hot Jupiters . . . 7
  - 1.2.1 Orbits, occurrence and composition . . . 7
  - 1.2.2 Atmospheres . . . 9
- 1.3 This thesis . . . 11

2 The Multi-site All-Sky CAmeRA **23**
- 2.1 Introduction . . . 24
- 2.2 Station design . . . 25
  - 2.2.1 Enclosure . . . 25
  - 2.2.2 Camera box . . . 27
  - 2.2.3 Optics . . . 27
  - 2.2.4 Electronics and computing . . . 30
- 2.3 Nominal operations . . . 31
- 2.4 Data analysis . . . 32
  - 2.4.1 On-site reduction pipeline . . . 32
- 2.5 Performance . . . 34
  - 2.5.1 Station performance . . . 34
  - 2.5.2 The point spread function and astrometry . . . 38
  - 2.5.3 Photometry . . . 38
- 2.6 Discussion and conclusion . . . 39

3 Data Calibration **49**
- 3.1 Introduction . . . 50
- 3.2 Primary calibration . . . 51
  - 3.2.1 Spatial . . . 53
  - 3.2.2 Temporal . . . 53
  - 3.2.3 Solution and caveats . . . 55
- 3.3 Secondary calibration . . . 59
  - 3.3.1 Methods . . . 62
  - 3.3.2 Comparison . . . 64
- 3.4 Transit detection . . . 67
- 3.5 Signal recovery tests . . . 68
  - 3.5.1 Performance of different calibration strategies . . . 68

3.5.2 Survey performance . . . 73
3.6 The A-star occurrence rate . . . 78
3.7 Summary and outlook . . . 78
3.A Details on solving Eqs. 3.4 and 3.7 . . . 80
3.A.1 Spatial . . . 80
3.A.2 Temporal . . . 81
3.B Correction maps . . . 81

4 MASCARA-1 b 91
4.1 Introduction . . . 92
4.2 Observations . . . 93
4.3 Stellar parameters . . . 94
4.4 System parameters . . . 95
4.4.1 Photometric transit fit . . . 95
4.4.2 Radial velocities and planet mass . . . 98
4.4.3 Rossiter-McLaughlin effect and projected spin-orbit angle . . . 99
4.5 Discussion and conclusions . . . 100

5 MASCARA-2 b 115
5.1 Introduction . . . 116
5.2 MASCARA & Discovery Observations . . . 117
5.3 Follow-up Observations . . . 119
5.3.1 Follow-up photometric observations . . . 119
5.3.2 Follow-up spectroscopic observations . . . 121
5.4 System and Stellar Parameters . . . 121
5.4.1 Photometric transit fitting . . . 121
5.4.2 Stellar parameters determination . . . 124
5.4.3 Radial velocity analysis . . . 124
5.4.4 Spectroscopic transit analysis . . . 128
5.5 Discussion and Conclusion . . . 128

Related Publications 141

Nederlandse Samenvatting 143

Curriculum Vitae 147

Acknowledgments 149

1 Introduction

As recently as the early 1990s, the question of whether planets existed outside our own solar system had yet to be answered. The first exoplanet detections occurred in 1992, when Wolszczan & Frail announced the discovery of two planets, a few times more massive than the earth, orbiting the pulsar PSR B1257+12 (Wolszczan and Frail, 1992). While this discovery was tantalizing, it was difficult to place it into context, as pulsars are by no means typical stars. Only a few years later, in 1995, Mayor & Queloz announced the discovery of a planet around the G-type star 51 Pegasi (Mayor and Queloz, 1995). Though this star was of ordinary solar-type, the planet was not. It has a mass about half that of Jupiter, yet it orbits its host star in only 4.23 days, far shorter than any planet in the solar system. Since the discovery of 51 Peg b the number of known exoplanets around main sequence stars has increased steadily, and several thousand exoplanets are known today. With this large number of planets the question of whether extrasolar planets exist has been definitively answered, yet the large range of observed exoplanet types has raised many new questions, such as how the observed planets formed, how they subsequently evolved and whether some of them could be habitable. In this introduction I will first provide a brief overview of the methods used to detect exoplanets. Subsequently, I discuss what we can learn about these planets and how this thesis contributes to answering the general science questions above.

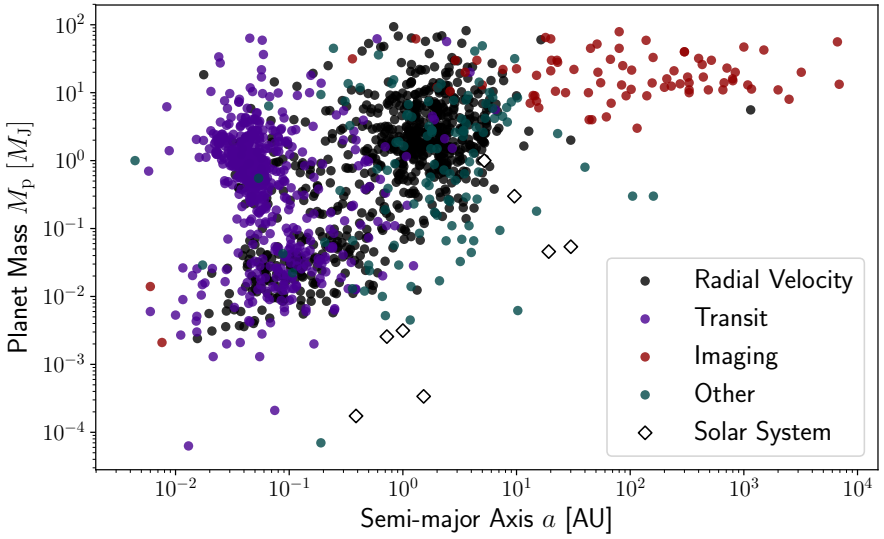

Figure 1.1: Planet mass versus orbital semi-major axis for all planets discovered to date. Extrasolar planets are marked with circles and coloured according to the method used in the detection of the exoplanet. The large diamonds indicate the solar system planets.

1.1 Detecting planets

The discovery of a planet around 51 Pegasi gave a strong impulse to the detection of extrasolar planets. Over the subsequent 20 years the number of detected exoplanets grew exponentially. At first planets were primarily detected through the radial velocity method, the same way 51 Peg b had been found. Starting in the early 2000s the transit method yielded its first detections, and is the most successful detection method today. Both the radial velocity and transit methods lack sensitivity to planets at larger separations (>1 AU), motivating the use of direct imaging as an exoplanet detection method in recent years.

Figure 1.1 shows the planet mass versus the orbital semi-major axis for all known exoplanets. They are coloured according to their detection method and the regions of parameters space where the different methods are most sensitive are clearly visible. Radial velocities are currently sensitive to planets out to about ∼5 AU, transits perform best at smaller semi-major axes, and direct imaging can detect planets out to very large separations.

1.1.1 Radial velocities and transits

Radial velocities are measured from shifts of spectral lines in the stellar spectrum, which are caused by the Doppler effect as the star orbits the center of mass of the star-planet system. For a circular orbit the observed radial velocity amplitude (K) is given by,

$$K = \left(\frac{2\pi G}{P}\right)^{1/3} \frac{M_{\rm p} \sin i}{(M_\star + M_{\rm p})^{2/3}} \tag{1.1}$$

where G is the gravitational constant, P the orbital period, $M_{\rm p}$ the mass of the planet, $M_\star$ the mass of the star, and i the inclination of the orbit relative to the observer's line of sight (e.g. Perryman, 2014). Radial velocity surveys are biased towards massive planets with short orbital periods as these produce the strongest signals. This explains why planets detected at larger separations tend to be more massive (see Fig. 1.1). Note that in most cases the true mass of a planet cannot be determined, only a lower limit, due to the unknown inclination.

Radial velocity surveys (e.g. Vogt et al., 2000; Mayor et al., 2003; Valenti and Fischer, 2005; Covino et al., 2013) generally require many observations per star over a long period of time, hence surveys tend to focus on small samples of spectroscopically well-behaved stars. Early-type stars (such as A-stars) are typically excluded from radial velocity surveys because they rotate rapidly, which broadens the spectral lines, exhibit pulsations, and have a reduced number of strong metal lines compared to solar-type stars, significantly reducing the accuracy with which radial velocities can be measured.

Soon after the discovery of the first exoplanets it was realised that for favourable inclinations, a planet would transit its host star. Detection of such transits, combined with radial velocity measurements, would allow for measurements of the true mass and radius of the planet. During a transit the planet passes in front of its host star, obscuring part of the star and causing a measurable decrease in brightness. The change in the measured flux (ΔF) relative to the out-of-transit flux (F) is proportional to the fraction of the stellar disk blocked by the planet,

$$\frac{\Delta F}{F} = \left(\frac{R_{\rm p}}{R_\star}\right)^2$$

where $R_{\rm p}$ is the radius of the planet and $R_\star$ the radius of the star. The quantity $\Delta F/F$ is usually referred to as the transit depth. Transit surveys are biased towards relatively large planets as these produce deeper transits. Furthermore, the probability that a given orbital configuration exhibits transits decreases as the semi-major axis increases, introducing a bias for smaller separations, in addition to the fact that transits occur more frequently for planets with shorter orbital periods.

The first planet to be observed in transit was HD 209458 b (Henry et al., 2000; Charbonneau et al., 2000), which was discovered using radial velocity measurements, constraining the mass and radius of the planet to $0.69\ M_{\rm J}$ and $1.38\ R_{\rm J}$. Subsequently, Charbonneau et al. (2002) showed that sodium could be detected in the atmosphere of HD 209458 b during transit, solidifying the value of transiting exoplanets for planetary characterization.

Recognizing the value of transiting exoplanets, the first ground-based transit surveys were initiated, and in 2003 the successful detection of OGLE-TR-56 b was reported (Konacki et al., 2003). Since then several ground-based transit surveys have contributed to the detection of new transiting exoplanets, such as TrES and XO (Alonso et al., 2004; McCullough et al., 2005), which found five and six planets respectively. The most successful ground-based surveys to date are HATNet and SuperWASP (Bakos et al., 2004; Pollacco et al.,

2006), which in over a decade of operations have found a total of $\sim$200 exoplanets. To achieve this, HATNet and SuperWASP use a battery of wide-field lenses to target stars with magnitudes typically in the range $10 < m_V < 13$, which ensures a sufficiently large number of stars are within the Field-of-View (FoV) of the cameras. Though targeted at fainter stars, HATNet and SuperWASP have found planets orbiting the significantly brighter stars HAT-P-2 ($m_V = 8.3$) and WASP-33 ($m_V = 8.7$) (Bakos et al., 2007; Collier Cameron et al., 2010). More recently, the KELT survey (Pepper et al., 2007) has targeted brighter stars $8 < m_V < 11$, with the brightest planet hosts discovered being KELT-11 ($m_V = 8.0$) and KELT-9 ($m_V = 7.6$) (Pepper et al., 2017; Gaudi et al., 2017), and is the closest comparison to MASCARA - the subject of this thesis.

Though successful, the Earth's atmosphere limits the precision achievable with ground-based instruments, preventing the detection of smaller planets - at least around solar-type stars. In order to overcome this limitation the CoRoT (Barge et al., 2008) and *Kepler* (Borucki et al., 2010) satellites performed transit surveys from space, leading to discoveries of the first rocky Earth-size planets (Léger et al., 2009; Batalha et al., 2011). CoRoT observed several $4\ \mathrm{deg}^2$ fields for 150 days, each field containing $5000 - 10000$ stars, however its relatively short time-baseline prevented it from targeting planets in Earth-like orbits. *Kepler* observed a single $115\ \mathrm{deg}^2$ field, containing 150,000 stars, for 4 years. In this way *Kepler* found thousands of exoplanets and was able to push towards the detection of planets in Earth-like orbits. Unfortunately, most of the CoRoT and *Kepler* planet host stars are too faint ($m_V \gtrsim 13$) for follow-up measurements intended to characterise the detected planets.

1.1.2 Direct imaging and other methods

Several other methods for detecting exoplanets exist, direct imaging, pulsar timing, astrometry, microlensing, and transit-timing variations. Of these methods, direct imaging is arguably the most promising. Direct imaging is currently most sensitive to planets on wider orbits ($a \gtrsim 10$ AU), complementing the radial velocity and transit methods. As the name suggests it aims to observe the planet directly, rather then by its indirect effect on the host star. The main challenge is suppressing the light of the host star, which for Earth-like planets (in reflected light) is a factor $>10^9$ brighter at visible wavelegths. To remove the stellar light coronagraphs are used, which block or attenuate the light coming from the star, allowing for the detection of the faint signals produced by planetary companions. For ground-based telescopes coronagraphs need to be operated in conjunction with adaptive optics, which correct for aberrations due to Earth's atmosphere. Currently, direct imaging is limited to young planetary systems for which the planets still radiate residual heat from their formation, making the infrared star-to-planet contrast significantly more favourable (Chabrier et al., 2000; Burrows et al., 2004).

Pulsar timing measures the orbit of the host star as induced by the planet, similar to the radial velocity method, but by measuring the change in arrival times of the radiation pulses these objects produce. As mentioned earlier this method was actually the first to successfully detect exoplanets, but pulsars are exotic host stars and only a few more planets have been found this way. It is not clear how these planets could have survived the preceding supernova, and they may actually have formed in the wake of the explosion. Astrometry aims to measure the orbit of the host star through accurate measurements of its position on the sky. The high accuracy and frequent measurements needed have prevented large scale

success with this method, however the *Gaia* mission (Gaia Collaboration et al., 2016) is very promising in this respect, and is expected to find several thousand exoplanets (Perryman et al., 2014; Snellen and Brown, 2018). Microlensing measures the change that occurs when a planetary system passes in front of a more distant star, acting as a lens to the distant star and causing it to appear brighter. Interestingly, it is also sensitive to planets that do not orbit a star, so-called free-floating planets (Han et al., 2004). However, measurements with this technique cannot be repeated, as it relies on a favourable alignment with a background star (Gaudi, 2012). Finally, transit-timing variations can be used to detect additional planets in systems where other transiting planets are known. In such a system, additional planets would modify the orbit of the known planet, changing the time at which the transit occurs by a small amount. If these transit-times can be measured for a sufficient number of orbits, additional planets can be identified even if they do not transit the host stars themselves. As this technique requires many transits and accurate transit-times, it has been most successful with the *Kepler* data (e.g. Holman et al., 2010; Steffen et al., 2013).

1.2 Hot Jupiters

Today, a wide variety of exoplanets has been discovered, from small rocky planets to massive gas giant planets. Many of these planets have no close analogues in the solar system, e.g. with particularly close-in or very wide orbits, or with intermediate masses between Earth and Neptune. One such class of planets are the hot Jupiters. They are gas giant planets with masses $0.3 - 13.6\ M_{\rm J}$ and ultra-short orbital periods $<$10 days - compared to that of Mercury of $\sim$88 days. The first exoplanet discovered, 51 Peg b, is such a hot Jupiter. They are the easiest class of object to find in transit and radial velocity surveys due to the strong observational biases.

Hot Jupiters are some of the most extreme planets known. As a result of their short orbital distances they are expected to receive high levels of irradiation and be tidally locked. The most extreme planets have day-side temperatures as hot as the effective temperatures of the coolest stars. Contrary to stars however, hot Jupiters are externally heated, making the structure of their atmospheres very different from that of stars. Their high temperatures make hot Jupiters extremely well suited for studies aimed at characterizing their atmospheres, as the temperature increases the scale-height of the atmosphere and thus the amplitude of the expected signal. The overarching scientific questions of exoplanet characterisation can be categorised around three topics: on their formation, their evolution, and possible habitability. Observational avenues that can be used to start to address these topics are orbital configurations, occurrence rates (as a function of mass and orbit), compositional constraints, and atmospheric studies.

1.2.1 Orbits, occurrence and composition

One of the first parameters that can be measured for the majority of newly discovered exoplanets is the orbital period. Precise radial velocity observations can additionally determine the eccentricity of the orbit, and its inclination can be constrained if the planet transits. Hot Jupiters are likely formed at much wider separations before migrating inward (Mizuno, 1980; Pollack et al., 1996). It is also found that most hot Jupiters are in circular

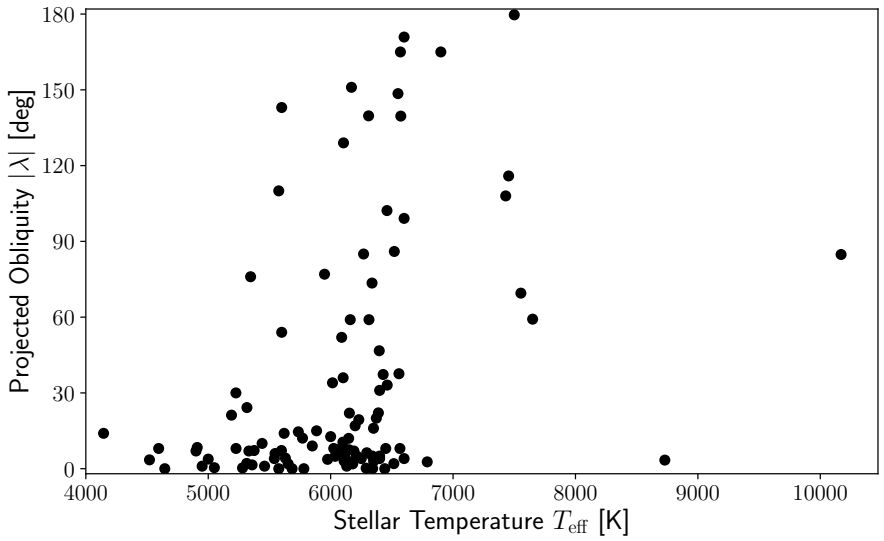

Figure 1.2: Obliquity versus stellar effective temperature for exoplanets. At $T_{\rm eff} \lesssim 6250$ K the obliquities are close to 0° as expected from planet formation theories. At higher temperatures the distribution is more random, suggesting some process modifies the alignment during the formation or evolution of planets around hot stars.

orbits ($e \sim 0$), which is expected due to circularization from tidal interaction with their host stars. The same mechanism should synchronise their spin-rotation with the orbital period on short time scales, tidally locking the planets (Mazeh, 2008; Goldreich and Soter, 1966).

For transiting hot Jupiters, measurements of the Rossiter-McLaughlin effect can be obtained, constraining the projected spin-orbit alignment. When the planet transits it blocks part of the rotating surface of the star, altering the stellar line profile in a way that depends on the angle between the plane of the planet orbit and the spin-rotation axis of the star (λ). Star and planet formation theory suggests that planets form in disks of gas and dust around their host stars. These disks rotate around the star and it is expected that the plane of the disk will be perpendicular to the rotation axis of the star. From this it follows that the orbital plane of the planet should also be perpendicular to the stellar rotation axis, giving $\lambda = 0°$. Figure 1.2 shows the known obliquities as a function of the stellar effective temperature ($T_{\rm eff}$). For stars with $T_{\rm eff} \lesssim 6250$ K, the measurements do indeed cluster near 0°, however at higher temperatures they appear to be randomly distributed. This difference suggest that for planets around hotter stars a process alters the spin-orbit alignment during either their formation or evolution (Winn et al., 2010; Albrecht et al., 2012). However, only a handful of measurements exist for hotter stars, and more obliquity measurements for planets around hot stars are required to confirm the trend and distinguish between proposed causes for the misalignment, such as gravitational interactions with other stars or planets in the system[1].

From the detected population of planets (see Fig. 1.1) occurrence rates may be deter-

[1]The possible causes of spin-orbit misalignment are listed in Sect. 4.5

mined, showing how likely a star is to posses a planet, what types of planets are more common, and whether this depends on the properties of the host stars. Batalha (2014), drawing from several occurrence rate studies, concluded that late-type main sequence stars are orbited by at least one planet. Though hot Jupiters are the most common type of planet detected by ground-based radial velocity and transit surveys, their occurrence rate is actually only $\sim 1\%$ (Mayor et al., 2011; Wright et al., 2012; Howard et al., 2012; Fressin et al., 2013). The high discovery rate of hot Jupiters detected is a result of the biases discussed in Sect. 1.1, rather than the true population of planets.

From combining transit and radial velocity measurements the planet mass and radius are obtained, constraining the bulk density of the planet, allowing inferences to be made about the composition of exoplanets. Like Jupiter and Saturn, hot Jupiters are expected to have a low density as they should be primarily composed of H and He. Figure 1.3 shows the radius versus mass for hot Jupiters, coloured by the equilibrium temperature of the planet. The solid black line indicates the expected relation between the mass and radius of a 3 Gyr old gas giant planet at 0.045 AU from the Sun. It is clear that many hot Jupiters have larger radii and thus lower densities than expected from a H/He composition, a result that holds even when accounting for variations in age and metallicity (Baraffe et al., 2008). This inflation might be related to the amount of flux they receive from their host star, as the most inflated planets also have the highest temperatures. There are several theories that attempt to explain the cause for these inflated radii, either by including an internal heating source (Bodenheimer et al., 2001; Miller et al., 2009; Batygin and Stevenson, 2010; Wu and Lithwick, 2013) or by slowing down the cooling and contraction of the planet during its evolution (Guillot and Showman, 2002; Burrows et al., 2007; Perna et al., 2010), but no definite answer has been identified yet.

1.2.2 Atmospheres

Much work has been done on characterising the atmospheric properties of exoplanets. The atmospheres of transiting exoplanets can be investigated using secondary eclipse measurements, by means of phase curve observations, and through transmission spectroscopy. During secondary eclipse the star blocks thermal emission and reflected light coming from the planet. Measuring this decrease in brightness using broadband photometry places constraints on the day-side temperature of the planet and the reflectivity, or albedo, of its atmosphere. In addition, spectra of the planet may be obtained by taking the difference between those obtained just before or after the eclipse, when both the star and planet contribute, and during the eclipse, containing only the star. Phase curves measure the change in brightness due to changes in the visible fraction of the planet day-side over the course of the orbit. From phase curve measurements the contrast between the planet's day- and night-side can be constrained, and the time of maximum brightness contains information on the dynamics of the atmosphere. Transmission spectroscopy measures small variations in the transit depth with wavelength, which are caused by changes in the optical depth of the atmosphere and can thus be interpreted as a spectrum.

The first detection of an exoplanet atmosphere was made by Charbonneau et al. (2002) who showed sodium was present in the atmosphere of the hot Jupiter HD 209458 b, using spectra taken with the STIS spectrograph on the Hubble Space Telescope (HST). Since then the atmospheres of exoplanets have been extensively studied, from space using the

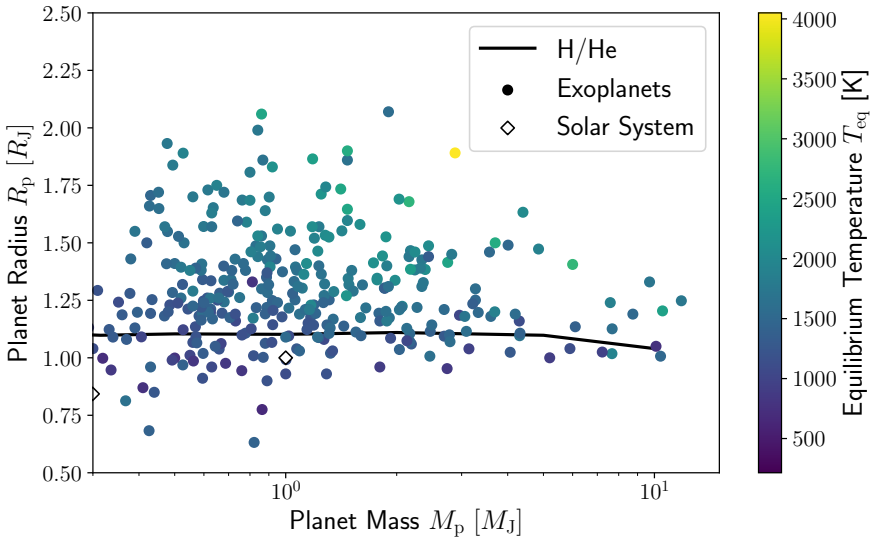

Figure 1.3: Planet mass versus planet radius, hot Jupiters are indicated by circles and solar system planets by the white diamonds. The hot Jupiters are coloured by their equilibrium temperature. The solid line, taken from Baraffe et al. (2008), indicates the mass-radius relation for a 3 Gyr year old H/He gas giant planet at 0.045 AU from the Sun.

STIS and WFC3 low-resolution spectrographs on HST and broadband photometry from *Spitzer* IRAC. STIS is an optical ($0.2 - 1$ μm) spectrograph which has been used to detect to Na and K as well as slopes due to Rayleigh scattering processes, while WFC3 in the near-infrared ($1.1 - 1.7$ μm) is primarily sensitive to H_2O, and *Spitzer* IRAC photometry places additional constraints in the far-infrared. The James Webb Space Telescope will revolutionise space-based spectroscopy of exoplanets by providing spectral coverage from $0.6 - 28$ μm (Beichman et al., 2014), it is currently set for launch in 2021, though Munroe (2018) predicts a 2026 launch.

From photometry and low-resolution spectroscopy it has been found that hot Jupiters have low albedos (Schwartz and Cowan, 2015). Due to tidal locking they often have high day-side temperatures and large day/night-side contrasts (Komacek et al., 2017). For many hot Jupiters it has also been found that their transit spectra contain no significant spectral features, indicative of high-altitude clouds and hazes blocking radiation coming from deeper layers of the atmospheres (e.g. Sing et al., 2016). Measurements of the atomic and molecular species present in hot Jupiter atmospheres could provide information on their formation. The C/O ratio in particular is thought to be a tracer of formation location in the protoplanetary disk (Öberg et al., 2011). Furthermore, the strong stellar irradiation hot Jupiters receive could cause inversions in the temperature structure of the atmosphere, if strong absorbers such as TiO or VO are present. Recently, the first robust evidence for the existence of thermal inversions was obtained when TiO was detected in the atmospheres of two hot Jupiters (Nugroho et al., 2017; Sedaghati et al., 2017).

In addition to the observations performed with space-based instrumentation, Snellen

et al. (2010) showed that high resolution ground-based spectroscopy can be effectively used to unambiguously identify molecular species, such as CO in the atmosphere of HD 209458 b, using cross-correlating techniques, targeting the many spectral molecular lines providing a unique fingerprint for a molecule. Since then, high-resolution spectroscopy has been used to infer the presence of CO, H_2O, TiO HCN, Fe, Fe^+ and Ti^+ in the atmospheres of hot Jupiters (e.g. Birkby et al., 2013; de Kok et al., 2013; Rodler et al., 2013; Nugroho et al., 2017; Hawker et al., 2018; Hoeijmakers et al., 2018). Once a molecule has been detected at high-resolution the shape and location of the cross-correlation profile provide additional information. It has been used to measure winds in the atmospheres of HD 209458 b and HD 189733 b (Snellen et al., 2010; Brogi et al., 2016), measure true masses for the non-transiting planets τ Boo b, HD 88138 b, ups And b and 51 Peg b (Brogi et al., 2012; Rodler et al., 2012; Lockwood et al., 2014; Piskorz et al., 2016, 2017; Birkby et al., 2017), and constrain the rotation rates of β Pic b, HD 189733 b and GQ Lupi b (Snellen et al., 2014; Brogi et al., 2016; Schwarz et al., 2016).

1.3 This thesis

This thesis is focused on the construction, software development, operation, data calibration and analysis, and the first results of the Multi-site All-Sky CAmeRA (MASCARA), which aims to find transiting exoplanets orbiting the brightest stars in the sky. Although *Kepler* and CoRoT have identified thousands of transiting planets, and ground-based surveys like SuperWASP and HATNet have found hundreds of hot Jupiters, they all stay well clear of the brightest stars. However, the brightest stars are particularly interesting, because they allow for the most detailed follow-up observations - in particular for the characterisation of their atmospheres. In addition, the bright star population is biased towards early-type stars, which are strongly under-represented in both radial velocity and transit surveys because mass measurements are near-impossible at faint magnitudes (since early-type stars are fast rotators) but can be accessible at the magnitudes probed by MASCARA. Comparison of the occurrence rates as a function of orbital period and planet mass, as well as their spin-orbital alignments, can shed interesting new light on the formation processes of hot Jupiters.

With this in mind, Snellen et al. (2012) proposed an all-sky transit survey of the brightest stars in the sky ($4 < m_V < 8.4$), the Multi-site All-Sky CAmeRA (MASCARA). MASCARA now consists of two stations, one in the northern hemisphere and one in the southern hemisphere. Each station uses five cameras to image the entire local sky with a cadence of 6.4 s. The first MASCARA station, shown in Fig. 2.1, is located at the Observatorio del Roque de los Muchachos and started nominal operations in January of 2015. The second station, shown in Fig. 1.4, is located at La Silla observatory and started nominal operations in November 2017. A sister-survey called bRing (Stuik et al., 2017), built using the same optics and using the same observing cadence as MASCARA, was also constructed in 2017. bRing consists of two stations in the southern hemisphere that each use two cameras to image stars with $\delta \lesssim -30°$. The bRing stations are located at the Sutherland Observing Station and Siding Spring Observatory.

Figure 1.4: The MASCARA station located at La Silla observatory in Chile, shown during the final stages of construction in June 2017. The camera box has been opened so the lenses can be cleaned, allowing the cameras and lenses to be viewed at the top of the instrument. The camera box can be seen at the bottom of the image as the black object with circular windows. The author (right) and Gilles Otten (left) are also visible.

Chapter 2 This chapter describes the optical and mechanical design of the MASCARA stations and outlines the observational strategy used by MASCARA. Each station uses five Kodak KAI-110002 interline CCDs equipped with commercial canon lenses, giving each camera a FoV of $53° \times 74°$. The camera mounts do not correct for the rotation of the Earth, and stare at fixed points on the local sky instead, i.e. stars move across the CCDs during the observations. The choice of fixed pointings for the cameras means that the roof is the only moving element of the stations, reducing the chance of mechanical failures. The stations take synchronized exposures every 6.4 sidereal seconds, with no read-out time between exposures thanks to the interline design of the CCDs. Each station takes $\sim$500 GB of raw exposures per night, prohibiting transfer and storage of the raw images. An on-site reduction pipeline creates astrometric solutions, performs aperture photometry and creates stacked images. These data products are transferred to Leiden for further processing.

Chapter 3 In this chapter the calibration pipeline, which is used to remove the systematic effects present in the MASCARA and bRing data, is described. The calibration pipeline had to account for systematics introduced by the motion of stars across the CCDs during the observations, a unique feature of MASCARA and bRing. The pipeline consists of a primary calibration step which uses groups of stars to remove the effects of the Earth's atmosphere, camera transmission, and intrapixel variations. Empirical secondary calibration methods are then used to remove residual trends from the photometry of individual stars. After calibration an RMS scatter of 10 mmag is achieved at $m_V \sim 7.5$. The performance of MASCARA is characterized by injecting realistic transit signals into the light curves and

identifying which signals can be recovered. From 1 year of data from the MASCARA station on La Palma, and injecting signals with $1 < P < 5$ days, we find 84.0%, 60.5% and 20.7% of the signals are recovered for transit depths of 2%, 1% and 0.5%, respectively. Furthermore there is a strong dependence on the observed declination, as 65.4% of all transit signals are recovered at $\delta > 0°$ versus 35.8% at $\delta < 0°$. With the first discoveries of MASCARA (see Chapters 4 and 5) we also made a first attempt to constrain the occurrence rate of hot-Jupiters around A-stars.

Chapters 4 and 5 These chapters present the first scientific results of MASCARA - the detections of MASCARA-1 b and MASCARA-2 b, two of the brightest hot Jupiter systems in the sky. MASCARA-1 b is in a 2.15 day orbit around the A-type star HD 201585 ($m_V = 8.3$). The planet has a radius of $1.5\ R_{\rm J}$ and a mass of $3.7\ M_{\rm J}$. The high temperature of its host star ($T_{\rm eff} = 7554$ K) and its close-in orbit ($a = 0.043$ AU) give MASCARA-1 b a high equilibrium temperature of 2570 K, making it suitable for high-resolution spectroscopy. Like other planets around hot stars it has a high obliquity, $\lambda = 69.5°$, apparently confirming the trend of planets around hot stars preferring misaligned orbits. MASCARA-2 b is in a 3.75 day orbit around the A-type star HD 185603 ($m_V = 7.6$). The planet has a radius of $1.83\ R_{\rm J}$ and a mass $<17\ M_{\rm J}$. Though not as hot as MASCARA-1 b, it nevertheless has a high equilibrium temperature of 2260 K, making it very suitable for high-resolution spectroscopy. Contrary to other planets around hot stars it has a low obliquity, $\lambda = 0.6°$, making it the first planet around a star with $T_{\rm eff} > 7000$ K whose orbit is perpendicular to the stellar spin axis.

Bibliography

Albrecht, S., Winn, J. N., Johnson, J. A., Howard, A. W., Marcy, G. W., Butler, R. P., Arriagada, P., Crane, J. D., Shectman, S. A., Thompson, I. B., Hirano, T., Bakos, G., and Hartman, J. D. (2012). Obliquities of Hot Jupiter Host Stars: Evidence for Tidal Interactions and Primordial Misalignments. *ApJ*, 757:18.

Alonso, R., Brown, T. M., Torres, G., Latham, D. W., Sozzetti, A., Mandushev, G., Belmonte, J. A., Charbonneau, D., Deeg, H. J., Dunham, E. W., O'Donovan, F. T., and Stefanik, R. P. (2004). TrES-1: The Transiting Planet of a Bright K0 V Star. *ApJ*, 613:L153–L156.

Bakos, G., Noyes, R. W., Kovács, G., Stanek, K. Z., Sasselov, D. D., and Domsa, I. (2004). Wide-Field Millimagnitude Photometry with the HAT: A Tool for Extrasolar Planet Detection. *PASP*, 116:266–277.

Bakos, G. Á., Kovács, G., Torres, G., Fischer, D. A., Latham, D. W., Noyes, R. W., Sasselov, D. D., Mazeh, T., Shporer, A., Butler, R. P., Stefanik, R. P., Fernández, J. M., Sozzetti, A., Pál, A., Johnson, J., Marcy, G. W., Winn, J. N., Sipőcz, B., Lázár, J., Papp, I., and Sári, P. (2007). HD 147506b: A Supermassive Planet in an Eccentric Orbit Transiting a Bright Star. *ApJ*, 670:826–832.

Baraffe, I., Chabrier, G., and Barman, T. (2008). Structure and evolution of super-Earth to super-Jupiter exoplanets. I. Heavy element enrichment in the interior. *A&A*, 482:315–332.

Barge, P., Baglin, A., Auvergne, M., Rauer, H., Léger, A., Schneider, J., Pont, F., Aigrain, S., Almenara, J.-M., Alonso, R., Barbieri, M., Bordé, P., Bouchy, F., Deeg, H. J., La Reza, D., Deleuil, M., Dvorak, R., Erikson, A., Fridlund, M., Gillon, M., Gondoin, P., Guillot, T., Hatzes, A., Hebrard, G., Jorda, L., Kabath, P., Lammer, H., Llebaria, A., Loeillet, B., Magain, P., Mazeh, T., Moutou, C., Ollivier, M., Pätzold, M., Queloz, D., Rouan, D., Shporer, A., and Wuchterl, G. (2008). Transiting exoplanets from the CoRoT space mission. I. CoRoT-Exo-1b: a low-density short-period planet around a G0V star. *A&A*, 482:L17–L20.

Batalha, N. M. (2014). Exploring exoplanet populations with NASA's Kepler Mission. *Proceedings of the National Academy of Science*, 111:12647–12654.

Batalha, N. M., Borucki, W. J., Bryson, S. T., Buchhave, L. A., Caldwell, D. A., Christensen-Dalsgaard, J., Ciardi, D., Dunham, E. W., Fressin, F., Gautier, III, T. N., Gilliland, R. L., Haas, M. R., Howell, S. B., Jenkins, J. M., Kjeldsen, H., Koch, D. G., Latham, D. W., Lissauer, J. J., Marcy, G. W., Rowe, J. F., Sasselov, D. D., Seager, S., Steffen, J. H., Torres, G., Basri, G. S., Brown, T. M., Charbonneau, D., Christiansen, J., Clarke, B., Cochran,

W. D., Dupree, A., Fabrycky, D. C., Fischer, D., Ford, E. B., Fortney, J., Girouard, F. R., Holman, M. J., Johnson, J., Isaacson, H., Klaus, T. C., Machalek, P., Moorehead, A. V., Morehead, R. C., Ragozzine, D., Tenenbaum, P., Twicken, J., Quinn, S., VanCleve, J., Walkowicz, L. M., Welsh, W. F., Devore, E., and Gould, A. (2011). Kepler's First Rocky Planet: Kepler-10b. *ApJ*, 729:27.

Batygin, K. and Stevenson, D. J. (2010). Inflating Hot Jupiters with Ohmic Dissipation. *ApJ*, 714:L238–L243.

Beichman, C., Benneke, B., Knutson, H., Smith, R., Lagage, P.-O., Dressing, C., Latham, D., Lunine, J., Birkmann, S., Ferruit, P., Giardino, G., Kempton, E., Carey, S., Krick, J., Deroo, P. D., Mandell, A., Ressler, M. E., Shporer, A., Swain, M., Vasisht, G., Ricker, G., Bouwman, J., Crossfield, I., Greene, T., Howell, S., Christiansen, J., Ciardi, D., Clampin, M., Greenhouse, M., Sozzetti, A., Goudfrooij, P., Hines, D., Keyes, T., Lee, J., McCullough, P., Robberto, M., Stansberry, J., Valenti, J., Rieke, M., Rieke, G., Fortney, J., Bean, J., Kreidberg, L., Ehrenreich, D., Deming, D., Albert, L., Doyon, R., and Sing, D. (2014). Observations of Transiting Exoplanets with the James Webb Space Telescope (JWST). *PASP*, 126:1134.

Birkby, J. L., de Kok, R. J., Brogi, M., de Mooij, E. J. W., Schwarz, H., Albrecht, S., and Snellen, I. A. G. (2013). Detection of water absorption in the day side atmosphere of HD 189733 b using ground-based high-resolution spectroscopy at 3.2 μm. *MNRAS*, 436:L35–L39.

Birkby, J. L., de Kok, R. J., Brogi, M., Schwarz, H., and Snellen, I. A. G. (2017). Discovery of Water at High Spectral Resolution in the Atmosphere of 51 Peg b. *AJ*, 153:138.

Bodenheimer, P., Lin, D. N. C., and Mardling, R. A. (2001). On the Tidal Inflation of Short-Period Extrasolar Planets. *ApJ*, 548:466–472.

Borucki, W. J., Koch, D., Basri, G., Batalha, N., Brown, T., Caldwell, D., Caldwell, J., Christensen-Dalsgaard, J., Cochran, W. D., DeVore, E., Dunham, E. W., Dupree, A. K., Gautier, T. N., Geary, J. C., Gilliland, R., Gould, A., Howell, S. B., Jenkins, J. M., Kondo, Y., Latham, D. W., Marcy, G. W., Meibom, S., Kjeldsen, H., Lissauer, J. J., Monet, D. G., Morrison, D., Sasselov, D., Tarter, J., Boss, A., Brownlee, D., Owen, T., Buzasi, D., Charbonneau, D., Doyle, L., Fortney, J., Ford, E. B., Holman, M. J., Seager, S., Steffen, J. H., Welsh, W. F., Rowe, J., Anderson, H., Buchhave, L., Ciardi, D., Walkowicz, L., Sherry, W., Horch, E., Isaacson, H., Everett, M. E., Fischer, D., Torres, G., Johnson, J. A., Endl, M., MacQueen, P., Bryson, S. T., Dotson, J., Haas, M., Kolodziejczak, J., Van Cleve, J., Chandrasekaran, H., Twicken, J. D., Quintana, E. V., Clarke, B. D., Allen, C., Li, J., Wu, H., Tenenbaum, P., Verner, E., Bruhweiler, F., Barnes, J., and Prsa, A. (2010). Kepler Planet-Detection Mission: Introduction and First Results. *Science*, 327:977.

Brogi, M., de Kok, R. J., Albrecht, S., Snellen, I. A. G., Birkby, J. L., and Schwarz, H. (2016). Rotation and Winds of Exoplanet HD 189733 b Measured with High-dispersion Transmission Spectroscopy. *ApJ*, 817:106.

Brogi, M., Snellen, I. A. G., de Kok, R. J., Albrecht, S., Birkby, J., and de Mooij, E. J. W. (2012). The signature of orbital motion from the dayside of the planet τ Boötis b. *Nature* , 486:502–504.

Burrows, A., Hubeny, I., Budaj, J., and Hubbard, W. B. (2007). Possible Solutions to the Radius Anomalies of Transiting Giant Planets. *ApJ*, 661:502–514.

Burrows, A., Sudarsky, D., and Hubeny, I. (2004). Spectra and Diagnostics for the Direct Detection of Wide-Separation Extrasolar Giant Planets. *ApJ*, 609:407–416.

Chabrier, G., Baraffe, I., Allard, F., and Hauschildt, P. (2000). Evolutionary Models for Very Low-Mass Stars and Brown Dwarfs with Dusty Atmospheres. *ApJ*, 542:464–472.

Charbonneau, D., Brown, T. M., Latham, D. W., and Mayor, M. (2000). Detection of Planetary Transits Across a Sun-like Star. *ApJ*, 529:L45–L48.

Charbonneau, D., Brown, T. M., Noyes, R. W., and Gilliland, R. L. (2002). Detection of an Extrasolar Planet Atmosphere. *ApJ*, 568:377–384.

Collier Cameron, A., Guenther, E., Smalley, B., McDonald, I., Hebb, L., Andersen, J., Augusteijn, T., Barros, S. C. C., Brown, D. J. A., Cochran, W. D., Endl, M., Fossey, S. J., Hartmann, M., Maxted, P. F. L., Pollacco, D., Skillen, I., Telting, J., Waldmann, I. P., and West, R. G. (2010). Line-profile tomography of exoplanet transits - II. A gas-giant planet transiting a rapidly rotating A5 star. *MNRAS*, 407:507–514.

Covino, E., Esposito, M., Barbieri, M., Mancini, L., Nascimbeni, V., Claudi, R., Desidera, S., Gratton, R., Lanza, A. F., Sozzetti, A., Biazzo, K., Affer, L., Gandolfi, D., Munari, U., Pagano, I., Bonomo, A. S., Collier Cameron, A., Hébrard, G., Maggio, A., Messina, S., Micela, G., Molinari, E., Pepe, F., Piotto, G., Ribas, I., Santos, N. C., Southworth, J., Shkolnik, E., Triaud, A. H. M. J., Bedin, L., Benatti, S., Boccato, C., Bonavita, M., Borsa, F., Borsato, L., Brown, D., Carolo, E., Ciceri, S., Cosentino, R., Damasso, M., Faedi, F., Martínez Fiorenzano, A. F., Latham, D. W., Lovis, C., Mordasini, C., Nikolov, N., Poretti, E., Rainer, M., Rebolo López, R., Scandariato, G., Silvotti, R., Smareglia, R., Alcalá, J. M., Cunial, A., Di Fabrizio, L., Di Mauro, M. P., Giacobbe, P., Granata, V., Harutyunyan, A., Knapic, C., Lattanzi, M., Leto, G., Lodato, G., Malavolta, L., Marzari, F., Molinaro, M., Nardiello, D., Pedani, M., Prisinzano, L., and Turrini, D. (2013). The GAPS programme with HARPS-N at TNG. I. Observations of the Rossiter-McLaughlin effect and characterisation of the transiting system Qatar-1. *A&A*, 554:A28.

de Kok, R. J., Brogi, M., Snellen, I. A. G., Birkby, J., Albrecht, S., and de Mooij, E. J. W. (2013). Detection of carbon monoxide in the high-resolution day-side spectrum of the exoplanet HD 189733b. *A&A*, 554:A82.

Fressin, F., Torres, G., Charbonneau, D., Bryson, S. T., Christiansen, J., Dressing, C. D., Jenkins, J. M., Walkowicz, L. M., and Batalha, N. M. (2013). The False Positive Rate of Kepler and the Occurrence of Planets. *ApJ*, 766:81.

Gaia Collaboration, Prusti, T., de Bruijne, J. H. J., Brown, A. G. A., Vallenari, A., Babusiaux, C., Bailer-Jones, C. A. L., Bastian, U., Biermann, M., Evans, D. W., and et al. (2016). The Gaia mission. *A&A*, 595:A1.

Gaudi, B. S. (2012). Microlensing Surveys for Exoplanets. *ARA&A*, 50:411–453.

Gaudi, B. S., Stassun, K. G., Collins, K. A., Beatty, T. G., Zhou, G., Latham, D. W., Bieryla, A., Eastman, J. D., Siverd, R. J., Crepp, J. R., Gonzales, E. J., Stevens, D. J., Buchhave, L. A., Pepper, J., Johnson, M. C., Colon, K. D., Jensen, E. L. N., Rodriguez, J. E., Bozza, V., Novati, S. C., D'Ago, G., Dumont, M. T., Ellis, T., Gaillard, C., Jang-Condell, H., Kasper, D. H., Fukui, A., Gregorio, J., Ito, A., Kielkopf, J. F., Manner, M., Matt, K., Narita, N., Oberst, T. E., Reed, P. A., Scarpetta, G., Stephens, D. C., Yeigh, R. R., Zambelli, R., Fulton, B. J., Howard, A. W., James, D. J., Penny, M., Bayliss, D., Curtis, I. A., Depoy, D. L., Esquerdo, G. A., Gould, A., Joner, M. D., Kuhn, R. B., Labadie-Bartz, J., Lund, M. B., Marshall, J. L., McLeod, K. K., Pogge, R. W., Relles, H., Stockdale, C., Tan, T. G., Trueblood, M., and Trueblood, P. (2017). A giant planet undergoing extreme-ultraviolet irradiation by its hot massive-star host. *Nature* , 546:514–518.

Goldreich, P. and Soter, S. (1966). Q in the Solar System. *Icarus*, 5:375–389.

Guillot, T. and Showman, A. P. (2002). Evolution of "51 Pegasus b-like" planets. *A&A*, 385:156–165.

Han, C., Chung, S.-J., Kim, D., Park, B.-G., Ryu, Y.-H., Kang, S., and Lee, D. W. (2004). Gravitational Microlensing: A Tool for Detecting and Characterizing Free-Floating Planets. *ApJ*, 604:372–378.

Hawker, G. A., Madhusudhan, N., Cabot, S. H. C., and Gandhi, S. (2018). Evidence for Multiple Molecular Species in the Hot Jupiter HD 209458b. *ApJ*, 863:L11.

Henry, G. W., Marcy, G. W., Butler, R. P., and Vogt, S. S. (2000). A Transiting "51 Peg-like" Planet. *ApJ*, 529:L41–L44.

Hoeijmakers, H. J., Ehrenreich, D., Heng, K., Kitzmann, D., Grimm, S. L., Allart, R., Deitrick, R., Wyttenbach, A., Oreshenko, M., Pino, L., Rimmer, P. B., Molinari, E., and Di Fabrizio, L. (2018). Atomic iron and titanium in the atmosphere of the exoplanet KELT-9b. *Nature* , 560:453–455.

Holman, M. J., Fabrycky, D. C., Ragozzine, D., Ford, E. B., Steffen, J. H., Welsh, W. F., Lissauer, J. J., Latham, D. W., Marcy, G. W., Walkowicz, L. M., Batalha, N. M., Jenkins, J. M., Rowe, J. F., Cochran, W. D., Fressin, F., Torres, G., Buchhave, L. A., Sasselov, D. D., Borucki, W. J., Koch, D. G., Basri, G., Brown, T. M., Caldwell, D. A., Charbonneau, D., Dunham, E. W., Gautier, T. N., Geary, J. C., Gilliland, R. L., Haas, M. R., Howell, S. B., Ciardi, D. R., Endl, M., Fischer, D., Fürész, G., Hartman, J. D., Isaacson, H., Johnson, J. A., MacQueen, P. J., Moorhead, A. V., Morehead, R. C., and Orosz, J. A. (2010). Kepler-9: A System of Multiple Planets Transiting a Sun-Like Star, Confirmed by Timing Variations. *Science*, 330:51.

Howard, A. W., Marcy, G. W., Bryson, S. T., Jenkins, J. M., Rowe, J. F., Batalha, N. M., Borucki, W. J., Koch, D. G., Dunham, E. W., Gautier, III, T. N., Van Cleve, J., Cochran, W. D., Latham, D. W., Lissauer, J. J., Torres, G., Brown, T. M., Gilliland, R. L., Buchhave, L. A., Caldwell, D. A., Christensen-Dalsgaard, J., Ciardi, D., Fressin, F., Haas, M. R., Howell, S. B., Kjeldsen, H., Seager, S., Rogers, L., Sasselov, D. D., Steffen, J. H., Basri, G. S., Charbonneau, D., Christiansen, J., Clarke, B., Dupree, A., Fabrycky, D. C.,

Fischer, D. A., Ford, E. B., Fortney, J. J., Tarter, J., Girouard, F. R., Holman, M. J., Johnson, J. A., Klaus, T. C., Machalek, P., Moorhead, A. V., Morehead, R. C., Ragozzine, D., Tenenbaum, P., Twicken, J. D., Quinn, S. N., Isaacson, H., Shporer, A., Lucas, P. W., Walkowicz, L. M., Welsh, W. F., Boss, A., Devore, E., Gould, A., Smith, J. C., Morris, R. L., Prsa, A., Morton, T. D., Still, M., Thompson, S. E., Mullally, F., Endl, M., and MacQueen, P. J. (2012). Planet Occurrence within 0.25 AU of Solar-type Stars from Kepler. *ApJS*, 201:15.

Komacek, T. D., Showman, A. P., and Tan, X. (2017). Atmospheric Circulation of Hot Jupiters: Dayside-Nightside Temperature Differences. II. Comparison with Observations. *ApJ*, 835:198.

Konacki, M., Torres, G., Jha, S., and Sasselov, D. D. (2003). An extrasolar planet that transits the disk of its parent star. *Nature* , 421:507–509.

Léger, A., Rouan, D., Schneider, J., Barge, P., Fridlund, M., Samuel, B., Ollivier, M., Guenther, E., Deleuil, M., Deeg, H. J., Auvergne, M., Alonso, R., Aigrain, S., Alapini, A., Almenara, J. M., Baglin, A., Barbieri, M., Bruntt, H., Bordé, P., Bouchy, F., Cabrera, J., Catala, C., Carone, L., Carpano, S., Csizmadia, S., Dvorak, R., Erikson, A., Ferraz-Mello, S., Foing, B., Fressin, F., Gandolfi, D., Gillon, M., Gondoin, P., Grasset, O., Guillot, T., Hatzes, A., Hébrard, G., Jorda, L., Lammer, H., Llebaria, A., Loeillet, B., Mayor, M., Mazeh, T., Moutou, C., Pätzold, M., Pont, F., Queloz, D., Rauer, H., Renner, S., Samadi, R., Shporer, A., Sotin, C., Tingley, B., Wuchterl, G., Adda, M., Agogu, P., Appourchaux, T., Ballans, H., Baron, P., Beaufort, T., Bellenger, R., Berlin, R., Bernardi, P., Blouin, D., Baudin, F., Bodin, P., Boisnard, L., Boit, L., Bonneau, F., Borzeix, S., Briet, R., Buey, J.-T., Butler, B., Cailleau, D., Cautain, R., Chabaud, P.-Y., Chaintreuil, S., Chiavassa, F., Costes, V., Cuna Parrho, V., de Oliveira Fialho, F., Decaudin, M., Defise, J.-M., Djalal, S., Epstein, G., Exil, G.-E., Fauré, C., Fenouillet, T., Gaboriaud, A., Gallic, A., Gamet, P., Gavalda, P., Grolleau, E., Gruneisen, R., Gueguen, L., Guis, V., Guivarc'h, V., Guterman, P., Hallouard, D., Hasiba, J., Heuripeau, F., Huntzinger, G., Hustaix, H., Imad, C., Imbert, C., Johlander, B., Jouret, M., Journoud, P., Karioty, F., Kerjean, L., Lafaille, V., Lafond, L., Lam-Trong, T., Landiech, P., Lapeyrere, V., Larqué, T., Laudet, P., Lautier, N., Lecann, H., Lefevre, L., Leruyet, B., Levacher, P., Magnan, A., Mazy, E., Mertens, F., Mesnager, J.-M., Meunier, J.-C., Michel, J.-P., Monjoin, W., Naudet, D., Nguyen-Kim, K., Orcesi, J.-L., Ottacher, H., Perez, R., Peter, G., Plasson, P., Plesseria, J.-Y., Pontet, B., Pradines, A., Quentin, C., Reynaud, J.-L., Rolland, G., Rollenhagen, F., Romagnan, R., Russ, N., Schmidt, R., Schwartz, N., Sebbag, I., Sedes, G., Smit, H., Steller, M. B., Sunter, W., Surace, C., Tello, M., Tiphène, D., Toulouse, P., Ulmer, B., Vandermarcq, O., Vergnault, E., Vuillemin, A., and Zanatta, P. (2009). Transiting exoplanets from the CoRoT space mission. VIII. CoRoT-7b: the first super-Earth with measured radius. *A&A*, 506:287–302.

Lockwood, A. C., Johnson, J. A., Bender, C. F., Carr, J. S., Barman, T., Richert, A. J. W., and Blake, G. A. (2014). Near-IR Direct Detection of Water Vapor in Tau Boötis b. *ApJ*, 783:L29.

Mayor, M., Marmier, M., Lovis, C., Udry, S., Ségransan, D., Pepe, F., Benz, W., Bertaux, J. ., Bouchy, F., Dumusque, X., Lo Curto, G., Mordasini, C., Queloz, D., and Santos, N. C.

(2011). The HARPS search for southern extra-solar planets XXXIV. Occurrence, mass distribution and orbital properties of super-Earths and Neptune-mass planets. *ArXiv e-prints*.

Mayor, M., Pepe, F., Queloz, D., Bouchy, F., Rupprecht, G., Lo Curto, G., Avila, G., Benz, W., Bertaux, J.-L., Bonfils, X., Dall, T., Dekker, H., Delabre, B., Eckert, W., Fleury, M., Gilliotte, A., Gojak, D., Guzman, J. C., Kohler, D., Lizon, J.-L., Longinotti, A., Lovis, C., Megevand, D., Pasquini, L., Reyes, J., Sivan, J.-P., Sosnowska, D., Soto, R., Udry, S., van Kesteren, A., Weber, L., and Weilenmann, U. (2003). Setting New Standards with HARPS. *The Messenger*, 114:20–24.

Mayor, M. and Queloz, D. (1995). A Jupiter-mass companion to a solar-type star. *Nature* , 378:355–359.

Mazeh, T. (2008). Observational Evidence for Tidal Interaction in Close Binary Systems. In Goupil, M.-J. and Zahn, J.-P., editors, *EAS Publications Series*, volume 29 of *EAS Publications Series*, pages 1–65.

McCullough, P. R., Stys, J. E., Valenti, J. A., Fleming, S. W., Janes, K. A., and Heasley, J. N. (2005). The XO Project: Searching for Transiting Extrasolar Planet Candidates. *PASP*, 117:783–795.

Miller, N., Fortney, J. J., and Jackson, B. (2009). Inflating and Deflating Hot Jupiters: Coupled Tidal and Thermal Evolution of Known Transiting Planets. *ApJ*, 702:1413–1427.

Mizuno, H. (1980). Formation of the Giant Planets. *Progress of Theoretical Physics*, 64:544–557.

Munroe, R. (2018). JWST Delays. *xkcd*, 2014.

Nugroho, S. K., Kawahara, H., Masuda, K., Hirano, T., Kotani, T., and Tajitsu, A. (2017). High-resolution Spectroscopic Detection of TiO and a Stratosphere in the Day-side of WASP-33b. *AJ*, 154:221.

Öberg, K. I., Murray-Clay, R., and Bergin, E. A. (2011). The Effects of Snowlines on C/O in Planetary Atmospheres. *ApJ*, 743:L16.

Pepper, J., Pogge, R. W., DePoy, D. L., Marshall, J. L., Stanek, K. Z., Stutz, A. M., Poindexter, S., Siverd, R., O'Brien, T. P., Trueblood, M., and Trueblood, P. (2007). The Kilodegree Extremely Little Telescope (KELT): A Small Robotic Telescope for Large-Area Synoptic Surveys. *PASP*, 119:923–935.

Pepper, J., Rodriguez, J. E., Collins, K. A., Johnson, J. A., Fulton, B. J., Howard, A. W., Beatty, T. G., Stassun, K. G., Isaacson, H., Colón, K. D., Lund, M. B., Kuhn, R. B., Siverd, R. J., Gaudi, B. S., Tan, T. G., Curtis, I., Stockdale, C., Mawet, D., Bottom, M., James, D., Zhou, G., Bayliss, D., Cargile, P., Bieryla, A., Penev, K., Latham, D. W., Labadie-Bartz, J., Kielkopf, J., Eastman, J. D., Oberst, T. E., Jensen, E. L. N., Nelson, P., Sliski, D. H., Wittenmyer, R. A., McCrady, N., Wright, J. T., Relles, H. M., Stevens, D. J., Joner, M. D., and Hintz, E. (2017). KELT-11b: A Highly Inflated Sub-Saturn Exoplanet Transiting the V = 8 Subgiant HD 93396. *AJ*, 153:215.

Perna, R., Menou, K., and Rauscher, E. (2010). Ohmic Dissipation in the Atmospheres of Hot Jupiters. *ApJ*, 724:313–317.

Perryman, M. (2014). *The Exoplanet Handbook*.

Perryman, M., Hartman, J., Bakos, G. Á., and Lindegren, L. (2014). Astrometric Exoplanet Detection with Gaia. *ApJ*, 797:14.

Piskorz, D., Benneke, B., Crockett, N. R., Lockwood, A. C., Blake, G. A., Barman, T. S., Bender, C. F., Bryan, M. L., Carr, J. S., Fischer, D. A., Howard, A. W., Isaacson, H., and Johnson, J. A. (2016). Evidence for the Direct Detection of the Thermal Spectrum of the Non-Transiting Hot Gas Giant HD 88133 b. *ApJ*, 832:131.

Piskorz, D., Benneke, B., Crockett, N. R., Lockwood, A. C., Blake, G. A., Barman, T. S., Bender, C. F., Carr, J. S., and Johnson, J. A. (2017). Detection of Water Vapor in the Thermal Spectrum of the Non-transiting Hot Jupiter Upsilon Andromedae b. *AJ*, 154:78.

Pollacco, D. L., Skillen, I., Collier Cameron, A., Christian, D. J., Hellier, C., Irwin, J., Lister, T. A., Street, R. A., West, R. G., Anderson, D. R., Clarkson, W. I., Deeg, H., Enoch, B., Evans, A., Fitzsimmons, A., Haswell, C. A., Hodgkin, S., Horne, K., Kane, S. R., Keenan, F. P., Maxted, P. F. L., Norton, A. J., Osborne, J., Parley, N. R., Ryans, R. S. I., Smalley, B., Wheatley, P. J., and Wilson, D. M. (2006). The WASP Project and the SuperWASP Cameras. *PASP*, 118:1407–1418.

Pollack, J. B., Hubickyj, O., Bodenheimer, P., Lissauer, J. J., Podolak, M., and Greenzweig, Y. (1996). Formation of the Giant Planets by Concurrent Accretion of Solids and Gas. *Icarus*, 124:62–85.

Rodler, F., Kürster, M., and Barnes, J. R. (2013). Detection of CO absorption in the atmosphere of the hot Jupiter HD 189733b. *MNRAS*, 432:1980–1988.

Rodler, F., Lopez-Morales, M., and Ribas, I. (2012). Weighing the Non-transiting Hot Jupiter τ Boo b. *ApJ*, 753:L25.

Schwartz, J. C. and Cowan, N. B. (2015). Balancing the energy budget of short-period giant planets: evidence for reflective clouds and optical absorbers. *MNRAS*, 449:4192–4203.

Schwarz, H., Ginski, C., de Kok, R. J., Snellen, I. A. G., Brogi, M., and Birkby, J. L. (2016). The slow spin of the young substellar companion GQ Lupi b and its orbital configuration. *A&A*, 593:A74.

Sedaghati, E., Boffin, H. M. J., MacDonald, R. J., Gandhi, S., Madhusudhan, N., Gibson, N. P., Oshagh, M., Claret, A., and Rauer, H. (2017). Detection of titanium oxide in the atmosphere of a hot Jupiter. *Nature* , 549:238–241.

Sing, D. K., Fortney, J. J., Nikolov, N., Wakeford, H. R., Kataria, T., Evans, T. M., Aigrain, S., Ballester, G. E., Burrows, A. S., Deming, D., Désert, J.-M., Gibson, N. P., Henry, G. W., Huitson, C. M., Knutson, H. A., Lecavelier Des Etangs, A., Pont, F., Showman, A. P., Vidal-Madjar, A., Williamson, M. H., and Wilson, P. A. (2016). A continuum from clear to cloudy hot-Jupiter exoplanets without primordial water depletion. *Nature* , 529:59–62.

Snellen, I. A. G., Brandl, B. R., de Kok, R. J., Brogi, M., Birkby, J., and Schwarz, H. (2014). Fast spin of the young extrasolar planet β Pictoris b. *Nature* , 509:63–65.

Snellen, I. A. G. and Brown, A. G. A. (2018). The mass of the young planet Beta Pictoris b through the astrometric motion of its host star. *Nature Astronomy*.

Snellen, I. A. G., de Kok, R. J., de Mooij, E. J. W., and Albrecht, S. (2010). The orbital motion, absolute mass and high-altitude winds of exoplanet HD209458b. *Nature* , 465:1049–1051.

Snellen, I. A. G., Stuik, R., Navarro, R., Bettonvil, F., Kenworthy, M., de Mooij, E., Otten, G., ter Horst, R., and le Poole, R. (2012). Ground-based search for the brightest transiting planets with the Multi-site All-Sky CAmeRA: MASCARA. In *Ground-based and Airborne Telescopes IV*, volume 8444 of *Proc. SPIE*, page 84440I.

Steffen, J. H., Fabrycky, D. C., Agol, E., Ford, E. B., Morehead, R. C., Cochran, W. D., Lissauer, J. J., Adams, E. R., Borucki, W. J., Bryson, S., Caldwell, D. A., Dupree, A., Jenkins, J. M., Robertson, P., Rowe, J. F., Seader, S., Thompson, S., and Twicken, J. D. (2013). Transit timing observations from Kepler - VII. Confirmation of 27 planets in 13 multiplanet systems via transit timing variations and orbital stability. *MNRAS*, 428:1077–1087.

Stuik, R., Bailey, J. I., Dorval, P., Talens, G. J. J., Laginja, I., Mellon, S. N., Lomberg, B. B. D., Crawford, S. M., Ireland, M. J., Mamajek, E. E., and Kenworthy, M. A. (2017). bRing: An observatory dedicated to monitoring the β Pictoris b Hill sphere transit. *A&A*, 607:A45.

Valenti, J. A. and Fischer, D. A. (2005). Spectroscopic Properties of Cool Stars (SPOCS). I. 1040 F, G, and K Dwarfs from Keck, Lick, and AAT Planet Search Programs. *ApJS*, 159:141–166.

Vogt, S. S., Marcy, G. W., Butler, R. P., and Apps, K. (2000). Six New Planets from the Keck Precision Velocity Survey. *ApJ*, 536:902–914.

Winn, J. N., Fabrycky, D., Albrecht, S., and Johnson, J. A. (2010). Hot Stars with Hot Jupiters Have High Obliquities. *ApJ*, 718:L145–L149.

Wolszczan, A. and Frail, D. A. (1992). A planetary system around the millisecond pulsar PSR1257 + 12. *Nature* , 355:145–147.

Wright, J. T., Marcy, G. W., Howard, A. W., Johnson, J. A., Morton, T. D., and Fischer, D. A. (2012). The Frequency of Hot Jupiters Orbiting nearby Solar-type Stars. *ApJ*, 753:160.

Wu, Y. and Lithwick, Y. (2013). Ohmic Heating Suspends, Not Reverses, the Cooling Contraction of Hot Jupiters. *ApJ*, 763:13.

2 The Multi-site All-Sky CAmeRA (MASCARA): Finding transiting exoplanets around bright ($m_V < 8$) stars

This paper describes the design, operations, and performance of the Multi-site All-Sky CAmeRA (MASCARA). Its primary goal is to find new exoplanets transiting bright stars, $4 < m_V < 8$, by monitoring the full sky. MASCARA consists of one northern station on La Palma, Canary Islands (fully operational since February 2015), one southern station at La Silla Observatory, Chile (operational from early 2017), and a data centre at Leiden Observatory in the Netherlands. Both MASCARA stations are equipped with five interline CCD cameras using wide field lenses (24 mm focal length) with fixed pointings, which together provide coverage down to airmass 3 of the local sky. The interline CCD cameras allow for back-to-back exposures, taken at fixed sidereal times with exposure times of 6.4 sidereal seconds. The exposures are short enough that the motion of stars across the CCD does not exceed one pixel during an integration. Astrometry and photometry are performed on-site, after which the resulting light curves are transferred to Leiden for further analysis. The final MASCARA archive will contain light curves for $\sim 70,000$ stars down to $m_V = 8.4$, with a precision of 1.5% per 5 minutes at $m_V = 8$.

G.J.J. Talens, A.-L. Lesage, G.P.P.L. Otten, R. Stuik, D. Pollacco and I.A.G Snellen

A&A, 601, A11, (2017)

2.1 Introduction

When the first hot Jupiters were discovered twenty years ago (Mayor and Queloz, 1995; Butler et al., 1997), it was realized that these sorts of planets have a significant probability to exhibit transits. The detection of these transits would confirm the hypothesis that the observed stellar radial velocity variations were indeed caused by the gravitational interaction with planets, and furthermore allow the determination of their size and true mass. Hence, all exoplanet systems newly discovered using the radial velocity method were photometrically monitored to search for transit signatures. The first transiting planet found in this way was HD209458b (Henry et al., 2000; Charbonneau et al., 2000) and the subsequent detection of an atmospheric signature (Charbonneau et al., 2002) further strengthened the scientific value of transiting exoplanets. HD209458b is still one of the two most-studied hot Jupiter systems known to date, together with HD189733b (Bouchy et al., 2005) which orbits a similarly bright star.

Initial attempts to directly search for transit signals via high-precision photometric monitoring of large star fields, such as Vulcan (Borucki et al., 2001) and STARE (Brown and Charbonneau, 2000), failed to find planets. This was possibly due to an underestimation of the amount of observing time required (Horne, 2001). It was not until the discovery of OGLE-TR-56 by the OGLE-III team (Konacki et al., 2003) that transit surveys proved to be a viable way of finding exoplanets. However, the OGLE-III targets were generally faint, $m_V > 15$, making radial velocity follow-up challenging. Subsequent transit surveys that targeted brighter stars have found many planets, starting with TrES (using three $10\,\mathrm{cm}$ telescopes; Alonso et al., 2004) and XO (using two lenses with $200\,\mathrm{mm}$ focal length; McCullough et al., 2005) which found five and six transiting planets, respectively, in the $m_V = 10 - 13$ magnitude range. The larger SuperWASP (Pollacco et al., 2006) and HATNet surveys (Bakos et al., 2004) have now been operational for more than a decade, each using a battery of wide-field lenses and finding a total of about two hundred planets orbiting stars in the $m_V = 10 - 13$ magnitude range. In addition, they found a few that are significantly brighter, for example WASP-33 ($m_V = 8.3$, Collier Cameron et al., 2010) and HAT-P-2 ($m_V = 8.7$, Bakos et al., 2007).

With the launch of the CoRoT (Barge et al., 2008) and *Kepler* satellites (Borucki et al., 2010) transit searches entered the space era. Without the negative influence of atmospheric scintillation a higher photometric stability can be reached, which allows for the detection of significantly smaller planets. This led to the discovery of the first rocky planets (Léger et al., 2009; Batalha et al., 2011). The NASA *Kepler* mission stared at a single 115 deg^2 field for four years, monitoring 150,000 stars and finding thousands of transiting planets. This greatly expanded our knowledge of the exoplanet population, almost down to Earth-size planets at Earth-size orbits. Unfortunately, most of the planet host stars are too faint to even obtain the masses of the exoplanets through radial velocity measurements, and detailed atmospheric characterization such as for HD209458b and HD189733b is currently not feasible even with the largest telescopes. The more recent K2 mission, utilizing the *Kepler* satellite after two reaction wheels had failed, does concentrate on brighter stars. However, these are still significantly fainter than the brightest transiting systems expected to exist in the sky at $m_V < 8$. Even the long-running ground-based SuperWASP and HATNet surveys hardly reach these bright stars. Conversely, radial velocity searches specifically target bright stars, but are limited by the amount of observing time needed for a single star and as such

cannot monitor all bright stars. Of the roughly $20,000$ bright stars with radii <2 $R_\odot$ only a few thousand have been searched for planets by means of radial velocity measurements.

For this reason we initiated a new ground-based transit survey project aimed specifically at bright stars, the Multi-Site All-Sky CAmeRA[1] (MASCARA). This paper describes the design and operations of the MASCARA stations in Sects. 2.2 and 2.3. The on-site photometry pipeline is outlined in Sect. 2.4 and the performance of the northern station is presented in Sect. 2.5. Finally, the place of MASCARA as part of the next generation of transit surveys is discussed in Sect. 2.6.

2.2 Station design

The brightest stars to exhibit planetary transits are expected at $m_V > 4$. Transit surveys such as HATNET and SuperWASP cover stars fainter than $m_V \sim 8$. This means that the bright end of the transiting exoplanet population was not covered by existing transit surveys. For this reason, stars in the $4 < m_V < 8$ magnitude range form the main target population of MASCARA. Therefore, it is required that $m_V = 4$ stars do not saturate. Furthermore, over the target magnitude range a precision of at least 1% per hour should be reached for MASCARA to be sensitive to hot Jupiters transiting solar-type stars. A genuine all-sky survey requires at least one station in both the northern and southern hemisphere to have access to the full sky. Furthermore, the design should be such that a station can be run as robotically as possible with low maintenance for a life time of several years.

A MASCARA station is roughly $1 \times 1 \times 1.5$ metres in size, houses five cameras in a temperature controlled camera box, and is designed to have a minimum of moving components (the roof and cooling fans). The northern station, shown in Fig. 2.1, is located at the Observatorio del Roque de los Muchachos ($28°45'25''$N, $7°53'33''$E, $2\,396$ m) on the island of La Palma (Canary Islands, Spain). The southern station is located at ESO's La Silla Observatory ($29°15'40''$S, $70°43'53''$W, $2\,400$ m) in Chile.

2.2.1 Enclosure

The cameras and electronics are protected by a custom enclosure designed at Leiden Observatory and built by FMI Manufacturing[2] and the NOVA optical IR group at ASTRON[3]. The enclosure consists of an outer wall with a door that provides access to the electronics inside the station, and a moveable roof. The roof was designed to move to the side of the enclosure to provide access to the entire visible sky. It uses two Kinematics[4] slewing drives and two motors that can open or close the roof in approximately twenty seconds. In case a single motor fails the other motor is powerful enough to close the roof.

An inner frame inside the enclosure provides the mount for the camera box. The inner frame is mechanically decoupled from the outer structure to minimize variations in the camera pointings that are caused by external forces such as the wind and the motion of the roof. Also attached to the inner frame is an electronics cabinet that contains the control hardware that allows remote operation of the station.

[1] http://mascara1.strw.leidenuniv.nl/
[2] http://www.fmi.nl/
[3] http://www.astron.nl/
[4] http://www.kinematicsmfg.com/

Figure 2.1: Northern MASCARA station on La Palma (Spain). The box next to the station contains the heat exchanger used in the decommissioned liquid cooling system.

2.2.2 Camera box

The cameras are located inside a camera box with a circular window for each camera. Around each window, four white LEDs with dispersers provide a light source for taking dome flats. Initially, the camera box of the northern station was temperature-controlled by means of liquid-cooled Peltier elements and a heat exchanger (see Fig. 2.1). However, in March 2015, the heat exchanger failed and we have operated without temperature-control for the camera box ever since, though the cameras themselves are still cooled. To be more robust against failures of individual components, the design of the southern station was changed. Excess heat is shifted from the camera box to the enclosure using Peltier elements equipped with heat sinks and subsequently removed from the enclosure by means of eight fans mounted in the outer walls of the enclosure.

Figure 2.2 shows the sky coverage for both stations. Each station monitors the entire visible sky down to airmass 2 and provides partial coverage down to airmass 3. For the northern station, the camera pointings correspond to the cardinal directions and zenith. The southern station was rotated $\sim 10^\circ$ eastwards to minimize obscuration by the MarLy telescope, and the altitude of the zenith camera was changed from 90° to 87° to break a degeneracy in the astrometric solution.

2.2.3 Optics

Figure 2.3 shows the optical assembly of the northern station mounted inside the camera box. The northern station uses Atik[5] 11000M interline CCD cameras that were modified by the manufacturer to allow fast and continuous readout. The southern station utilizes FLI[6] ML11002 interline CCD cameras. Both the Atik and FLI cameras use the Kodak KAI-11002 front-illuminated interline CCD with microlens array. We use interline CCDs because they provide electronic shutters. Each camera takes over 150,000 exposures per month prohibiting the use of consumer cameras using shutters, and the use of a separate shutter was deemed to result in undesirable mechanical complexity. Interline CCDs also allow the simultaneous exposing and reading of images, hence eliminating overheads.

The CCDs have 4008×2672 pixels of $9\ \mu\mathrm{m}$, with a peak quantum efficiency of $50\ \%$ at $500\ \mathrm{nm}$ (See Fig. 2.4). The full well depth of the CCD is $60\,000\ e^-$ with a $>1000\times$ anti-blooming protection, which is important when the Moon is in the field. The Atik cameras are read with 16-bit resolution at $12\ \mathrm{MHz}$ and have a gain of $0.6\ e^-\ \mathrm{ADU}^{-1}$. We measure the Atik dark current and read noise in continuous exposure mode at $-15\ ^\circ\mathrm{C}$ to be $\sim 5\ \mathrm{ADU\ s}^{-1}$ and 25 ADU respectively. The FLI cameras are read with 16-bit resolution at $12\ \mathrm{MHz}$, and have a gain of $0.8\ e^-\ \mathrm{ADU}^{-1}$. We measure the FLI dark current and read noise in non-continuous exposure mode at $-10\ ^\circ\mathrm{C}$ to be $\sim 0.05\ \mathrm{ADU\ s}^{-1}$ and 18 ADU respectively. The Atik cameras provide cooling to a maximum of 38° C below ambient using a two-stage Peltier and a fan. The FLI cameras provide thermoelectric cooling to a maximum of 55° C below ambient.

Each camera is equipped with a Canon $24\ \mathrm{mm}\ f/1.4$ USM L II lens with a $17\ \mathrm{mm}$ aperture. These lenses provide a field-of-view (FoV) of $53^\circ \times 74^\circ$ per camera and an image scale of $\sim 1'\ \mathrm{pixel}^{-1}$. They are slightly defocused to prevent saturation of the $m_V = 4$ stars

[5] http://www.atik-cameras.com/
[6] http://www.flicamera.com/

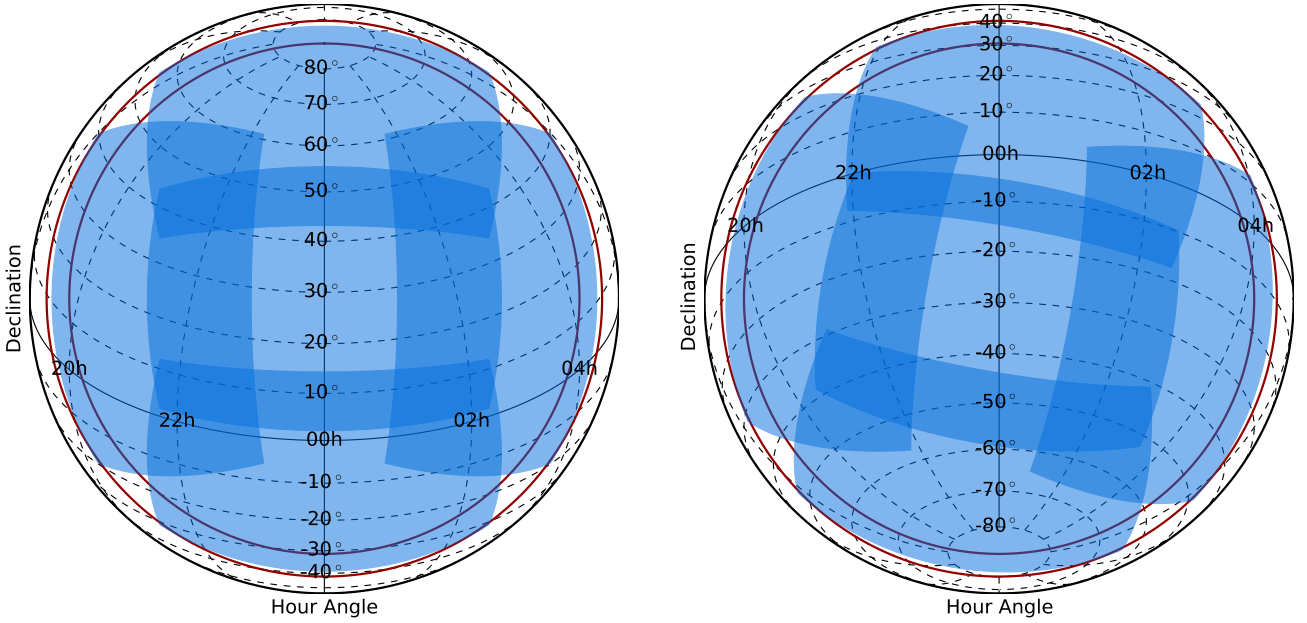

Figure 2.2: Field-of-view for the northern (*left*) and southern (*right*) station. The coverage of the individual CCDs are indicated in blue. The red lines indicate airmass 2 and 3. The southern station was rotated $\sim 10^\circ$ eastwards to minimize obscuration by the MarLy telescope.

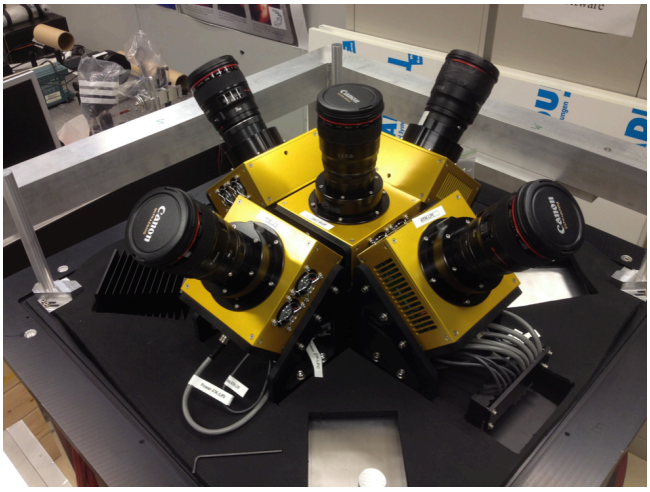

Figure 2.3: Atik cameras and 24 mm lenses of the northern station mounted on the base of the camera box during testing at Leiden Observatory.

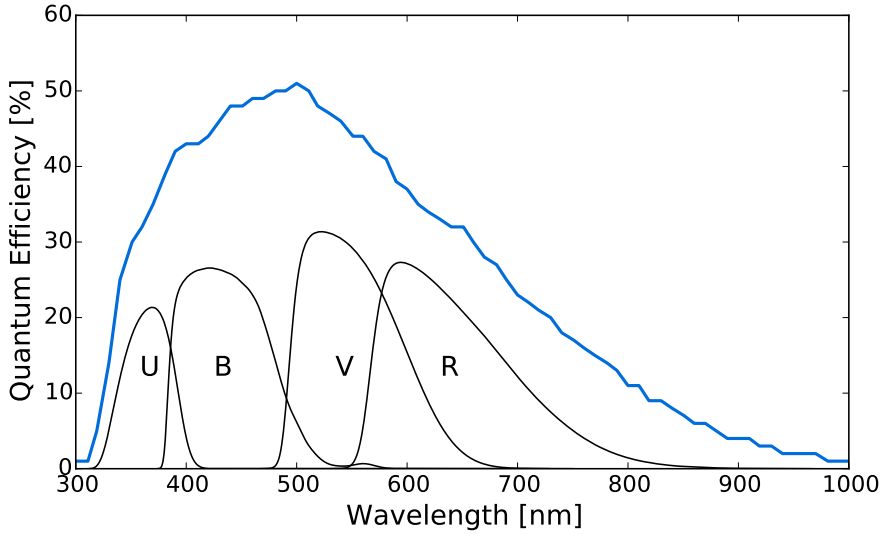

Figure 2.4: Quantum efficiency as a function of wavelength for the Kodak KAI-11002 CCD, as provided by the manufacturer. The peak quantum efficiency is 50% at 500 nm. The U, B, V and R filters are indicated on an arbitrary scale for comparison, and no filter is used in the MASCARA optics.

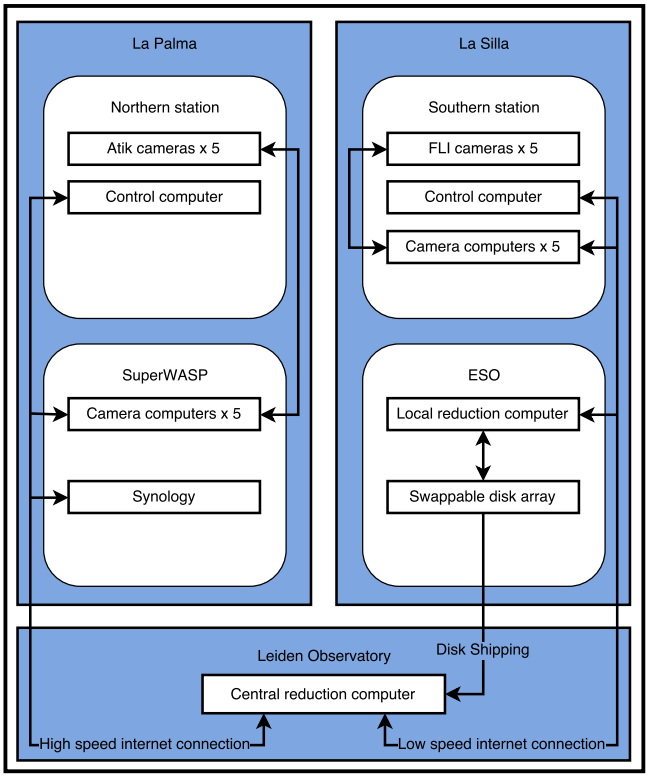

Figure 2.5: Schematic representation of the MASCARA project, showing the cameras and computers at the northern and southern station, and the data centre.

and reduce the impact of pixel-to-pixel sensitivity variations. The cameras are not equipped with any filters.

2.2.4 Electronics and computing

Figure 2.5 shows a schematic overview of the hardware used at the northern and southern stations and the data centre at Leiden Observatory. Each station is operated by six computers, comprising one control computer and five camera computers. A GPS clock is used for accurate time-keeping and three sensors monitor the temperature and humidity in the enclosure, camera box and electronics cabinet. Two uninterruptible power supplies (UPSs) channel power to the station.

The northern station is operated in collaboration with SuperWASP (Pollacco et al., 2006). The control computer and Globalsat BU353S4 GPS clock are located inside the MASCARA enclosure, whereas the camera computers, data storage, and UPSs are positioned inside the SuperWASP enclosure. For the first eighteen months of operations the camera computers were connected to the cameras through 20-m USB cables, but these were replaced by USB optical fibres in August 2016 after being identified as a source of unreliability. All computers are HP ProDesk 490 G1 computers running Windows 8, containing

a 500 GB SSD and a 4 TB HDD. Additional data storage and back-up is provided by a Synology DS1813+ data storage system operating in RAID-6, resulting in 22 TB of effective disk space, which is enough for up to four weeks of raw and reduced data. The light curves produced by the northern station are transferred to the data centre at Leiden Observatory on daily basis through a high speed internet connection. Weather information is obtained from the SuperWASP weather station.

All control and camera computers of the southern station are located inside the MASCARA enclosure. Rack-mounted Dell Poweredge R230 E3-1240 v5 computers are used running Windows 10. Each computer contains a 1 TB SSD and an 8 TB HDD. For timekeeping, a Galleon NTS-4000-GPS-R GPS server is used. An optical fibre connects the station to the local ESO server room where the local reduction computer, a Dell Poweredge R730xd 2x Xeon E5-2660 v3, provides 64 TB of effective storage on a RAID-6 system, which is enough for three months of raw and reduced data. The light curves produced by the southern station are transferred to the data centre at Leiden Observatory by means of disk shipping every three months, using two 8 TB swappable disks. To optimize our workflow and spot potential problems with the data early, additional analysis of the light curves is performed on-site using the local reduction computer. Weather information is obtained from the available La Silla weather stations.

At the MASCARA data centre at Leiden Observatory we have the central reduction computer, a Dell Poweredge R720xd 2x Xeon E5-2660, which is used for all further analysis of the data taken by the MASCARA stations. It currently provides 44 TB of effective disk space on a RAID-6 system, and will be expanded as needed in the future. In addition to the data archive kept on the central reduction computer the data are also backed-up to separate disks.

2.3 Nominal operations

Each MASCARA station is fully automated, and is operated through python software running on the control computer. Each of the cameras is controlled by its own camera computer, which is slaved to the control computer. The cameras are cooled to -15° C during the night. Observations are taken in continuous exposure mode at fixed sidereal times with an integration time of 6.4 sidereal seconds. We opted for observations at fixed sidereal times to make it possible for difference imaging techniques to be applied to the data, despite the fixed pointings. However, this feature is currently not used in the data analysis. The exposure time was motivated by the saturation level of bright stars, read-time of the detector, and the desire to fit an integer number of exposures in one sidereal day.

Preparations for the night's observations start when the sun altitude passes 0°. Each camera starts by taking a series of calibration frames consisting of twenty bias frames, dark frames and dome flats. The dome flats are only taken for instrumental monitoring purposes and are not used for the data analysis. The darks and flats are taken in continuous exposure mode with the same 6.4 second exposure time as the science observations. When the sun altitude passes -10° the weather conditions are assessed. The weather is considered suitable for observing if all of the following conditions are met:

- No rain is detected.

- The outside humidity is below 80%.
- The outside temperature exceeds 0° C.
- The wind speed is below 50 km h^{-1}.
- The sky temperature is below -25° C, which is indicative of clear skies.
- The humidity inside the enclosure is below 90%.
- The temperature inside the camera box is below 50° C.
- Communication with the weather station and the humidity sensors is working.

If all conditions are met at the beginning of the night, the dome is opened and science images are taken. If any of the conditions cease to be met the dome is closed and is not re-opened until all conditions are met again for fifteen consecutive minutes. The observations end when the sun altitude again passes -10°. At this time the dome is closed and a second series of calibration frames is taken.

During the day, an on-site reduction pipeline is run on the data taken during the preceding night. The data products of this pipeline are transferred to Leiden Observatory whereas the raw data is backed-up on the HDD drives of the camera computers and (for the northern station) the Synology storage system. Sufficient storage space is present to archive at least four weeks of raw data before deletion. In principle, this will allow for the search for transient events in the raw data.

2.4 Data analysis

The MASCARA data analysis pipeline consists of two consecutive parts: the on-site reduction pipeline discussed here, and the post-processing pipeline which will be described in an forthcoming paper.

2.4.1 On-site reduction pipeline

Because each of the five cameras takes one 22 MB image every 6.4 seconds, a single station produces up to 600 GB of raw data per night. Neither the transfer nor the long-term saving of the raw data is feasible for budgetary reasons. Instead, an on-site reduction pipeline performs image calibration, astrometry and photometry, producing light curves and binned images which amount to $\sim$25 GB per night per station. For the northern station these data products are transferred to Leiden data centre via the internet. For the southern station the data are shipped to Leiden on disk every three months.

2.4.1.1 Calibration and astrometry

Biases, dark frames, and dome flats taken at the beginning of the night are processed to produce a master dark and master flat, as is done for the calibration frames taken at the end of the night. The mean μ_b and rms σ_b of the master bias is used to asses the quality of the darks. Any dark with a mean, μ_d, exceeding $\mu_b + 2\sigma_b$ is rejected and the remaining

darks are averaged together to create the master dark. If there are fewer than ten good darks, no master dark is created and the last master dark from a previous night is used instead. Although a master flat is created, it is not used in our analysis because we found that including the flatfield correction reduced the quality of the photometry. We believe this reduction in photometric quality is a result of large scale non-uniformity in the illumination used, resulting in insufficient stability in the flatfield images. The master dark is subtracted from each science frame to correct for the bias and darkcurrent of the camera, as well as providing a first-order correction for hot pixels.

The pipeline uses the All-Sky Compiled Catalogue (ASCC, Kharchenko, 2001; Kharchenko and Roeser, 2009) as input for the astrometry and photometry. Stars brighter than $m_V = 7$, which typically number $1,500$ stars per image, are used to find the astrometric solution. The solution consists of the standard world coordinate system (WCS) transformations and two distortion polynomials. The distortion polynomials are necessary to correct for a predominantly radial offset between the WCS positions and the observed positions. We use sixth-order polynomials in the WCS positions without higher-order cross-terms to fit the residuals between the observed and the WCS-only positions.

The astrometric solution is updated at the beginning of the night, at every fiftieth image in the exposure sequence and after interruptions in the data taking. The parameters of the WCS transformations are only updated when the astrometric solution has changed by more than 2 pixels, otherwise only the distortion polynomials are updated.

2.4.1.2 Binned images

Every sequence of fifty images is stacked to create a binned image. Because the cameras have a fixed pointing, significant shifts need to be applied to the images to correct for the motion of the stars. In addition, the large FoV means the magnitude and direction of the shifts vary across the image. Therefore each image is divided into tiles of 32×32 pixels, discarding four rows at the top and bottom of the image and eight columns on both the left and right. The centre of each of these tiles is subsequently shifted to its position at the mid-time of the fifty images, using only the WCS transformations. Therefore, tiles are shifted in time by a maximum of 160 seconds and the maximum offset on the position of the pixels near the edge of a tile is 0.3 pixels. Tiles are then added to the stack using nearest neighbour interpolation, introducing a maximum offset of 0.7 pixels. When the last image has been added to the stack, it is divided by the total number of individual images added at each pixel to produce the binned image. The binned images are saved using the *Hcompress*[7] algorithm using a scale parameter of one, resulting in file sizes of 5 MB that then total ~ 0.5 GB per camera per night. The binned images allow us to store all of the collected data at reduced cadence and make it possible to study fainter stars.

2.4.1.3 Photometry

Aperture photometry is performed on each individual image for stars with $2 < m_V < 8.4$ in the ASCC catalogue, which typically number $6,500$ stars per image. The CCD coordinates of the stars are obtained using the astrometric solution, and aperture photometry is performed in apertures of 2.5 and 4.5 pixels. The sky background is estimated in an annulus

[7] `http://www.stsci.edu/software/hcompress.html`

between 6 and 21 pixels. We refer to this photometry as the "fast" light curves. "Slow" light curves are similarly obtained by performing aperture photometry on the binned images for stars down to $m_V < 10$, which typically number $40,000$ stars per image. Photometry on the binned images is performed before compression. The astrometric corrections are re-evaluated on the binned image before computing the star positions. For the slow lightcurves, photometry is performed in apertures of 2.5, 3.5, 4.5, and 5.5 pixels, and the sky background is estimated in an annulus between 6 and 21 pixels. The 6.4 second fast cadence and 320 second slow cadence lightcurves are saved in the HDF5 file format resulting in file sizes of $\sim$3 GB and $\sim$0.5 GB per camera per night.

The on-site reduction pipeline takes between 6-10 hours to complete for a full night of data. Figures showing the reduced lightcurves of several bright stars are automatically produced each night for each camera and sent to the MASCARA team to serve as a daily monitor of the MASCARA system.

2.5 Performance

The northern station was commisioned on La Palma in October 2014. The southern station will be commissioned in early 2017. In this section, we discuss the performance and data quality of the northern station using the first year of data.

2.5.1 Station performance

After one month of operation, the northern station experienced an increasing number of camera failures. Subsequently, observations ceased completely at the end of November 2014. The cause of the camera failures was identified as submersion of the amplifier units on the $20-\mathrm{m}$ USB cables in the cable duct between the MASCARA station and the SuperWASP enclosure. The USB cables were replaced late January 2015, making sure the amplifiers were located inside the SuperWASP enclosure. Figure 2.6 presents the observing statistics for the year 2015, showing the number of dark hours, hours of good weather, and hours of data taken per night. On average, about 22% of good weather was lost to camera failures, mostly in winter. We carefully monitored these failures and identified humidity, cross-talk between the cables, and grounding as possible causes for the failures. In August 2016, we replaced the USB cables again, this time with USB optical fibres, and from that moment we have had nearly perfect (99%) uptime on the cameras.

In March 2015, temperature-control of the camera box was lost when the heat exchanger failed. Because the cameras themselves have limited ability to cool relative to the camera box ambient temperature T_{cb}, we had to change the temperature of the cameras to be $-15\ ^{\circ}\mathrm{C}$ when possible, and $T_{\mathrm{cb}} - 40\ ^{\circ}\mathrm{C}$ otherwise. In July 2015, an on-site inspection of the heat exchanger found that the failure had most likely been caused by a dust storm from the Sahara desert (Calima). Because it was probable that a new heat exchanger would break down in the same fashion, a decision was made not to replace the heat exchanger. Despite a slight increase in thermal noise, the impact of losing the heat exchanger has been minimal and we still easily achieve our original target precision of 1% per hour. For the southern station, we changed the design to cool the camera box by means of air-cooled Peltiers.

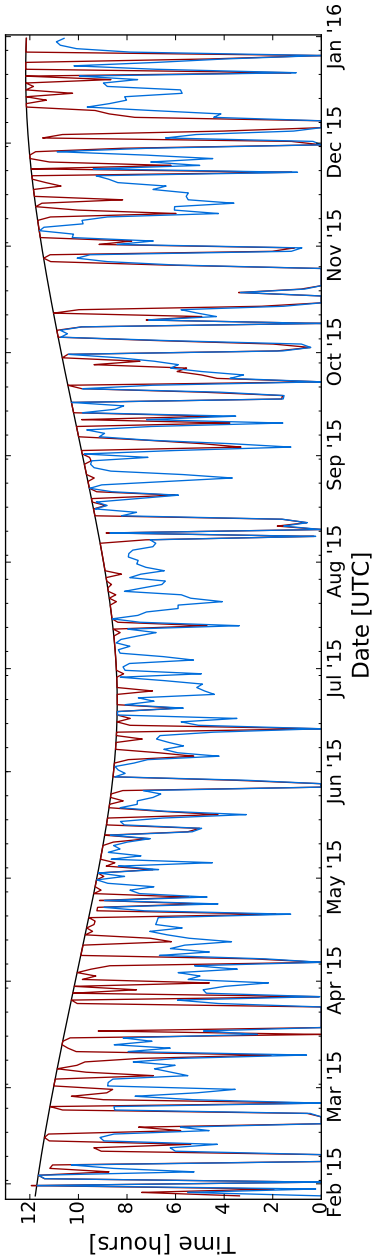

Figure 2.6: Observing statistics of 2015 for the northern station. The black line shows the duration of the night, the red line the amount of time the dome was open (i.e. the weather conditions were met), and the blue line the time data was taken averaged over the five cameras.

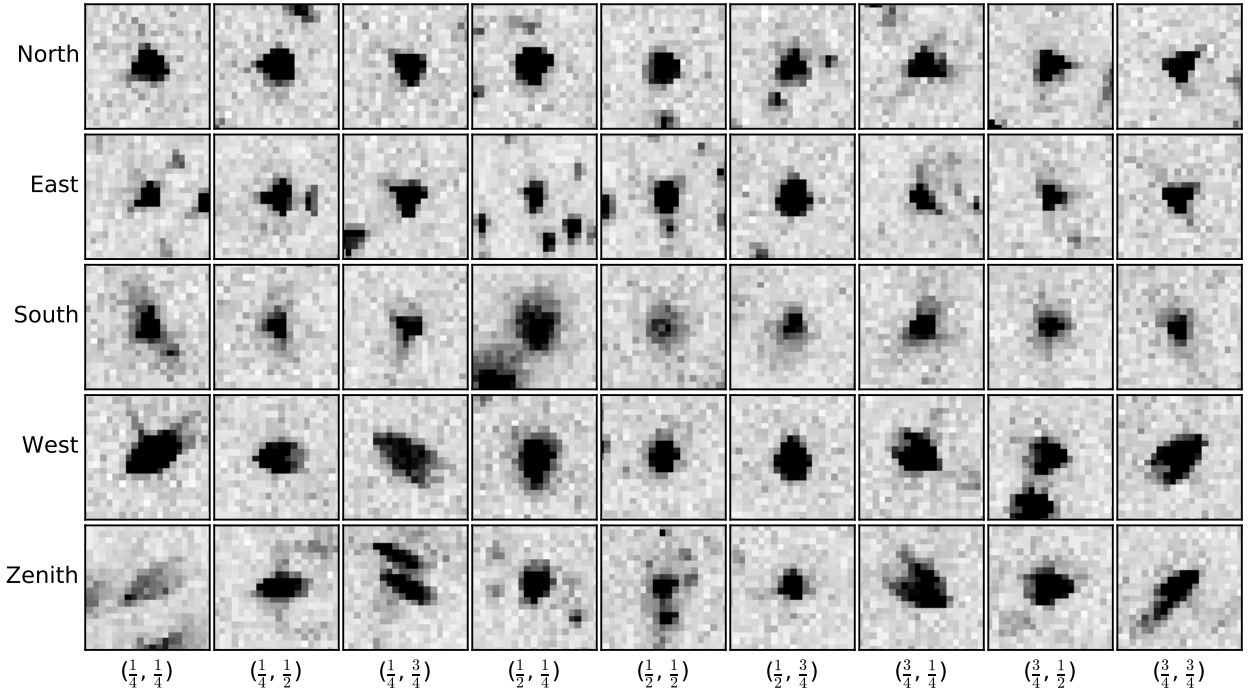

Figure 2.7: Representative PSFs for the cameras of the northern station, taken from the 6.4 s exposures made by the cameras on July 7 2016 23:42:16 UT. Stars with $6 < m_V < 7$ were selected close to the points of a 3×3 grid across the CCD with coordinates at $\frac{1}{4}$, $\frac{1}{2}$ and $\frac{3}{4}$ the size of the image in both x and y. The colour scale of each PSF was adjusted to run from -3 to 9 times the standard deviation on the local background. Near the centre (column $(\frac{1}{2}, \frac{1}{2})$) the PSFs are symmetric, whereas toward the edges they are distorted by varying degrees of coma that are introduced by the optics.

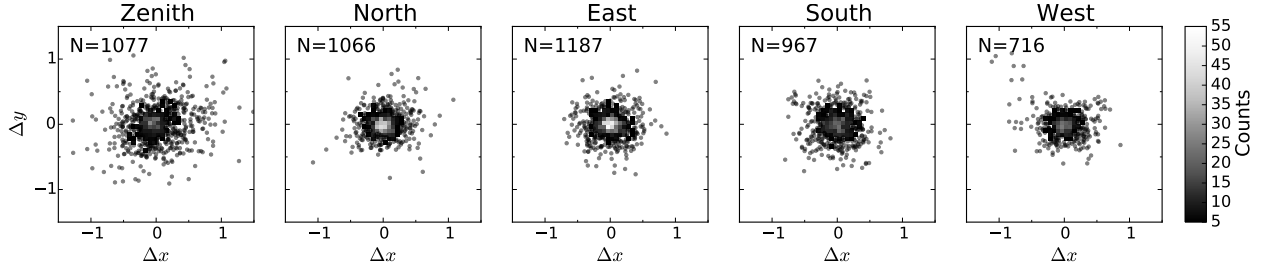

Figure 2.8: Residuals between the observed and predicted stellar position for the cameras of the northern station for an image taken on July 11 2016 00:05:08 UT. Each panel shows the difference in the observed and predicted x, y positions for approximately $1,000$ stars used in the astrometric solution. Typical standard deviations in both the x and y residuals are $\sim$0.2 pixels for the north, east, south and west cameras and $\sim$0.3 pixels for the zenith camera, probably due to stronger vignetting.

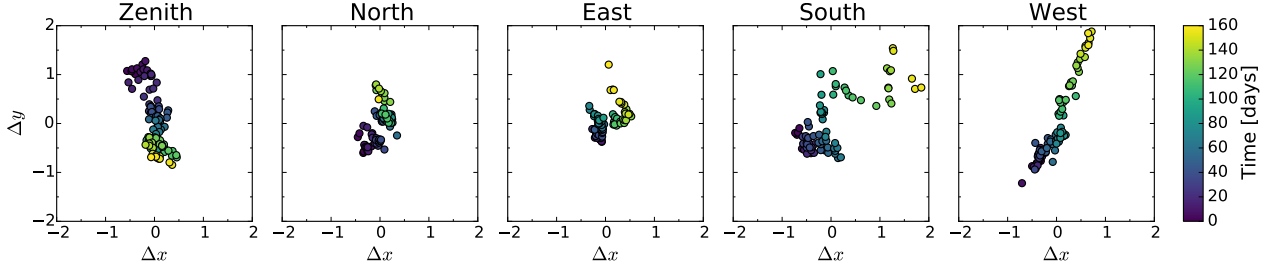

Figure 2.9: Change in the pointing of the cameras of the northern station during a 160 day period between July 16 2015 and December 23 2015. Each panel shows the mean subtracted x, y position of a particular star at a fixed sidereal time, chosen such that its location is close to the centre of the CCD. The panels show drifts in the pointing of the individual cameras of 1–2 pixels over this five months period.

2.5.2 The point spread function and astrometry

Figure 2.7 shows the point spread function (PSF) of stars with $6 < m_V < 7$ on a 3×3 grid across the CCDs of the northern station. The PSFs show the effects of the slight defocus and aberrations inherent to wide field optical systems, most importantly coma. Stars in the centre of the CCD have symmetric PSFs whereas those in the corners are strongly distorted.

Figure 2.8 shows the residuals between the detected stellar positions and the positions predicted by the astrometric solution for images taken on July 11 2016 00:05:08 UT. The residuals show a symmetric distribution around zero with typical standard deviation of $\sim$0.2 pixels in both x and y for the north, east, south and west cameras. The standard deviation on the residuals of the zenith camera is slightly larger at $\sim$0.3 pixels, which is likely caused by stronger vignetting in this camera resulting in larger uncertainties in the measured stellar positions. Figure 2.9 shows the change in the x, y position of a fixed point on the sky at a fixed sidereal time over an observing season. In the ideal case, when the MASCARA cameras undergo no changes in pointing, the x, y positions stay constant at the origin. It can be seen that the pointing of the cameras changes by only a few pixels over the 160 day period shown. These are most likely caused by thermal expansion and contraction of components such as the inner frame and the lens mounts. Overall, the pointing stability of the cameras are of the order of $1-2$ pixels over long timescales. Not shown in the figure are the typical nightly variations in the pointing that are caused by thermal settling of the lens-camera system, which is typically of the order of a few tenths of pixels.

2.5.3 Photometry

Figure 2.10 shows an example of a raw light curve taken by the northern station. Two kinds of spatial systematics are evident in the lightcurve, vignetting and intrapixel variations. The vignetting is responsible for the overall shape of the lightcurve and is the result of a decrease in the transmission of the optics for off-axis light rays found in many wide-field optical systems. Intrapixel variations, suspected to be mainly due to the microlens array blocking a changing fraction of the total light as the star moves across the CCD, are responsible for sinusoidal modulations seen most clearly in the zenith camera. Not directly visible in this lightcurve are the effects of temporal systematics (e.g. atmospheric transmission) and PSF variations, the latter of which modifies the fraction of the total starlight inside the photometric aperture.

A detailed description of the analysis required to remove these systematic effects is beyond the scope of this text, but will be given in a forthcoming paper. Here we briefly outline the analysis so we can discuss the quality of the final light curves. In short, we employ a version of the coarse decorrelation algorithm (Collier Cameron et al., 2006) that was altered to include corrections for MASCARA's spatial systematics in order to remove the the spatial and temporal systematics present in the data. Next, the data are binned by 50 points to a cadence of 320 seconds. Finally, the PSF variations are corrected by fitting sinusoids in the local sidereal time to the binned data for each individual star.

Figure 2.11 shows the RMS scatter on the final binned light curves for the west camera of the northern station. We achieve an RMS of $\sim$2% at $m_V = 8.4$ going down to $\sim$0.5% at $m_V = 4$, and similar results for the other cameras. At the faint end performance is limited

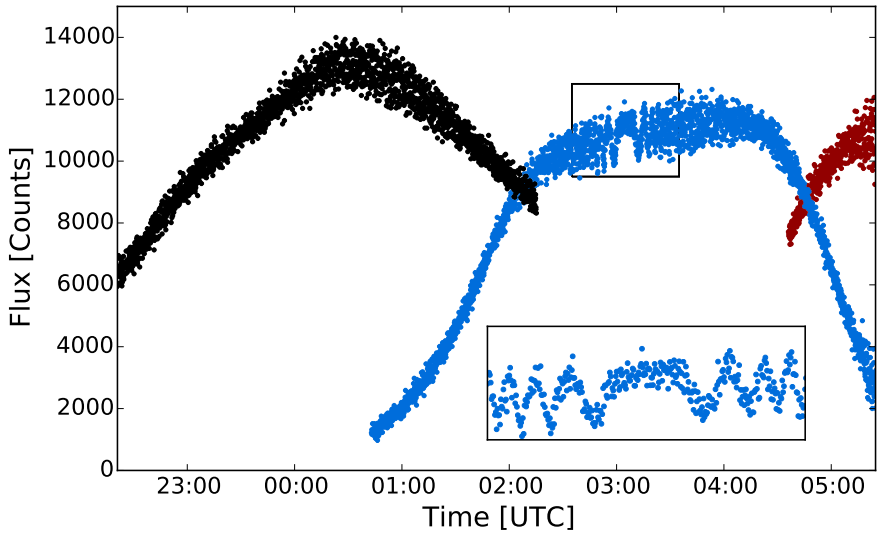

Figure 2.10: Raw lightcurve of HD189733 taken by the northern station on June 18 2015. The photometry in the 2.5 pixel aperture is shown for the west (red), zenith (blue) and east (black) cameras. The effects of vignetting are visible for all cameras, causing a decrease in flux near the edges of the CCD. The effects of intrapixel variations are most visible in the zenith camera, causing the sinusoidal modulations in the centre of the light curve.

by the photon noise of the sky background, whereas at the bright end the limiting factors are scintillation noise and residual systematics.

2.6 Discussion and conclusion

In the magnitude range targeted by MASCARA we expect to find a few (2-5) hot Jupiters around Sun-like (FGK) stars and a similar number around earlier spectral types (Snellen et al., 2012). To show that MASCARA is indeed capable of finding these sorts of systems, as well as demonstrate its potential for variable star research, Fig. 2.12 shows the phase-folded light curves for the known transiting exoplanet host HD189733 and the star RR Lyrae. HD189733 is a magnitude $m_V = 7.7$ star orbited by a hot Jupiter with a period of $P = 2.21857312$ days and a transit depth of $\sim$2.2% (Bouchy et al., 2005). The transit is clearly visible in the folded MASCARA data, which have an RMS of $\sim 1\%$. RR Lyrae is a magnitude $m_V = 7.1$ star that shows, and gives its name to, a type of periodic variability. For RR Lyrae this variability has a period of $P = 0.56677439$ days and the data have been folded to twice this period.

A number of surveys with a similar all-sky design, but targeting fainter stars, are in various stages of development and operation, for example HATPI[8], Evryscope (Law et al., 2015) and the Fly's Eye Camera System (Pál et al., 2013). These surveys employ a similar strategy of utilizing multiple cameras attached to a single mount to survey large fractions of the

[8] `http://hatpi.org/`

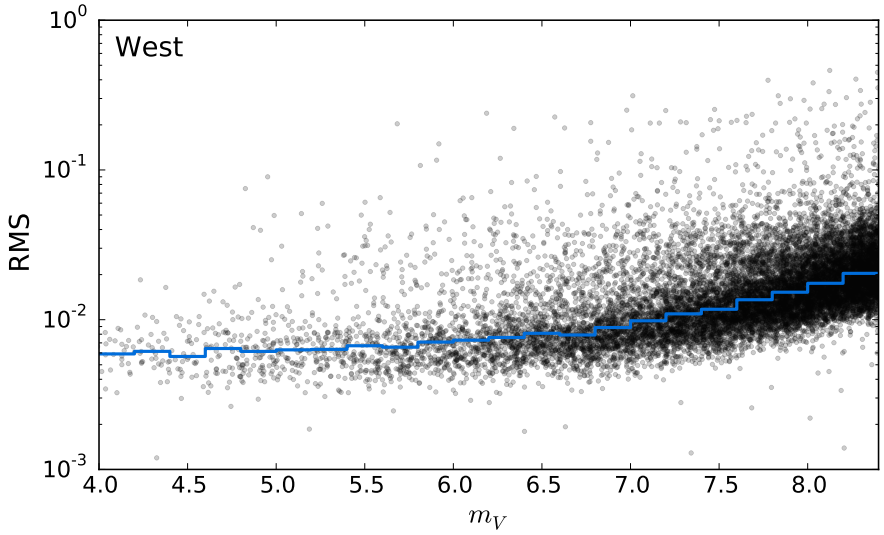

Figure 2.11: RMS achieved for the west camera of the northern station during the second quarter of 2015. Shown are the RMS on the five-minute binned lightcurves of individual stars with >500 data points (black points) and the median relation in bins of $\Delta m_V = 0.2$ (blue line). We achieve an RMS of $\sim$0.5% at the bright end of our magnitude range and $\sim$2% at the faint end. Similar RMS is achieved by the other cameras.

visible sky simultaneously, but they employ tracking on this mount as opposed to MASCARA's fixed pointings. Besides MASCARA, several other transit surveys searching for targets suitable for characterization have come online in recent years, for example the Next Generation Transit Survey (NGTS), the Kilodegree Extremely Little Telescope (KELT), the TRAnsiting Planets and PlanetesImals Small Telescope (TRAPPIST) and MEarth (West et al., 2016; Pepper et al., 2007; Jehin et al., 2011; Nutzman and Charbonneau, 2008). The NGTS focuses on achieving greater precision on fainter stars ($m_V < 13$) to push towards Neptune- and Earth-sized planets that are suitable for characterization with the James Web Space Telescope (JWST) and the European Extremely Large Telescope (E-ELT). The KELT survey targets stars with magnitudes $8 < m_V < 11$, just below the primary target population of MASCARA. They have recently published the detection of a planet around KELT-11 (Pepper et al., 2016), their brightest confirmed planet host to date at $m_V = 8.0$. TRAPPIST and MEarth target M-dwarfs in an effort to detect Earth-size planets, resulting in the detection of GJ1214b (Charbonneau et al., 2009), GJ 1132b (Berta-Thompson et al., 2015), and TRAPPIST-1b and c (Gillon et al., 2016). However, MASCARA aims to provide *continuous* and *all-sky* coverage of targets in the magnitude range $4 < m_V < 8$, significantly expanding the discovery space towards brighter stars.

During the MASCARA design phase NASA approved the Transiting Exoplanet Survey Satellite (TESS, Ricker et al., 2015), whose all-sky survey will include the same magnitude range as MASCARA. Fortunately, with a TESS launch date of early 2018, MASCARA has a head start of several years. Furthermore, for a large part of the sky TESS will monitor stars for only four weeks. This will allow for an interesting synergy between MASCARA and

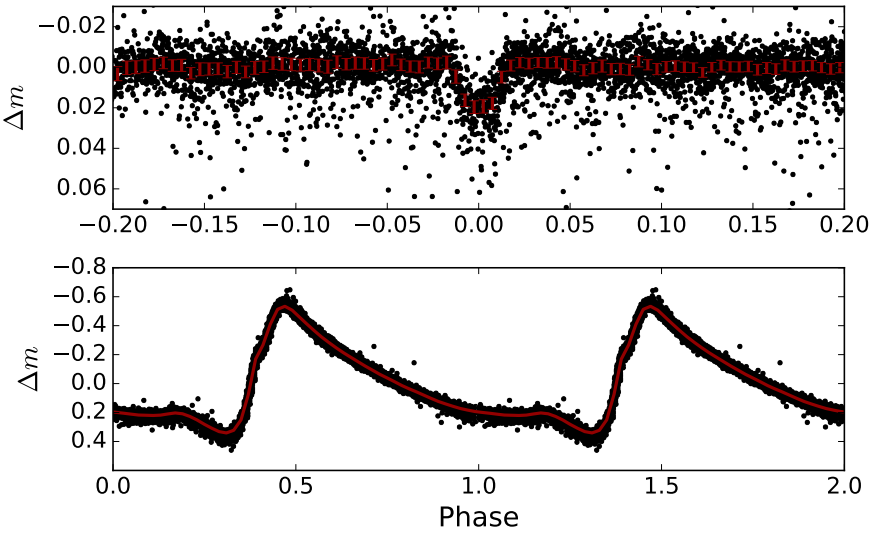

Figure 2.12: Light curves of HD189733 (*top*) and RR Lyrae (*bottom*). For HD189733 the reduced data (black points) have been folded to the orbital period of HD189733b and the folded light curve has been binned by 0.005 in phase (red errorbars). The errorbars have been scaled by a factor five for clarity. For RR Lyrae the reduced data has been folded to twice the period of its variability (black points) and the folded lightcurve has been binned by 0.02 in phase (red line). We note that the scatter away from the red line is primarily caused by residual systematics in the data taken by the zenith camera, which suffers from the strongest vignetting.

TESS. Although the photometric precision of MASCARA is between one and two orders of magnitude lower than that achieved by TESS, it will provide light curves of at least several years for all targets, thus providing valuable information on long-term variability and revealing longer period planets in the combined TESS + MASCARA data.

In conclusion, the northern and southern MASCARA stations survey all bright stars, $4 < m_V < 8$, and the northern station has been shown to achieve a precision of 1.5% per five minutes, well in excess of the original goal of 1% per hour. In addition to its primary goal of finding transiting exoplanets MASCARA will also create an archive of $70,000$ light curves suitable for studying variable stars. As such, MASCARA is capable of finding nearly any hot Jupiter transiting a solar-type star in the targeted magnitude range, and will provide new targets for exoplanet characterization.

Acknowledgements

We thank the anonymous referee for their helpful comments and suggestions. IS acknowledges support from a NWO VICI grant (639.043.107). This project has received funding from the European Research Council (ERC) under the European Union's Horizon 2020 research and innovation programme (grant agreement nr. 694513). We thank Johan Pragt, Sjouke Kuindersma, Menno de Haan and Eddy Elswijk of ASTRON and the NOVA Optical IR group for their aid in production of the enclosure and final testing at Dwingeloo.

We thank Alan Chopping and Juerg Rey of the Isaac Newton Group for their support during the commissioning of the northern station. We extend our thanks to the Director and staff of the Isaac Newton Group of Telescopes for their support of the MASCARA operations. We have benefited greatly from the publicly available programming language Python, including the numpy, matplotlib, pyfits, scipy and h5py packages.

Bibliography

Alonso, R., Brown, T. M., Torres, G., Latham, D. W., Sozzetti, A., Mandushev, G., Belmonte, J. A., Charbonneau, D., Deeg, H. J., Dunham, E. W., O'Donovan, F. T., and Stefanik, R. P. (2004). TrES-1: The Transiting Planet of a Bright K0 V Star. *ApJ*, 613:L153–L156.

Bakos, G., Noyes, R. W., Kovács, G., Stanek, K. Z., Sasselov, D. D., and Domsa, I. (2004). Wide-Field Millimagnitude Photometry with the HAT: A Tool for Extrasolar Planet Detection. *PASP*, 116:266–277.

Bakos, G. Á., Kovács, G., Torres, G., Fischer, D. A., Latham, D. W., Noyes, R. W., Sasselov, D. D., Mazeh, T., Shporer, A., Butler, R. P., Stefanik, R. P., Fernández, J. M., Sozzetti, A., Pál, A., Johnson, J., Marcy, G. W., Winn, J. N., Sipőcz, B., Lázár, J., Papp, I., and Sári, P. (2007). HD 147506b: A Supermassive Planet in an Eccentric Orbit Transiting a Bright Star. *ApJ*, 670:826–832.

Barge, P., Baglin, A., Auvergne, M., Rauer, H., Léger, A., Schneider, J., Pont, F., Aigrain, S., Almenara, J.-M., Alonso, R., Barbieri, M., Bordé, P., Bouchy, F., Deeg, H. J., La Reza, D., Deleuil, M., Dvorak, R., Erikson, A., Fridlund, M., Gillon, M., Gondoin, P., Guillot, T., Hatzes, A., Hebrard, G., Jorda, L., Kabath, P., Lammer, H., Llebaria, A., Loeillet, B., Magain, P., Mazeh, T., Moutou, C., Ollivier, M., Pätzold, M., Queloz, D., Rouan, D., Shporer, A., and Wuchterl, G. (2008). Transiting exoplanets from the CoRoT space mission. I. CoRoT-Exo-1b: a low-density short-period planet around a G0V star. *A&A*, 482:L17–L20.

Batalha, N. M., Borucki, W. J., Bryson, S. T., Buchhave, L. A., Caldwell, D. A., Christensen-Dalsgaard, J., Ciardi, D., Dunham, E. W., Fressin, F., Gautier, III, T. N., Gilliland, R. L., Haas, M. R., Howell, S. B., Jenkins, J. M., Kjeldsen, H., Koch, D. G., Latham, D. W., Lissauer, J. J., Marcy, G. W., Rowe, J. F., Sasselov, D. D., Seager, S., Steffen, J. H., Torres, G., Basri, G. S., Brown, T. M., Charbonneau, D., Christiansen, J., Clarke, B., Cochran, W. D., Dupree, A., Fabrycky, D. C., Fischer, D., Ford, E. B., Fortney, J., Girouard, F. R., Holman, M. J., Johnson, J., Isaacson, H., Klaus, T. C., Machalek, P., Moorehead, A. V., Morehead, R. C., Ragozzine, D., Tenenbaum, P., Twicken, J., Quinn, S., VanCleve, J., Walkowicz, L. M., Welsh, W. F., Devore, E., and Gould, A. (2011). Kepler's First Rocky Planet: Kepler-10b. *ApJ*, 729:27.

Berta-Thompson, Z. K., Irwin, J., Charbonneau, D., Newton, E. R., Dittmann, J. A., Astudillo-Defru, N., Bonfils, X., Gillon, M., Jehin, E., Stark, A. A., Stalder, B., Bouchy, F., Delfosse, X., Forveille, T., Lovis, C., Mayor, M., Neves, V., Pepe, F., Santos, N. C., Udry, S., and Wünsche, A. (2015). A rocky planet transiting a nearby low-mass star. *Nature* , 527:204–207.

Borucki, W. J., Caldwell, D., Koch, D. G., Webster, L. D., Jenkins, J. M., Ninkov, Z., and Showen, R. (2001). The Vulcan Photometer: A Dedicated Photometer for Extrasolar Planet Searches. *PASP*, 113:439–451.

Borucki, W. J., Koch, D., Basri, G., Batalha, N., Brown, T., Caldwell, D., Caldwell, J., Christensen-Dalsgaard, J., Cochran, W. D., DeVore, E., Dunham, E. W., Dupree, A. K., Gautier, T. N., Geary, J. C., Gilliland, R., Gould, A., Howell, S. B., Jenkins, J. M., Kondo, Y., Latham, D. W., Marcy, G. W., Meibom, S., Kjeldsen, H., Lissauer, J. J., Monet, D. G., Morrison, D., Sasselov, D., Tarter, J., Boss, A., Brownlee, D., Owen, T., Buzasi, D., Charbonneau, D., Doyle, L., Fortney, J., Ford, E. B., Holman, M. J., Seager, S., Steffen, J. H., Welsh, W. F., Rowe, J., Anderson, H., Buchhave, L., Ciardi, D., Walkowicz, L., Sherry, W., Horch, E., Isaacson, H., Everett, M. E., Fischer, D., Torres, G., Johnson, J. A., Endl, M., MacQueen, P., Bryson, S. T., Dotson, J., Haas, M., Kolodziejczak, J., Van Cleve, J., Chandrasekaran, H., Twicken, J. D., Quintana, E. V., Clarke, B. D., Allen, C., Li, J., Wu, H., Tenenbaum, P., Verner, E., Bruhweiler, F., Barnes, J., and Prsa, A. (2010). Kepler Planet-Detection Mission: Introduction and First Results. *Science*, 327:977.

Bouchy, F., Udry, S., Mayor, M., Moutou, C., Pont, F., Iribarne, N., da Silva, R., Ilovaisky, S., Queloz, D., Santos, N. C., Ségransan, D., and Zucker, S. (2005). ELODIE metallicity-biased search for transiting Hot Jupiters. II. A very hot Jupiter transiting the bright K star HD 189733. *A&A*, 444:L15–L19.

Brown, T. M. and Charbonneau, D. (2000). The STARE Project: a Transit Search for Hot Jupiters. In Garzón, G., Eiroa, C., de Winter, D., and Mahoney, T. J., editors, *Disks, Planetesimals, and Planets*, volume 219 of *Astronomical Society of the Pacific Conference Series*, page 584.

Butler, R. P., Marcy, G. W., Williams, E., Hauser, H., and Shirts, P. (1997). Three New "51 Pegasi-Type" Planets. *ApJ*, 474:L115–L118.

Charbonneau, D., Berta, Z. K., Irwin, J., Burke, C. J., Nutzman, P., Buchhave, L. A., Lovis, C., Bonfils, X., Latham, D. W., Udry, S., Murray-Clay, R. A., Holman, M. J., Falco, E. E., Winn, J. N., Queloz, D., Pepe, F., Mayor, M., Delfosse, X., and Forveille, T. (2009). A super-Earth transiting a nearby low-mass star. *Nature* , 462:891–894.

Charbonneau, D., Brown, T. M., Latham, D. W., and Mayor, M. (2000). Detection of Planetary Transits Across a Sun-like Star. *ApJ*, 529:L45–L48.

Charbonneau, D., Brown, T. M., Noyes, R. W., and Gilliland, R. L. (2002). Detection of an Extrasolar Planet Atmosphere. *ApJ*, 568:377–384.

Collier Cameron, A., Guenther, E., Smalley, B., McDonald, I., Hebb, L., Andersen, J., Augusteijn, T., Barros, S. C. C., Brown, D. J. A., Cochran, W. D., Endl, M., Fossey, S. J., Hartmann, M., Maxted, P. F. L., Pollacco, D., Skillen, I., Telting, J., Waldmann, I. P., and West, R. G. (2010). Line-profile tomography of exoplanet transits - II. A gas-giant planet transiting a rapidly rotating A5 star. *MNRAS*, 407:507–514.

Collier Cameron, A., Pollacco, D., Street, R. A., Lister, T. A., West, R. G., Wilson, D. M., Pont, F., Christian, D. J., Clarkson, W. I., Enoch, B., Evans, A., Fitzsimmons, A.,

Haswell, C. A., Hellier, C., Hodgkin, S. T., Horne, K., Irwin, J., Kane, S. R., Keenan, F. P., Norton, A. J., Parley, N. R., Osborne, J., Ryans, R., Skillen, I., and Wheatley, P. J. (2006). A fast hybrid algorithm for exoplanetary transit searches. *MNRAS*, 373:799–810.

Gillon, M., Jehin, E., Lederer, S. M., Delrez, L., de Wit, J., Burdanov, A., Van Grootel, V., Burgasser, A. J., Triaud, A. H. M. J., Opitom, C., Demory, B.-O., Sahu, D. K., Bardalez Gagliuffi, D., Magain, P., and Queloz, D. (2016). Temperate Earth-sized planets transiting a nearby ultracool dwarf star. *Nature* , 533:221–224.

Henry, G. W., Marcy, G. W., Butler, R. P., and Vogt, S. S. (2000). A Transiting "51 Peg-like" Planet. *ApJ*, 529:L41–L44.

Horne, K. (2001). Planetary Transit Searches: Hot Jupiters Galore. In Dent, W. R. F., editor, *Techniques for the Detection of Planets and Life beyond the Solar System*, page 5.

Jehin, E., Gillon, M., Queloz, D., Magain, P., Manfroid, J., Chantry, V., Lendl, M., Hutsemékers, D., and Udry, S. (2011). TRAPPIST: TRAnsiting Planets and PlanetesImals Small Telescope. *The Messenger*, 145:2–6.

Kharchenko, N. V. (2001). All-sky compiled catalogue of 2.5 million stars. *Kinematika i Fizika Nebesnykh Tel*, 17:409–423.

Kharchenko, N. V. and Roeser, S. (2009). VizieR Online Data Catalog: All-Sky Compiled Catalogue of 2.5 million stars (Kharchenko+ 2009). *VizieR Online Data Catalog*, 1280.

Konacki, M., Torres, G., Jha, S., and Sasselov, D. D. (2003). An extrasolar planet that transits the disk of its parent star. *Nature* , 421:507–509.

Law, N. M., Fors, O., Ratzloff, J., Wulfken, P., Kavanaugh, D., Sitar, D. J., Pruett, Z., Birchard, M. N., Barlow, B. N., Cannon, K., Cenko, S. B., Dunlap, B., Kraus, A., and Maccarone, T. J. (2015). Evryscope Science: Exploring the Potential of All-Sky Gigapixel-Scale Telescopes. *PASP*, 127:234.

Léger, A., Rouan, D., Schneider, J., Barge, P., Fridlund, M., Samuel, B., Ollivier, M., Guenther, E., Deleuil, M., Deeg, H. J., Auvergne, M., Alonso, R., Aigrain, S., Alapini, A., Almenara, J. M., Baglin, A., Barbieri, M., Bruntt, H., Bordé, P., Bouchy, F., Cabrera, J., Catala, C., Carone, L., Carpano, S., Csizmadia, S., Dvorak, R., Erikson, A., Ferraz-Mello, S., Foing, B., Fressin, F., Gandolfi, D., Gillon, M., Gondoin, P., Grasset, O., Guillot, T., Hatzes, A., Hébrard, G., Jorda, L., Lammer, H., Llebaria, A., Loeillet, B., Mayor, M., Mazeh, T., Moutou, C., Pätzold, M., Pont, F., Queloz, D., Rauer, H., Renner, S., Samadi, R., Shporer, A., Sotin, C., Tingley, B., Wuchterl, G., Adda, M., Agogu, P., Appourchaux, T., Ballans, H., Baron, P., Beaufort, T., Bellenger, R., Berlin, R., Bernardi, P., Blouin, D., Baudin, F., Bodin, P., Boisnard, L., Boit, L., Bonneau, F., Borzeix, S., Briet, R., Buey, J.-T., Butler, B., Cailleau, D., Cautain, R., Chabaud, P.-Y., Chaintreuil, S., Chiavassa, F., Costes, V., Cuna Parrho, V., de Oliveira Fialho, F., Decaudin, M., Defise, J.-M., Djalal, S., Epstein, G., Exil, G.-E., Fauré, C., Fenouillet, T., Gaboriaud, A., Gallic, A., Gamet, P., Gavalda, P., Grolleau, E., Gruneisen, R., Gueguen, L., Guis, V., Guivarc'h, V., Guterman, P., Hallouard, D., Hasiba, J., Heuripeau, F., Huntzinger, G., Hustaix, H., Imad, C., Imbert, C., Johlander, B., Jouret, M., Journoud, P., Karioty, F.,

Kerjean, L., Lafaille, V., Lafond, L., Lam-Trong, T., Landiech, P., Lapeyrere, V., Larqué, T., Laudet, P., Lautier, N., Lecann, H., Lefevre, L., Leruyet, B., Levacher, P., Magnan, A., Mazy, E., Mertens, F., Mesnager, J.-M., Meunier, J.-C., Michel, J.-P., Monjoin, W., Naudet, D., Nguyen-Kim, K., Orcesi, J.-L., Ottacher, H., Perez, R., Peter, G., Plasson, P., Plesseria, J.-Y., Pontet, B., Pradines, A., Quentin, C., Reynaud, J.-L., Rolland, G., Rollenhagen, F., Romagnan, R., Russ, N., Schmidt, R., Schwartz, N., Sebbag, I., Sedes, G., Smit, H., Steller, M. B., Sunter, W., Surace, C., Tello, M., Tiphène, D., Toulouse, P., Ulmer, B., Vandermarcq, O., Vergnault, E., Vuillemin, A., and Zanatta, P. (2009). Transiting exoplanets from the CoRoT space mission. VIII. CoRoT-7b: the first super-Earth with measured radius. *A&A*, 506:287–302.

Mayor, M. and Queloz, D. (1995). A Jupiter-mass companion to a solar-type star. *Nature* , 378:355–359.

McCullough, P. R., Stys, J. E., Valenti, J. A., Fleming, S. W., Janes, K. A., and Heasley, J. N. (2005). The XO Project: Searching for Transiting Extrasolar Planet Candidates. *PASP*, 117:783–795.

Nutzman, P. and Charbonneau, D. (2008). Design Considerations for a Ground-Based Transit Search for Habitable Planets Orbiting M Dwarfs. *PASP*, 120:317–327.

Pál, A., Mészáros, L., Csépány, G., Jaskó, A., Schlaffer, F., Vida, K., Mező, G., Döbrentei, L., Farkas, E., Kiss, C., Oláh, K., and Regály, Z. (2013). The Fly's Eye Camera System: An instrument design for large étendue time-domain survey. *Astronomische Nachrichten*, 334:932.

Pepper, J., Pogge, R. W., DePoy, D. L., Marshall, J. L., Stanek, K. Z., Stutz, A. M., Poindexter, S., Siverd, R., O'Brien, T. P., Trueblood, M., and Trueblood, P. (2007). The Kilodegree Extremely Little Telescope (KELT): A Small Robotic Telescope for Large-Area Synoptic Surveys. *PASP*, 119:923–935.

Pepper, J., Rodriguez, J. E., Collins, K. A., Johnson, J. A., Fulton, B. J., Howard, A. W., Beatty, T., Stassun, K. G., Isaacson, H., Colón, K. d., Lund, M. B., Kuhn, R. B., Siverd, R. J., Gaudi, B. S., Tan, T. G., Curtis, I., Stockdale, C., Mawet, D., Bottom, M., James, D., Zhou, G., Bayliss, D., Cargile, P., Bieryla, A., Penev, K., Latham, D. W., Labadie-Bartz, J., Kielkopf, J., Eastman, J. D., Oberst, T. E., Jensen, E. L. N., Nelson, P., Sliski, D. H., Wittenmyer, R. A., McCrady, N., Wright, J. T., and Relles, H. M. (2016). KELT-11b: A Highly Inflated Sub-Saturn Exoplanet Transiting the V=8 Subgiant HD 93396. *ArXiv e-prints*.

Pollacco, D. L., Skillen, I., Collier Cameron, A., Christian, D. J., Hellier, C., Irwin, J., Lister, T. A., Street, R. A., West, R. G., Anderson, D. R., Clarkson, W. I., Deeg, H., Enoch, B., Evans, A., Fitzsimmons, A., Haswell, C. A., Hodgkin, S., Horne, K., Kane, S. R., Keenan, F. P., Maxted, P. F. L., Norton, A. J., Osborne, J., Parley, N. R., Ryans, R. S. I., Smalley, B., Wheatley, P. J., and Wilson, D. M. (2006). The WASP Project and the SuperWASP Cameras. *PASP*, 118:1407–1418.

Ricker, G. R., Winn, J. N., Vanderspek, R., Latham, D. W., Bakos, G. Á., Bean, J. L., Berta-Thompson, Z. K., Brown, T. M., Buchhave, L., Butler, N. R., Butler, R. P., Chaplin, W. J.,

Charbonneau, D., Christensen-Dalsgaard, J., Clampin, M., Deming, D., Doty, J., De Lee, N., Dressing, C., Dunham, E. W., Endl, M., Fressin, F., Ge, J., Henning, T., Holman, M. J., Howard, A. W., Ida, S., Jenkins, J. M., Jernigan, G., Johnson, J. A., Kaltenegger, L., Kawai, N., Kjeldsen, H., Laughlin, G., Levine, A. M., Lin, D., Lissauer, J. J., MacQueen, P., Marcy, G., McCullough, P. R., Morton, T. D., Narita, N., Paegert, M., Palle, E., Pepe, F., Pepper, J., Quirrenbach, A., Rinehart, S. A., Sasselov, D., Sato, B., Seager, S., Sozzetti, A., Stassun, K. G., Sullivan, P., Szentgyorgyi, A., Torres, G., Udry, S., and Villasenor, J. (2015). Transiting Exoplanet Survey Satellite (TESS). *Journal of Astronomical Telescopes, Instruments, and Systems*, 1(1):014003.

Snellen, I. A. G., Stuik, R., Navarro, R., Bettonvil, F., Kenworthy, M., de Mooij, E., Otten, G., ter Horst, R., and le Poole, R. (2012). Ground-based search for the brightest transiting planets with the Multi-site All-Sky CAmeRA: MASCARA. In *Ground-based and Airborne Telescopes IV*, volume 8444 of *Proc. SPIE*, page 84440I.

West, R. G., Pollacco, D., Wheatley, P., Goad, M., Queloz, D., Rauer, H., Watson, C., Udry, S., Bannister, N., Bayliss, D., Bouchy, F., Burleigh, M., Cabrera, J., Chaushev, A., Chazelas, B., Crausaz, M., Csizmadia, S., Eigmüller, P., Erikson, A., Genolet, L., Gillen, E., Grange, A., Günther, M., Hodgkin, S., Kirk, J., Lambert, G., Louden, T., McCormac, J., Metrailler, L., Neveu, M., Smith, A., Thompson, A., Raddi, R., Walker, S. R., Jenkins, J., and Jordán, A. (2016). The Next Generation Transit Survey Becomes Operational at Paranal. *The Messenger*, 165:10–12.

3 Data calibration for the MASCARA and bRing instruments

Aims. MASCARA and bRing are photometric surveys designed to detect variability caused by exoplanets in stars with $m_V < 8.4$. Such variability signals are typically small and require an accurate calibration algorithm, tailored to the survey, in order to be detected. This paper presents the methods developed to calibrate the raw photometry of the MASCARA and bRing stations and characterizes the performance of the methods and instruments.
Methods. For the primary calibration a modified version of the coarse decorrelation algorithm is used, which corrects for the extinction due to the earth's atmosphere, the camera transmission, and intrapixel variations. Residual trends are removed from the light curves of individual stars using empirical secondary calibration methods. In order to optimize these methods, as well as characterize the performance of the instruments, transit signals were injected in the data.
Results. After optimal calibration an RMS scatter of 10 mmag at $m_V \sim 7.5$ is achieved in the light curves. By injecting transit signals with periods between one and five days in the MASCARA data obtained by the La Palma station over the course of one year, we demonstrate that MASCARA La Palma is able to recover 84.0%, 60.5% and 20.7% of signals with depths of 2%, 1% and 0.5% respectively, with a strong dependency on the observed declination, recovering 65.4% of all transit signals at $\delta > 0°$ versus 35.8% at $\delta < 0°$. Using the full three years of data obtained by MASCARA La Palma to date, similar recovery rates are extended to periods up to ten days. We derive a preliminary occurrence rate for hot Jupiters around A-stars of $>0.4\%$, knowing that many hot Jupiters are still overlooked. In the era of TESS, MASCARA and bRing will provide an interesting synergy for finding long-period (>13.5 days) transiting gas-giant planets around the brightest stars.

G.J.J. Talens, E.R. Deul, R. Stuik, O. Burggraaff, A.-L. Lesage, J.F.P. Spronck, S. N. Mellon, J.I. Bailey, III, E.E. Mamajek, M.A. Kenworthy and I.A.G Snellen

Accepted for publication in A&A.

3.1 Introduction

Exoplanet transit survey instruments, as with all astronomical instrumentation, have to take care of systematic effects in the data. Some of these systematics, such as airmass effects, clouds and point spread function (PSF) modulations are present in many of such surveys and general methods have been developed for their removal, for example SYSREM (Tamuz et al., 2005) and the trend filtering algorithm (TFA; Kovács et al., 2005). Both of these methods use an ensemble of observed stars to remove systematics that are common in many light curves. Other systematics are unique to specific surveys, such as shutter shadows (SuperWASP; Collier Cameron et al., 2006), scattered light from earth (CoRoT; Grziwa et al., 2012) and cosmic ray impact sensitivity variations (*Kepler*; Stumpe et al., 2012). The presence of these survey specific systematics means that, rather than using a general pipeline, a unique calibration pipeline is written for most surveys. Nevertheless, many of these pipelines are built around the same principle, using ensembles of stars to remove common systematics. The *Kepler* pre-search data conditioning (PDC; Stumpe et al., 2012; Smith et al., 2012) is a well-known example of such a pipeline. The data obtained by the MASCARA and bRing instruments also contains instrument specific systematics, caused by the stars moving across the detectors during the night. In this paper we describe the systematics present in the data obtained by the MASCARA and bRing surveys, and the calibration pipeline used to remove them.

The Multi-site All-Sky CAmeRA (MASCARA; Talens et al., 2017b) consists of two observing stations, one located at the Observatorio del Roque de los Muchachos in the northern hemisphere, and one located at La Silla observatory in the southern hemisphere. Each station employs five cameras, pointed at the cardinal directions and zenith, to observe all bright stars ($m_V < 8.4$) down to airmass three in order to detect transiting exoplanets. These exoplanets make ideal targets for atmospheric characterization at high spectral resolution. To date two new exoplanets have been found with MASCARA (Talens et al., 2017a, 2018; Lund et al., 2017), with several more candidates still awaiting conformation.

The β Pictoris b Ring project (bRing; Stuik et al., 2017) consists of two observing stations in the southern hemisphere, located at the Sutherland observing station and Siding Spring observatory. Each station employs two cameras, pointed to the east and west, to observe all bright stars ($m_V < 8.4$) with $\delta \lesssim -30°$. The main goal of bRing is to monitor the star β Pictoris for the predicted 2017/2018 Hill Sphere transit of the directly imaged exoplanet β Pic b in an attempt to detect circumplanetary material, such as a ring system similar to the one found around the exoplanet J 1407 b (Mamajek et al., 2012). Furthermore, bRing searches for evidence of stellar variability in the bright stars it monitors (Mellon et al., in prep).

Together MASCARA and bRing monitor all bright stars in the sky with a total of 14 cameras and provide near continuous coverage for stars with $\delta \lesssim -30°$; both surveys are sensitive to evidence of stellar variability from sources such as exoplanets (Talens et al., 2017a, 2018) and pulsations (Mellon et al., in prep). For convenience, each of the 14 cameras is referred to by a three letter identifier, with the first two letters identifying the observing site and the last letter the camera by its pointing direction, for example LSE for the east camera of the station at La Silla observatory, see Table 3.1 for the other identifiers.

The stations take synchronized observations of the sky at 6.4 sidereal second intervals for a total of 13500 observing slots per sidereal day. Each MASCARA exposure lasts the

Table 3.1: Summary of observing stations.

Instrument	Observatory	Site ID	Cameras	Camera IDs[a]
MASCARA	Roque de los Muchachos	LP (La Palma)	5	N,E,S,W,C
MASCARA	La Silla	LS (La Silla)	5	N,E,S,W,C
bRing	Sutherland	SA (South Africa)	2	E,W
bRing	Siding Spring	AU (Australia)	2	E,W

Notes. [a] The cameras pointing towards zenith are identified with a 'C' for 'central'.

full 6.4 sidereal seconds, while bRing alternates between taking 6.4 and 2.55 sidereal second exposures, to accommodate the bright ($m_V = 3.86$) β Pic system. Each exposure is uniquely identified by its LSTSEQ[1], an index indicating the 6.4 second exposure slot during which it was taken, and exposures taken at the same local sidereal time are identified using the LSTIDX, defined as $\text{LSTIDX} = (\text{LSTSEQ} \mod 13500)$.

MASCARA and bRing exposures are processed by an on-site reduction pipeline which performs astrometry, creates stacked images and performs photometry. The MASCARA observations were originally designed for difference imaging photometry (Talens et al., 2017b); however, difference imaging algorithms were found to be unable to keep pace with the data acquisition rate and aperture photometry is used instead. The aperture photometry is performed on stars with $m_V < 8.4$ in the raw images, producing light curves at 6.4 s cadence (fast light curves), and on stars with $m_V < 10$ in the stacked images, producing light curves at 320 s cadence (slow light curves). The reduced data are then transferred to Leiden for calibration.

This paper details the calibration of the fast light curves, describing the primary calibration of the data in Sect. 3.2, and a secondary calibration, tailored to find short duration periodic features such as transiting exoplanets, in Sect. 3.3. The transit detection algorithm is described in Sect. 3.4 and signal recovery test are presented in Sect. 3.5. In Sect. 3.6 we present an estimate of the occurrence rate of hot Jupiters around A-stars. Finally, in Sect. 3.7 we summarize the results and present our conclusions.

3.2 Primary calibration

Three main systematics are common to all MASCARA and bRing photometry (see also Fig. 10 of Talens et al., 2017b). First, extinction due to the earth's atmosphere, such as clouds, Calima and airmass effects. Second, the changing transmission of the lenses and changes in the fraction of light in the photometric aperture due to changes in the PSF shape with position on the CCD. Third, the intrapixel variations, a sinusoidal modulation due to the interline design of the CCDs.

We correct these effects for each of the cameras individually using baselines of $\sim$15 days, running from the 1st to the 15th and from the 16th to the end of each month, denoted 'A' and 'B' respectively. These baselines are long enough to disentangle the atmospheric and camera dependent effects even when several nights are dominated by the atmosphere, while

[1]The LSTSEQ is defined from the local sidereal time at La Palma starting from LST $= 0$ h at UTC 2012-12-31 18:29:10.68

simultaneously short enough to keep the memory required for calibration reasonable. For each baseline data flagged by the on-site reduction[2] is removed and the raw flux measurements and uncertainties are converted to magnitudes, using

$$m_{it} = -2.5 \log_{10} \left(\frac{F_{it}}{t_{\mathrm{exp,t}}} \right) + 25. \tag{3.1}$$

In this equation F_{it} is the raw flux in analog-to-digital units (ADUs), m_{it} the magnitude and $t_{\mathrm{exp,t}}$ the corresponding exposure time. The offset of 25 magnitudes is arbitrary and for the MASCARA station on La Palma the division by the exposure time is not performed, as this only became necessary after the conception of bRing with its alternating exposure times. The index i identifies the star and the index t is short for the LSTSEQ. The combination of i and t uniquely identifies each data point for a particular camera. Subsequently we correct for the main systematics using a variation on the coarse decorrelation algorithm, proposed by Collier Cameron et al. (2006), modified to include the effects of the transmission and intrapixel variations, which leads to the log-likelihood equation:

$$\begin{aligned} \ln L = -\frac{1}{2} \sum_{i,t} \Bigg[& \ln(2\pi(\sigma_{it}^2 + \sigma_i^2 + \sigma_{qt}^2)) + \\ & \frac{(m_{it} - m_i - c_{qt} - T_{nk} - f(x_{it}, y_{it}))^2}{\sigma_{it}^2 + \sigma_i^2 + \sigma_{qt}^2} \Bigg]. \end{aligned} \tag{3.2}$$

In this equation m_{it} and σ_{it} are the raw magnitudes and uncertainties. We describe these data as a sum of m_i, the mean magnitude of the star, c_{qt}, the atmospheric correction, T_{nk}, the transmission correction and $f(x_{it}, y_{it})$, a function describing the intrapixel variations. For the function $f(x_{it}, y_{it})$ we adopt the form,

$$\begin{aligned} f(x_{it}, y_{it}) = & a_{nl} \sin(2\pi x_{it}) + b_{nl} \cos(2\pi x_{it}) + \\ & c_{nl} \sin(2\pi y_{it}) + d_{nl} \cos(2\pi y_{it}), \end{aligned} \tag{3.3}$$

describing the intrapixel variations as sinusoids in the position on the CCD x_{it}, y_{it}, with amplitudes $a_{nl}, b_{nl}, c_{nl}, d_{nl}$. Following Collier Cameron et al. (2006) we also solve for additional uncertainties σ_i, which reduces the influence of variable stars and residual trends (see Sect. 3.3), and σ_{qt}, which reduces the effects of cloudy data on the overall solution. The inclusion of these additional uncertainties eliminates the need for additional data selection or sigma clipping.

The indices q, n, k and l indicate the spatial dependence of these corrections, which are solved onto discretized grids. These indices, obtained from quantities uniquely identified by i and t, will be described in detail in the next sections. Equation 3.2 is iteratively solved for T_{nk} and $a_{nl}, b_{nl}, c_{nl}, b_{nl}$, which we will refer to as the spatial component, and m_i, σ_i and c_{qt}, σ_{qt}, the temporal component.

[2]Some flags are not implemented in the on-site reduction of MASCARA La Palma and are performed on the fly instead.

3.2.1 Spatial

During most nights the effects of the lens transmission and intrapixel variations are the dominant systematics in the MASCARA and bRing light curves, as such we start the iterative procedure by solving for the spatial corrections. For convenience we define $\bar{m}_{it} = m_{it} - m_i - c_{qt}$ and $\bar{\sigma}^2_{it} = \sigma^2_{it} + \sigma^2_i + \sigma^2_{qt}$ so that we may rewrite eq. 3.2 as

$$\ln L = -\frac{1}{2} \sum_{i,t} \left[\ln(2\pi\bar{\sigma}^2_{it}) + \frac{(\bar{m}_{it} - T_{nk} - f(x_{it}, y_{it}))^2}{\bar{\sigma}^2_{it}} \right], \tag{3.4}$$

and solve for the spatial corrections. For the spatial dependence of transmission T_{nk}, we use a polar grid in hour angle (HA) and declination (δ) where

$$k = \left\lceil \frac{\mathrm{HA}_{it}}{6.4\ \mathrm{s}} \right\rceil \text{ and } n = \left\lceil \frac{\delta_i + 90^\circ}{0.25^\circ} \right\rceil. \tag{3.5}$$

The resolution along the hour angle axis emerges naturally from the 6.4 s observational cadence and fixed sidereal observations times employed by MASCARA and bRing and is therefore set to 6.4 s. The resolution along the declination axis is motivated by the requirement that there is a sufficient number of stars in each declination ring n while not making the rings too wide to properly sample the transmission. After testing several resolutions we decided on rings with a width of 0.25° for a total of 720 rings across the sky. Figure 3.1 shows a histogram of the number of stars in each ring for the zenith, north and east cameras of MASCARA La Palma (LPC, LPN, LPE) during the first half of October 2016 (baseline 2016-10-A), similar distributions are obtained for other cameras and baselines. For the LPC and LPE cameras the majority of the rings contain >50 stars, resulting in reliable correction terms. For the LPN camera the distribution has a long tail towards zero, a consequence of the decreasing area of each ring as we move towards the pole.

For the intrapixel variations, described by $a_{nl}, b_{nl}, c_{nl}, d_{nl}$ we also use a polar grid in hour angle and declination, employing the same index n along the declination axis while defining

$$l = \left\lceil \frac{\mathrm{HA}_{it}}{320\ \mathrm{s}} \right\rceil, \tag{3.6}$$

along the hour angle axis. By setting a resolution of 320 s, a factor 50 lower than the resolution used for the transmission map, we ensure the cells nl contain a sufficient range of x, y to properly sample the sinusoids.

3.2.2 Temporal

After obtaining corrections for the lens transmission and intrapixel variations we solve for the atmospheric extinction corrections. Let us define $\tilde{m}_{it} = m_{it} - T_{nk} - f(x_{it}, y_{it})$ so that we may rewrite eq. 3.2 as

$$\ln L = -\frac{1}{2} \sum_{i,t} \left[\ln(2\pi(\sigma^2_{it} + \sigma^2_i + \sigma^2_{qt})) + \frac{(\tilde{m}_{it} - m_i - c_{qt})^2}{\sigma^2_{it} + \sigma^2_i + \sigma^2_{qt}} \right]. \tag{3.7}$$

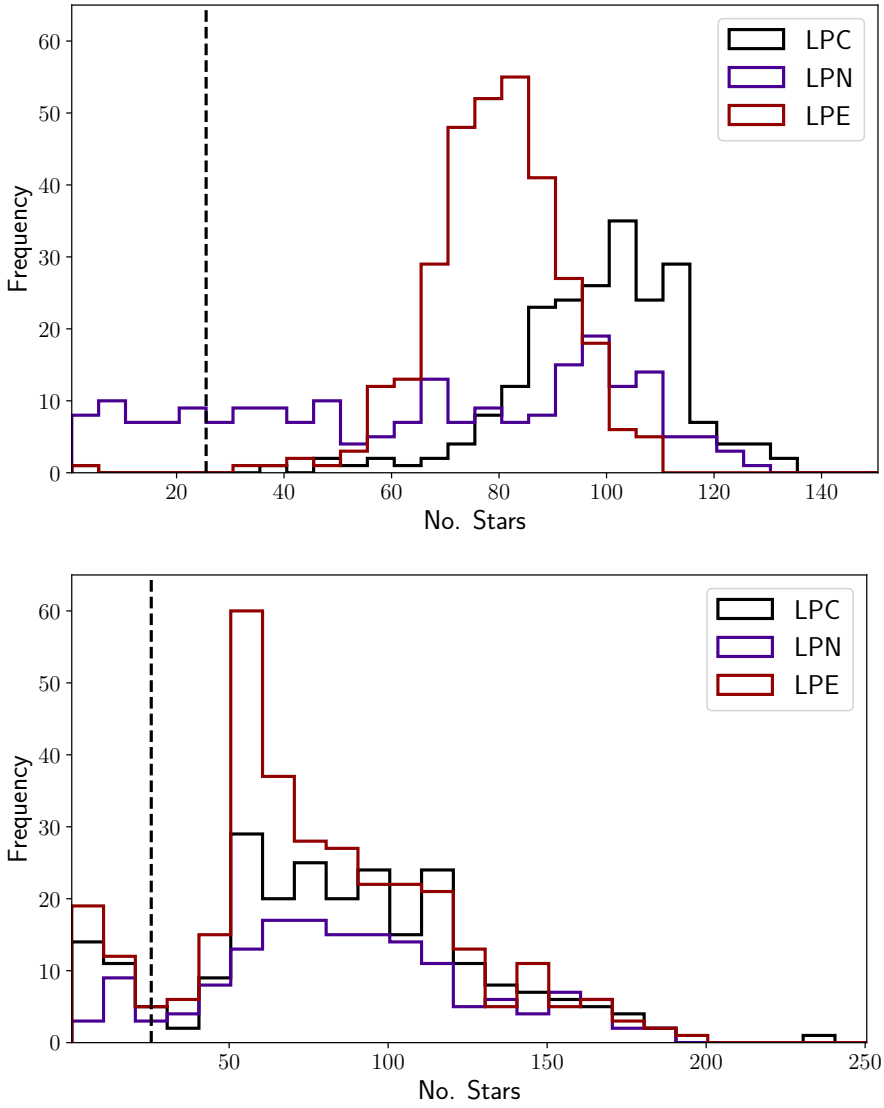

Figure 3.1: Histograms illustrating how the number of stars observed sets the resolution of the Polar and HEALPix grids for the LPC, LPN and LPE cameras during the 2016-10-A baseline, the black dotted line indicates 25 stars per resolution element. *Left:* frequency of rings in the polar grid containing a certain number of stars. *Right:* frequency of patches in the HEALPix grid containing a certain number of stars.

In this form the equation most closely resembles that of the coarse decorrelation presented by Collier Cameron et al. (2006). However, the large field of view (FoV) of the individual cameras ($53^\circ \times 74^\circ$) means the implicit assumption made by Collier Cameron et al. (2006) that any atmospheric corrections can be averaged over the FoV breaks down. In order to take this into account we subdivide the sky into patches of right ascension and declination identified by the index q. For this division of the sky we use the Hierarchical Equal Area isoLatitude Pixelization (HEALPix; Górski et al., 2005). As with the declination rings our choice for the resolution of the HEALPix grid, set by the $N_{\rm side}$ parameter, is motivated by the requirement that there is a sufficient number of stars in each patch q while also optimally sampling the position dependence of the atmospheric extinction. Based on this we use a HEALPix grid with $N_{\rm side} = 8$, resulting in 768 patches across the sky, each with an area of $53.7\ \mathrm{deg}^2$. Figure 3.1 shows a histogram of the number of stars in each patch for the LPC, LPN and LPE cameras during the 2016-10-A baseline. As for the rings most patches contain >50 stars, resulting in reliable correction terms. In addition, the design of the HEALPix grid avoids the polar singularity of the polar grid. However, due to the projection of the HEALPix grid onto the CCDs some patches are never fully observed, causing a secondary peak towards zero for all cameras.

3.2.3 Solution and caveats

We solve Eq. 3.4 and Eq. 3.7 iteratively, initially setting $c_{qt} = 0$, $\sigma_i = 0$ and $\sigma_{qt} = 0$. Furthermore, we fix the mean magnitudes to the known visual magnitudes of the stars ($m_i = m_{V,i}$) in order to keep the reference level the same over time-scales longer than the individual baselines. Because the indices q and n are solely dependent on quantities related to the stars i we can further solve individual rings n and individual patches q independently when solving Eq. 3.4 and Eq. 3.7, respectively. However, in the full solution all corrections depend on one another to some degree as stars in the same ring n will contribute to different patches q and vice versa. Further details on how Eqs. 3.4 and 3.7 are solved can be found in appendix 3.A.

Figure 3.2 illustrates the spatial corrections, in the shape of the solution of Eq. 3.4, for the LPC camera during the 2016-10-A baseline for a particular ring n. Panel (a) shows the photometry of all stars in the ring as function of hour angle, after subtracting the temporal corrections. The stars are ordered according to the starting time of their observations. At the beginning of the night there were some thin clouds and though the atmospheric correction has already been subtracted there is more noise on the stars observed early in the night. Panel (b) shows the transmission corrections T_{nk}. Panel (c) shows the residuals after subtracting the transmission corrections from the data. The noise due to clouds is now more evident, and the fringe-like pattern introduced by the intrapixel variations has become visible, peaking between HA $-00h30m$ and $00h00m$. Panel (d) shows the intrapixel corrections $f(x_{it}, y_{it})$. We note here that the free parameters a_{nl}, b_{nl}, c_{nl} and d_{nl} depend only on the hour angle for fixed n, all other structure comes from the positions of the stars on the CCD (x_{it}, y_{it}) and is not the result of optimizing free parameters. Panel (e) shows the residuals after subtracting both the transmission and intrapixel corrections from the data.

Figure 3.3 illustrates the temporal corrections, in the shape of the solution of Eq. 3.7, for the LPC camera during the 2016-10-A baseline for a particular patch q. Panel (a) shows

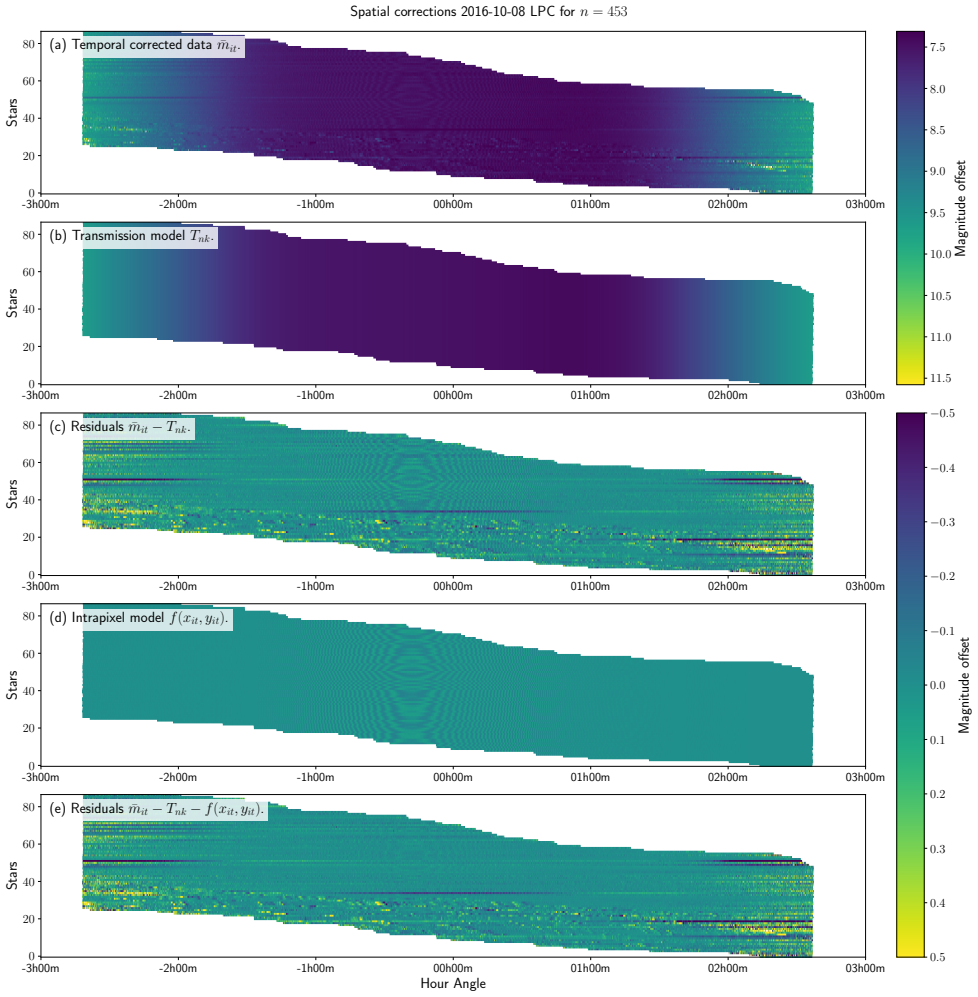

Figure 3.2: Data, model and residuals for ring $n = 543$ of the LPC camera during the 2016-10-A baseline. For clarity only the night of 2016-10-08 is shown and the median of the residual rows has been subtracted from all panels, removing small normalization differences due to keeping the m_i fixed. *(a)* Photometric time-series for the stars in ring $n = 453$ during the night of 2016-10-08 as a function of the hour angle after subtracting the mean magnitude m_i and cloud corrections c_{qt}. *(b)* The transmission corrections T_{nk} obtained from solving Eq. 3.2 *(c)* The residuals after subtracting the transmission corrections. *(d)* The intrapixel corrections $f(x_{it}, y_{it})$ obtained from solving Eq. 3.2. *(e)* The residuals after subtracting the intrapixel corrections.

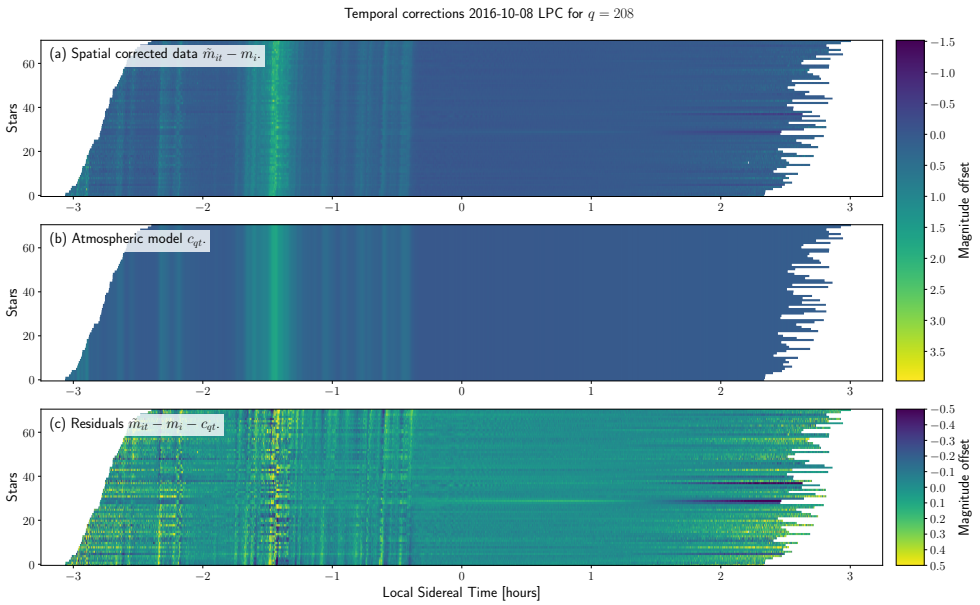

Figure 3.3: Data, model and residuals for patch $q = 208$ of the LPC camera during the 2016-10-A baseline. For clarity only the night of 2016-10-08 is shown and the median of the residual rows has been subtracted from all panels, removing small normalization differences due to keeping the m_i fixed. *(a)* Photometric time-series for the stars in patch $q = 208$ during the night of 2016-10-08 as a function of local sidereal time after subtracting the transmission and intrapixel corrections T_{nk} and $f(x_{it}, y_{it})$. For clarity the mean magnitude m_i has also been removed. *(b)* The atmospheric corrections c_{qt} obtained from solving Eq. 3.2. *(c)* The residuals after subtracting the atmospheric corrections.

the photometry of all stars in the sky-patch as a function of sidereal time, after subtracting the spatial corrections and the mean magnitudes. Several nearly vertical features are present at times when the stars were obscured by thin clouds. Panel (b) shows the atmospheric extinction corrections c_{qt}. Panel (c) shows the residuals after subtracting the atmospheric extinction correction from the data. The residuals are slightly skewed, caused by motion of the clouds across the sky-patch and extinction gradients in the clouds covering the sky-patch. In both Fig. 3.2 and Fig. 3.3 individual stars show residuals trends, the possible origins of these trends are discussed in Sect. 3.3.

Figure 3.4 shows the full transmission map for the LPC camera during the 2016-10-A baseline. The on-sky projection of this camera is representative of the LPC, LPS, LSC and LSN cameras of the MASCARA stations. For these cameras stars move approximately horizontally along the CCD. Small variations in the normalization of the different declination rings n are present because the photometry only truly samples the transmission along the direction of motion of the stars and the normalization between declination rings is imposed by setting the magnitudes of the stars.

Figure 3.5 shows the full intrapixel amplitude maps for the LPC camera during the 2016-10-A baseline. For this particular camera the intrapixel variations depend more strongly on the y position, but in general they depend more strongly on either x or y. In the top row (x dependence) an arc is visible at the bottom of the CCD where the quality of the solution

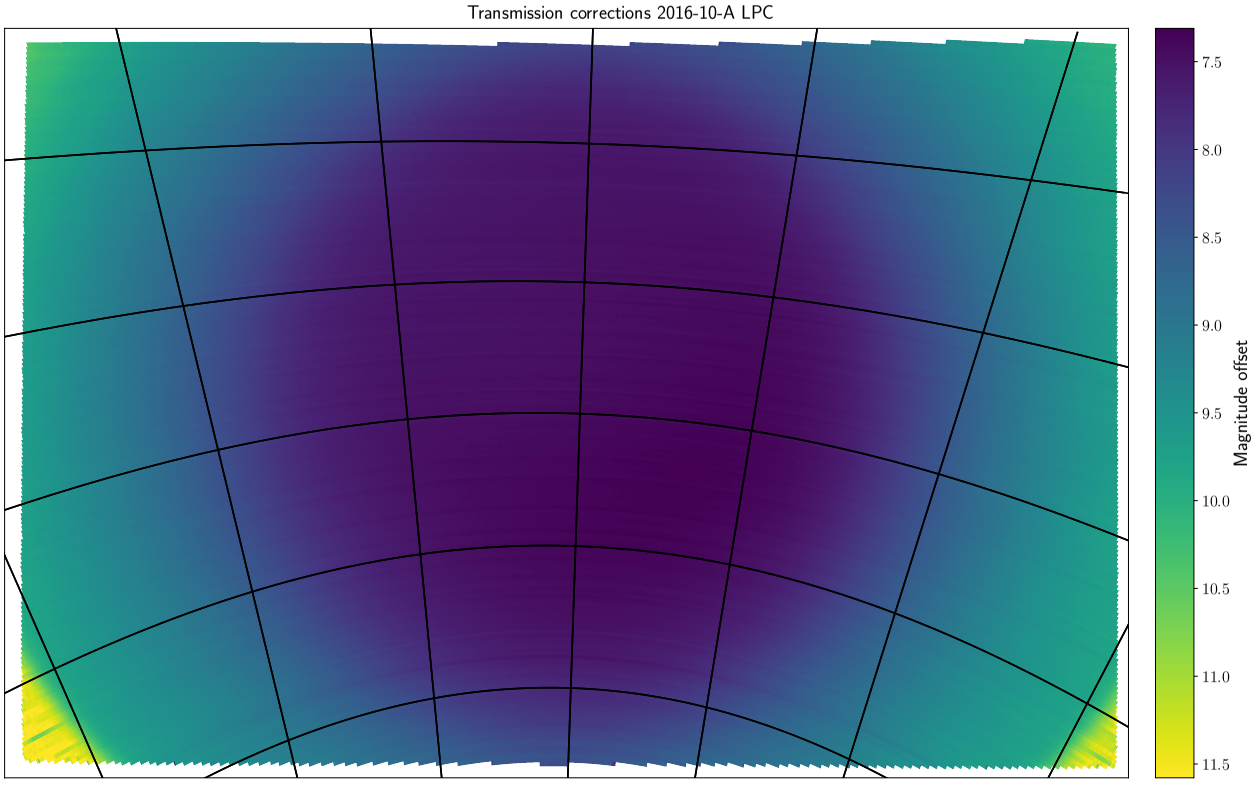

Figure 3.4: The transmission map obtained from solving Eq. 3.2 with all data obtained with the LPC camera during the 2016-10-A baseline. The maps are shown projected onto the CCD and a grid in hour angle and declination is overlaid on top.

decreases, similarly in the bottom row (y dependence) a curved vertical area near the centre of the CCD is degraded. In these regions of the CCD the change in the x or y position of a star between exposures is either close to 1 pixel or less than $1/50$th of a pixel, resulting in a poor sampling of the sinusoidal modulations in the cell nl. Such structures are present in the intrapixel maps of all MASCARA and bRing cameras, with their shapes determined by the on-sky orientation of the camera. Examples of the transmission and intrapixel maps for other on-sky orientations are shown in appendix 3.B.

Figure 3.6 shows the atmospheric corrections for LPC camera during the 2016-10-A baseline at four different times, and a movie of the atmospheric extinction map during the night of 2016-10-08 is available online[3]. The stars move across the LPC camera from left-to-right, as seen by the change in the location of the sky-patches, while some thin clouds moved across the FoV from right-to-left.

After computing the correction terms, calibrated light curves are obtained by subtracting the correction terms from the raw magnitudes. Next, the photometry is flagged and removed if <25 points were used in computing c_{qt}, T_{nk} or $a_{nl}, b_{nl}, c_{nl}, d_{nl}$ in order to remove data where the corrections are poorly constrained. This removes rings and patches to the left of the black dashed line in Fig. 3.1. In addition we flag and remove photometry if $\sigma_{qt} > 0.05$, to remove data where atmospheric extinction was significant. The remaining data points are binned in sets of 50, using consecutive LSTSEQ, to a cadence of 320 sidereal seconds. When a set of 50 data points is incomplete, the existing points are binned and the number of raw data points used in the bin is recorded. Finally, the individual $\sim$15 day baselines are combined in sets of three months ('quarters') for each camera. We will refer to these calibrated and binned light curves as the quarterly data.

3.3 Secondary calibration

After removing the effects of the atmospheric extinction, transmission and intrapixel variations and binning the data to a cadence of 320 sidereal seconds, residual systematic trends are observed in the quarterly light curves of individual stars. These residuals can be divided into two broad categories, first a daily repeating trend that depends primarily on the local sidereal time, which acts as a proxy for the position of the star on the CCD. Second, long term variations in the baseline.

The daily trend is systematic in nature, caused by the variable shape of the stellar PSF with position on the CCD (Talens et al., 2017b), which changes the fraction of the stellar light within the photometric aperture and the amount of blended light from neighbouring stars in a way that is unique to each target. The long-term variations can be both physical and systematic in nature, with the main systematic long-term changes caused by an overestimation of the sky background when the moon is visible, producing an artificial dimming in the light curves that varies with the moon phase. Since we are interested in exoplanet transit signals we remove all long-term variations, indiscriminate of their origin. As an example of these trends Fig. 3.7 shows the quarterly light curve of the known transiting exoplanet host star HD 189733 as observed by the LPC camera during the third quarter of 2016 (2016Q3). The top panel shows the light curve as a function of the Julian date, revealing apparent dimming due to the Moon at $\sim$20 days, $\sim$48 days and $\sim$76 days. The bottom panel shows

[3] `http://home.strw.leidenuniv.nl/~talens/data/clouds_vmag_20161008LPC.mp4`

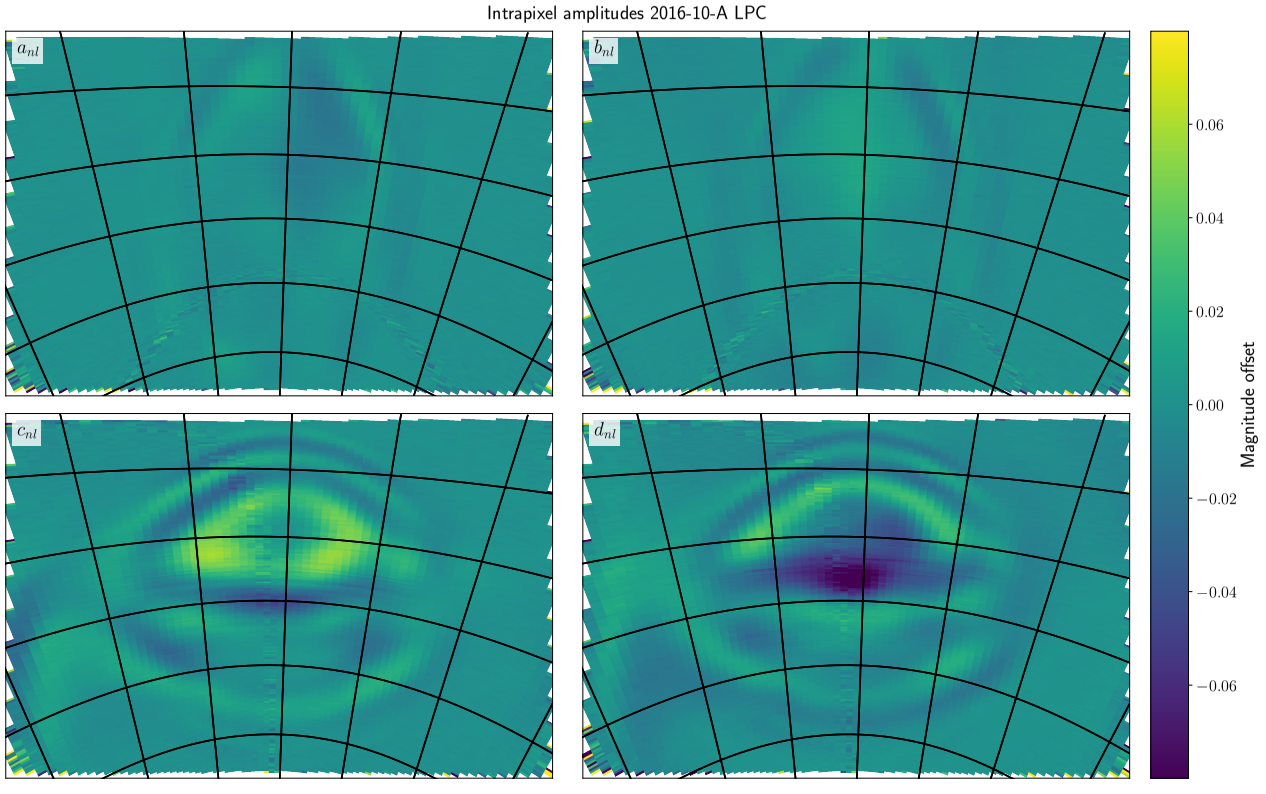

Figure 3.5: The intrapixel amplitude maps obtained from solving Eq. 3.2 with all data obtained with the LPC camera during the 2016-10-A baseline. The maps are shown projected onto the CCD and a grid in hour angle and declination is overlaid on top. The top panels show the amplitudes a_{nl} and b_{nl} of the $\sin(2\pi x_{it})$ and $\cos(2\pi x_{it})$ terms, the bottom panels show the amplitudes c_{nl} and d_{nl} of the $\sin(2\pi y_{it})$ and $\cos(2\pi y_{it})$ terms.

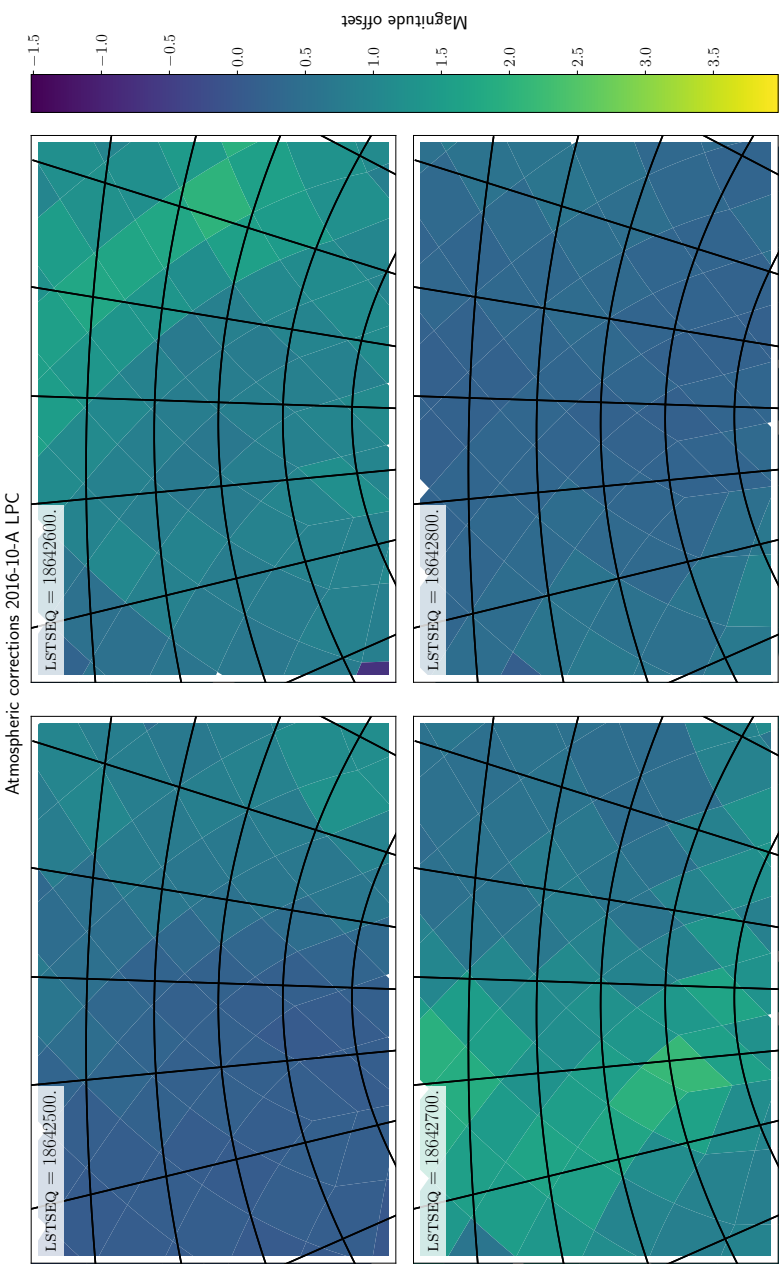

Figure 3.6: The atmospheric corrections obtained from solving Eq. 3.2 with all data obtained with the LPC camera during the 2016-10-A baseline. Each panel shows the solution at a different LSTSEQ during the night of 2016-10-08 with an interval of 100 exposures or 640 sidereal seconds. The maps are shown projected onto the CCD and a grid in hour angle and declination is overlaid on top. A movie of the atmospheric corrections during the night of 2016-10-08 is available online (see footnote 3).

the light curve as a function of the local sidereal time, revealing the trend with CCD position resulting from changes in the PSF. The PSF effect is also responsible for the apparent scatter towards fainter magnitudes seen in the top panel at times <60 days. This scatter is caused by the faint end of the PSF effect at sidereal times <18 hours, which disappears later in the quarter as these sidereal times are no longer observed.

The methods presented below for removing these trends are applied to the quarterly light curves, before combining the different cameras and quarters for the transit search (Sect. 3.4). Applying these methods before the transit search is only valid because the signals of interest have low amplitudes and short durations, minimizing the impact of the signal on the removal of these trends. When the amplitude or the duration of the signal of interest are large, or when performing detailed modelling of any astrophysical signal present in the data, these methods should be run jointly with a model for the signal in question, which may be as simple as a phase-binned mean of the light curve (Burggraaff et al., 2018). Furthermore, when investigating long-term variability using MASCARA data the removal of long-term trends most be either turned off, or the long-term trends that were removed must be added back to the data.

3.3.1 Methods

Three different methods for performing the secondary calibration were developed: Fourier, Legendre and Local Linear. We discuss each of these methods below.

Fourier Guided by the daily repetition of the PSF effect, this method consists of the sum of two discrete Fourier series, one in the Julian date and one in the local sidereal time, with high frequencies removed to prevent over-fitting the data. The use of the Fourier method resulted in the successful detection of MASCARA-1 b (Talens et al., 2017a); however, it is poorly motivated. The model does not account for global offsets and the number of degrees of freedom has to be artificially increased to account for the fact that the trends are not in fact periodic. This extra freedom comes from adding a sinusoid with half the lowest frequency to both series.

Legendre In order to improve on the shortcomings of the Fourier method a second method using Legendre polynomials was developed. Contrary to Fourier functions, Legendre polynomials ($P_n(x)$) form an orthogonal basis on a fixed interval, which matches better to the daily variations. A sum of two Legendre polynomials is used, one in the Julian date (JD) and one in the local sidereal time (LST). The JD and LST are scaled, and in the case of the LST wrapped, so that their values are optimally mapped onto the interval where the polynomials are orthogonal. In addition, a linear dependence on the sky background (SKY) is included in the LST polynomial to correct for the effect of the Moon on the sky background level. In short, we model the magnitude as

$$m_t = \sum_{m=0}^{M} (a_m + b_m \mathrm{SKY}_t) P_m(\mathrm{LST}_t) + \sum_{n=1}^{N} c_n P_n(\mathrm{JD}_t), \tag{3.8}$$

where a_m, b_m and c_n are the polynomial coefficients. The polynomial orders M and N are determined from the baselines in JD and wrapped LST according to

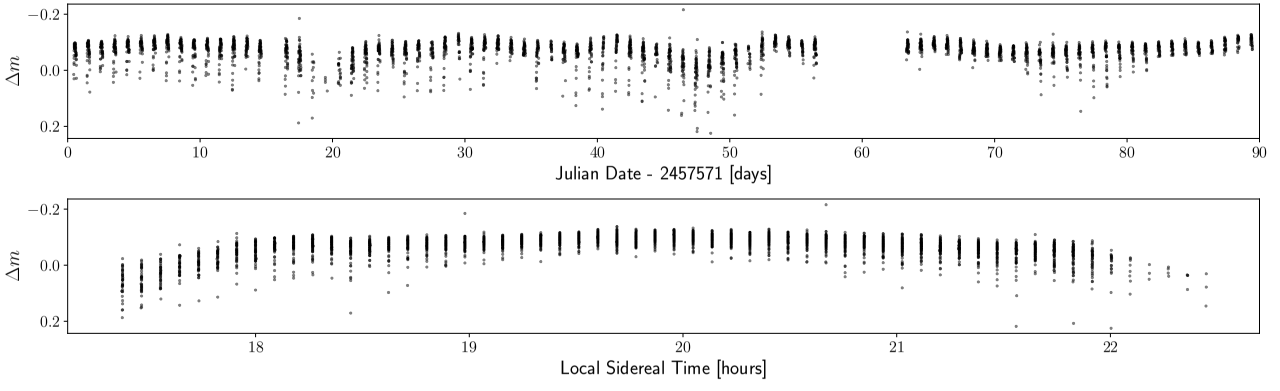

Figure 3.7: Light curve of HD 189733 as observed by the LPC camera during 2016Q3. The top panel shows the light curve as a function of the Julian date, highlighting the long-term variations, in particular the effect of the moon is visible at ∼20 days, ∼48 days and ∼76 days. The bottom panel shows the light curve as a function of the local sidereal time, highlighting the PSF effect.

$$M = \left\lfloor \frac{\text{LST}_{\max} - \text{LST}_{\min}}{s_{\text{LST}}} \right\rfloor \text{ and } N = \left\lfloor \frac{\text{JD}_{\max} - \text{JD}_{\min}}{s_{\text{JD}}} \right\rfloor, \tag{3.9}$$

where $s_{\text{LST}} = 15$ min and $s_{\text{JD}} = 5$ days are the typical scales associated with the PSF effect and the long-term variations. We solve Eq. 3.8 iteratively, computing the residuals of the best-fit model at each iteration and excluding outliers from the next iteration at the 10σ level, where the median absolute deviation (MAD) is used as a robust estimator of σ. The Legendre method was used in the detection of MASCARA-2 b (Talens et al., 2018), with $s_{\text{JD}} = 3$ days, without the linear SKY dependence, and without the iterative scheme.

Local Linear The third method we developed does not depend on a particular choice of basis functions. Local Linear corrects the PSF effect by fitting a linear function of the SKY, x position and y position to all measurements taken at the same LST, which are identified using the LSTIDX (see Sect. 3.1), and removes the long-term variations using a weighted moving mean with a window $s_{\text{JD}} = 5$ days. The linear fit and moving mean are iteratively refined until convergence is reached. The linear function describing the PSF effect can be written as

$$m_t = a_n + b_n(x_t - \bar{x}_n) + c_n(y_t - \bar{y}_n) + d_n \text{SKY}_t, \tag{3.10}$$

where n is short for the LSTIDX, a_n, b_n, c_n and d_n are the coefficients, x_t, y_t and SKY_t are the CCD coordinates and sky background corresponding to the measurement and $\bar{x}_n$ and $\bar{y}_n$ are the average positions at each LSTIDX.

The inclusion of the x and y positions provides a marked improvement as they correct small changes in the measured fluxes resulting from astrometric drift, which is neglected in all the other calibrations. Unlike the Legendre method the Local Linear method does not include outlier rejection in its iterative scheme. The independent nature of the linear fits at different values of the LSTIDX makes it unsuitable, as outlier rejection might remove too many points at a particular LSTIDX.

3.3.2 Comparison

As an example of the differences between these methods Fig. 3.8 shows the quarterly light curve of HD 189733, observed by the LPC camera during 2016Q3, as a function of the orbital phase of the hot Jupiter companion ($P = 2.21857520$ days, Baluev et al., 2015). Panel (a) shows the data after the primary calibration and panels (b), (c) and (d) show a comparison between the three methods. The improvement from applying the secondary calibration methods to the light curve is evident, with over a factor two improvement in the RMS. The differences between the different methods are more subtle, with particularly the correction of outlier data points showing improvement going from Fourier to Legendre and finally to the Local Linear method.

To quantify the merit of each of these methods Fig. 3.9 shows the RMS scatter as a function of magnitude for stars observed by the west cameras of each station during a specific quarter. We find that the Fourier and Legendre methods provide similar performance for

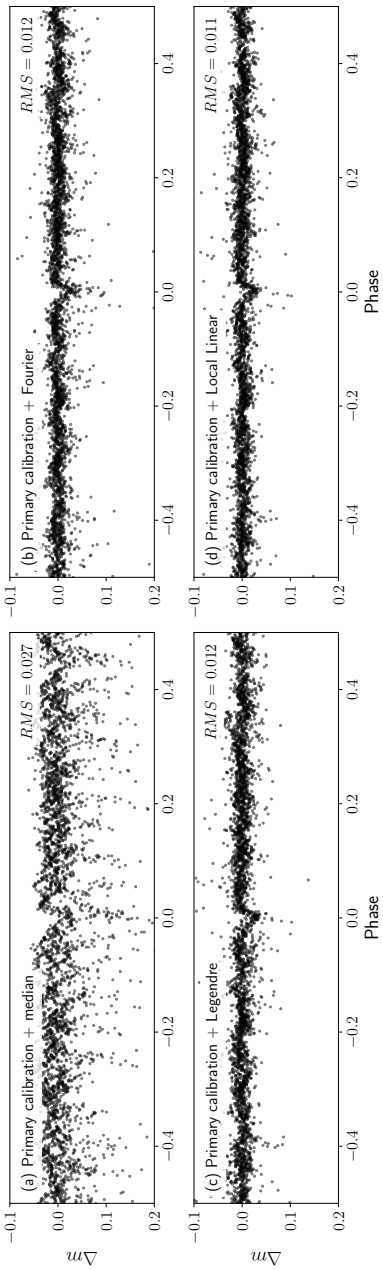

Figure 3.8: Light curve of HD 189733 as observed by the LPC camera during 2016Q3. The data have been phase-folded to the orbital period of HD 189733 b. Panel (a) shows the light curve after primary calibration, with the median subtracted for clarity. Panels (b), (c) and (d) show the light curve for each of the secondary calibration methods, Fourier, Legendre and Local Linear respectively. The RMS scatter on the light curve is noted in the top-right of each panel.

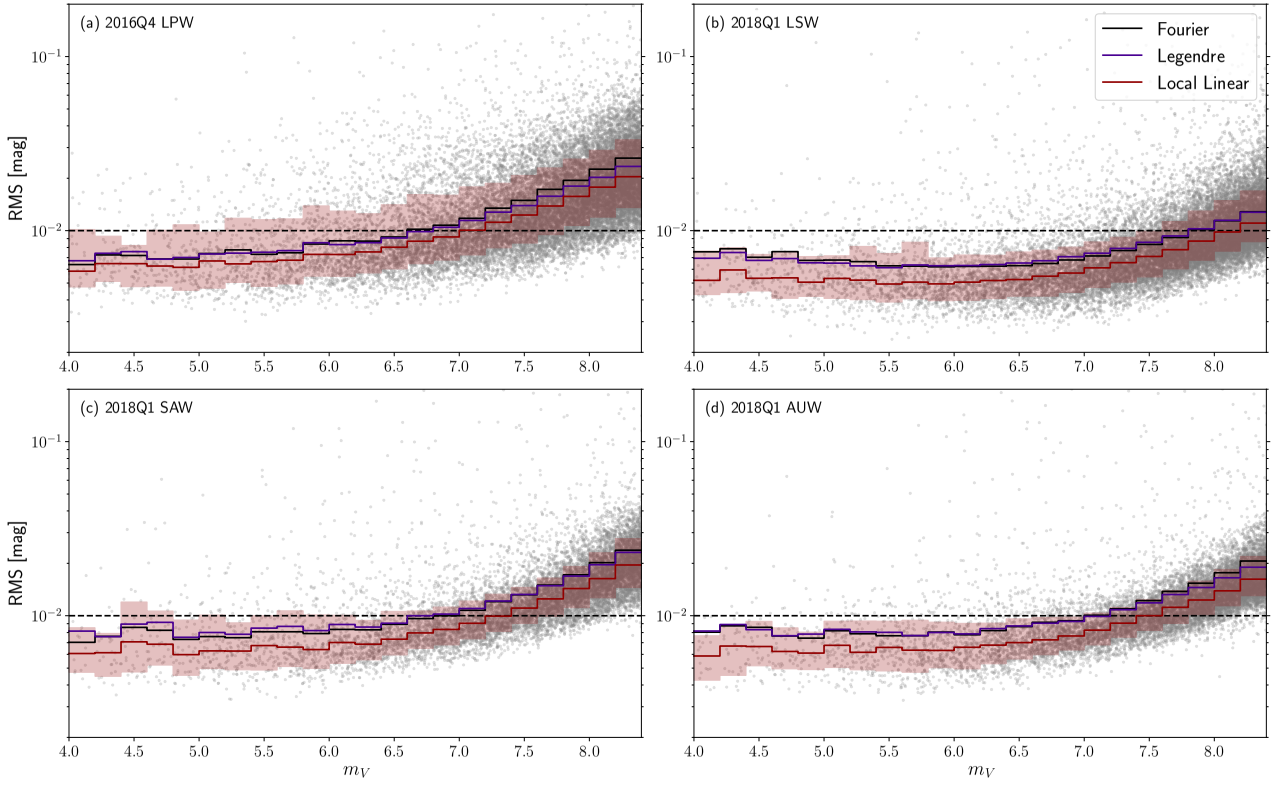

Figure 3.9: RMS scatter as a function of magnitude for stars observed by the west cameras of each station over the course of a quarter. The curves show the median RMS in bins of 0.2 mag for the three secondary calibration methods. For the Local Linear method the 1σ percentiles (coloured area), and the RMS scatter values of individual stars (grey points) are also indicated. The dashed black line shows the 10 mmag noise level. Only light curves with >500 quarterly data points were used.

all cameras at all magnitudes while the Local Linear method provides a marked improvement ranging from $\Delta\mathrm{RMS} \sim 1$ mmag for the brightest stars to $\Delta\mathrm{RMS} \sim 3$ mmag for the faintest stars. We also see that there are individual differences in performance between the different cameras with LPW reaching the 10 mmag RMS level at $m_V \sim 7.1$, SAW and AUW at $m_V \sim 7.3$, while AUE reaches this level at the fainter magnitude of $m_V \sim 8.1$. In addition to reaching 10 mmag RMS level at the brightest magnitude the LPW camera also shows the largest spread in achieved RMS as a function of magnitude. This difference between MASCARA La Palma and the southern stations is most likely a result of implementing a more robust method for obtaining the sky background on the southern stations. The relative performance of the three methods is a general feature observed in all MASCARA and bRing cameras, as are the individual performance differences between the cameras.

3.4 Transit detection

In order to detect the periodic signals of transiting exoplanets we use the box least-squares algorithm (BLS, Kovács et al., 2002) with the optimized parameter grid of Ofir (2014). The quarterly light curves are read and points binned from ≤ 45 raw data points (out of a maximum of 50 per binning interval) are discarded before the secondary calibration is applied to individual cameras and quarters. The different cameras and quarters are then combined and the fully calibrated light curves are passed to the transit search algorithm where barycentric Julian dates are computed and outliers are rejected at the 3σ level, using the MAD as a robust estimator of σ and setting a lower limit of 50 mmag to prevent discarding transit signals. These data are then used to compute the BLS periodogram for each star.

After computing the BLS periodogram the strongest peak is identified and the parameters of the associated box-fit, namely orbital period, transit depth, transit duration and epoch are recorded. In addition, a number of diagnostic quantities, used in the literature to identify good transit candidates, are computed. We calculate the anti-transit ratio (Burke et al., 2006), the amplitude and the signal-to-noise ratio of ellipsoidal variations (Collier Cameron et al., 2006), the signal detection efficiency (Kovács et al., 2002) and the signal-to-pink-noise (Pont et al., 2006). We further store the number of in-transit data points, the number of observed transits, the largest gap in the phase coverage relative to the transit duration, the fraction of points at phase < 0.5 and the difference between the mean and median magnitude. Finally, the periodogram, best-fit parameters and diagnostic quantities are saved to disk.

Subsequently, diagnostic figures are made for all stars for which the strongest peak corresponds to a dimming of the star. As an example, Fig. 3.10 shows the diagnostic figure for HD 189733 from a BLS run on three years of data from the La Palma station. It includes the BLS periodogram, the light curve phase-folded to the strongest peak, half the peak period and twice the peak period. All diagnostic quantities and figures are then inserted into a database that also contains the input catalogue (ASCC, Kharchenko, 2001; Kharchenko and Roeser, 2009) estimates of stellar properties based on *Gaia* DR1 and DR2 (Gaia Collaboration et al., 2016a,b, 2018) and links to SIMBAD (Wenger et al., 2000) and the international variable star index (VSX, Watson et al., 2006). The database contains a number of fixed queries tailored to finding candidate transiting exoplanets and allows for dynamic queries with constraints on multiple tables. Nominally, the fixed queries are used

to select the most promising candidates before manually vetting them based on the diagnostic image and external information on known (nearby) variable stars. The status of each candidate is recorded in the database through the use of tags, indicating the current status, and user comments, recording the reasoning for the status and the history of the object.

3.5 Signal recovery tests

In order to characterize the performance of the primary and secondary calibration, as well as the performance of MASCARA as a transit survey, we carried out two sets of signal recovery tests. For these tests we injected transit signals in a subset of the light curves and ran the BLS algorithm to see how many signals we could recover successfully.

For each signal recovery test we drew a sample of 5000 stars for signal injection. To prevent this sample from being dominated by the fainter stars we set the probability of a star being selected proportional to m_V^{-2}, in addition we drew the sample without replacement, so no star is used twice. Subsequently, transit signals were injected with orbital periods ($P_{\rm inj}$) in the interval $[1, 5)$ days, epochs (T_0) in the interval $[0, P_{\rm inj})$ days, depths ($p^2 = (R_p/R_\star)^2$) from the set $\{0.005, 0.01, 0.02\}$, impact parameters (b) from the set $\{0.0, 0.5\}$ and stellar densities ($\rho_\star$) from the set $\{0.4, 0.9, 1.4\}$ g cm^{-3}. We used $\rho_\star$ as our fifth parameter, rather than the semi-major axis or transit duration, to ensure we injected realistic transits covering a range of spectral types. Transit light curves were computed from these parameters using BATMAN (Kreidberg et al., 2014), including a linear limb darkening law with coefficient set to 0.6, and injected into the light curves of the selected stars. Next we used the BLS algorithm to compute periodograms for all injected light curves and selected the period corresponding to the strongest peak, $P_{\rm rec}$. We counted a signal as recovered when

$$\frac{|P_{\rm inj} - NP_{\rm rec}|}{P_{\rm inj}} < 10^{-3}, \tag{3.11}$$

with $P_{\rm rec}$ the recovered period and $N = 1,\ 2,\ \frac{1}{2}$ and $\frac{1}{3}$, such that the harmonics are counted as successful recoveries.

3.5.1 Performance of different calibration strategies

The goal of the first set of tests is to characterize the performance of the primary and secondary calibration, determining how the recovery rates change with variations on the calibration algorithms. As such we report in this section only the total number of recovered transit signals, independent of the transit parameters. We will discuss how the recovery rate depends on the transit parameters in Sect. 3.5.2, where we characterize the performance of MASCARA as a transit survey.

For this set of tests we injected signals in the raw 6.4 s light curves obtained during the fourth quarter of 2016 by the La Palma station (2016Q4). Before drawing the sample of 5000 stars for signal injection, we pre-selected those stars that had been observed for >300 hours across >60 days, that is to say averaging at least five hours of data per night, to guarantee their light curves contained sufficient data for signal recovery to be possible. We used the

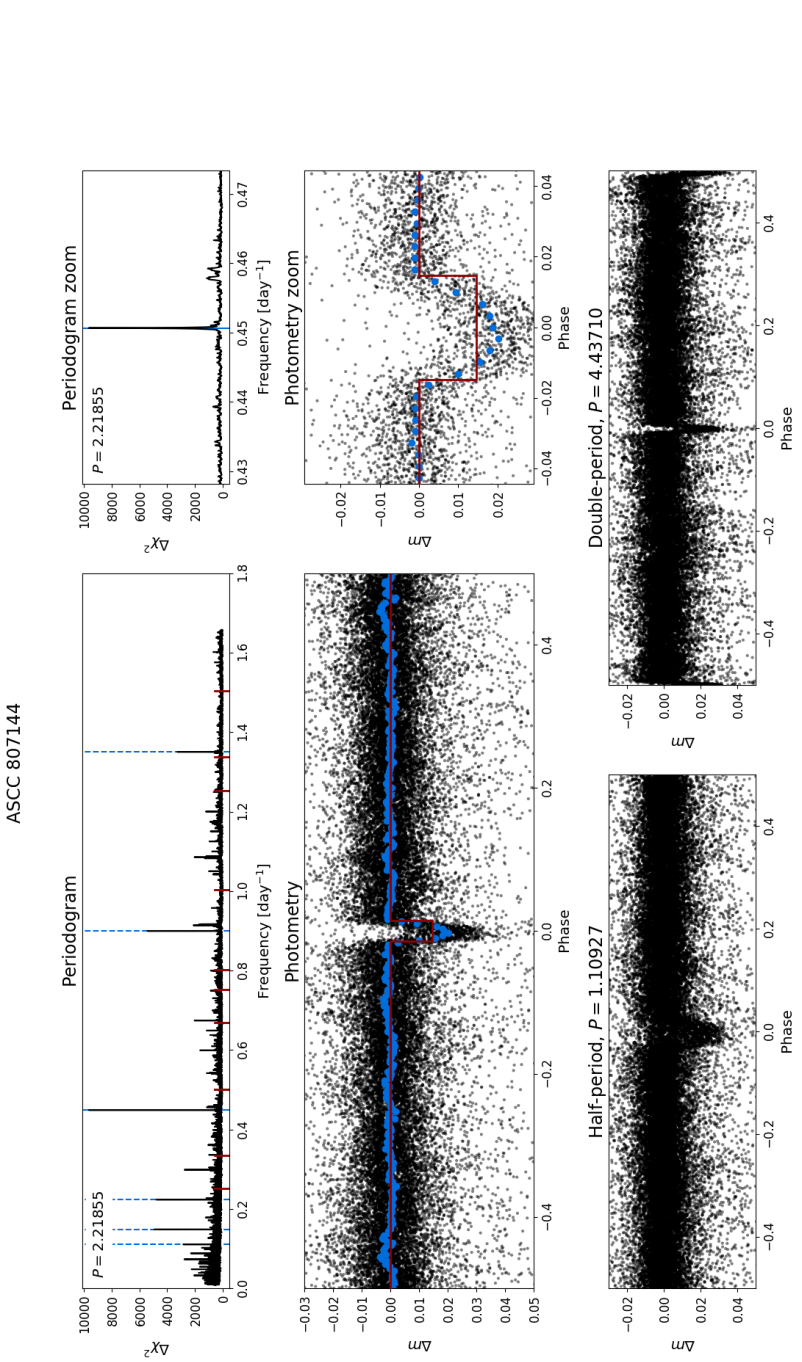

Figure 3.10: Diagnostic figure showing the results of a transit search run on three years of data from the La Palma station for the star HD 189733. The top row shows the full BLS periodogram (left) and a zoom on the peak period (right). Both panel include the periodogram (black line), lines indicating the peak period and its harmonics (blue dashed lines) and lines indicating the sidereal period and its harmonics (red lines). The middle row shows the full phase-folded light curve (left) and a zoom on the transit (right), Both panels include the light curve (black dots), the phase-binned light curve (blue points) and the best-fit box model (red line). The bottom row shows the light curve phase-folded to half the peak period (left) and twice the peak period (right).

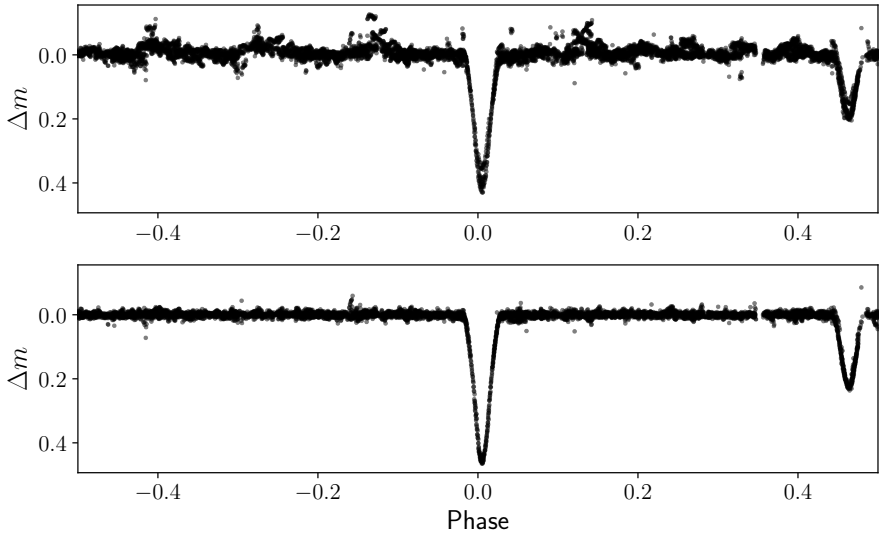

Figure 3.11: Light curve of the Algol-type eclipsing binary KW Hya, obtained by the La Silla station during 2017Q4 and 2018Q1, phase-folded to the orbital period of $P = 7.7499942$ days. The top panels shows the result of using the Legendre method without outlier rejection, while the bottom panel includes outlier rejection.

same injected dataset in all recovery tests described in this section so that any change in the number of recovered signals, $N_{\rm rec}$, is due to changes in the calibration methods.

We started by keeping the primary calibration fixed and running variations on the Legendre secondary calibration method. For the Legendre method we varied the values of $s_{\rm JD}$ and $s_{\rm LST}$ which set the polynomial orders, investigated the effect of the linear SKY dependence and the impact of excluding outliers when determining the best-fit parameters. Table 3.2 lists the different variations and the number of recovered signals for each variation. Of the 5000 injected signals, around 2000 signals were recovered by the optimal variation of the Legendre method. Typically, $s_{\rm JD} = 5$ days is the optimal choice for removing the long-term variations with smaller values over-fitting the data (e.g. $s_{\rm JD} = 1$ day) and larger values not providing enough freedom to correct for the long-term variations. For example, when $s_{\rm JD} = 7$ days the companion to HD 189733 is not detected, as the intrinsic variability of the star is not sufficiently removed. For the PSF effect we find that the shortest value of $s_{\rm lst} = 15$ min is preferred regardless of the value of $s_{\rm jd}$. There is also a preference for including the SKY dependence with an increase in $N_{\rm rec}$ of $100 - 150$ signals when it is included. Finally, the inclusion of iterative outlier rejection appears to have little influence on the number of recovered signals. However, in practice we find that the iterative outlier rejection does have an effect on eclipsing binaries whose primary eclipses are relatively deep and short when compared to the orbital period, that is stars where the outlier rejection excludes the real signal from the fit. An example of such a star is shown in Fig. 3.11 with the top panel showing the light curve without outlier rejection and the bottom panel with outlier rejection. For this reason we keep the outlier rejection, and note that the Legendre secondary calibration method might be optimal for the detection of this type of binary.

Table 3.2: Results of varying the Legendre secondary calibration method. The default models for all secondary calibrations methods are shown in bold face.

Name	s_{JD} [days]	s_{LST} [min]	SKY term	Iterative	N_{rec} of 5000
Ref_Fourier					1739
Ref_LocLin					2267
Var_sjd1p0_NoIter	1	15	Yes	No	885
Var_sjd3p0_NoIter[a]	3	15	Yes	No	1839
Var_sjd3p0_slst30_NoIter	3	30	Yes	No	1833
Var_sjd3p0_slst60_NoIter	3	60	Yes	No	1646
Var_NoIter	5	15	Yes	No	2003
Var_slst30_NoIter	5	30	Yes	No	1987
Var_slst60_NoIter	5	60	Yes	No	1800
Var_sjd7p0_NoIter	7	15	Yes	No	1854
Var_sjd7p0_slst30_NoIter	7	30	Yes	No	1838
Var_sjd7p0_slst60_NoIter	7	60	Yes	No	1697
Var_NoSky_NoIter	5	15	No	No	1854
Var_slst30_NoSky_NoIter	5	30	No	No	1838
Var_slst60_NoSky_NoIter	5	60	No	No	1697
Var_Iter5sig	5	15	Yes	5σ	1995
Ref_Legendre	5	15	Yes	10σ	2006
Var_Iter15sig	5	15	Yes	15σ	2000
Var_Iter20sig	5	15	Yes	20σ	2003

Notes. [a] Used in the discovery of MASCARA-2 b (Talens et al., 2018).

Table 3.3: Results of varying the Local Linear secondary calibration method. The default models for all secondary calibrations methods are shown in bold face.

Name	$s_{\rm JD}$	x, y terms	SKY term	$N_{\rm rec}$
	[days]			of 5000
Ref_Fourier				1739
Ref_Legendre				2006
Var_sjd1p0	1	Yes	Yes	1495
Var_sjd3p0	3	Yes	Yes	2234
Ref_LocLin	5	Yes	Yes	2267
Var_sjd7p0	7	Yes	Yes	2206
Var_sjd3p0_NoPos	3	No	Yes	2092
Var_NoPos	5	No	Yes	2126
Var_sjd7p0_NoPos	7	No	Yes	2079
Var_sjd3p0_NoSky	3	Yes	No	2078
Var_NoSky	5	Yes	No	2075
Var_sjd7p0_NoSky	7	Yes	No	1930

Next, we again kept the primary calibration fixed and ran variations on the Local Linear secondary calibration method. For the Local Linear method we tested the window size for the weighted running mean $s_{\rm jd}$, and investigated the effect of the positional and SKY dependencies. Table 3.3 lists the different variations and the number of recovered signals for each variation. Of the 5000 injected signals, 2267 signals are recovered by the optimal variation of the Local Linear method. As with the Legendre method, the Local Linear method performs optimally when the window of the long-term variations is set to $s_{\rm JD} = 5$ days. The inclusion of both the positional and SKY dependencies are also favoured with almost 200 more detections when including the SKY term and over 100 more when including the positional terms. Most importantly, the best variation of the Local Linear method recovers over 250 signals more than the best variation of the Legendre method.

Tables 3.2 and 3.3 show that of the three secondary calibration methods presented, the Local Linear method recovers the largest number of injected signals. However, comparing which of the 5000 signals are recovered by each method shows that a total of 237 signal are recovered by either or both of the Fourier and Legendre methods but not by the Local Linear method. Inspection of these signals revealed no apparent dependence on the injected transit parameters or stellar parameters, nor a particular systematic effect preventing their detection by the Local Linear method. As such we conclude that while the Local Linear is our preferred secondary calibration method, there is merit to continued use of the Fourier and Legendre methods as detectable signals may otherwise be missed. Furthermore, we continue to update existing methods and test new methods as our understanding of the data improves.

Finally, we ran variations on the primary calibration, while using the optimal Local Linear secondary calibration method. We attempted to increase the HA resolution of the intrapixel amplitude maps from 320 s to 128 s, investigated the effect of leaving the magnitudes m_i as free parameters and tried to use a polar grid with declination rings of a fixed area, avoiding the excess of rings containing $<$50 stars for cameras observing the poles (see Fig. 3.1) at the cost of resolution near the poles. We did not vary the total number of rings

Table 3.4: Results of varying the primary calibration. All recovery test were run with the Local Linear secondary calibration method.

Name	m_i	Polar rings	Index l	$N_{\rm rec}$ of 5000
Ref_Primary	$m_{V,i}$	Fixed width	320 s	2267
Var_Nl675	$m_{V,i}$	Fixed width	128 s	2242
Var_EqArea	$m_{V,i}$	Fixed area	320 s	2255
Var_mFree	m_i	Fixed width	320 s	2285
Var_mFree_EqArea	m_i	Fixed area	320 s	2316

in the polar grid or the resolution of the HEALPix grid as they are strongly motivated by the number of available stars. The same goes for the HA resolution of the transmission map which is motivated by the observational cadence. Table 3.4 lists the different variations and the number of recovered signals for each variation. We find that increasing the HA resolution of the intrapixel amplitudes slightly decreases the number of recovered signals, as does using equal-area declination rings in the polar grid. When we leave the magnitudes as a free parameter however $N_{\rm rec}$ increase by 18 signals, and if we combine the free magnitudes with equal-area declination rings the recovery rate increase by 49 signals compared to the reference model. We nevertheless prefer to keep the magnitudes fixed, as this ensures a fixed reference level across timescales longer than the $\sim$15 day calibration baselines. Figure 3.12 shows the light curve of HD 205555 as a function of the LST and coloured by the Julian date, the top panel shows the result with the m_i as free parameters and the bottom panel with the $m_i = m_{V,i}$. In the case of the free m_i the normalization of the data changes with the LST coverage. During the first calibration baseline of the quarter we observed the full LST range shown and thus the full PSF effect while during subsequent baselines the observed LST values and the associated section of the PSF effect changes, shifting the corresponding sections of data. When we keep the m_i fixed we find that this shift does not occur as we are using the same mean magnitudes across the quarter. In the case of HD 205555 the shifts in m_i are caused by the changing LST coverage, but intrinsic variability has the same effect even in the absence of strong LST variations. For example, an RR Lyrae type variable will be observed with different phase coverage during every $\sim$15 day baseline, resulting in similar shifts when leaving the m_i as free parameters.

3.5.2 Survey performance

The goal of the second set of tests is to characterize the performance of MASCARA as a transit survey, determining how the recovery rates depend on stellar and transit parameters. For these test we used one year (2016) and three years (2015-2017) of observations obtained by the La Palma station. For these tests a sample of 5000 stars was drawn without any preselection on the amount of data obtained for each star, and the signals were injected in the light curves after the primary calibration. Injecting the signals after the primary calibration is not expected to have a major impact on the result, as the presence of injected signals on the primary calibration was found to be negligible for the recovery tests presented in Sect. 3.5.1, with $\sim$95.5% of the correction terms changed by $<$1 mmag. In order to improve the statistics each light curve was duplicated 11 times, with different transit signals injected in

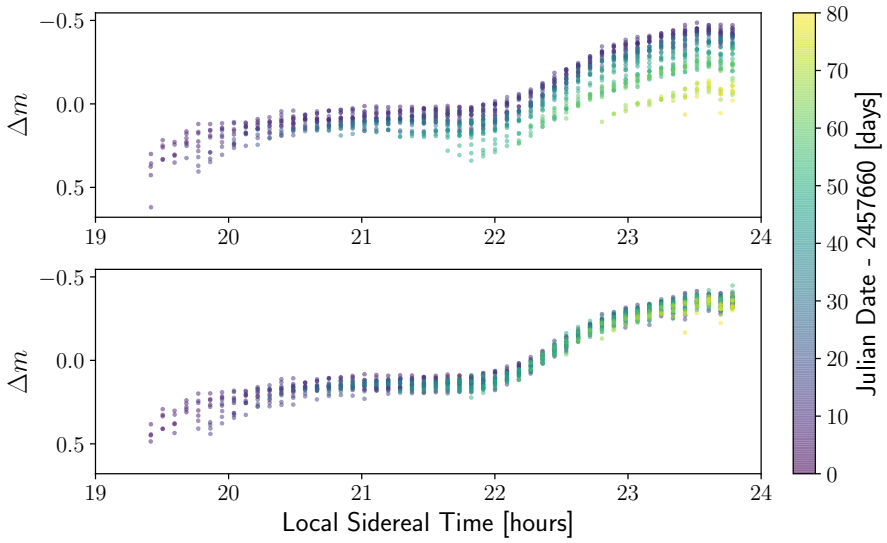

Figure 3.12: Light curve of HD 205555, as observed by the LPC camera during 2016Q4, as a function of the local sidereal time and coloured by the Julian date of the observations. The top panels shows the data after primary calibration with the magnitudes, m_i, as free parameters, while the bottom panel shows the data after primary calibration with the $m_i = m_{V,i}$.

the first ten duplicates and the 11th acting as a reference. For the test using three years of data we extend the range of $P_{\rm inj}$ to $[1, 10)$ days. We used the optimal Local Linear secondary calibration method for both the one year and three years of data.

After running the signal recovery test on one year of data we found that seven stars were rejected by the BLS algorithm because insufficient data was available. We further removed 119 stars with $m_V < 4$, focusing on the range $4 < m_V < 8.4$ where MASCARA was designed for optimal performance but we note that the input catalogue does contain brighter stars, of the 48,740 remaining signals 54.8% are recovered overall. Table 3.5 lists the recovery fractions for a number of different subsets of the sample and Fig. 3.13 shows the recovery fractions as a function of $P_{\rm inj}$, m_v, α and δ for the different transit depths p^2.

The recovery fraction depends only weakly on the values of b and $\rho_\star$, ranging from $\sim$50% to $\sim$60%, with higher values of both parameters resulting in lower recovery fractions. This dependence is expected as higher values of b and $\rho_\star$ result in shorter transits for fixed orbital periods, reducing the amount of in-transit data and increasing the total amount of data needed to obtain a detection. The recovery fraction depends strongly on p^2, recovering 84%, 60.5% and 20.7% for the different depths, and showing a steep drop in recovered signals going from $p^2 = 0.01$ to $p^2 = 0.005$. The dependence on the injected period is shown in panel (a) of Fig. 3.13 for each value of p^2. The recovery fraction decreases as a function of the injected period, as fewer transits are observed on a fixed baseline, and strong dips are present at integer multiples of one day, where ground-based surveys are less sensitive due to gaps in the coverage.

The dependence on stellar magnitude, right ascension and declination are shown in

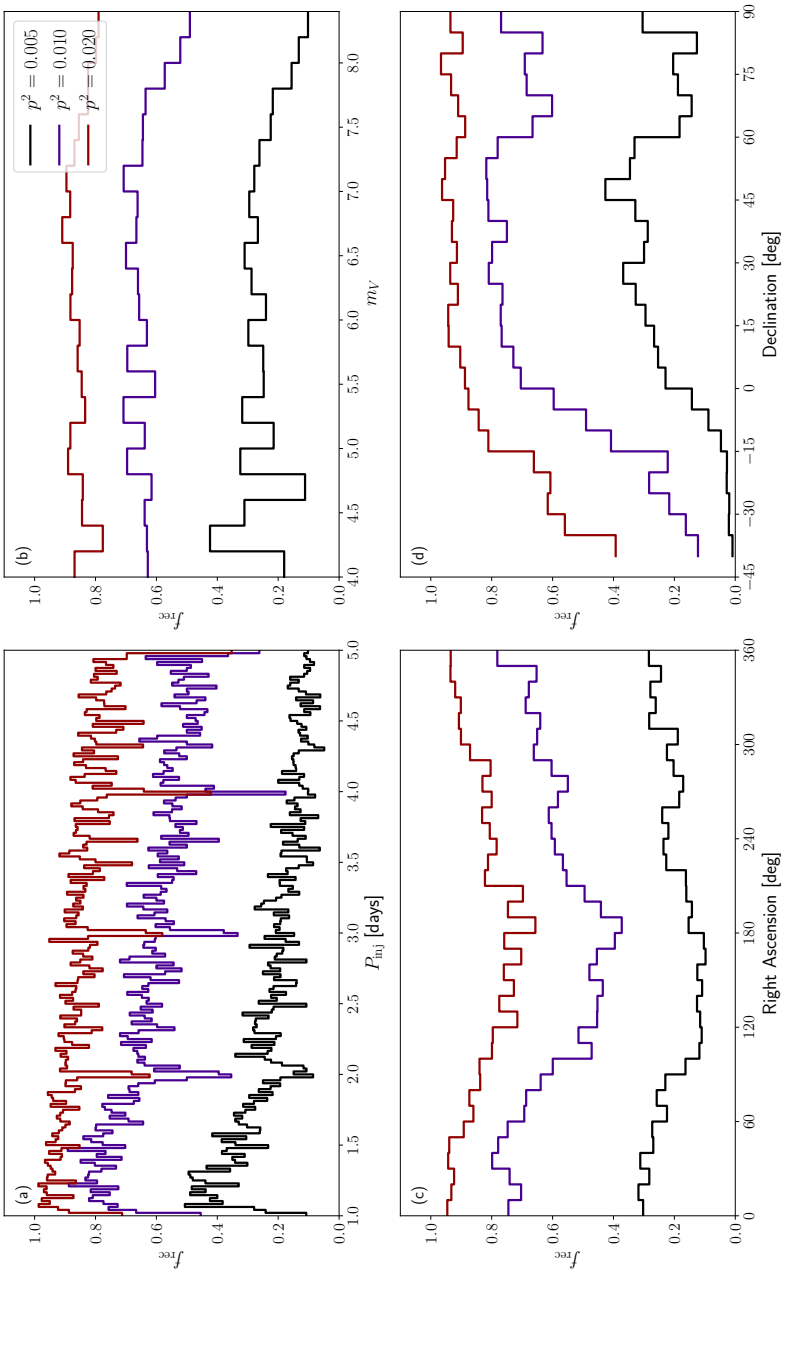

Figure 3.13: Fraction of transit signals recovered from one year of data from the La Palma station. The curves show the fraction of recovered signals for the different transit depths. The panels show the recovery rates as a function of different parameters: *(a)* as a function of the injected period in 192 bins of 0.5 hours, *(b)* as a function of the visual magnitude in 22 bins of 0.2 magnitudes, *(c)* as a function of the right ascension in 36 bins of 10° and *(d)* as a function of the declination in 27 bins of 5°.

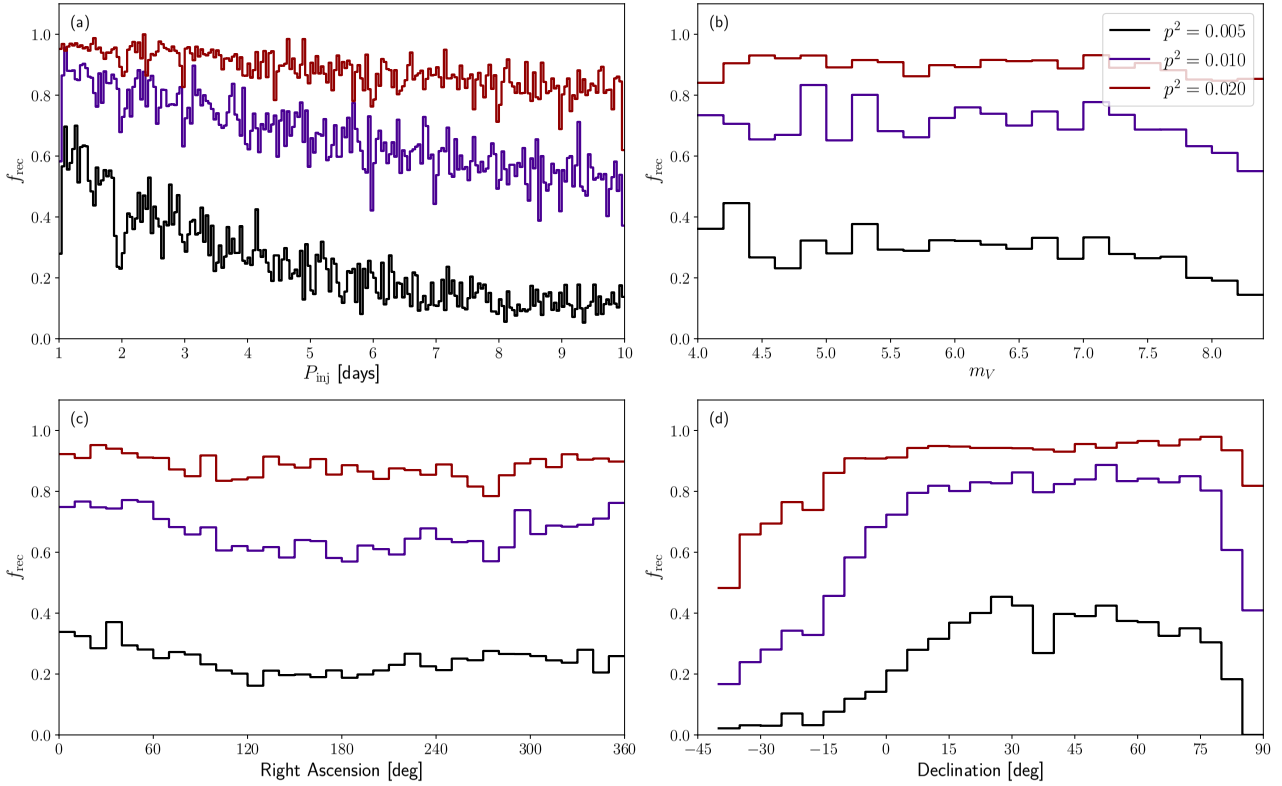

Figure 3.14: Fraction of transit signals recovered from three years of data from the La Palma station. Panels and curves are the same as in Fig. 3.13 with the exception of panel *(a)*, which now shows the data in 216 bins of 1 hour.

Table 3.5: Results of signal recovery tests on data from the La Palma station, for one year of data with periods between one and five days and three years of data with periods between one and ten days.

Selection	$f_{\rm rec}$ [%]	$f_{\rm rec}$ [%]
	1 year	3 years
All	54.8	59.6
$\delta > 0^\circ$	65.4	70.1
$\delta < 0^\circ$	35.8	40.8
$p^2 = 0.005$	20.7	24.7
$p^2 = 0.01$	60.5	66.7
$p^2 = 0.02$	84.0	88.1
$b = 0.0$	57.7	62.7
$b = 0.5$	51.8	56.4
$\rho_\star = 0.4$ g cm^{-3}	59.5	64.1
$\rho_\star = 0.9$ g cm^{-3}	54.1	59.0
$\rho_\star = 1.4$ g cm^{-3}	50.9	55.6

panels (b), (c) and (d) of Fig. 3.13 for each value of p^2. As a function of m_V the recovery rate is relatively flat for $m_V < 7.5$, before dropping off towards fainter magnitudes, qualitatively matching the achieved RMS as a function of magnitude (see Fig. 3.9). We find a sinusoidal behaviour with α, which can be explained by the changes in the length of the night across the year as stars observed in winter will have more data available. Finally, as a function of the declination we find that the recovery rate peaks between $0^\circ < \delta < 60^\circ$ with a small drop at $\delta > 60^\circ$ and a steep drop-off at $\delta < 0^\circ$. These features can be explained by the on-sky coverage of the La Palma station (Talens et al., 2017b, Fig. 2), at $\delta > 60^\circ$ the sky is observed by only the LPN camera while between $-20^\circ < \delta < 60^\circ$ we cover the sky with three or four cameras, and with significant overlap between the cameras. The recovery fraction drops at $\delta \sim 0^\circ$ rather that $\delta \sim -20^\circ$ because the width of the hour angle window as a function of the declination becomes the limiting factor on the amount of data obtained for each star. The HA coverage is $\sim$8 h at $\delta \sim 0^\circ$, comparable to the length of the shortest night, and shrinks to $\sim$5 h at $\delta \sim -20^\circ$. The area below $\delta = 0^\circ$ accounts for a large fraction of the total observed area, so we also report recovery rates for $\delta > 0^\circ$ and $\delta < 0^\circ$ as 65.4% and 34.8%, respectively.

After running the signal recovery test on three years of data we found three stars were rejected by the BLS algorithm because insufficient data was available, and we removed 125 stars with $m_V < 4$, leaving 48,720 signals. The results are listed in Table 3.5 and shown if Fig. 3.14.

With three years of MASCARA data we obtain slightly better performance out to ten day orbital periods than we did out to five day periods with only one year of data. We also find similar dependencies on the transit and stellar parameters, and a slightly improved recovery rate for periods $<$5 days, particularly for the shallowest transits ($p^2 = 0.005$). From panels (b) and (c) of Fig. 3.14 we see that for the deepest transits ($p^2 = 0.02$) the dependencies on m_V and α show less structure than those of shallower transits, suggesting that for the deeper transits we are no longer limited by the RMS or changes in the data volume with time of year, though from panel (d) we see that changes in the data volume with declination remain a limiting factor. The only other major difference is a decrease in

the number of signals recovered in the declination bin closes to the pole for $p^2 = 0.01$ and $p^2 = 0.005$, however this could be a consequence of the small area of this bin, which reduces the number of available stars and increases the uncertainty on the result. In fact, for the three year recovery test only five distinct stars were selected in this declination bin. Considering only the region of parameter space where MASCARA La Palma performs best we find that with three years of data we recover a total 93% of signals with $1 < P < 5$ days and depths $\geq 1\%$ at $\delta > 0°$, versus 84% in one year of data.

3.6 The A-star occurrence rate

Using the results of the signal recovery analysis, and the hot Jupiters detected by MASCARA La Palma, it is possible to place a first constraint on the occurrence of hot Jupiter around A-type stars. From radial velocity (RV) surveys the occurrence rate of hot Jupiters around FGK-stars is estimated to to be $\sim 1\%$ (e.g. Mayor et al., 2011; Wright et al., 2012), while transit surveys such as *Kepler* suggest a lower occurrence rate of $\sim 0.4\%$ (e.g. Howard et al., 2012; Fressin et al., 2013). Furthermore, RV surveys of evolved stars indicate that the occurrence rate of massive planets increases with stellar mass (e.g. Reffert et al., 2015; Ghezzi et al., 2018). The occurrence rate of hot Jupiters around A-stars has not been constrained, because A-stars are typically excluded from RV surveys, and difficult to follow-up at the fainter magnitudes probed by most transit surveys. Within the magnitude range observed by MASCARA ($4 < m_V < 8.4$) four planets have been discovered transiting A-stars, WASP-33, MASCARA-1, MASCARA-2 and KELT-9 (Collier Cameron et al., 2010; Talens et al., 2017a, 2018; Lund et al., 2017; Gaudi et al., 2017) all of which are detected in the three year dataset from MASCARA La Palma. All of these stars are located in the northern hemisphere ($\delta > 0°$) and the transits have depths ranging from 0.7% to 1.4%. The ASCC catalogue contains 7,320 A-stars in the northern hemisphere. From this we can make a simple estimate of the occurrence rate of hot Jupiters around A-stars, correcting for the geometric transit probability ($R_\star/a$, Borucki and Summers, 1984) and the completeness of MASCARA in the northern hemisphere (70.1%, see Table 3.5). We find an occurrence rate of 0.4% for hot Jupiters around A-stars, consistent with results for FGK-stars from other transits surveys. This is nevertheless a preliminary estimate, and should be considered a lower limit, as the sample size is small and incomplete. Several MASCARA candidates still await follow-up in the northern hemisphere and observations in the southern hemisphere are just beginning. Furthermore, currently only the significantly bloated hot Jupiters are found, as a $1\ R_\mathrm{J}$ planet around a $2\ R_\odot$ A-star would produce a 0.25% transit, and may be missed.

3.7 Summary and outlook

In this paper we described the methods used to process the raw photometry obtained by MASCARA and bRing for the purpose of detecting transiting exoplanets. For the primary calibration we use a modified version of the coarse decorrelation algorithm (Collier Cameron et al., 2006) to remove instrumental systematics, next we apply a secondary calibration method designed to remove residual systematics from individual stars and remove

long-term variations, which are not of interest in the context of transit detection. Finally, we search these data for transit signals using the Box Least-Squares algorithm and place the results in a database which we use to select and vet promising candidates for follow-up observations.

In order to assess the quality of the calibrated data and the ability of MASCARA to detect transiting exoplanets we computed the RMS scatter as a function of magnitude, demonstrating an RMS of 10 mmag is obtained at $m_V \sim 7.5$, depending on the camera considered. In addition, we performed signal recovery tests, a more powerful diagnostic of the data quality in the context of transit detection, demonstrating that with one year of data obtained by the La Palma station we can recover 54.8% of signals with periods between one and five days. With this test we identified two main causes for missed detections. First, the quality of the photometry, with 84%, 60.5% and 20.7% of 2%, 1% and 0.5% depth transits recovered, respectively. Second, the data volume obtained at different declinations, recovering 65.4% at $\delta > 0^\circ$ versus 35.8% at $\delta < 0^\circ$. Finally, we demonstrated that with the full three years of data available for the La Palma station we can obtain similar recovery rates on signals with periods between one and ten days, and recover 93% of transits of 1% or deeper with $1 < P < 5$ days at $\delta > 0^\circ$.

Over the course of 2017 the MASCARA station at La Silla and the two bRing stations have begun observing the southern sky. At the time of writing we have not yet obtained a full years worth of data from MASCARA La Silla, preventing us from performing a comparable signal recovery test for the southern hemisphere. However, based on the RMS curves presented in Fig. 3.9 we expect to obtain at least similar, and probably improved, performance with MASCARA La Silla. The La Silla station observes the sky between $-90^\circ < \delta < 40^\circ$, providing the region with $-40^\circ < \delta < 0^\circ$ with coverage comparable to the that provided by MASCARA La Palma between $0^\circ < \delta < 40^\circ$, filling in the gap where the recovery rates from the La Palma station are low. Furthermore, at the declinations where the MASCARA La Silla FoV overlaps with the bRing FoV, at $\delta \lesssim -30^\circ$, the near continuous temporal coverage obtained reduces the baseline needed for reliable transit detections at a given orbital period. Using data from the southern stations a number of transit candidates have already been identified and follow-up efforts have started.

Using the results from our signal recovery tests, and the hot Jupiters detected by MASCARA La Palma, we placed a lower limit of 0.4% on the occurrence rate of hot Jupiters around A-type stars. This number is consistent with previous results for the occurrence rates of hot Jupiters around FGK stars from RV (e.g. Mayor et al., 2011; Wright et al., 2012) and transit surveys (e.g. Howard et al., 2012; Fressin et al., 2013). We expect to be able to improve our constraint on the occurrence rate in the future, as additional candidate planets still await verification in the north and south, but caution that $\sim 1\ R_\mathrm{J}$ hot Jupiters orbiting A stars are beyond the photometric precision of MASCARA and bRing.

Our ability to blindly find signals with periods as long as 10 days demonstrates the possibilities of combining MASCARA data with that of the TESS satellite (Ricker et al., 2015), which was launched in April 2018. TESS will obtain photometry for the same stars observed by MASCARA at higher precision but on much shorter baselines, 27 days over most of the sky with longer baselines closer to the ecliptic poles. As a result TESS might only observe one transit event for periods between 13.5 and 27 days, placing constraints on the transit shape and epoch, but not the period. However, this information can be used to run specialized transit searches on the MASCARA data of these stars, boosting the signal by

utilizing the transit shape and epoch from TESS and by running the search jointly with the secondary calibration methods. In this way, we expect to be able to place constraints on the orbital periods of some of the TESS single transit candidates, making potential follow-up of these targets less time intensive.

Acknowledgements

I.S. acknowledges support from a NWO VICI grant (639.043.107). This project has received funding from the European Research Council (ERC) under the European Union's Horizon 2020 research and innovation programme (grant agreement nr. 694513). E.E.M. and S.N.M. acknowledge support from the NASA NExSS programme. S.N.M. is a U.S. Department of Defense SMART scholar sponsored by the U.S. Navy through SSC-LANT. Part of this research was conducted at Jet Propulsion Laboratory, California Institute of Technology, under a contract with the National Aeronautics and Space Administration. Construction of the bRing observatory at Siding Springs, Australia would not be possible without a University of Rochester University Research Award, help from Mike Culver and Rich Sarkis (UR), and generous donations of time, services, and materials from Joe and Debbie Bonvissuto of Freight Expediters, Michael Akkaoui and his team at Tanury Industries, Robert Harris and Michael Fay at BCI, Koch Division, Mark Paup, Dave Mellon, and Ray Miller and the Zippo Tool Room. This work has made use of data from the European Space Agency (ESA) mission *Gaia* (`https://www.cosmos.esa.int/gaia`), processed by the *Gaia* Data Processing and Analysis Consortium (DPAC,`https://www.cosmos.esa.int/web/gaia/dpac/consortium`). Funding for the DPAC has been provided by national institutions, in particular the institutions participating in the *Gaia* Multilateral Agreement. This research has made use of the SIMBAD database, operated at CDS, Strasbourg, France. This research has made use of the International Variable Star Index (VSX) database, operated at AAVSO, Cambridge, Massachusetts, USA. We have benefited greatly from the publicly available programming language Python, including the numpy, matplotlib, astropy, scipy and h5py packages.

3.A Details on solving Eqs. 3.4 and 3.7

3.A.1 Spatial

Since the index n solely depends on quantities related to the star i Eq. 3.4 can be written as

$$\ln L = -\frac{1}{2}\sum_{n}\sum_{i\in n,t}\left[\ln(2\pi\bar{\sigma}_{it}^2) + \frac{(\bar{m}_{it} - T_{nk} - f(x_{it}, y_{it}))^2}{\bar{\sigma}_{it}^2}\right], \tag{3.12}$$

and each ring n can be solved independently. Setting the derivatives to zero results in:

$$\frac{\partial}{\partial T_{nk}} \ln L_n = 0 = \sum_{i,t \in n,k} \frac{\bar{m}_{it} - T_{nk} - f(x_{it}, y_{it})}{\bar{\sigma}_{it}^2} \tag{3.13}$$

$$\frac{\partial}{\partial a_{nl}} \ln L_n = 0 = \sum_{i,t \in n,l} \frac{\bar{m}_{it} - T_{nk} - f(x_{it}, y_{it})}{\bar{\sigma}_{it}^2}. \tag{3.14}$$

These equations are solved iteratively for T_{nk} and the amplitudes a_{nl}, b_{nl}, c_{nl}, d_{nl}. First T_{nk} is obtained from Eq. 3.13 while keeping the amplitudes fixed. Then the amplitudes are obtained simultaneously by solving Eq. 3.14 using a linear least-squares solver while keeping T_{nk} fixed. These steps are then repeated until convergence is reached.

3.A.2 Temporal

Since the index q solely depends on quantities related to the star i Eq. 3.7 can be written as

$$\ln L = -\frac{1}{2} \sum_q \sum_{i \in q,t} \left[\ln(2\pi(\sigma_{it}^2 + \sigma_i^2 + \sigma_{qt}^2)) + \frac{(\tilde{m}_{it} - m_i - c_{qt})^2}{\sigma_{it}^2 + \sigma_i^2 + \sigma_{qt}^2} \right], \tag{3.15}$$

and each patch q can be solved independently. Taking derivatives with respect to the variables m_i, σ_i and c_{qt}, σ_{qt} and setting them to zero gives:

$$\frac{\partial}{\partial m_i} \ln L_q = 0 = \sum_t \frac{\tilde{m}_{it} - m_i - c_{qt}}{\sigma_{it}^2 + \sigma_i^2 + \sigma_{qt}^2} \tag{3.16}$$

$$\frac{\partial}{\partial \sigma_i} \ln L_q = 0 = \sum_t \left[-\frac{1}{\sigma_{it}^2 + \sigma_i^2 + \sigma_{qt}^2} + \frac{(\tilde{m}_{it} - m_i - c_{qt})^2}{(\sigma_{it}^2 + \sigma_i^2 + \sigma_{qt}^2)^2} \right] \tag{3.17}$$

$$\frac{\partial}{\partial c_{qt}} \ln L_q = 0 = \sum_{i \in q} \frac{\tilde{m}_{it} - m_i - c_{qt}}{\sigma_{it}^2 + \sigma_i^2 + \sigma_{qt}^2} \tag{3.18}$$

$$\frac{\partial}{\partial \sigma_{qt}} \ln L_q = 0 = \sum_{i \in q} \left[-\frac{1}{\sigma_{it}^2 + \sigma_i^2 + \sigma_{qt}^2} + \frac{(\tilde{m}_{it} - m_i - c_{qt})^2}{(\sigma_{it}^2 + \sigma_i^2 + \sigma_{qt}^2)^2} \right]. \tag{3.19}$$

These equations are then solved iteratively for σ_i (fixing $m_i = m_{V,i}$ as described in Sect. 3.2) and c_{qt}, σ_{qt}. First σ_i is obtained by using a bisector method to solve Eq. 3.17 while keeping c_{qt} and σ_{qt} fixed. Then c_{qt} and σ_{qt} are jointly solved using a bisector method along σ_{qt}, first solving Eq. 3.18 for c_{qt} before evaluating Eq. 3.19 for the next bisection, all while keeping σ_i fixed. For the bisector method we consider an interval of $[0, 2)$ for both σ_i and σ_{qt}, and iterate until convergence is reached.

3.B Correction maps

Figures 3.15, 3.16 and 3.17 show the transmission and intrapixel amplitude maps for the LSW, LSS and AUE cameras, respectively. We selected these cameras in order to show a

representative range of on-sky orientations (together with the maps shown for the LPC camera in Sect. 3.2), and show the effect of local obscurations. The on-sky orientation of the LSW camera is representative of the LPE, LPW, LSE and LSW cameras of the MASCARA stations. For these cameras stars move approximately diagonally across the short axis of the CCDs. For this particular camera the intrapixel variations depend primarily on the x position, with almost no dependence on the y position, and poor sampling of x and y results in a decrease in quality near the bottom left of panels (a) and (b) and an arc on the left side of panels (c) and (d). The top-left corner of the CCD is masked because of the presence of a radio mast in that location. The on-sky orientation of the LSS camera is representative of the LPN and LSS cameras of the MASCARA stations. These cameras contain the poles and stars move across the CCDs in arcs. For this particular camera the intrapixel variations depend equally on the x and y positions and the quality of the solution decreases in an arc at the bottom of panels (a) and (b) and a vertical line down the centre of panels (c) and (d). The top-right corner of the CCD is masked to remove the MarLy telescope. The on-sky orientation of the AUE camera is representative of all bRing cameras and is qualitatively similar to LPN and LSS, though it sees less of the pole. For this particular camera the intrapixel variations depend more strongly on the x position, though a clear dependence on the y position is also present, and the quality of the solution decreases in an arc at the bottom of panels (a) and (b) and a diagonal down the centre of panels (c) and (d). The top-left and bottom-right corners are masked to remove obscurations by a building and a tree.

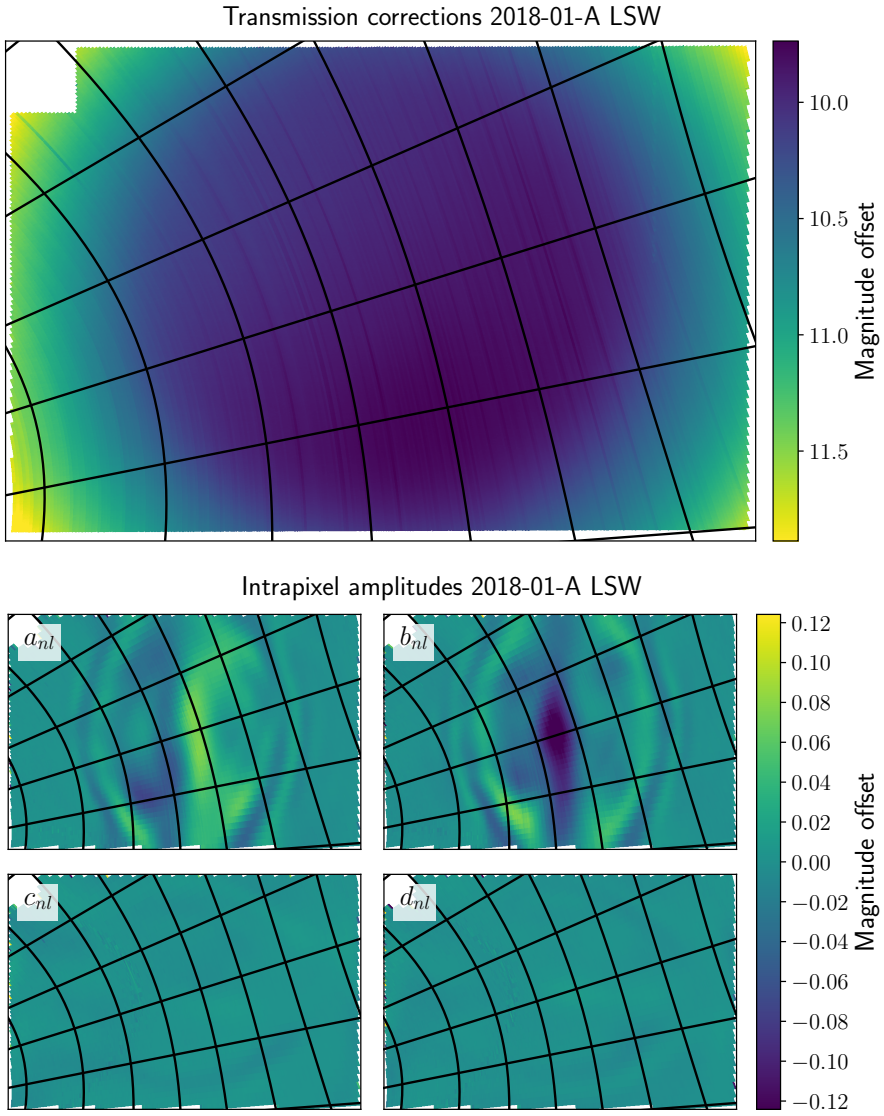

Figure 3.15: The transmission and intrapixel amplitude maps obtained from running the primary calibration on the 2018-01-A baseline of the LSW camera. The maps are shown projected onto the CCD and a grid in hour angle and declination is overlaid on top.

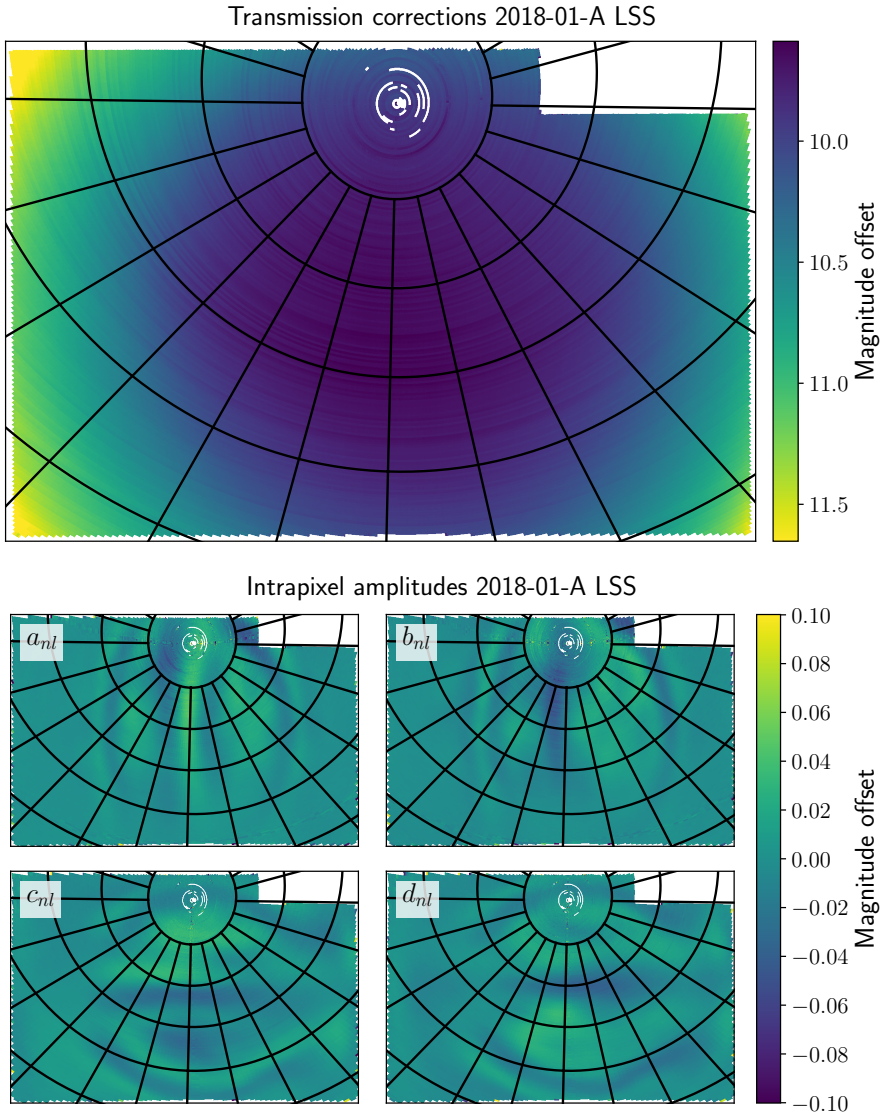

Figure 3.16: Same as Fig. 3.15 for the 2018-01-A baseline of the LSS camera.

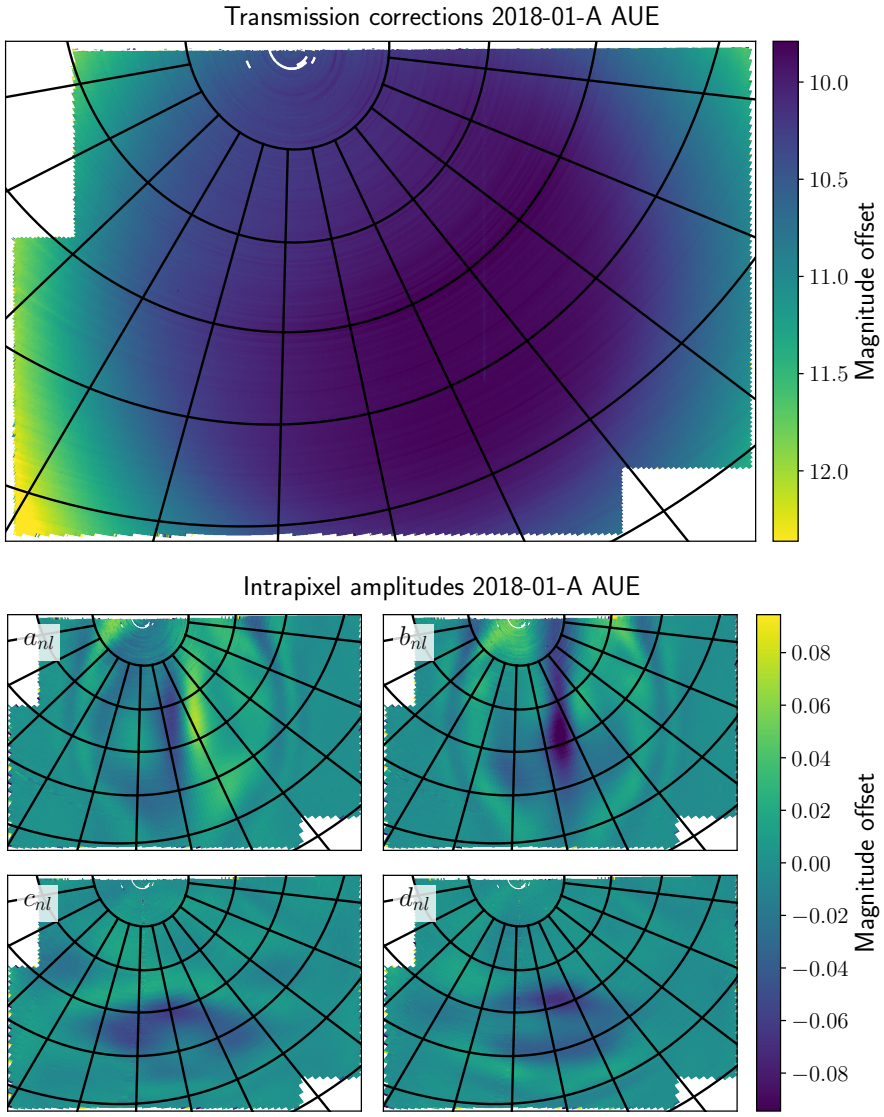

Figure 3.17: Same as Fig. 3.15 for the 2018-01-A baseline of the AUE camera.

Bibliography

Baluev, R. V., Sokov, E. N., Shaidulin, V. S., Sokova, I. A., Jones, H. R. A., Tuomi, M., Anglada-Escudé, G., Benni, P., Colazo, C. A., Schneiter, M. E., D'Angelo, C. S. V., Burdanov, A. Y., Fernández-Lajús, E., Başt ürk, Ö., Hentunen, V.-P., and Shadick, S. (2015). Benchmarking the power of amateur observatories for TTV exoplanets detection. *MNRAS*, 450:3101–3113.

Borucki, W. J. and Summers, A. L. (1984). The photometric method of detecting other planetary systems. *Icarus*, 58:121–134.

Burggraaff, O., Talens, G. J. J., Spronck, J., Lesage, A.-L., Stuik, R., Otten, G. P. P. L., Van Eylen, V., Pollacco, D., and Snellen, I. A. G. (2018). Studying bright variable stars with the Multi-site All-Sky CAmeRA (MASCARA). *ArXiv e-prints*.

Burke, C. J., Gaudi, B. S., DePoy, D. L., and Pogge, R. W. (2006). Survey for Transiting Extrasolar Planets in Stellar Systems. III. A Limit on the Fraction of Stars with Planets in the Open Cluster NGC 1245. *AJ*, 132:210–230.

Collier Cameron, A., Guenther, E., Smalley, B., McDonald, I., Hebb, L., Andersen, J., Augusteijn, T., Barros, S. C. C., Brown, D. J. A., Cochran, W. D., Endl, M., Fossey, S. J., Hartmann, M., Maxted, P. F. L., Pollacco, D., Skillen, I., Telting, J., Waldmann, I. P., and West, R. G. (2010). Line-profile tomography of exoplanet transits - II. A gas-giant planet transiting a rapidly rotating A5 star. *MNRAS*, 407:507–514.

Collier Cameron, A., Pollacco, D., Street, R. A., Lister, T. A., West, R. G., Wilson, D. M., Pont, F., Christian, D. J., Clarkson, W. I., Enoch, B., Evans, A., Fitzsimmons, A., Haswell, C. A., Hellier, C., Hodgkin, S. T., Horne, K., Irwin, J., Kane, S. R., Keenan, F. P., Norton, A. J., Parley, N. R., Osborne, J., Ryans, R., Skillen, I., and Wheatley, P. J. (2006). A fast hybrid algorithm for exoplanetary transit searches. *MNRAS*, 373:799–810.

Fressin, F., Torres, G., Charbonneau, D., Bryson, S. T., Christiansen, J., Dressing, C. D., Jenkins, J. M., Walkowicz, L. M., and Batalha, N. M. (2013). The False Positive Rate of Kepler and the Occurrence of Planets. *ApJ*, 766:81.

Gaia Collaboration, Brown, A. G. A., Vallenari, A., Prusti, T., de Bruijne, J. H. J., Babusiaux, C., and Bailer-Jones, C. A. L. (2018). Gaia Data Release 2. Summary of the contents and survey properties. *ArXiv e-prints*.

Gaia Collaboration, Brown, A. G. A., Vallenari, A., Prusti, T., de Bruijne, J. H. J., Mignard, F., Drimmel, R., Babusiaux, C., Bailer-Jones, C. A. L., Bastian, U., and et al. (2016a). Gaia Data Release 1. Summary of the astrometric, photometric, and survey properties. *A&A*, 595:A2.

Gaia Collaboration, Prusti, T., de Bruijne, J. H. J., Brown, A. G. A., Vallenari, A., Babusiaux, C., Bailer-Jones, C. A. L., Bastian, U., Biermann, M., Evans, D. W., and et al. (2016b). The Gaia mission. *A&A*, 595:A1.

Gaudi, B. S., Stassun, K. G., Collins, K. A., Beatty, T. G., Zhou, G., Latham, D. W., Bieryla, A., Eastman, J. D., Siverd, R. J., Crepp, J. R., Gonzales, E. J., Stevens, D. J., Buchhave, L. A., Pepper, J., Johnson, M. C., Colon, K. D., Jensen, E. L. N., Rodriguez, J. E., Bozza, V., Novati, S. C., D'Ago, G., Dumont, M. T., Ellis, T., Gaillard, C., Jang-Condell, H., Kasper, D. H., Fukui, A., Gregorio, J., Ito, A., Kielkopf, J. F., Manner, M., Matt, K., Narita, N., Oberst, T. E., Reed, P. A., Scarpetta, G., Stephens, D. C., Yeigh, R. R., Zambelli, R., Fulton, B. J., Howard, A. W., James, D. J., Penny, M., Bayliss, D., Curtis, I. A., Depoy, D. L., Esquerdo, G. A., Gould, A., Joner, M. D., Kuhn, R. B., Labadie-Bartz, J., Lund, M. B., Marshall, J. L., McLeod, K. K., Pogge, R. W., Relles, H., Stockdale, C., Tan, T. G., Trueblood, M., and Trueblood, P. (2017). A giant planet undergoing extreme-ultraviolet irradiation by its hot massive-star host. *Nature* , 546:514–518.

Ghezzi, L., Montet, B. T., and Johnson, J. A. (2018). Retired A Stars Revisited: An Updated Giant Planet Occurrence Rate as a Function of Stellar Metallicity and Mass. *ApJ*, 860:109.

Górski, K. M., Hivon, E., Banday, A. J., Wandelt, B. D., Hansen, F. K., Reinecke, M., and Bartelmann, M. (2005). HEALPix: A Framework for High-Resolution Discretization and Fast Analysis of Data Distributed on the Sphere. *ApJ*, 622:759–771.

Grziwa, S., Pätzold, M., and Carone, L. (2012). The needle in the haystack: searching for transiting extrasolar planets in CoRoT stellar light curves. *MNRAS*, 420:1045–1052.

Howard, A. W., Marcy, G. W., Bryson, S. T., Jenkins, J. M., Rowe, J. F., Batalha, N. M., Borucki, W. J., Koch, D. G., Dunham, E. W., Gautier, III, T. N., Van Cleve, J., Cochran, W. D., Latham, D. W., Lissauer, J. J., Torres, G., Brown, T. M., Gilliland, R. L., Buchhave, L. A., Caldwell, D. A., Christensen-Dalsgaard, J., Ciardi, D., Fressin, F., Haas, M. R., Howell, S. B., Kjeldsen, H., Seager, S., Rogers, L., Sasselov, D. D., Steffen, J. H., Basri, G. S., Charbonneau, D., Christiansen, J., Clarke, B., Dupree, A., Fabrycky, D. C., Fischer, D. A., Ford, E. B., Fortney, J. J., Tarter, J., Girouard, F. R., Holman, M. J., Johnson, J. A., Klaus, T. C., Machalek, P., Moorhead, A. V., Morehead, R. C., Ragozzine, D., Tenenbaum, P., Twicken, J. D., Quinn, S. N., Isaacson, H., Shporer, A., Lucas, P. W., Walkowicz, L. M., Welsh, W. F., Boss, A., Devore, E., Gould, A., Smith, J. C., Morris, R. L., Prsa, A., Morton, T. D., Still, M., Thompson, S. E., Mullally, F., Endl, M., and MacQueen, P. J. (2012). Planet Occurrence within 0.25 AU of Solar-type Stars from Kepler. *ApJS*, 201:15.

Kharchenko, N. V. (2001). All-sky compiled catalogue of 2.5 million stars. *Kinematika i Fizika Nebesnykh Tel*, 17:409–423.

Kharchenko, N. V. and Roeser, S. (2009). VizieR Online Data Catalog: All-Sky Compiled Catalogue of 2.5 million stars (Kharchenko+ 2009). *VizieR Online Data Catalog*, 1280.

Kovács, G., Bakos, G., and Noyes, R. W. (2005). A trend filtering algorithm for wide-field variability surveys. *MNRAS*, 356:557–567.

Kovács, G., Zucker, S., and Mazeh, T. (2002). A box-fitting algorithm in the search for periodic transits. *A&A*, 391:369–377.

Kreidberg, L., Bean, J. L., Désert, J.-M., Benneke, B., Deming, D., Stevenson, K. B., Seager, S., Berta-Thompson, Z., Seifahrt, A., and Homeier, D. (2014). Clouds in the atmosphere of the super-Earth exoplanet GJ1214b. *Nature* , 505:69–72.

Lund, M. B., Rodriguez, J. E., Zhou, G., Gaudi, B. S., Stassun, K. G., Johnson, M. C., Bieryla, A., Oelkers, R. J., Stevens, D. J., Collins, K. A., Penev, K., Quinn, S. N., Latham, D. W., Villanueva, Jr., S., Eastman, J. D., Kielkopf, J. F., Oberst, T. E., Jensen, E. L. N., Cohen, D. H., Joner, M. D., Stephens, D. C., Relles, H., Corfini, G., Gregorio, J., Zambelli, R., Esquerdo, G. A., Calkins, M. L., Berlind, P., Ciardi, D. R., Dressing, C., Patel, R., Gagnon, P., Gonzales, E., Beatty, T. G., Siverd, R. J., Labadie-Bartz, J., Kuhn, R. B., Colón, K. D., James, D., Pepper, J., Fulton, B. J., McLeod, K. K., Stockdale, C., Calchi Novati, S., DePoy, D. L., Gould, A., Marshall, J. L., Trueblood, M., Trueblood, P., Johnson, J. A., Wright, J., McCrady, N., Wittenmyer, R. A., Johnson, S. A., Sergi, A., Wilson, M., and Sliski, D. H. (2017). KELT-20b: A Giant Planet with a Period of $P \sim 3.5$ days Transiting the $V \sim 7.6$ Early A Star HD 185603. *AJ*, 154:194.

Mamajek, E. E., Quillen, A. C., Pecaut, M. J., Moolekamp, F., Scott, E. L., Kenworthy, M. A., Collier Cameron, A., and Parley, N. R. (2012). Planetary Construction Zones in Occultation: Discovery of an Extrasolar Ring System Transiting a Young Sun-like Star and Future Prospects for Detecting Eclipses by Circumsecondary and Circumplanetary Disks. *AJ*, 143:72.

Mayor, M., Marmier, M., Lovis, C., Udry, S., Ségransan, D., Pepe, F., Benz, W., Bertaux, J. ., Bouchy, F., Dumusque, X., Lo Curto, G., Mordasini, C., Queloz, D., and Santos, N. C. (2011). The HARPS search for southern extra-solar planets XXXIV. Occurrence, mass distribution and orbital properties of super-Earths and Neptune-mass planets. *ArXiv e-prints*.

Ofir, A. (2014). Optimizing the search for transiting planets in long time series. *A&A*, 561:A138.

Pont, F., Zucker, S., and Queloz, D. (2006). The effect of red noise on planetary transit detection. *MNRAS*, 373:231–242.

Reffert, S., Bergmann, C., Quirrenbach, A., Trifonov, T., and Künstler, A. (2015). Precise radial velocities of giant stars. VII. Occurrence rate of giant extrasolar planets as a function of mass and metallicity. *A&A*, 574:A116.

Ricker, G. R., Winn, J. N., Vanderspek, R., Latham, D. W., Bakos, G. Á., Bean, J. L., Berta-Thompson, Z. K., Brown, T. M., Buchhave, L., Butler, N. R., Butler, R. P., Chaplin, W. J., Charbonneau, D., Christensen-Dalsgaard, J., Clampin, M., Deming, D., Doty, J., De Lee, N., Dressing, C., Dunham, E. W., Endl, M., Fressin, F., Ge, J., Henning, T., Holman, M. J., Howard, A. W., Ida, S., Jenkins, J. M., Jernigan, G., Johnson, J. A., Kaltenegger, L., Kawai, N., Kjeldsen, H., Laughlin, G., Levine, A. M., Lin, D., Lissauer, J. J., MacQueen, P., Marcy, G., McCullough, P. R., Morton, T. D., Narita, N., Paegert, M., Palle, E., Pepe, F., Pepper, J., Quirrenbach, A., Rinehart, S. A., Sasselov, D., Sato, B., Seager, S., Sozzetti,

A., Stassun, K. G., Sullivan, P., Szentgyorgyi, A., Torres, G., Udry, S., and Villasenor, J. (2015). Transiting Exoplanet Survey Satellite (TESS). *Journal of Astronomical Telescopes, Instruments, and Systems*, 1(1):014003.

Smith, J. C., Stumpe, M. C., Van Cleve, J. E., Jenkins, J. M., Barclay, T. S., Fanelli, M. N., Girouard, F. R., Kolodziejczak, J. J., McCauliff, S. D., Morris, R. L., and Twicken, J. D. (2012). Kepler Presearch Data Conditioning II - A Bayesian Approach to Systematic Error Correction. *PASP*, 124:1000.

Stuik, R., Bailey, J. I., Dorval, P., Talens, G. J. J., Laginja, I., Mellon, S. N., Lomberg, B. B. D., Crawford, S. M., Ireland, M. J., Mamajek, E. E., and Kenworthy, M. A. (2017). bRing: An observatory dedicated to monitoring the β Pictoris b Hill sphere transit. *A&A*, 607:A45.

Stumpe, M. C., Smith, J. C., Van Cleve, J. E., Twicken, J. D., Barclay, T. S., Fanelli, M. N., Girouard, F. R., Jenkins, J. M., Kolodziejczak, J. J., McCauliff, S. D., and Morris, R. L. (2012). Kepler Presearch Data Conditioning I - Architecture and Algorithms for Error Correction in Kepler Light Curves. *PASP*, 124:985.

Talens, G. J. J., Albrecht, S., Spronck, J. F. P., Lesage, A.-L., Otten, G. P. P. L., Stuik, R., Van Eylen, V., Van Winckel, H., Pollacco, D., McCormac, J., Grundahl, F., Fredslund Andersen, M., Antoci, V., and Snellen, I. A. G. (2017a). MASCARA-1 b. A hot Jupiter transiting a bright $m_V = 8.3$ A-star in a misaligned orbit. *A&A*, 606:A73.

Talens, G. J. J., Justesen, A. B., Albrecht, S., McCormac, J., Van Eylen, V., Otten, G. P. P. L., Murgas, F., Palle, E., Pollacco, D., Stuik, R., Spronck, J. F. P., Lesage, A.-L., Grundahl, F., Fredslund Andersen, M., Antoci, V., and Snellen, I. A. G. (2018). MASCARA-2 b. A hot Jupiter transiting the $m_V = 7.6$ A-star HD 185603. *A&A*, 612:A57.

Talens, G. J. J., Spronck, J. F. P., Lesage, A.-L., Otten, G. P. P. L., Stuik, R., Pollacco, D., and Snellen, I. A. G. (2017b). The Multi-site All-Sky CAmeRA (MASCARA). Finding transiting exoplanets around bright ($m_V < 8$) stars. *A&A*, 601:A11.

Tamuz, O., Mazeh, T., and Zucker, S. (2005). Correcting systematic effects in a large set of photometric light curves. *MNRAS*, 356:1466–1470.

Watson, C. L., Henden, A. A., and Price, A. (2006). The International Variable Star Index (VSX). *Society for Astronomical Sciences Annual Symposium*, 25:47.

Wenger, M., Ochsenbein, F., Egret, D., Dubois, P., Bonnarel, F., Borde, S., Genova, F., Jasniewicz, G., Laloë, S., Lesteven, S., and Monier, R. (2000). The SIMBAD astronomical database. The CDS reference database for astronomical objects. *A&AS*, 143:9–22.

Wright, J. T., Marcy, G. W., Howard, A. W., Johnson, J. A., Morton, T. D., and Fischer, D. A. (2012). The Frequency of Hot Jupiters Orbiting nearby Solar-type Stars. *ApJ*, 753:160.

4 MASCARA-1 b: A hot Jupiter transiting a bright $m_V = 8.3$ A-star in a misaligned orbit

We report the discovery of MASCARA-1 b, which is the first exoplanet discovered with the Multi-site All-Sky CAmeRA (MASCARA). This exoplanet is a hot Jupiter orbiting a bright $m_V = 8.3$, rapidly rotating ($v \sin i_\star > 100$ km s^{-1}) A8 star with a period of $2.148780 \pm 8 \times 10^{-6}$ days. The planet has a mass and radius of 3.7 ± 0.9 $M_{\rm Jup}$ and 1.5 ± 0.3 $R_{\rm Jup}$, respectively. As with most hot Jupiters transiting early-type stars, we find a misalignment between the planet orbital axis and the stellar spin axis, which may be a signature of the formation and migration histories of this family of planets. MASCARA-1 b has a mean density of 1.5 ± 0.9 g cm^{-3} and an equilibrium temperature of 2570^{+50}_{-30} K, that is one of the highest temperatures known for a hot Jupiter to date. The system is reminiscent of WASP-33, but the host star lacks apparent delta-scuti variations, making the planet an ideal target for atmospheric characterization. We expect this to be the first of a series of hot Jupiters transiting bright early-type stars that will be discovered by MASCARA.

G.J.J. Talens, S. Albrecht, J.F.P. Spronck, A.-L. Lesage, G.P.P.L. Otten, R. Stuik, V. Van Eylen, H. Van Winckel, D. Pollacco, J. McCormac, F. Grundahl, M. Fredslund Andersen, V. Antoci and I.A.G Snellen

A&A, 606, A73, (2017)

4.1 Introduction

Since the discovery of the first exoplanet by Mayor and Queloz (1995) the number of new planets detected has been growing exponentially. First from ground-based radial velocity (Vogt et al., 2000; Valenti and Fischer, 2005; Jenkins et al., 2009) and transit surveys (Bakos et al., 2004; Pollacco et al., 2006) and in recent years from the CoRoT and *Kepler* satellites (Barge et al., 2008; Borucki et al., 2010). Today, several thousand exoplanets are known and our understanding of the population has grown immensely. In particular, we now know that on average a late-type main-sequence star is orbited by at least one planet (Batalha, 2014).

Despite these advances, observational biases mean we still know only a few planets transiting both bright and early-type stars. The Multi-site All-Sky CAmeRA (MASCARA; Talens et al., 2017) transit survey aims to fill this gap in parameter space by monitoring all stars with magnitudes $4 < m_V < 8.4$. MASCARA consists of a northern and a southern station, each equipped with five cameras to cover the entire local sky down to airmass 2 and partially down to airmass 3. In this way MASCARA is expected to find several new transiting hot Jupiters around bright stars, some of which will be of early spectral types (Snellen et al., 2012).

MASCARA was designed to find Jupiter-like planets transiting bright stars because these allow detailed atmospheric characterization. Observations of the planet transmission spectra during transit and thermal emission at secondary eclipse, coupled with detailed atmospheric models, can be used to constrain atmospheric properties such as temperature structure, composition, and the presence of clouds and hazes (Madhusudhan and Seager, 2009; Sing et al., 2011; Deming et al., 2013; Kreidberg et al., 2014; Sing et al., 2016). Such observations, however, are expensive if not impossible on fainter stars. In particular, the use of high-resolution transmission spectroscopy has been limited to a few bright targets such as HD 209458 and HD 189733 (Snellen et al., 2010; Brogi et al., 2016), which were first discovered through radial velocity observations.

In addition to finding planets around bright stars, the all-sky, magnitude-limited sample targeted by MASCARA is biased towards early-type stars, which are particularly challenging to follow up at fainter magnitudes. Studying the hot Jupiter population around hot stars is interesting for several reasons. First, these hot Jupiters have the highest equilibrium temperatures, which is expected to have a significant impact on their atmospheric structure and composition, such as the occurrence of inversion layers due to the presence of specific molecular compounds (e.g. TiO/VO Hubeny et al., 2003; Fortney et al., 2008) high up in the atmospheres (e.g. Burrows et al. (2007); O'Donovan et al. (2010) but see also Schwarz et al. (2015)). Second, hot Jupiters around early-type stars receive more UV radiation than similar planets around late-type stars. This UV radiation may drive unique chemical processes in the atmospheres of these planets (Casewell et al., 2015). Finally, comparing their orbital properties with those of hot Jupiters orbiting solar-type stars may shed light on their formation. For example, the large incidence of misaligned orbits for hot Jupiters orbiting early-type stars (Winn et al., 2010; Schlaufman, 2010; Albrecht et al., 2012) may be linked to orbital migration processes (e.g. Fabrycky and Tremaine, 2007; Nagasawa et al., 2008).

In this paper we present the discovery of MASCARA-1 b, which is the first exoplanet discovered by MASCARA. MASCARA-1 b orbits the $m_V = 8.3$ A8 star HD 201585 with a period of 2.15 days. We present our observations in Section 4.2. Stellar and system pa-

rameters are described in Sects. 4.3 and 4.4, and we conclude with a discussion in Sect. 4.5.

4.2 Observations

The northern station of MASCARA, located on La Palma, started science operations in early 2015 and produces photometry for all stars with $4 < m_V < 8.4$ at a cadence of 6.4 seconds down to airmass $\sim$3 (Talens et al., 2017). The raw MASCARA photometry is processed using a heavily modified version of the coarse decorrelation algorithm described in Collier Cameron et al. (2006) to remove instrumental systematics and earth-atmospheric effects. Subsequently, the data are binned to a cadence of 320 seconds and further detrended by means of an empirical fit to remove both residual variations linked to the target positions on the CCDs and long-term trends in the data. Finally, a box least-squares (BLS; Kovács et al., 2002) transit search algorithm is used to find potential transit signals. The details of the data reduction and transit search algorithms will be discussed in an upcoming paper (Talens et al. in prep).

After running the BLS algorithm on data taken between February and December 2015, MASCARA-1 (HD 201585, HIP 104513) was among the most promising stars to be listed as a potential exoplanet host. We obtained high-dispersion spectra at R = 85,000 from the HERMES spectograph (Raskin et al., 2011) at the 1.2 m Mercator telescope on La Palma taken between June and September 2016 (see Table 4.1). A total of 13 spectra were taken and reduced using the HERMES pipeline[1], allowing us to characterize the host star and constrain the companion mass from radial velocity (RV) measurements.

In addition to the MASCARA photometry, two transits were observed with the 0.4m NITES telescope (McCormac et al., 2014) on La Palma. 1,092 images with 10s exposure times were obtained with a Johnson-Bessel R-band filter on 23 July 2016 and 887 images with 15s exposure times were obtained in the V-band on 17 September 2016. The telescope was defocused slightly on both nights to avoid saturation. The data were reduced in Python with CCDPROC (Craig et al., 2015) using a master bias, dark and flat. Master calibrations were made using a minimum of 21 of each frame. Non-variable comparison stars were selected by hand and aperture photometry was extracted using SEP (Barbary, 2016; Bertin and Arnouts, 1996). The shift between each defocused image was measured using the DONUTS (McCormac et al., 2013) algorithm and the photometry apertures were re-centred between frames. The final aperture size is chosen to minimize the RMS of the data points out of transit. The $0.66''$ pixel scale of NITES versus $1'$ for MASCARA allowed us to check against a faint eclipsing binary system within the MASCARA photometric aperture that could have explained the apparent transit signal.

Additional confirmation about the nature of the system, as well as a measurement of its spin-orbit angle, can come from a detection of the Rossiter-McLaughlin effect using in-transit spectroscopy (e.g. Zhou et al., 2016). We therefore obtained 28 high-dispersion echelle spectra at R$\sim$90,000 using the automated 1m Hertzsprung SONG telescope (Andersen et al., 2014) at Observatorio del Teide on 30 September 2016 (see Table 4.1). The observations were taken with 10 minute exposure times and a slit width of 1.2 arcsec and spanned $\sim$5 hr in total, covering the transit and post-egress. Ingress occurred during evening

[1] `http://hermes-as.oma.be/manuals/cookbook6.0.pdf`

Table 4.1: Observations used in the discovery of MASCARA-1 b.

Instrument	Date	$N_{\rm obs}$	$t_{\rm exp}$ [s]
MASCARA	Feb. 2015 - Sept. 2016	32705	320
HERMES	15 June 2016	1	1400
HERMES	17 July 2016	1	800
HERMES	18 July 2016	1	800
NITES	23 July 2016	1092	10
HERMES	5 Sept. 2016	1	1100
HERMES	7 Sept. 2016	1	1200
HERMES	7 Sept. 2016	1	1100
HERMES	9 Sept. 2016	1	1100
HERMES	10 Sept. 2016	1	1000
HERMES	10 Sept. 2016	1	1200
HERMES	11 Sept. 2016	1	1000
HERMES	12 Sept. 2016	1	1200
HERMES	13 Sept. 2016	1	900
HERMES	14 Sept. 2016	1	1100
NITES	17 Sept. 2016	887	15
SONG	30 Sept. 2016	28	600

twilight. Spectra were extracted from the observations following the procedure outlined in Grundahl et al. (2017), subsequently bad pixels were removed and the spectra were normalized.

4.3 Stellar parameters

At $m_V = 8.3$, most basic properties of MASCARA-1 are available in the literature. The parallax was already measured by Hipparcos (van Leeuwen, 2007) to be 5.0 ± 0.7 mas, implying a distance of 201.6 ± 28.9 pc. Recently, the GAIA DR1 (Gaia Collaboration et al., 2016) lists a parallax of 5.3 ± 0.3 mas (188.7 ± 10.7 pc) within 1σ of the Hipparcos value. For our analysis we adopted the GAIA parallax.

McDonald et al. (2012) combined the Hipparcos parallaxes with photometry from a number of surveys, including SDSS and 2MASS, to determine the effective temperature and luminosity of over 100,000 stars, including MASCARA-1 for which they derive an effective temperature of 7554 K and a bolometric luminosity of 14.98 $L_\odot$. We verified the effective temperature by fitting the wings of the hydrogen lines in the combined HERMES spectra with PHOENIX spectral models (Husser et al., 2013) and find $T_{\rm eff} = 7600 \pm 150$ K, which is consistent with the work by McDonald et al. (2012). For our further analysis, we used the values as derived by McDonald et al. (2012), assuming uncertainties of 150 K and 5 $L_\odot$ on $T_{\rm eff}$ and L_*, respectively[2] ; these uncertainties are not reported by the authors. We updated the luminosity for the new GAIA distance to be 13.1 ± 3.0 $L_\odot$. From the bolometric

[2]For $T_{\rm eff}$ we assumed an uncertainty comparable to our own analysis. For L_* the error on the distance alone implies an uncertainty of 4.3 $L_\odot$, which we round up to account for uncertainties in the total flux.

luminosity and effective temperature, we derived a stellar radius of $R_* = 2.1 \pm 0.2$ $R_\odot$. We used BAGEMASS (Maxted et al., 2015), a stellar evolution MCMC code, to determine the stellar mass and age from the effective temperature, metallicity, and stellar density[3], finding 1.72 ± 0.07 $M_\odot$ and 1.0 ± 0.2 Gyr, respectively. As an extra check we also computed the stellar radius from the BAGEMASS output and found a value of 1.97 ± 0.07 $R_\odot$, which is consistent with the radius derived from the GAIA parallax.

From the HERMES radial velocity pipeline[4] we also obtained the stellar equatorial rotation speed $v \sin i_\star = 106.7 \pm 0.4$ km s^{-1}.

4.4 System parameters

The system parameters were derived from modelling the available photometric and spectroscopic observations. The transit shape was fitted via the available MASCARA and NITES photometric data. The mass of the planet was constrained with the HERMES radial velocity measurements and the projected spin-orbit angle was obtained from the SONG transit data.

4.4.1 Photometric transit fit

A Mandel and Agol (2002) model was fitted to the photometric data taken by MASCARA with a Markov-chain Monte Carlo (MCMC) approach with the PYTHON packages BATMAN and EMCEE (Kreidberg, 2015; Foreman-Mackey et al., 2013). We fit a circular transit model, optimizing for the normalization F_0, transit epoch T_p, orbital period P, transit duration T_{14}, planet-to-star radius ratio p, and impact parameter b using uniform priors on all parameters. We employed a quadratic limb darkening law with fixed coefficients from Claret (2000), using values of $u_1 = 0.2609$, $u_2 = 0.3405$, appropriate for the host star. Subsequently, the NITES photometry was also fitted with the same model, except with the orbital period fixed to the best-fit value obtained from the MASCARA photometry and separate normalization factors F_1 and F_2 for each transit. In the modelling presented here we do not include the possible effects of non-spherical geometry, which can influence T_{14} and b, or gravity darkening, which can modify p. Both of these effects might play a role for a rapid rotator such as MASCARA-1. The best-fit parameter values and uncertainties, obtained from the median and the 16th and 84th percentiles of the output MCMC chains, are listed in Table 4.2.

We found that all orbital parameters are consistent between the MASCARA and NITES data with exception of the planet-to-star ratio p, which takes the value of $0.063^{0.002}_{-0.001}$ for the MASCARA data and $0.078^{0.002}_{-0.001}$ for the NITES data. We considered the possibility that this difference in the value of p is a result of blended light in the MASCARA photometry, caused by the $1'$ pixel scale of MASCARA, which would decrease the transit depth and thus the value of p. However, a simple calculation shows that we would need $\sim$35% blended light in the MASCARA aperture, which is more than can be explained by the background sources present; we conservatively estimate these sources to contribute a maximum

[3]The stellar density was obtained from the fit to the transit light curve as described in Sect. 4.4.1 using the relations of Seager and Mallén-Ornelas (2003).

[4]See footnote 1

Table 4.2: Transit model parameters and their best-fit values obtained from fits to the MASCARA data, NITES data, and the combined photometric data set.

Parameter	Symbol	Units	MASCARA	NITES	MASCARA + NITES
Reduced chi-square	χ^2_ν	-	1.98	0.51	1.98
Norm. MASCARA	F_0	-	1.00021 ± 0.00004	-	1.00032 ± 0.00004
Norm. NITES	F_1	-	-	1.0000 ± 0.0002	0.99962 ± 0.00009
Norm. NITES	F_2	-	-	1.0002 ± 0.0002	0.99975 ± 0.00009
Epoch	T_p	BJD	2457097.277 ± 0.002	2457097.2751 ± 0.0009	2457097.278 ± 0.002
Period	P	d	2.14879 ± 0.00001	2.14879 (fixed)	2.148780 ± 0.000008
Duration	T_{14}	h	$4.06^{+0.08}_{-0.07}$	$4.1^{+0.08}_{-0.06}$	4.05 ± 0.03
Planet-to-star ratio[a]	$p = R_p/R_*$	-	$0.063^{+0.002}_{-0.001}$	$0.078^{+0.002}_{-0.001}$	0.0735 ± 0.0007
Impact parameter	b	-	0.2 ± 0.2	0.3 ± 0.2	0.2 ± 0.1
Eccentricity	e	-	0 (fixed)	0 (fixed)	0 (fixed)

Notes. [a] The best-fit value of p differs significantly between fits and as we are unable to reconcile the different data we adopt $p = 0.07 \pm 0.01$ as our final value.

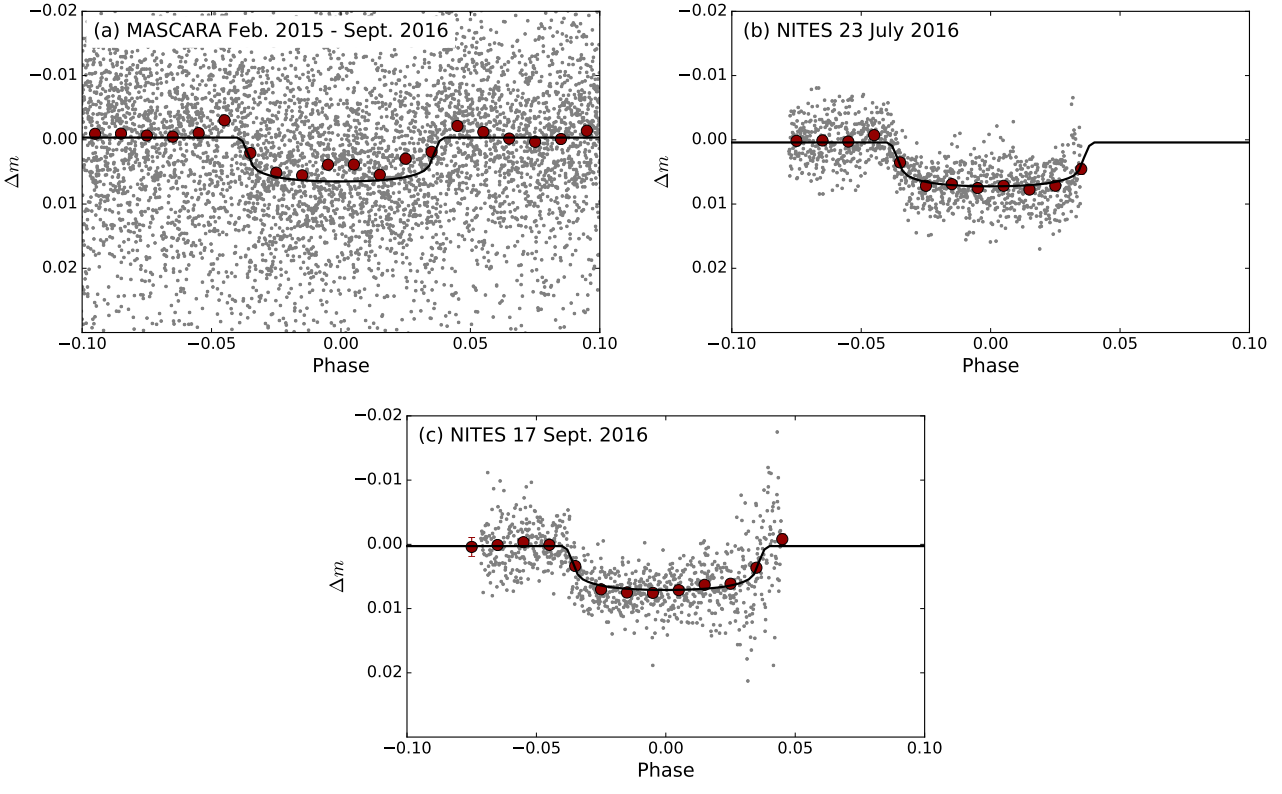

Figure 4.1: Photometry and best-fit models used in the characterization of MASCARA-1 b. Panel (a) MASCARA photometry obtained between February 2015 and September 2016. Shown are the 320 s cadence data (grey points), the data binned by 0.01 in phase (red points), and the best-fit transit model (black line). Panels (b) and (c) NITES transit observations taken on 23 July 2016 and 17 September 2016, respectively. Shown are the data (grey points), the data binned by 0.01 in phase (red points), and the best-fit transit model (black line).

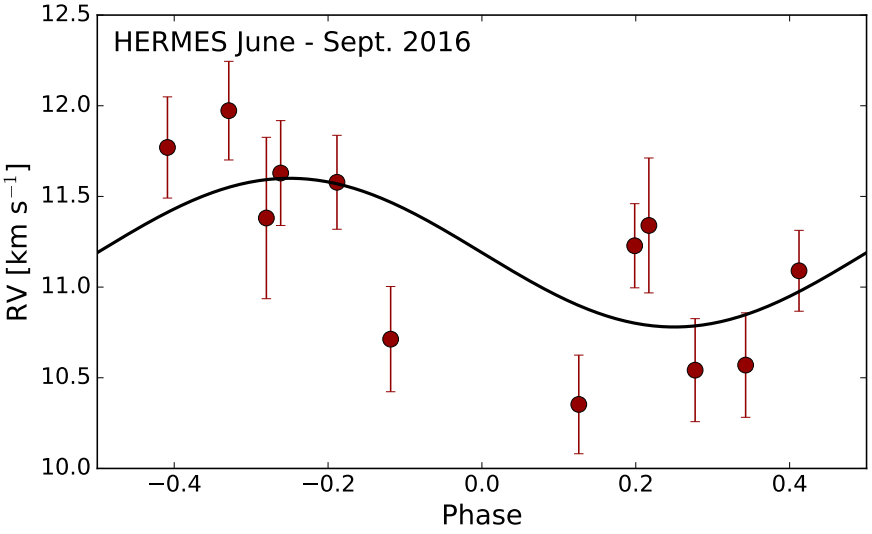

Figure 4.2: HERMES RV measurements of MASCARA-1 obtained from July to September 2016. Shown are the data (red points) and the best-fit model (black line). The high projected rotation speed of the star, $v \sin i_\star = 106.7$ km s^{-1}, results in relatively large uncertainties on the RV measurements of order 300 m s^{-1}.

of $\sim$20% of the total light. Another possibility comes from the algorithm used to process the MASCARA data, as we are still in the process of investigating possible systematic changes introduced by our methods.

To further investigate this discrepancy we performed a joint fit to the MASCARA and NITES photometry. The reduced chi-square value for the NITES fit indicates that we overestimated the uncertainties on the photometry; this is plausible since we assumed a conservative model for the scintillation noise, i.e. the dominant source of noise in the observations, when calculating the uncertainties. To ensure that we place a similar weight on both the MASCARA and NITES observations, we reduced the NITES uncertainties by a factor 2 for the joint fit. The results of the joint fit are shown in Fig. 4.1 and the parameters are listed in Table 4.2. From the joint fit we obtain $p = 0.0735 \pm 0.0007$, which is significantly different from both the NITES and MASCARA values. Also, the lack of baseline in the NITES observations results in a lower normalization in the joint fit, helping to reduce any dicrepancy in the depths. We are unable at this time to explain this discrepancy and adopt a value of $p = 0.07 \pm 0.01$, i.e. midway between and consistent with both the MASCARA and NITES values, for the derivation of the planet radius listed in Table 4.4.

4.4.2 Radial velocities and planet mass

We determined stellar radial velocities and their uncertainties from the HERMES spectra via the standard pipeline[5], in which a mask of individual lines is cross-correlated with the data to obtain an average line profile. For the observations of MASCARA-1, the HermesF0Mask

[5]See footnote 1

was used as it is closest to the spectral type of the star of the available masks. The average line profile was subsequently fitted with a rotationally broadened line profile, the dominant source of broadening, to obtain the radial velocities and their uncertainties. The obtained uncertainties are relatively large ($\sim$300 m s^{-1}) because of the high equatorial rotation speed of the star. The epochs of the RV-data points are phase folded using the best-fit orbital solution derived from the photometry. A circular orbital solution was fitted to the data keeping the period and epoch fixed to the values derived above. The RV data and best-fit solution are shown in Fig. 4.2, and the best-fit parameters are listed in Table 4.3. The amplitude of the stellar radial velocity variation is not well constrained to $K = 400 \pm 100$ m s^{-1}, corresponding to a planet mass of $M_p = 3.7 \pm 0.9$ $M_{\rm jup}$.

4.4.3 Rossiter-McLaughlin effect and projected spin-orbit angle

To consolidate the confirmation of the planetary nature of the companion and determine the projection of the spin-orbit angle (obliquity), we observed the systems during a transit with the SONG telescope (See section 4.2). Simple cross-correlation functions (CCFs) are created from the obtained spectra using a stellar template appropriate for MASCARA-1. [6] The CCFs are shown in Fig. 3 panel A (top left).

To analyse the distortions of the stellar absorption lines and measure the projected obliquity (λ), we used the code presented in Albrecht et al. (2007), including updates presented in Albrecht et al. (2013). In short, we created a pixelated stellar disk in which each pixel is assigned a radial velocity based on stellar rotation, and micro- and macro-turbulence (see e.g. Gray, 1984). Here the point spread function (PSF) of the spectrograph is included in the width of the Gaussian function representing the micro-turbulence. We did not include convective blueshift as the CCFs do not have a high enough S/N to constrain this parameter and in turn the influence on λ is small. The light contribution of each pixel in our model is governed by a quadratic limb darkening model. For each observation, a model stellar absorption line is created. During transit, the integration is carried out only over the surface not blocked by the companion. These model CCFs are then compared to the observed CCFs, taking into account shifts due to the orbital velocity.

We ran an MCMC to obtain confidence intervals for λ and $v \sin i_\star$, the parameters of interest. For this we allowed the following parameters to vary: λ, $v \sin i_\star$, macro-turbulence (ζ), micro-turbulence (ν), transit epoch T_p, planet-to-star radius ratio p, scaled semi-major axis a/R_*, cosine of the orbital inclination $\cos i$, stellar systemic velocity $\gamma_{\rm SONG}$, stellar RV amplitude K, and limb darkening parameters $u_1 + u_2$. We used prior information from the photometric and RV observations for the parameters T_p, a/R_*, p, and K. We further used the prior information for the impact parameter b, and the transit duration T_{14} also derived from photometry (Table 4.2), 0.6 ± 0.1 for $u_1 + u_2$ (Claret et al., 2013), and uniform priors on all other parameters. Finally for each calculation of the likelihood we allowed each of the observed CCFs to be offset and scaled in intensity (see also Albrecht et al., 2013). This way we included the influence of the non-perfect normalization of the spectra into the uncertainty interval of the final parameters. A mismatch in the continuum normalization of the observed spectrum and the template spectrum causes an offset in the baseline of

[6] The template was created using the interactive data language (IDL) interface SYNPLOT (I. Hubeny, private communication) to the spectrum synthesis program SYNSPEC (Hubeny et al., 1995), utilizing a Kurucz model atmosphere (see `http://kurucz.harvard.edu/grids.html`).

the obtained CCF. In addition, the size of the CCFs depends on the S/N of the spectra, which did vary throughout the observations. In Tab. 4.3 we report the results for the above parameters, including the 68% confidence intervals from the analysis of the CCFs.

With a projected obliquity of $69.5 \pm 0.3°$, we find that the rotation axis of MASCARA-1 is misaligned with respect to the orbit of the planet. This can also be seen in Fig. 4.3 panel B, where the planet shadow is isolated. Despite a low impact parameter, the trail of the planet does not reach from $-v \sin i_\star$ to $+v \sin i_\star$, as would be the case if the planet travelled near the stellar equator. For central transits and large misalignments the amplitude of the RM effect is reduced, as the planet travels from pole to pole, and not over the equator. If the impact parameter were larger, MASCARA-1 b would have travelled largely over the receding stellar surface area. We also find that the SONG data prefer a small impact parameter ($b = 0.122 \pm 0.012$), which is consistent with the photometry ($b = 0.2 \pm 0.1$). The transit mid-point is found 7 min later than expected from the photometric ephemeris. We argue that the formal uncertainty in the projected rotation speed ($v \sin i_\star = 109.0 \pm 0.1$ km s^{-1}) underestimates the true uncertainty in this parameter. MASCARA-1 is a fast rotator and we expect a departure from the perfect spherical shape assumed in our analysis. In addition, we also expect a significant gravity darkening. This would result in a dark band along the equator for large $i_\star$ and an apparent increase in the stellar limb darkening for low $i_\star$. We therefore argue that an uncertainty of 3 km s^{-1} is more appropriate for the projected rotation speed. We find that our data favour a larger than expected limb darkening $u_1 + u_2 = 0.9 \pm 0.1$, which we attribute to the simplified physics in our model rather than to a true disagreement with the model limb darkening parameters. Indeed if our data had a high S/N, we might be able to determine $i_\star$ and therefore the actual obliquity (Ψ) in this system from the RM data alone. However given the S/N in our SONG data we postponed such an analysis until such a data set is available. We also expect the uncertainty in λ to be about $4°$, i.e. larger then the formal value quoted above, for the same reasons that we expect the $v \sin i_\star$ uncertainty to be underestimated.

4.5 Discussion and conclusions

Table 4.4 lists the final physical parameters describing the MASCARA-1 system. We find a planetary mass and radius of 3.7 ± 0.9 M$_{\rm Jup}$ and 1.5 ± 0.3 R$_{\rm Jup}$, albeit with a large uncertainty on the mass caused by the high spin-rotation velocity of the star. The uncertainty on M_p can be reduced by obtaining more RV measurements and we have started a monitoring campaign for this purpose. MASCARA-1 b orbits a bright A star in $2.148780 \pm 8 \times 10^{-6}$ days at a distance of 0.043 ± 0.005 AU. The high temperature of the host star means that MASCARA-1 b has a high equilibrium temperature of 2570^{+50}_{-30} K ($A_B = 0$), making it one of the hottest gas giants known.

Figure 4.4 shows the location of MASCARA-1 b in the planetary mass-radius diagram. From this we can see that while the radius is large it is not the most extreme case found to date, although it is the most irradiated of the more massive ($M_p > 3$ M$_{\rm Jup}$) hot Jupiters. MASCARA-1 b also follows the empirical relationship between mass, radius, equilibrium temperature, host star metallicity, and tidal heating from Enoch et al. (2012). Figure 4.5 shows the location of MASCARA-1 compared to other stars hosting transiting exoplanets as a function of visual magnitude and effective temperature. It is clear that MASCARA-1

Table 4.3: Model parameters used in fitting the RV and RM measurements and their best-fit values.

Parameter	Symbol	Units	HERMES	SONG
Epoch[a]	T_p	BJD	2457097.278 (fixed)	2457097.283 ± 0.0022
Period	P	d	2.148780 (fixed)	2.148780 (fixed)
Duration[a]	T_{14}	h	-	4.15 ± 0.0030
Planet-to-star ratio[a]	$p = R_p/R_*$	-	-	0.0795 ± 0.00065
Impact parameter[a]	b	-	-	0.122 ± 0.012
Eccentricity	e	-	0 (fixed)	0 (fixed)
RV amplitude[a]	K	m s^{-1}	400 ± 100	190 ± 90
Systemic velocity[b]	γ	km s^{-1}	11.20 ± 0.08	8.52 ± 0.02
Projected obliquity	λ	$^\circ$	-	69.5 ± 4
Micro turbulence	ν	km s^{-1}	-	0.4 ± 0.3
Macro turbulence	ζ	km s^{-1}	-	7.3 ± 0.2
Projected rotation speed	$v \sin i_\star$	km s^{-1}	-	109 ± 3

Notes. [a] For the SONG analysis, the best-fit parameters from the photometry and radial velocities were used to set Gaussian priors on T_p, T_{14}, p, b, and K. [b] We find a significant offset between the values for γ derived from the HERMES and SONG data. An analysis of our methods revealed the offset; this offset likely originates from a difference in the spectral templates used in reducing the HERMES and SONG data, but does not influence our results.

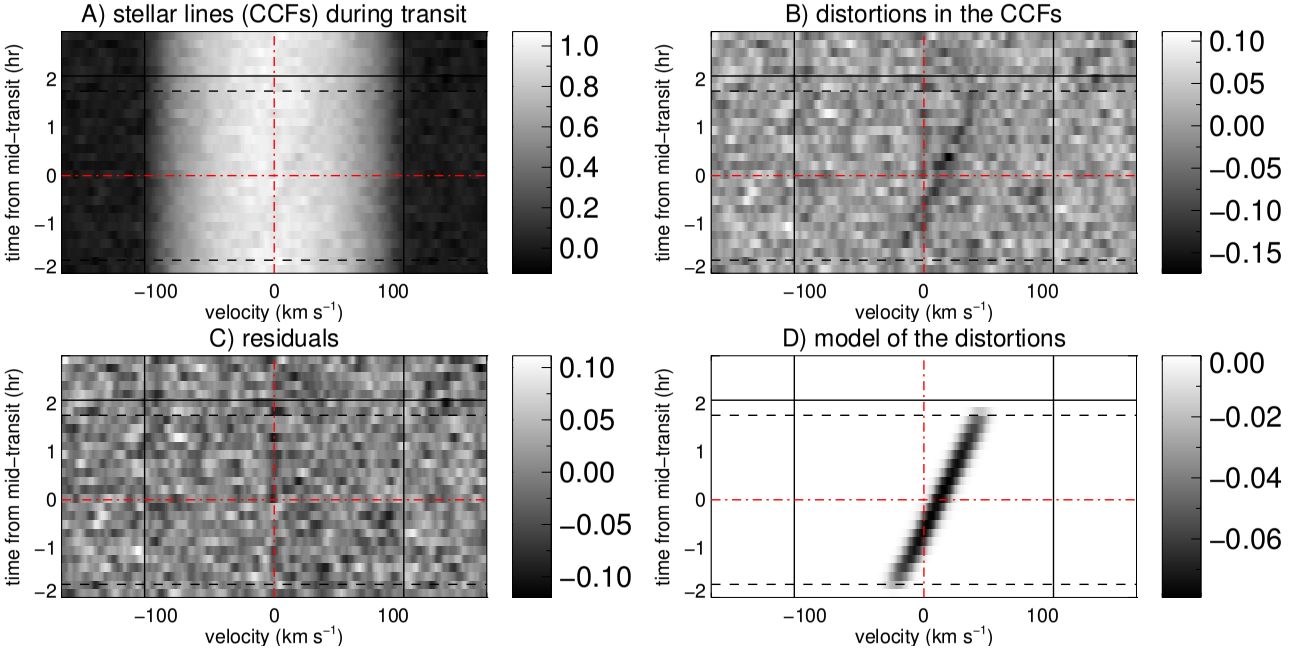

Figure 4.3: Observations of MASCARA-1 during and after the transit of MASCARA-1 b. In each panel, the solid horizontal line indicates the end of transit and the dashed lines indicate the end of ingress and beginning of egress. The solid black vertical lines show the best-fit value for $v \sin i_\star$. The dashed-dotted red lines indicate the mid-transit time and rest-frame velocity of the star. *Panel A:* The observed CCFs are shown in greyscale. *Panel B:* The same as in Panel A, but with the best-fit model for the undisturbed stellar CCF subtracted, isolating the distortions due to the planetary transit over the rotating stellar photosphere. *Panel C:* Residuals after our best-fitting model, including the planetary transit, is subtracted. *Panel D:* The corresponding model to the data represented in Panel B is shown.

Table 4.4: Parameters describing the MASCARA-1 system, derived from the best-fit models to the photometric and spectroscopic data.

Parameter	Symbol	Value
Stellar parameters		
Identifiers		HD 201585, HIP 104513
Right ascension		$21^h10^m12.37^s$
Declination		$+10°44'19.9''$
Spectral type		A8
V-band magnitude	m_V	8.3
Age[a]		1.0 ± 0.2 Gyr
Effective temperature[b]	$T_{\rm eff}$	7554 ± 150 K
Projected rotation speed	$v \sin i_\star$	109 ± 4 km s^{-1}
Surface gravity	$\log g$	4
Metallicity	[Fe/H]	0
Stellar mass[a]	M_*	1.72 ± 0.07 M$_\odot$
Stellar radius	R_*	2.1 ± 0.2 R$_\odot$
Stellar density	ρ_*	$0.33^{+0.02}_{-0.04}$ g cm^{-3}
Planet parameters		
Planet radius[c]	R_p	1.5 ± 0.3 R$_{\rm Jup}$
Planet mass	M_p	3.7 ± 0.9 M$_{\rm Jup}$
Planet density	ρ_p	1.5 ± 0.9 g cm^{-3}
Equilibrium temperature[d]	$T_{\rm eq}$	2570^{+50}_{-30} K
System parameters		
Epoch	T_p	2457097.278 ± 0.002 BJD
Period	P	2.148780 ± 0.000008 days
Semi-major axis	a	0.043 ± 0.005 AU
Inclination	i	$87^{\circ}{}^{+2}_{-3}$
Eccentricity	e	0 (fixed)
Projected obliquity	λ	$69.5° \pm 3$

Notes. [a] Computed using the BAGEMASS code from Maxted et al. (2015) [b] Taken from McDonald et al. (2012), assuming a typical uncertainty. [c] Assuming $p = 0.07 \pm 0.01$. [d] Computed assuming uniform redistribution and a Bond albedo of zero.

lies in a part of host star parameter space that has been largely unexplored to date, as it is a bright early-type star.

Currently there are only a few host stars with effective temperatures larger than 7000 K for which the stellar obliquity is known (e.g. WASP-33 Collier Cameron et al. (2010), KELT-17 Zhou et al. (2016), Kepler-13 Mazeh et al. (2012), see also Fig. 4.5)[7] while some constraints exists for other similar systems such as HAT-P-57 (Hartman et al., 2015). This small group of systems displays a large spread in spin orbit alignments and MASCARA-1 confirms this trend. So far it is not clear what causes the large obliquities. They might be caused by dynamical interactions (e.g. Fabrycky and Tremaine, 2007; Nagasawa et al., 2008), however they might also be a general feature of star formation. The proposed mechanisms include chaotic star formation (Bate et al., 2010; Thies et al., 2011), magnetic star-disk interaction (Lai et al., 2011; Foucart and Lai, 2011; Spalding and Batygin, 2015), torques due to neighbouring stars (Batygin, 2012; Lai, 2014), tidal dissipation (Rogers and Lin, 2013), and internal gravity waves (Rogers et al., 2013). We can differentiate between the different theories by measuring obliquities in systems with varying multiplicity, planet mass, orbital separation, and stellar mass and structure (e.g. Albrecht et al., 2013). Detecting and characterizing exoplanets orbiting early-type main-sequence stars should lead to a better understanding of the environment in which planets form.

Since it orbits a bright host star MASCARA-1 b is a particularly interesting target for atmospheric characterization via transmission spectroscopy. This exoplanet is reminiscent of the WASP-33 system (Collier Cameron et al., 2010), in which a 2.1 $M_{\rm Jup}$ hot Jupiter transits a $T_{\rm eff} = 7400$ K A-star. However, while follow-up observations of WASP-33 are significantly hampered by the delta-scuti variations of its host star, no such variability is detected in MASCARA-1. Assuming a temperature of 2550 K and a hydrogen/helium atmosphere, MASCARA-1 b has an atmospheric scale height of $H = 215$ km, implying that an absorption feature that extends out to $5 \times H$ results in a transmission signal of 0.01%. Interestingly, the sodium feature of the host star is significantly weaker than for a solar type star, in addition to being velocity broadened to 106 km s^{-1}. This will make it significantly more straightforward to isolate the planet atmospheric sodium absorption from stellar effects , for example due to the Rossiter-McLaughlin effect (e.g. Snellen et al., 2008; Di Gloria et al., 2015).

The detection of MASCARA-1 b shows that the Multi-site All-Sky CAmeRA has the potential to increase the number of transiting exoplanets suitable for high-resolution atmospheric studies (e.g. Snellen et al., 2010; Brogi et al., 2012) and to expand our knowledge of planets orbiting early-type stars. The northern MASCARA station on La Palma has now gathered over two years of data and the southern station in La Silla starts observations in June 2017. We expect to find several more planets around both early- and late-type stars in the coming years.

Acknowledgements

IS acknowledges support from a NWO VICI grant (639.043.107). This project has received funding from the European Research Council (ERC) under the European Union's Hori-

[7] Visit `www.astro.keele.ac.uk/jkt/tepcat/rossiter.html` for an up-to-date list of obliquity measurements.

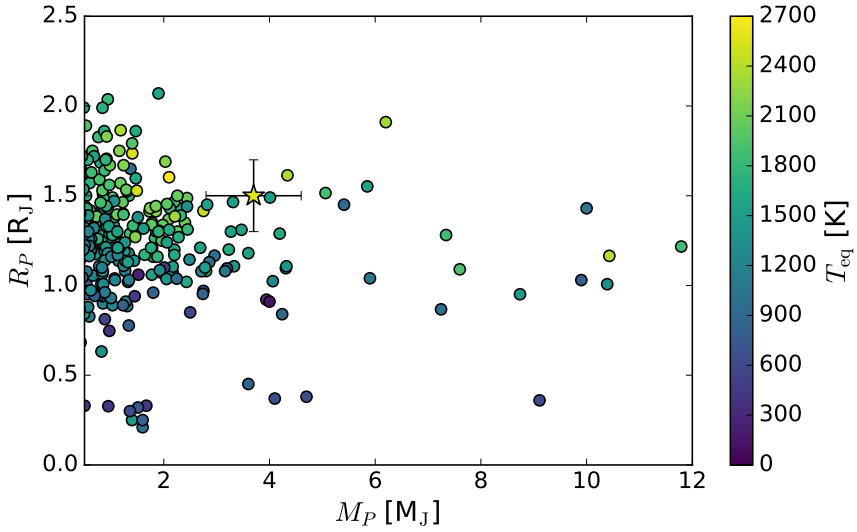

Figure 4.4: Mass-radius relationship for transiting exoplanets. MASCARA-1 b is indicated by the star marker and the points are coloured by the theoretical equilibrium temperature.

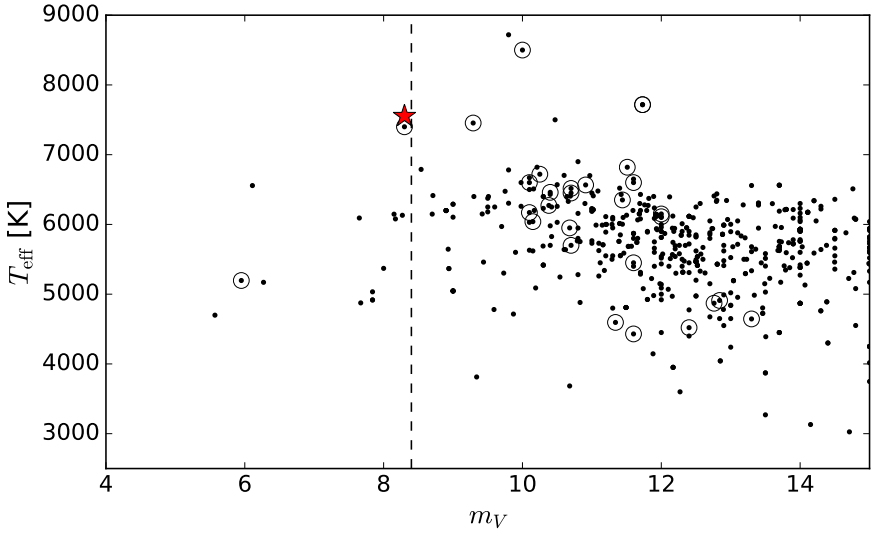

Figure 4.5: Effective temperature vs. visual magnitude for stars hosting transiting exoplanets. MASCARA-1 is indicated by the red star and systems for which the obliquity has been measured are indicated by open circles. MASCARA targets stars to the left of the dashed black line ($4 < m_V < 8.4$).

zon 2020 research and innovation programme (grant agreement nr. 694513). Based on observations made with the Mercator Telescope, operated on the island of La Palma by the Flemmish Community, at the Spanish Observatorio del Roque de los Muchachos of the Instituto de Astrofísica de Canarias. Based on observations obtained with the HERMES spectrograph, which is supported by the Research Foundation - Flanders (FWO), Belgium, the Research Council of KU Leuven, Belgium, the Fonds National de la Recherche Scientifique (F.R.S.-FNRS), Belgium, the Royal Observatory of Belgium, the Observatoire de Genève, Switzerland and the Thüringer Landessternwarte Tautenburg, Germany. Based on observations made with the Hertzsprung SONG telescope operated on the island of Tenerife by the Aarhus and Copenhagen Universities in the Spanish Observatorio del Teide of the Instituto de Astrofísica de Canarias. The Hertzsprung SONG telescope is funded by the Danish National Research Foundation, Villum Foundation, and Carlsberg Foundation. This research has made use of the SIMBAD database, operated at CDS, Strasbourg, France. This research has made use of the VizieR catalogue access tool, CDS, Strasbourg, France. We have benefited greatly from the publicly available programming language Python, including the numpy, matplotlib, pyfits, scipy and h5py packages.

Bibliography

Albrecht, S., Reffert, S., Snellen, I., Quirrenbach, A., and Mitchell, D. S. (2007). The spin axes orbital alignment of both stars within the eclipsing binary system V1143 Cyg using the Rossiter-McLaughlin effect. *A&A*, 474:565–573.

Albrecht, S., Winn, J. N., Johnson, J. A., Howard, A. W., Marcy, G. W., Butler, R. P., Arriagada, P., Crane, J. D., Shectman, S. A., Thompson, I. B., Hirano, T., Bakos, G., and Hartman, J. D. (2012). Obliquities of Hot Jupiter Host Stars: Evidence for Tidal Interactions and Primordial Misalignments. *ApJ*, 757:18.

Albrecht, S., Winn, J. N., Marcy, G. W., Howard, A. W., Isaacson, H., and Johnson, J. A. (2013). Low Stellar Obliquities in Compact Multiplanet Systems. *ApJ*, 771:11.

Andersen, M. F., Grundahl, F., Christensen-Dalsgaard, J., Frandsen, S., Jørgensen, U. G., Kjeldsen, H., Pallé, P., Skottfelt, J., Sørensen, A. N., and Weiss, E. (2014). Hardware and software for a robotic network of telescopes - SONG. In *Revista Mexicana de Astronomia y Astrofisica Conference Series*, volume 45 of *Revista Mexicana de Astronomia y Astrofisica Conference Series*, pages 83–86.

Bakos, G., Noyes, R. W., Kovács, G., Stanek, K. Z., Sasselov, D. D., and Domsa, I. (2004). Wide-Field Millimagnitude Photometry with the HAT: A Tool for Extrasolar Planet Detection. *PASP*, 116:266–277.

Barbary, K. (2016). SEP: Source extractor as a library. *The Journal of Open Source Software*, 1(6).

Barge, P., Baglin, A., Auvergne, M., Rauer, H., Léger, A., Schneider, J., Pont, F., Aigrain, S., Almenara, J.-M., Alonso, R., Barbieri, M., Bordé, P., Bouchy, F., Deeg, H. J., La Reza, D., Deleuil, M., Dvorak, R., Erikson, A., Fridlund, M., Gillon, M., Gondoin, P., Guillot, T., Hatzes, A., Hebrard, G., Jorda, L., Kabath, P., Lammer, H., Llebaria, A., Loeillet, B., Magain, P., Mazeh, T., Moutou, C., Ollivier, M., Pätzold, M., Queloz, D., Rouan, D., Shporer, A., and Wuchterl, G. (2008). Transiting exoplanets from the CoRoT space mission. I. CoRoT-Exo-1b: a low-density short-period planet around a G0V star. *A&A*, 482:L17–L20.

Batalha, N. M. (2014). Exploring exoplanet populations with NASA's Kepler Mission. *Proceedings of the National Academy of Science*, 111:12647–12654.

Bate, M. R., Lodato, G., and Pringle, J. E. (2010). Chaotic star formation and the alignment of stellar rotation with disc and planetary orbital axes. *MNRAS*, 401:1505–1513.

Batygin, K. (2012). A primordial origin for misalignments between stellar spin axes and planetary orbits. *Nature* .

Bertin, E. and Arnouts, S. (1996). SExtractor: Software for source extraction. *A&AS*, 117:393–404.

Borucki, W. J., Koch, D., Basri, G., Batalha, N., Brown, T., Caldwell, D., Caldwell, J., Christensen-Dalsgaard, J., Cochran, W. D., DeVore, E., Dunham, E. W., Dupree, A. K., Gautier, T. N., Geary, J. C., Gilliland, R., Gould, A., Howell, S. B., Jenkins, J. M., Kondo, Y., Latham, D. W., Marcy, G. W., Meibom, S., Kjeldsen, H., Lissauer, J. J., Monet, D. G., Morrison, D., Sasselov, D., Tarter, J., Boss, A., Brownlee, D., Owen, T., Buzasi, D., Charbonneau, D., Doyle, L., Fortney, J., Ford, E. B., Holman, M. J., Seager, S., Steffen, J. H., Welsh, W. F., Rowe, J., Anderson, H., Buchhave, L., Ciardi, D., Walkowicz, L., Sherry, W., Horch, E., Isaacson, H., Everett, M. E., Fischer, D., Torres, G., Johnson, J. A., Endl, M., MacQueen, P., Bryson, S. T., Dotson, J., Haas, M., Kolodziejczak, J., Van Cleve, J., Chandrasekaran, H., Twicken, J. D., Quintana, E. V., Clarke, B. D., Allen, C., Li, J., Wu, H., Tenenbaum, P., Verner, E., Bruhweiler, F., Barnes, J., and Prsa, A. (2010). Kepler Planet-Detection Mission: Introduction and First Results. *Science*, 327:977.

Brogi, M., de Kok, R. J., Albrecht, S., Snellen, I. A. G., Birkby, J. L., and Schwarz, H. (2016). Rotation and Winds of Exoplanet HD 189733 b Measured with High-dispersion Transmission Spectroscopy. *ApJ*, 817:106.

Brogi, M., Snellen, I. A. G., de Kok, R. J., Albrecht, S., Birkby, J., and de Mooij, E. J. W. (2012). The signature of orbital motion from the dayside of the planet τ Boötis b. *Nature* , 486:502–504.

Burrows, A., Hubeny, I., Budaj, J., Knutson, H. A., and Charbonneau, D. (2007). Theoretical Spectral Models of the Planet HD 209458b with a Thermal Inversion and Water Emission Bands. *ApJ*, 668:L171–L174.

Casewell, S. L., Lawrie, K. A., Maxted, P. F. L., Marley, M. S., Fortney, J. J., Rimmer, P. B., Littlefair, S. P., Wynn, G., Burleigh, M. R., and Helling, C. (2015). Multiwaveband photometry of the irradiated brown dwarf WD0137-349B. *MNRAS*, 447:3218–3226.

Claret, A. (2000). A new non-linear limb-darkening law for LTE stellar atmosphere models. Calculations for -5.0 $<=$ log[M/H] $<=$ +1, 2000 K $<=$ T_{eff} $<=$ 50000 K at several surface gravities. *A&A*, 363:1081–1190.

Claret, A., Hauschildt, P. H., and Witte, S. (2013). New limb-darkening coefficients for Phoenix/1d model atmospheres. II. Calculations for 5000 K $\leq$ T_{eff} $\leq$ 10 000 K Kepler, CoRot, Spitzer, uvby, UBVRIJHK, Sloan, and 2MASS photometric systems. *A&A*, 552:A16.

Collier Cameron, A., Guenther, E., Smalley, B., McDonald, I., Hebb, L., Andersen, J., Augusteijn, T., Barros, S. C. C., Brown, D. J. A., Cochran, W. D., Endl, M., Fossey, S. J., Hartmann, M., Maxted, P. F. L., Pollacco, D., Skillen, I., Telting, J., Waldmann, I. P., and West, R. G. (2010). Line-profile tomography of exoplanet transits - II. A gas-giant planet transiting a rapidly rotating A5 star. *MNRAS*, 407:507–514.

Collier Cameron, A., Pollacco, D., Street, R. A., Lister, T. A., West, R. G., Wilson, D. M., Pont, F., Christian, D. J., Clarkson, W. I., Enoch, B., Evans, A., Fitzsimmons, A.,

Haswell, C. A., Hellier, C., Hodgkin, S. T., Horne, K., Irwin, J., Kane, S. R., Keenan, F. P., Norton, A. J., Parley, N. R., Osborne, J., Ryans, R., Skillen, I., and Wheatley, P. J. (2006). A fast hybrid algorithm for exoplanetary transit searches. *MNRAS*, 373:799–810.

Craig, M. W., Crawford, S. M., Deil, C., Gomez, C., Günther, H. M., Heidt, N., Horton, A., Karr, J., Nelson, S., Ninan, J. P., Pattnaik, P., Rol, E., Schoenell, W., Seifert, M., Singh, S., Sipocz, B., Stotts, C., Streicher, O., Tollerud, E., Walker, N., and ccdproc Contributors (2015). ccdproc: CCD data reduction software. Astrophysics Source Code Library.

Deming, D., Wilkins, A., McCullough, P., Burrows, A., Fortney, J. J., Agol, E., Dobbs-Dixon, I., Madhusudhan, N., Crouzet, N., Desert, J.-M., Gilliland, R. L., Haynes, K., Knutson, H. A., Line, M., Magic, Z., Mandell, A. M., Ranjan, S., Charbonneau, D., Clampin, M., Seager, S., and Showman, A. P. (2013). Infrared Transmission Spectroscopy of the Exoplanets HD 209458b and XO-1b Using the Wide Field Camera-3 on the Hubble Space Telescope. *ApJ*, 774:95.

Di Gloria, E., Snellen, I. A. G., and Albrecht, S. (2015). Using the chromatic Rossiter-McLaughlin effect to probe the broadband signature in the optical transmission spectrum of HD 189733b. *A&A*, 580:A84.

Enoch, B., Collier Cameron, A., and Horne, K. (2012). Factors affecting the radii of close-in transiting exoplanets. *A&A*, 540:A99.

Fabrycky, D. and Tremaine, S. (2007). Shrinking Binary and Planetary Orbits by Kozai Cycles with Tidal Friction. *ApJ*, 669:1298–1315.

Foreman-Mackey, D., Hogg, D. W., Lang, D., and Goodman, J. (2013). emcee: The MCMC Hammer. *PASP*, 125:306.

Fortney, J. J., Lodders, K., Marley, M. S., and Freedman, R. S. (2008). A Unified Theory for the Atmospheres of the Hot and Very Hot Jupiters: Two Classes of Irradiated Atmospheres. *ApJ*, 678:1419–1435.

Foucart, F. and Lai, D. (2011). Evolution of spin direction of accreting magnetic protostars and spin-orbit misalignment in exoplanetary systems - II. Warped discs. *MNRAS*, 412:2799–2815.

Gaia Collaboration, Brown, A. G. A., Vallenari, A., Prusti, T., de Bruijne, J. H. J., Mignard, F., Drimmel, R., Babusiaux, C., Bailer-Jones, C. A. L., Bastian, U., and et al. (2016). Gaia Data Release 1. Summary of the astrometric, photometric, and survey properties. *A&A*, 595:A2.

Gray, D. F. (1984). Measurements of rotation and turbulence in F, G, and K dwarfs. *ApJ*, 281:719–722.

Grundahl, F., Fredslund Andersen, M., Christensen-Dalsgaard, J., Antoci, V., Kjeldsen, H., Handberg, R., Houdek, G., Bedding, T. R., Pallé, P. L., Jessen-Hansen, J., Silva Aguirre, V., White, T. R., Frandsen, S., Albrecht, S., Andersen, M. I., Arentoft, T., Brogaard, K., Chaplin, W. J., Harpsøe, K., Jørgensen, U. G., Karovicova, I., Karoff, C., Kjærgaard

Rasmussen, P., Lund, M. N., Sloth Lundkvist, M., Skottfelt, J., Norup Sørensen, A., Tronsgaard, R., and Weiss, E. (2017). First Results from the Hertzsprung SONG Telescope: Asteroseismology of the G5 Subgiant Star μ Herculis. *ApJ*, 836:142.

Hartman, J. D., Bakos, G. Á., Buchhave, L. A., Torres, G., Latham, D. W., Kovács, G., Bhatti, W., Csubry, Z., de Val-Borro, M., Penev, K., Huang, C. X., Béky, B., Bieryla, A., Quinn, S. N., Howard, A. W., Marcy, G. W., Johnson, J. A., Isaacson, H., Fischer, D. A., Noyes, R. W., Falco, E., Esquerdo, G. A., Knox, R. P., Hinz, P., Lázár, J., Papp, I., and Sári, P. (2015). HAT-P-57b: A Short-period Giant Planet Transiting a Bright Rapidly Rotating A8V Star Confirmed Via Doppler Tomography. *AJ*, 150:197.

Hubeny, I., Burrows, A., and Sudarsky, D. (2003). A Possible Bifurcation in Atmospheres of Strongly Irradiated Stars and Planets. *ApJ*, 594:1011–1018.

Hubeny, I., Lanz, T., and Jeffrey, C. (1995). SYNSPEC: a User's Guide. *Newsl. on Analysis of Astronomical Spectra*, 20.

Husser, T.-O., Wende-von Berg, S., Dreizler, S., Homeier, D., Reiners, A., Barman, T., and Hauschildt, P. H. (2013). A new extensive library of PHOENIX stellar atmospheres and synthetic spectra. *A&A*, 553:A6.

Jenkins, J. S., Jones, H. R. A., Goździewski, K., Migaszewski, C., Barnes, J. R., Jones, M. I., Rojo, P., Pinfield, D. J., Day-Jones, A. C., and Hoyer, S. (2009). First results from the Calan-Hertfordshire Extrasolar Planet Search: exoplanets and the discovery of an eccentric brown dwarf in the desert. *MNRAS*, 398:911–917.

Kovács, G., Zucker, S., and Mazeh, T. (2002). A box-fitting algorithm in the search for periodic transits. *A&A*, 391:369–377.

Kreidberg, L. (2015). batman: BAsic Transit Model cAlculatioN in Python. *PASP*, 127:1161.

Kreidberg, L., Bean, J. L., Désert, J.-M., Benneke, B., Deming, D., Stevenson, K. B., Seager, S., Berta-Thompson, Z., Seifahrt, A., and Homeier, D. (2014). Clouds in the atmosphere of the super-Earth exoplanet GJ1214b. *Nature* , 505:69–72.

Lai, D. (2014). Star-disc-binary interactions in protoplanetary disc systems and primordial spin-orbit misalignments. *MNRAS*, 440:3532–3544.

Lai, D., Foucart, F., and Lin, D. N. C. (2011). Evolution of spin direction of accreting magnetic protostars and spin-orbit misalignment in exoplanetary systems. *MNRAS*, 412:2790–2798.

Madhusudhan, N. and Seager, S. (2009). A Temperature and Abundance Retrieval Method for Exoplanet Atmospheres. *ApJ*, 707:24–39.

Mandel, K. and Agol, E. (2002). Analytic Light Curves for Planetary Transit Searches. *ApJ*, 580:L171–L175.

Maxted, P. F. L., Serenelli, A. M., and Southworth, J. (2015). Bayesian mass and age estimates for transiting exoplanet host stars. *A&A*, 575:A36.

Mayor, M. and Queloz, D. (1995). A Jupiter-mass companion to a solar-type star. *Nature* , 378:355–359.

Mazeh, T., Nachmani, G., Sokol, G., Faigler, S., and Zucker, S. (2012). Kepler KOI-13.01 - Detection of beaming and ellipsoidal modulations pointing to a massive hot Jupiter. *A&A*, 541:A56.

McCormac, J., Pollacco, D., Skillen, I., Faedi, F., Todd, I., and Watson, C. A. (2013). DONUTS: A Science Frame Autoguiding Algorithm with Sub-Pixel Precision, Capable of Guiding on Defocused Stars. *PASP*, 125:548.

McCormac, J., Skillen, I., Pollacco, D., Faedi, F., Ramsay, G., Dhillon, V. S., Todd, I., and Gonzalez, A. (2014). A search for photometric variability towards M71 with the Near-Infrared Transiting ExoplanetS Telescope. *MNRAS*, 438:3383–3398.

McDonald, I., Zijlstra, A. A., and Boyer, M. L. (2012). Fundamental parameters and infrared excesses of Hipparcos stars. *MNRAS*, 427:343–357.

Nagasawa, M., Ida, S., and Bessho, T. (2008). Formation of Hot Planets by a Combination of Planet Scattering, Tidal Circularization, and the Kozai Mechanism. *ApJ*, 678:498–508.

O'Donovan, F. T., Charbonneau, D., Harrington, J., Madhusudhan, N., Seager, S., Deming, D., and Knutson, H. A. (2010). Detection of Planetary Emission from the Exoplanet Tres-2 Using Spitzer/IRAC. *ApJ*, 710:1551–1556.

Pollacco, D. L., Skillen, I., Collier Cameron, A., Christian, D. J., Hellier, C., Irwin, J., Lister, T. A., Street, R. A., West, R. G., Anderson, D. R., Clarkson, W. I., Deeg, H., Enoch, B., Evans, A., Fitzsimmons, A., Haswell, C. A., Hodgkin, S., Horne, K., Kane, S. R., Keenan, F. P., Maxted, P. F. L., Norton, A. J., Osborne, J., Parley, N. R., Ryans, R. S. I., Smalley, B., Wheatley, P. J., and Wilson, D. M. (2006). The WASP Project and the SuperWASP Cameras. *PASP*, 118:1407–1418.

Raskin, G., van Winckel, H., Hensberge, H., Jorissen, A., Lehmann, H., Waelkens, C., Avila, G., de Cuyper, J.-P., Degroote, P., Dubosson, R., Dumortier, L., Frémat, Y., Laux, U., Michaud, B., Morren, J., Perez Padilla, J., Pessemier, W., Prins, S., Smolders, K., van Eck, S., and Winkler, J. (2011). HERMES: a high-resolution fibre-fed spectrograph for the Mercator telescope. *A&A*, 526:A69.

Rogers, T. M. and Lin, D. N. C. (2013). On the Tidal Dissipation of Obliquity. *ApJ*, 769:L10.

Rogers, T. M., Lin, D. N. C., McElwaine, J. N., and Lau, H. H. B. (2013). Internal Gravity Waves in Massive Stars: Angular Momentum Transport. *ApJ*, 772:21.

Schlaufman, K. C. (2010). Evidence of Possible Spin-orbit Misalignment Along the Line of Sight in Transiting Exoplanet Systems. *ApJ*, 719:602–611.

Schwarz, H., Brogi, M., de Kok, R., Birkby, J., and Snellen, I. (2015). Evidence against a strong thermal inversion in HD 209458b from high-dispersion spectroscopy. *A&A*, 576:A111.

Seager, S. and Mallén-Ornelas, G. (2003). A Unique Solution of Planet and Star Parameters from an Extrasolar Planet Transit Light Curve. *ApJ*, 585:1038–1055.

Sing, D. K., Fortney, J. J., Nikolov, N., Wakeford, H. R., Kataria, T., Evans, T. M., Aigrain, S., Ballester, G. E., Burrows, A. S., Deming, D., Désert, J.-M., Gibson, N. P., Henry, G. W., Huitson, C. M., Knutson, H. A., Lecavelier Des Etangs, A., Pont, F., Showman, A. P., Vidal-Madjar, A., Williamson, M. H., and Wilson, P. A. (2016). A continuum from clear to cloudy hot-Jupiter exoplanets without primordial water depletion. *Nature* , 529:59–62.

Sing, D. K., Pont, F., Aigrain, S., Charbonneau, D., Désert, J.-M., Gibson, N., Gilliland, R., Hayek, W., Henry, G., Knutson, H., Lecavelier Des Etangs, A., Mazeh, T., and Shporer, A. (2011). Hubble Space Telescope transmission spectroscopy of the exoplanet HD 189733b: high-altitude atmospheric haze in the optical and near-ultraviolet with STIS. *MNRAS*, 416:1443–1455.

Snellen, I. A. G., Albrecht, S., de Mooij, E. J. W., and Le Poole, R. S. (2008). Ground-based detection of sodium in the transmission spectrum of exoplanet HD 209458b. *A&A*, 487:357–362.

Snellen, I. A. G., de Kok, R. J., de Mooij, E. J. W., and Albrecht, S. (2010). The orbital motion, absolute mass and high-altitude winds of exoplanet HD209458b. *Nature* , 465:1049–1051.

Snellen, I. A. G., Stuik, R., Navarro, R., Bettonvil, F., Kenworthy, M., de Mooij, E., Otten, G., ter Horst, R., and le Poole, R. (2012). Ground-based search for the brightest transiting planets with the Multi-site All-Sky CAmeRA: MASCARA. In *Ground-based and Airborne Telescopes IV*, volume 8444 of *Proc. SPIE*, page 84440I.

Spalding, C. and Batygin, K. (2015). Magnetic Origins of the Stellar Mass-Obliquity Correlation in Planetary Systems. *ApJ*, 811:82.

Talens, G. J. J., Spronck, J. F. P., Lesage, A.-L., Otten, G. P. P. L., Stuik, R., Pollacco, D., and Snellen, I. A. G. (2017). The Multi-site All-Sky CAmeRA (MASCARA). Finding transiting exoplanets around bright ($m_V < 8$) stars. *A&A*, 601:A11.

Thies, I., Kroupa, P., Goodwin, S. P., Stamatellos, D., and Whitworth, A. P. (2011). A natural formation scenario for misaligned and short-period eccentric extrasolar planets. *MNRAS*, 417:1817–1822.

Valenti, J. A. and Fischer, D. A. (2005). Spectroscopic Properties of Cool Stars (SPOCS). I. 1040 F, G, and K Dwarfs from Keck, Lick, and AAT Planet Search Programs. *ApJS*, 159:141–166.

van Leeuwen, F. (2007). Validation of the new Hipparcos reduction. *A&A*, 474:653–664.

Vogt, S. S., Marcy, G. W., Butler, R. P., and Apps, K. (2000). Six New Planets from the Keck Precision Velocity Survey. *ApJ*, 536:902–914.

Winn, J. N., Fabrycky, D., Albrecht, S., and Johnson, J. A. (2010). Hot Stars with Hot Jupiters Have High Obliquities. *ApJ*, 718:L145–L149.

Zhou, G., Rodriguez, J. E., Collins, K. A., Beatty, T., Oberst, T., Heintz, T. M., Stassun, K. G., Latham, D. W., Kuhn, R. B., Bieryla, A., Lund, M. B., Labadie-Bartz, J., Siverd, R. J., Stevens, D. J., Gaudi, B. S., Pepper, J., Buchhave, L. A., Eastman, J., Colón, K., Cargile, P., James, D., Gregorio, J., Reed, P. A., Jensen, E. L. N., Cohen, D. H., McLeod, K. K., Tan, T. G., Zambelli, R., Bayliss, D., Bento, J., Esquerdo, G. A., Berlind, P., Calkins, M. L., Blancato, K., Manner, M., Samulski, C., Stockdale, C., Nelson, P., Stephens, D., Curtis, I., Kielkopf, J., Fulton, B. J., DePoy, D. L., Marshall, J. L., Pogge, R., Gould, A., Trueblood, M., and Trueblood, P. (2016). KELT-17b: A Hot-Jupiter Transiting an A-star in a Misaligned Orbit Detected with Doppler Tomography. *AJ*, 152:136.

5 MASCARA-2 b: A hot Jupiter transiting the $m_V = 7.6$ A-star HD 185603

In this paper we present MASCARA-2 b, a hot Jupiter transiting the $m_V = 7.6$ A2 star HD 185603. Since early 2015, MASCARA has taken more than 1.6 million flux measurements of the star, corresponding to a total of almost 3000 hours of observations, revealing a periodic dimming in the flux with a depth of 1.3%. Photometric follow-up observations were performed with the NITES and IAC80 telescopes and spectroscopic measurements were obtained with the Hertzsprung SONG telescope. We find MASCARA-2 b orbits HD 185603 with a period of $3.474119^{+0.000005}_{-0.000006}$ days at a distance of 0.057 ± 0.006 AU, has a radius of 1.83 ± 0.07 $\mathrm{R_J}$ and place a 99% upper limit on the mass of < 17 $\mathrm{M_J}$. HD 185603 is a rapidly rotating early-type star with an effective temperature of 8980^{+90}_{-130} K and a mass and radius of $1.89^{+0.06}_{-0.05}$ $M_\odot$, 1.60 ± 0.06 $R_\odot$, respectively. Contrary to most other hot Jupiters transiting early-type stars, the projected planet orbital axis and stellar spin axis are found to be aligned with $\lambda = 0.6 \pm 4^\circ$. The brightness of the host star and the high equilibrium temperature, 2260 ± 50 K, of MASCARA-2 b make it a suitable target for atmospheric studies from the ground and space. Of particular interest is the detection of TiO, which has recently been detected in the similarly hot planets WASP-33 b and WASP-19 b.

G.J.J. Talens, A. B. Justesen, S. Albrecht, J. McCormac, V. Van Eylen, G.P.P.L. Otten, F. Murgas, E. Palle, D. Pollacco, R. Stuik, J.F.P. Spronck, A.-L. Lesage, F. Grundahl, M. Fredslund Andersen, V. Antoci and I.A.G. Snellen

A&A, 612, A57, (2018)

5.1 Introduction

Since the first discoveries of extrasolar planets in the mid-nineties the number of known exoplanets has been growing rapidly, first through radial velocity surveys (Vogt et al., 2000; Valenti and Fischer, 2005) and later through the first succesfull gound-based transit surveys such as HAT (Bakos et al., 2004) and SuperWASP (Pollacco et al., 2006). These early surveys uncovered a population of gas giant planets at small orbital distances, the so-called hot Jupiters, of which a few hundred are known today. More recently the space-based transit surveys, CoRoT (Barge et al., 2008) and in particular *Kepler* (Borucki et al., 2010), have revolutionised the study of extrasolar planets, finding more than a thousand confirmed planets, revealing their occurrence as function of orbital distance and planet radius, and providing the first estimates of $\eta_{\rm E}$ – the fraction of stars that harbour a rocky planet in their habitable zone (Fressin et al., 2013; Dressing and Charbonneau, 2015).

Since both CoRoT and *Kepler* surveyed relatively small fractions of the sky the planet host stars typically have faint apparent magnitudes. This is partly mitigated by K2, the reincarnation of the *Kepler* mission after two of the four reaction wheels of the spacecraft failed (Howell et al., 2014), which is covering nineteen *Kepler* fields up to early 2019. On the other hand the ground-based surveys have now monitored a large fraction of the sky, however their saturation limits usually prevent the discovery of systems at $m_V \gtrsim 8.5$, and until recently almost all known transiting systems brighter than this limit were first found through their radial velocity variations.

The brightest transiting exoplanets are scientifically extremely valuable. First of all, radial velocity follow-up to determine their masses is viable even for systems transiting early-type stars, where rapid stellar rotation and few spectral lines pose a challenge. This also applies to observations of the spectroscopic transit to determine a system's spin-orbit alignment (Collier Cameron et al., 2010). Secondly, atmospheric characterisation at high spectral resolution can only be achieved on bright systems. For example, ground-based high-dispersion detections of transmission signals from carbon monoxide and water have only been achieved for the bright HD 209458 and HD 189733 hot Jupiter systems (Snellen et al., 2010; Brogi et al., 2016). Thirdly, the stellar parameters of the host can be determined to a high accuracy, allowing in-depth analyses.

Mainly for these reasons, NASA is planning to launch the Transiting Exoplanet Survey Satellite (TESS) by the end of 2018. This first all-sky transit survey will identify planets ranging from Earth-sized to gas giants, for a wide range of stellar types and orbital distances (Ricker et al., 2015). Ground-based initiatives to probe the bright end of the transiting exoplanet population include the Kilo-degree Extremely Little Telescope (KELT) survey (Pepper et al., 2007), which consists of two wide-field $26^\circ \times 26^\circ$ telescopes, in the northern and southern hemisphere, which have been operational since 2005 and 2009, respectively. KELT has, among other bright objects, discovered the brightest hot Jupiter system to date, KELT-9, with an apparent magnitude of $m_V = 7.56$ (Gaudi et al., 2017).

This paper describes the discovery of MASCARA-2 b, the second planet discovered by the Multi-Site All-Sky CAmeRA (Talens et al., 2017b) which previously discovered MASCARA-1 b (Talens et al., 2017a). MASCARA-2 b is a hot Jupiter transiting a $m_V = 7.58$ A2 star. Section 5.2 describes MASCARA and the discovery observations of the new planetary system. Section 5.3 describes the follow-up observations, including transit confirmation with the NITES and IAC80 telescopes, and radial velocity and spectroscopic transit

observations with the SONG telescope. Section 5.4 presents the subsequent analysis to derive the system parameters of MASCARA-2, which are presented and discussed in Section 5.5.

5.2 MASCARA & Discovery Observations

The primary objective of the Multi-site All-Sky CAmeRA (MASCARA; Talens et al., 2017b) is to find transiting planetary systems at $m_V < 8$. It consists of two stations, one in the northern hemisphere at the Observatorio del Roque de los Muchachos, La Palma (Canary Islands, Spain), which has been operational since early 2015, and one in the southern hemisphere at the European Southern Observatory at La Silla (Chile), which saw first light in June 2017. Each station consists of five interline CCD cameras equipped with wide-field lenses that together monitor the entire local sky down to airmass 2 and partly down to airmass 3 (Talens et al., 2017b). The cameras point at fixed points on the local sky, meaning stars follow the same track across the CCDs each night. Images are taken with an exposure time of 6.4 seconds, short enough such that the motion of stars during an exposure is less than one pixel. Read-out of each image takes place during the next exposure so that no observing time is lost. The images are taken at the same sidereal times each night and astrometric solutions are updated every 50 images ($\sim$5 minutes). The astrometric solutions are used to perform aperture photometry on all known stars brighter than $m_V < 8.4$. Due to the large data volume collected ($\sim$15 terabytes per station per month) the raw data is overwritten after several weeks. A permanent record of the night sky is kept in the form of 50-frame averages of the raw images, allowing possible future searches for transients or other phenomena. Details of the subsequent analysis, converting the raw flux measurements into calibrated stellar light curves, will be described in detail in Talens et al. (2018, in prep.). In short, for each camera the position dependent transmission is determined from the combined light curves of all stars observed over a period of two weeks. Furthermore, the time dependent throughput of the Earth atmosphere (clouds, hazes, etc.) is determined for every image across a coarse sky-grid. In addition, each star exhibits a unique systematic trend as function of local siderial time, as a result of two effects. First, there are strong directional variations in the point-spread function (PSF) of the camera system, which cause variations in the contribution of possible neighbouring stars to the photometric aperture. Second, there are residual transmission variations due to differences in the colors of the stars. This PSF effect is corrected for each star individually by means of an empirical fit. The calibrated lightcurves are subsequently searched for transit events using the Box Least-Squares (BLS) algorithm (Kovács et al., 2002).

MASCARA-2 (HD 185603, HIP 96618) has been observed by the northern MASCARA station since early 2015. Its nightly path along the sky passes across the East, Zenith, and West cameras. To date, more than 1.6 million photometric measurements have been taken, totalling almost 3000 hours of observing time. The final calibrated 5-minute binned light curve exhibits an (outlier rejected) dispersion of $\sim$1.5%. The top panel of Fig. 5.1 shows the BLS periodogram, revealing a strong peak at a frequency of $1/3.474\ \mathrm{days}^{-1}$, the bottom panel shows the light curve, phase folded to this frequency. A transit-like signal is detected at 12.7σ.

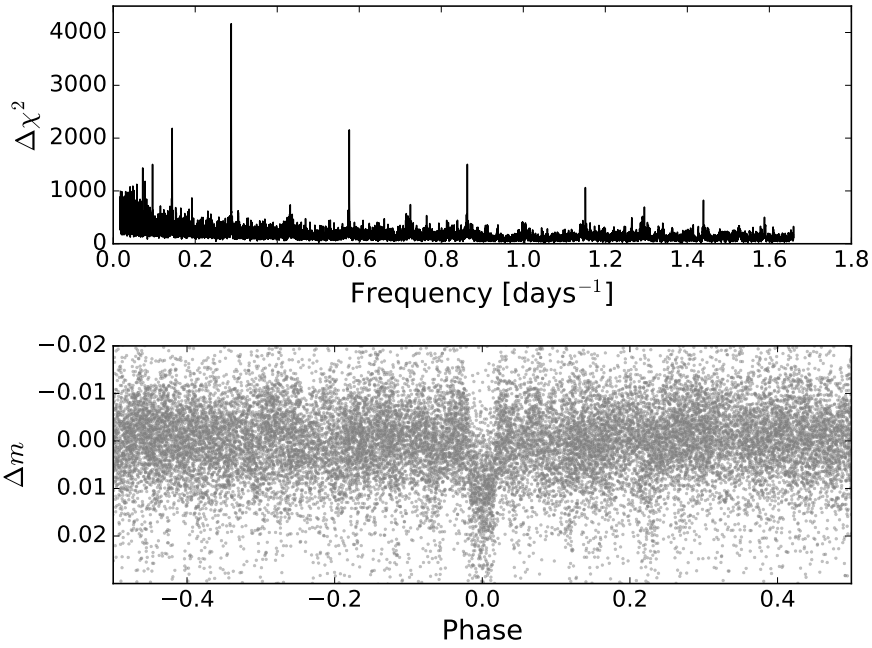

Figure 5.1: Discovery data of MASCARA-2 b. *Top panel*: BLS periodogram of the calibrated MASCARA light curve obtained between February 2015 and December 2016. The peak in the periodogram is located at a frequency of 0.288 days^{-1}. *Bottom panel*: The calibrated MASCARA data, consisting of 24309 points after binning to a cadence of 320 s. The data has been phase-folded to a period of 3.474 days, corresponding to the peak in the periodogram.

5.3 Follow-up Observations

After the detection of the transit-like signal in the MASCARA data, several follow-up observations had to be taken to confirm the planetary nature of the system and to measure its main characteristics. First, follow-up photometric transit observations are required to reject the possibility that the transit-like signal is caused by variability in a background object in the few-arcminute vicinity of the bright star, and to refine the shape of the transit. Second, spectroscopic transit observations are needed to definitely establish that the transit occurs in front of the bright target star, and allow the determination of the projected spin-orbital alignment of the system. Finally, radial velocity measurements are required to determine the mass of the transiting object, or at least to demonstrate that it is within the planetary mass range and not a brown or red dwarf star. Table 5.1 lists all photometric and spectroscopic observations used in the discovery of MASCARA-2 b.

5.3.1 Follow-up photometric observations

On June 4, 2017 we observed a transit of MASCARA-2 b with the 0.4m NITES telescope (McCormac et al., 2014) on La Palma and the 0.8m IAC80 telescope[1] at Observatorio del Teide. The NITES data consists of 940 images taken in Johnson-Bessel R-band filter, each with an exposure time of 10 seconds, with the telescope defocused to avoid saturation. The data are reduced in the same way as for the MASCARA-1 b follow-up observations (Talens et al., 2017a) using Python with CCDPROC (Craig et al., 2015), utilising a master bias, dark and flat. Non-variable comparison stars are then selected by hand and aperture photometry is extracted using SEP (Barbary, 2016; Bertin and Arnouts, 1996). The shift between each defocused image is measured using the DONUTS (McCormac et al., 2013) algorithm, and the photometric apertures are re-centered between frames. The final aperture size is chosen to minimise the dispersion of the data points out of transit, resulting in an RMS of $\sim$4.3 mmag.

The IAC80 data was obtained using the CAMELOT instrument [2], and consists of 398 images also taken in the R filter. We used the standard 2-channel readout mode covering the full $10' \times 10'$ field of view of the instrument. Each image had an exposure time of 40 seconds, and the telescope was extremely defocused to avoid saturation. The data were reduced using standard Pyraf routines performing aperture photometry after alignment of all the science frames. As in the case of NITES, the final aperture size is chosen to minimise the dispersion of the data points out of transit, resulting in an RMS in the light curve of $\sim$1.6 mmag.

The light curves taken by IAC80 and NITES clearly show the transit event and the higher spatial resolution of these observations ($0.3 - 0.66''$/pixel versus $1'$/pixel for MASCARA) confirms that the transit is not caused by a non-related background eclipsing binary inside the MASCARA photometric aperture.

[1] http://www.iac.es/OOCC/instrumentation/iac80/

[2] http://www.iac.es/OOCC/wp-content/uploads/telescopes/IAC80/documentos/User_manual.pdf

Table 5.1: Observations used in the discovery of MASCARA-2 b.

Instrument	Observatory	Date	$N_{\rm obs}$	$t_{\rm exp}$ [s]	Filter/Spectral range
MASCARA	Roque de los Muchachos	Feb. 2015 - Dec. 2016	24309	320	None
SONG	Teide	May-June 2017	16	600	4400 – 6900 Å
SONG	Teide	28 May 2017	19	600	4400 – 6900 Å
SONG	Teide	04 June 2017	30	600	4400 – 6900 Å
NITES	Roque de los Muchachos	04 June 2017	940	10	R
CAMELOT@IAC80	Teide	04 June 2017	398	40	R

5.3.2 Follow-up spectroscopic observations

Over the course of May and June 2017 sixteen spectra were obtained using the automated 1m Hertzsprung SONG telescope (Andersen et al., 2014) at Observatorio del Teide, for the purpose of characterizing the host star and constraining the planet mass from the radial velocities. In addition, during the nights of May 28, 2017 and June 4, 2017 the SONG telescope observed one partial and one full transit, spanning a total of 3 and 5 hours respectively. For the second night of observations 1 hour around egress was missed since the star was too close to zenith to be observed with SONG. High-dispersion $R = 90,000$ echelle spectra were obtained, covering the wavelength range from 4400 to 6900 Å. All spectra were taken with 10 minute exposure times, utilising a slitwidth of 1.2 arcseconds. The spectra were extracted from the observations following the procedure outlined in Grundahl et al. (2017), subsequently bad pixels were removed and the spectra were normalised. The reduced spectra have a typical signal-to-noise ratio of 75.

5.4 System and Stellar Parameters

5.4.1 Photometric transit fitting

The modelling of the photometric transit is performed in a similar way as for MASCARA-1 b (Talens et al., 2017a). A Mandel and Agol (2002) model is fitted to the MASCARA data using a Markov-chain Monte Carlo (MCMC) approach using the Python packages BATMAN and EMCEE (Kreidberg, 2015; Foreman-Mackey et al., 2013). We use a circular transit model ($e = 0$), optimising for the transit epoch T_p, the orbital period P, the transit duration T_{14}, the planet-to-star radius ratio p and the impact parameter b using uniform priors on all parameters. For the baseline we choose to include the polynomials used to correct for the PSF effect (Sect. 5.2) in our fitting routines, and fit the uncorrected MASCARA data. We employ a quadratic limb darkening law with fixed coefficients for V-band from Claret and Bloemen (2011), using values of $u_1 = 0.2752$ and $u_2 = 0.3179$, appropriate for the host star. Subsequently, the NITES and IAC80 photometric data sets are also fitted using the same model, except with the orbital period fixed to the best fit value obtained from the MASCARA photometry and a quadratic baseline model. Since the NITES and IAC80 data were taken in R-band, they were fitted with the R-band limb darkening coefficients from Claret and Bloemen (2011) of $u_1 = 0.2163$ and $u_2 = 0.2814$. The best-fit parameter values and uncertainties were obtained from the median and the 16th and 84th percentiles of the output MCMC chains.

Table 5.2 lists the reduced chi-square and best-fit parameters for each dataset. The large reduced chi-square of the MASCARA data indicates that the errorbars are likely underestimated while those on the NITES and IAC80 data are overestimated. To obtain reliable values and uncertainties on the transit parameters we scaled the errorbars so $\chi^2_\nu = 1$ for each individual dataset before performing a joint fit to all photometric data. The resulting best-fit parameters are listed in Table 5.2 while Fig. 5.2 shows the photometry, after subtracting the baseline model, and best-fit transit model. The best-fit parameters of the joint fit are in good agreement with the fits to the individual datasets, with the exception of T_{14} and b, which are significantly longer and higher for the MASCARA fit. We believe this is not surprising. Part of this tension can be explained by the underestimated errorbars producing underes-

Table 5.2: Parameters and best-fit values used in modelling the MASCARA, NITES and IAC80 photometric data.

Parameter	Symbol	Units	MASCARA	NITES	IAC80	Joint[a]
Reduced chi-square	χ^2_ν	-	3.42	0.52	0.66	1.00
Epoch	T_p	BJD	2457909.593 ± 0.001	$2457909.5905^{+0.0008}_{-0.0009}$	2457909.5907 ± 0.0004	$2457909.5906^{+0.0003}_{-0.0002}$
Period	P	d	3.474135 ± 0.00001	3.474135 (fixed)	3.474135 (fixed)	$3.474119^{+0.000005}_{-0.000006}$
Duration[b]	T_{14}	h	$3.88^{+0.09}_{-0.07}$	$3.51^{+0.10}_{-0.07}$	3.55 ± 0.07	3.55 ± 0.03
Planet-to-star ratio	$p = R_p/R_\star$	-	0.115 ± 0.002	$0.115^{+0.006}_{-0.005}$	$0.118^{+0.004}_{-0.003}$	0.115 ± 0.001
Impact parameter[b]	b	-	$0.64^{+0.05}_{-0.06}$	0.3 ± 0.2	$0.46^{+0.07}_{-0.12}$	$0.47^{+0.04}_{-0.06}$
Eccentricity	e	-	0 (fixed)	0 (fixed)	0 (fixed)	0 (fixed)

Notes. [a] The errorbars were scaled so $\chi^2_\nu = 1$ for each individual dataset before performing the joint fit. [b] The best-fit values of T_{14} and b differ significantly between MASCARA and the Joint fit. This difference most likely originates from the algorithms used to calibrate the MASCARA data, which are known to potentially modify the transit shape.

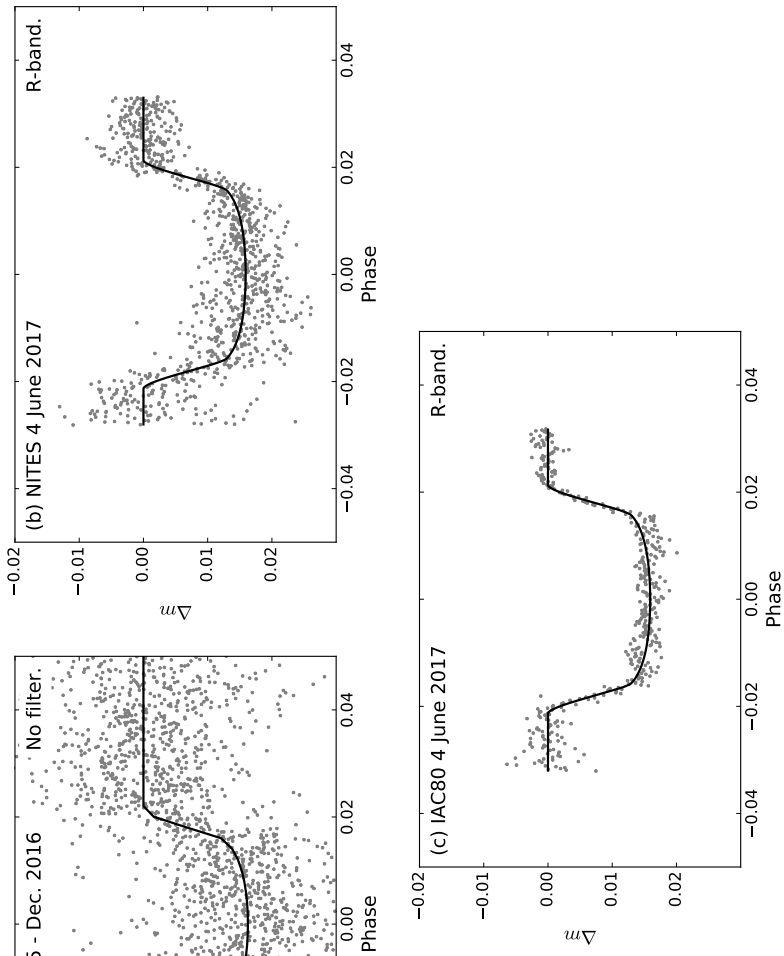

Figure 5.2: Photometric data (grey points) after subtraction of the best-fit baseline model, and best-fit transit model (black line) for MASCARA-2 b. *(a)* The calibrated MASCARA data obtained from February 2015 to December 2016. *(b)* The NITES data obtained during the night of the 04 June 2017. *(c)* The IAC80 data obtained during the night of the 04 June 2017.

timated uncertainties on the best-fit parameters of the MASCARA fit. Furthermore, the baseline model of the MASCARA data contains considerable freedom, and in the joint fit the NITES and IAC80 contain more information on the transit shape, driving the baseline solution. This freedom in the MASCARA shape stems from the significant data manipulations required in the calibration of the MASCARA data utilizing algorithms that are known to modify the shape of the transit. From the best-fit transit parameters we obtain a measurement of the stellar density, $\rho_\odot = 0.68^{+0.07}_{-0.06}$ g cm^{-3}

5.4.2 Stellar parameters determination

A great benefit for the characterisation of transiting systems in MASCARA is that for most stars the basic properties are already available in the literature at these bright apparent magnitudes - as is the case for MASCARA-2 (HD 185603; HIP 96618). Hipparcos (van Leeuwen, 2007) lists a parallax of 8.73 ± 0.5 mas, which is refined by the first data release of GAIA (Lindegren et al., 2016) to 7.16 ± 0.34 mas, corresponding to a distance of 140 ± 7 pc. Just as for MASCARA-1, McDonald et al. (2012) determined the effective temperature and luminosity of MASCARA-2 (as for more than 100,000 other bright stars) by combining the photometry of a number of surveys with the Hipparcos distance. They find an effective temperature of $T_{\rm eff} = 8809$ K and a bolometric luminosity (corrected to the GAIA parallax) of 15.1 L$_\odot$, but provide no uncertainties.

From an analysis of the SONG spectra with iSpec (Blanco-Cuaresma et al., 2014) we independently determine the stellar parameters. For this analysis we first use BASTA (Silva Aguirre et al., 2015) with a grid of BaSTI isochrones (Pietrinferni et al., 2004) to convert the photometric stellar density to a prior on the surface gravity. We modify iSpec to include the $\log g$ prior in the spectroscopic fitting process and derive the effective temperature, surface gravity, metallicity and projected rotation speed of the host star. Using BASTA, we then fit the spectroscopically derived effective temperature and metallicity with the photometric stellar density to derive the final stellar parameters.

The resulting parameters are $T_{\rm eff} = 8980^{+90}_{-130}$ K, $\log g = 4.31 \pm 0.02$, [Fe/H] $= -0.02 \pm 0.07$ and $v \sin i_\star = 117 \pm 3$ km s^{-1}. The SONG effective temperature lies within 1σ of the McDonald et al. (2012) value. Since the latter do not quote uncertainties, and taking into account the precision of the available GAIA parallax, we assume an effective temperature of $T_{\rm eff} = 8980^{+90}_{-130}$ K and a bolometric luminosity of 15 ± 3 L$_\odot$ for the remainder of the analysis.

We determine the stellar mass, radius and age to be $1.89^{+0.06}_{-0.05}$ M$_\odot$, 1.60 ± 0.06 R$_\odot$ and 200^{+100}_{-50} Myr. From the bolometric luminosity and effective temperature, we independently derive a stellar radius of $R_\star = 1.7 \pm 0.2$ R$_\odot$, consistent with the spectroscopically determined radius.

5.4.3 Radial velocity analysis

For the RV analysis we use the spectra taken out-of-transit, 15 in total, excluding the spectra taken for the RM measurements and one in-transit spectrum taken at another time. The RM data are excluded because their small phase coverage might cause short time-scale effects in the star, such as pulsations, to bias the results while for the out-of-transit data such short time-scale effects are not coherent and can be accounted for using a jitter term.

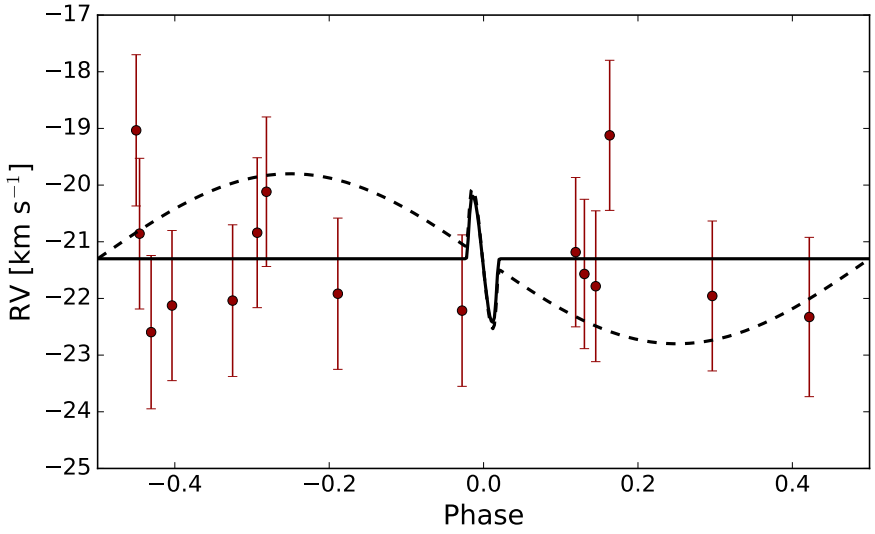

Figure 5.3: SONG RV data (red points) derived from the out-of-transit spectra, with the jitter term included in the uncertainties, best-fit model (solid black line) and 99% upper limit (dashed black line) for the RV variations of MASCARA-2. The high rotational velocity of the host star, 114 ± 3 km s^{-1} broadens the spectral lines, reducing the accuracy of the individual RV points.

RVs were obtained from the spectra by cross-correlating the individual spectral orders with a stellar template corresponding to the best-fit spectroscopic parameters, generated using MOOG and assuming a Kurucz ATLAS9 stellar atmosphere (Kirby, 2011). The resulting cross-correlation functions (CCFs) were subsequently fitted using a rotationally broadened line profile to determine velocity shifts. The final RV measurement of each observation was determined from the weighted-mean of the measurements from the individual orders.

Since the projected equatorial rotation velocity of the star is very high rotational broadening is the dominant component in the line-profile, resulting in substantial uncertainties on the RV measurements of $\sim$300 m s^{-1}, which combined with a jitter term results in a typical uncertainty of $\sim$1 km s^{-1}. The RV data points are phase folded using the best-fit period and epoch as derived from the photometry, and a circular orbital solution is fitted to the data, keeping the period and epoch fixed to the photometric values and allowing the RV amplitude K, systemic velocity γ and the jitter term σ_j to vary.

Table 5.3 lists the best-fit parameters and Fig. 5.3 shows the RV data and the best-fit model, including the RM variations described in the next section. We are unable to constrain the amplitude of the RV variations, finding $K = 0.0 \pm 0.6$ km s^{-1} (solid line in Fig. 5.3) and instead place a 99% upper limit of $K < 1.5$ km s^{-1} (dashed line in Fig. 5.3), corresponding to a limit on the companion mass of $M_p < 17\,\mathrm{M_J}$, indicating that the companion is indeed in the planetary mass regime.

Table 5.3: Parameters and best-fit values used in modelling the SONG RV and RM data.

Parameter	Symbol	Units	RV	RM
Epoch	T_p	BJD	2457909.5906 (fixed)	2457058.42722 ± 0.0003
Period	P	d	3.474119 (fixed)	3.474135 (fixed)
Scaled semi-major axis	$a/R_\star$	-	-	7.5 ± 0.04
Planet-to-star ratio	$p = R_p/R_\star$	-	-	0.1133 ± 0.0007
Cosine of the inclination	$\cos i$	-	-	0.066 ± 0.002
Eccentricity	e	-	0 (fixed)	0 (fixed)
RV amplitude[a]	K	km s^{-1}	0 ± 600	-1000 ± 300
Systemic velocity[a]	γ	km s^{-1}	-21.3 ± 0.4	-21.07 ± 0.03
RV jitter	σ_j	km s^{-1}	$1.3^{+0.5}_{-0.3}$	-
Projected obliquity	λ	$^\circ$	-	0.6 ± 4
Micro turbulence	ν	km s^{-1}	-	2.0 ± 0.5
Macro turbulence	ζ	km s^{-1}	-	15.1 ± 0.6
Projected rotation speed	$v \sin i_\star$	km s^{-1}	-	114 ± 3
Limb darkening (SONG)[b]	$u_1 + u_2$	-	-	0.63 ± 0.01
Limb darkening (IAC80)[b]	$u_1 + u_2$	-	-	0.42 ± 0.04

Notes. [a] Since the small phase coverage of the spectroscopic transit observations might cause short time-scale effects in the star, such as pulsations, to bias the observations we prefer the values for K and γ obtained from the RV modelling where such short time-scale effects are not coherent and included in the jitter term. [b] We employed Gaussian priors with a width of 0.05 on $u_1 + u_2$ using the appropriate limb-darkening coefficients from Claret and Bloemen (2011) for $u_1 + u_2$.

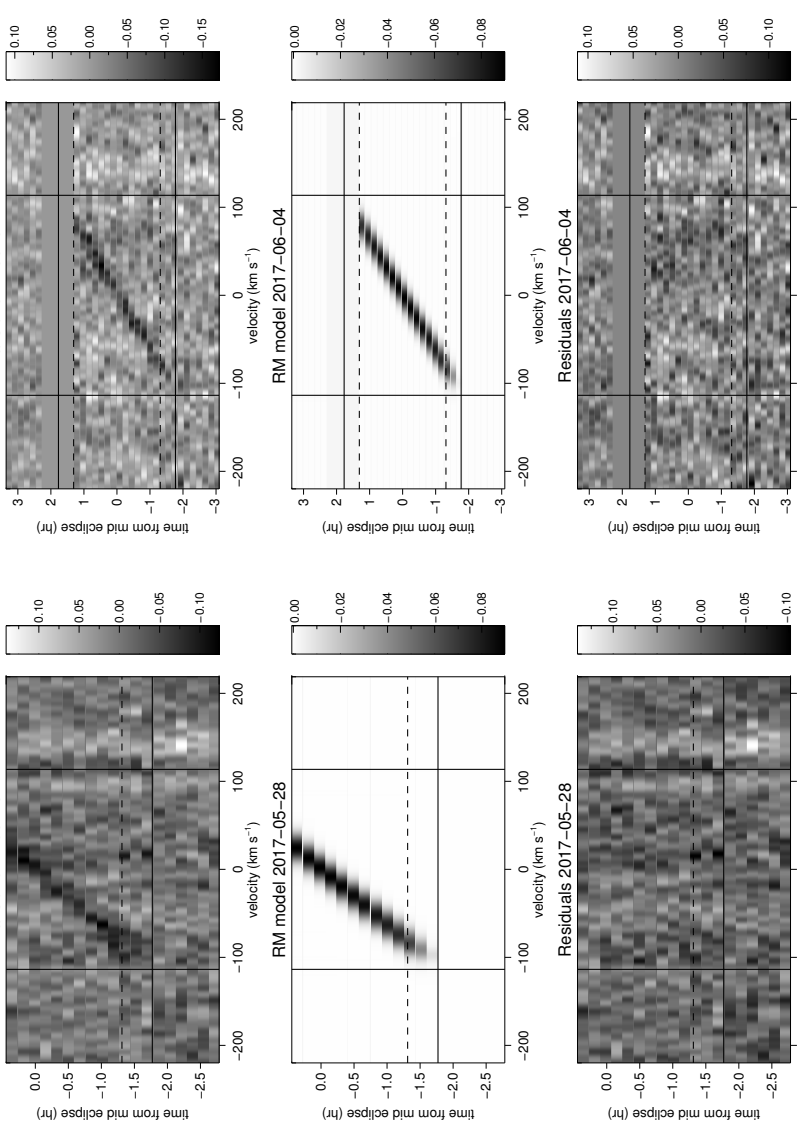

Figure 5.4: Rossiter-McLaughlin measurements of MASCARA-2 during the transits occuring in the nights of May 28 (*left column*) and June 4 (*right column*). On June 4 one hour around egress was missed since the star was too close to zenith to be observed with SONG. In each panel the solid horizontal lines indicate the beginning of ingress and the end of egress and the dashed horizontal lines indicate the end of ingress and the beginning of egress. The vertical lines indicate the width of the best-fit rotational broadening profile. Shown in the rows are the observed CCFs after subtracting the average line profile and revealing the planet shadow (*top*), the best-fit model to the observations (*middle*) and the residuals of the observations after subtracting the best-fit model. (*bottom*).

5.4.4 Spectroscopic transit analysis

A crucial element in confirming the planetary nature of the transiting system is the measurement of the spectroscopic transit, which confirms that a dark object is transiting the bright, fast spinning star, and in addition determines the projected spin-orbit angle of the system. Analysis of the SONG data was performed in a similar way as for the MASCARA-1 system (Talens et al., 2017a). CCFs were created from the SONG spectra using a stellar template as described in the previous section and the individual orders were co-added to obtain a single CCF for each observation. The resulting CCFs are shown in the top row of Fig. 5.4, after subtraction of the average line profile.

We used the code from Albrecht et al. (2013) as described in Talens et al. (2017a) to measure the projected obliquity, λ, from the CCFs. As for the MASCARA-1 analysis, an MCMC was run to obtain confidence intervals for λ and $v \sin i_\star$, while also optimizing the micro- and macro-turbulence, the transit epoch T_p, the planet-to-star radius ratio p, scaled semi-major axis $a/R_\star$, the cosine of the orbital inclination $\cos i$, the stellar systemic velocity γ, the stellar RV amplitude K, and the quadratic limb darkening parameters. For the spectroscopic observations we take limb darkening parameters of $u_1 = 0.27$ and $u_2 = 0.32$ (Claret and Bloemen, 2011) and allow $u_1 + u_2$ to vary with a Gaussian prior of 0.59 ± 0.05. While running the MCMC on the 49 CCFs obtained during the two transit nights we simultaneously fit the IAC80 photometry. This adds the stellar limb darkening in the R band as an additional free parameter. Here we use the same R band limb darkening as in Sect. 5.4.1 to set a Gaussian prior of $u_1 + u_2 = 0.4977 \pm 0.05$ while keeping $u_1 - u_2$ fixed. Each time the likelihood is calculated, two free parameters are optimised for each observation allowing for offsets and scaling in intensity. This should include possible effects of non-perfect normalisation and the changing signal-to-noise of the spectra.

The middle and bottom rows of Fig. 5.4 show the best-fit models and their residuals. We detect a clear signal from the planet as it crosses the disk of the star and determine a projected spin-orbit angle of $0.6 \pm 0.5^\circ$ indicating that the system is aligned. The orbital parameters T_p, $a/R_\star$, p and $\cos i$ are in good agreement with those derived from photometry alone, and provide us with an improved measurement of the stellar density $\rho_\odot = 0.66 \pm 0.01$ g cm^{-3}, consistent with the value derived from the photometry. The derived value of $v \sin i_\star = 113.6 \pm 0.2$ km s^{-1} is somewhat lower than the spectroscopic value which we attribute to the inclusion of macro-turbulence here. We argue that the formal uncertainties in the projected obliquity and projected rotation speed underestimate the true uncertainty in these parameters. Since the host star is a rapid rotator we expect both a departure from spherical symmetry and the presence of gravity darkening, whose effects are not included in the modelling presented here. We therefore argue that uncertainties of 4° and 3 km s^{-1} are more appropriate for the projected obliquity and projected rotation speed.

5.5 Discussion and Conclusion

We list the final parameters describing MASCARA-2 b and its host star in Table 5.4. We find that MASCARA-2 b orbits its host star in $3.474119^{+0.000005}_{-0.000006}$ days at a distance of 0.057 ± 0.006 AU. It has a radius of 1.83 ± 0.07 R$_\mathrm{J}$ and we report a 99% upper limit of < 17 M$_\mathrm{J}$ for the mass. We continue to take RV measurements to further constrain the mass of the planet.

Table 5.4: Parameters describing the MASCARA-2 system, derived from the best-fit models to the photometric and spectroscopic data.

Parameter	Symbol	Value
Stellar parameters		
Identifiers		HD 185603; HIP 96618
Right Ascension		$19^h38^m38.73^s$
Declination		$+31°13'09.2''$
Spectral Type		A2
V-band magnitude	m_V	7.6
Age		200^{+100}_{-50} Myr
Effective temperature	$T_{\rm eff}$	8980^{+90}_{-130} K
Projected rotation speed	$v \sin i_\star$	114 ± 3 km s^{-1}
Surface gravity	$\log g$	4.31 ± 0.02
Metallicity	[Fe/H]	-0.02 ± 0.07
Stellar mass	$M_\star$	$1.89^{+0.06}_{-0.05}$ M$_\odot$
Stellar radius	$R_\star$	1.60 ± 0.06 R$_\odot$
Stellar density	$\rho_\star$	0.66 ± 0.01 g cm^{-3}
Planet parameters		
Planet radius	R_p	1.83 ± 0.07 R$_{\rm J}$
Planet mass	M_p	< 17 M$_{\rm J}$
Equilibrium temperature[a]	$T_{\rm eq}$	2260 ± 50 K
System parameters		
Epoch	T_p	$2457909.5906^{+0.0003}_{-0.0002}$ BJD
Period	P	$3.474119^{+0.000005}_{-0.000006}$ days
Semi-major axis	a	0.057 ± 0.006 AU
Inclination	i	$86.4^{+0.5}_{-0.4}$ °
Eccentricity	e	0 (fixed)
Projected obliquity	λ	0.6 ± 4 °

Notes. [a] Computed assuming uniform redistribution and a Bond albedo of zero.

MASCARA-2 b orbits a hot ($T_{\rm eff} > 7000$ K), early-type star, one of only eleven Hot Jupiters transiting hot stars known to date and of just four (WASP-33 b, KELT-9 b, MASCARA-1 b, MASCARA-2 b, Collier Cameron et al., 2010; Gaudi et al., 2017; Talens et al., 2017a) orbiting stars brighter than $m_V = 8.4$. Of the fainter systems, three were discovered in the *Kepler* field (Kepler-13A b,Kepler-1171 b,Kepler-1571 b, Mazeh et al., 2012; Morton et al., 2016), three by KELT (KELT-13 b,KELT-17 b,KELT-19A b, Temple et al., 2017; Zhou et al., 2016; Siverd et al., 2017) and HATP-57 b (Hartman et al., 2015). Less than halve of these planets have secure mass measurements and in general the sample is still too small to make a meaningful comparison of planet and orbital parameters to those of systems with late-type host stars. Surprisingly, the projected spin-orbit angle of MASCARA-2 b is found to be consistent with zero, contrary to what is typically found for planets around early-type stars (Winn et al., 2010; Schlaufman, 2010; Albrecht et al., 2012). While we only measure the projected alignment, it is highly unlikely for a misaligned system to produce a projected obliquity of $0.6 \pm 4^\circ$. It will be interesting to investigate why this system is aligned when similar systems are not.

Planet formation theory predicts that gas giant planets occur more frequently around more massive stars (Ida and Lin, 2005; Kennedy and Kenyon, 2008), since the mass of the planet forming disk scales with the mass of the host stars. Radial velocity surveys have confirmed this prediction for planets orbiting giant stars (e.g. Reffert et al., 2015). However, gas giants planets are expected to form on wide orbits (Lin et al., 1996; Bodenheimer et al., 2000), requiring migration to shorter orbits for transit surveys to be able to detect them. It is not yet clear how stellar mass may influence the outcome of migration processes. In this context the observed obliquity distribution of transiting planets around massive early-type stars might provide constraints on which migration mechanism is responsible (Fabrycky and Tremaine, 2007; Nagasawa et al., 2008).

The brightness of its host star and its high equilibrium temperature make MASCARA-2 b highly suitable for atmospheric studies. Using high-resolution transmission spectroscopy obtained from the ground we will be able to detect Na and K in the optical and CO and H_2O in the infrared. In particular the stellar alkali lines are significantly weaker than for solar-type stars, making the disentanglement of the planetary and stellar lines significantly easier. From space-based transit and eclipse spectroscopy with the HST and the JWST NIRISS instrument it will be possible to detect molecules such as CO, CH_4, NH_3 and H^+ and constrain the temperature-pressure profile of the atmosphere. However, the host star is of such brightness that it may staturate in other JWST instruments. Of particular interest is the possible detection of TiO, which is expected to be present in the atmospheres of highly irradiated ($T_{\rm eq} > 2000$ K) planets and a possible cause of inversion layers. Nugroho et al. (2017) and Sedaghati et al. (2017) recently claimed detections of TiO in the atmospheres of WASP-33 b and WASP-19 b, using data obtained from the ground and space respectively. MASCARA-2 b has an equilibrium temperature comparable to those of WASP-33 b and WASP-19 b making it an excellent target for attempting similar measurements.

The NASA TESS satellite (Ricker et al., 2015) will also contribute to the characterization of the atmosphere, in particular it will measure the combination of dayside thermal and reflected starlight through the secondary eclipse, and their longitudinal distribution through the phase curve, constraining global circulation on this world.

We expect MASCARA to reveal many more bright transiting systems. Of the 14 transiting systems with $m_V < 8.4$ known to date only two are located in the southern hemi-

sphere. A second MASCARA station at the European Southern Observatory at La Silla, Chile, will start operations from July 2017 to unveil this planet population in the southern hemisphere.

During the preparation of this paper, our team became aware of another paper reporting the discovery of a planet orbiting HD 185603 (Lund et al., 2017), published by the KELT collaboration. No information about any results or analysis was shared between the groups prior to the submission of both papers, and we would like the thank the KELT team for their collegiality and willingness to work with the MASCARA team to submit these discoveries simultaneously.

Acknowledgements

IS acknowledges support from a NWO VICI grant (639.043.107). This project has received funding from the European Research Council (ERC) under the European Union's Horizon 2020 research and innovation programme (grant agreement nr. 694513). Simon Albrecht and Anders Justesen acknowledge support by the Danish Council for Independent Research, through a DFF Sapere Aude Starting Grant nr. 4181-00487B. Based on observations made with the Hertzsprung SONG telescope operated on the island of Tenerife by the Aarhus and Copenhagen Universities in the Spanish Observatorio del Teide of the Instituto de Astrofísica de Canarias. The Hertzsprung SONG telescope is funded by the Danish National Research Foundation, Villum Foundation, and Carlsberg Foundation. This research has made use of the SIMBAD database, operated at CDS, Strasbourg, France. This research has made use of the VizieR catalogue access tool, CDS, Strasbourg, France. We have benefited greatly from the publicly available programming language Python, including the numpy, matplotlib, pyfits, scipy and h5py packages.

Bibliography

Albrecht, S., Winn, J. N., Johnson, J. A., Howard, A. W., Marcy, G. W., Butler, R. P., Arriagada, P., Crane, J. D., Shectman, S. A., Thompson, I. B., Hirano, T., Bakos, G., and Hartman, J. D. (2012). Obliquities of Hot Jupiter Host Stars: Evidence for Tidal Interactions and Primordial Misalignments. *ApJ*, 757:18.

Albrecht, S., Winn, J. N., Marcy, G. W., Howard, A. W., Isaacson, H., and Johnson, J. A. (2013). Low Stellar Obliquities in Compact Multiplanet Systems. *ApJ*, 771:11.

Andersen, M. F., Grundahl, F., Christensen-Dalsgaard, J., Frandsen, S., Jørgensen, U. G., Kjeldsen, H., Pallé, P., Skottfelt, J., Sørensen, A. N., and Weiss, E. (2014). Hardware and software for a robotic network of telescopes - SONG. In *Revista Mexicana de Astronomia y Astrofisica Conference Series*, volume 45 of *Revista Mexicana de Astronomia y Astrofisica Conference Series*, pages 83–86.

Bakos, G., Noyes, R. W., Kovács, G., Stanek, K. Z., Sasselov, D. D., and Domsa, I. (2004). Wide-Field Millimagnitude Photometry with the HAT: A Tool for Extrasolar Planet Detection. *PASP*, 116:266–277.

Barbary, K. (2016). SEP: Source extractor as a library. *The Journal of Open Source Software*, 1(6).

Barge, P., Baglin, A., Auvergne, M., Rauer, H., Léger, A., Schneider, J., Pont, F., Aigrain, S., Almenara, J.-M., Alonso, R., Barbieri, M., Bordé, P., Bouchy, F., Deeg, H. J., La Reza, D., Deleuil, M., Dvorak, R., Erikson, A., Fridlund, M., Gillon, M., Gondoin, P., Guillot, T., Hatzes, A., Hebrard, G., Jorda, L., Kabath, P., Lammer, H., Llebaria, A., Loeillet, B., Magain, P., Mazeh, T., Moutou, C., Ollivier, M., Pätzold, M., Queloz, D., Rouan, D., Shporer, A., and Wuchterl, G. (2008). Transiting exoplanets from the CoRoT space mission. I. CoRoT-Exo-1b: a low-density short-period planet around a G0V star. *A&A*, 482:L17–L20.

Bertin, E. and Arnouts, S. (1996). SExtractor: Software for source extraction. *A&AS*, 117:393–404.

Blanco-Cuaresma, S., Soubiran, C., Heiter, U., and Jofré, P. (2014). Determining stellar atmospheric parameters and chemical abundances of FGK stars with iSpec. *A&A*, 569:A111.

Bodenheimer, P., Hubickyj, O., and Lissauer, J. J. (2000). Models of the in Situ Formation of Detected Extrasolar Giant Planets<FNOTEREF RID="FN1">1</FNOTEREF>,. *Icarus*, 143:2–14.

Borucki, W. J., Koch, D., Basri, G., Batalha, N., Brown, T., Caldwell, D., Caldwell, J., Christensen-Dalsgaard, J., Cochran, W. D., DeVore, E., Dunham, E. W., Dupree, A. K., Gautier, T. N., Geary, J. C., Gilliland, R., Gould, A., Howell, S. B., Jenkins, J. M., Kondo, Y., Latham, D. W., Marcy, G. W., Meibom, S., Kjeldsen, H., Lissauer, J. J., Monet, D. G., Morrison, D., Sasselov, D., Tarter, J., Boss, A., Brownlee, D., Owen, T., Buzasi, D., Charbonneau, D., Doyle, L., Fortney, J., Ford, E. B., Holman, M. J., Seager, S., Steffen, J. H., Welsh, W. F., Rowe, J., Anderson, H., Buchhave, L., Ciardi, D., Walkowicz, L., Sherry, W., Horch, E., Isaacson, H., Everett, M. E., Fischer, D., Torres, G., Johnson, J. A., Endl, M., MacQueen, P., Bryson, S. T., Dotson, J., Haas, M., Kolodziejczak, J., Van Cleve, J., Chandrasekaran, H., Twicken, J. D., Quintana, E. V., Clarke, B. D., Allen, C., Li, J., Wu, H., Tenenbaum, P., Verner, E., Bruhweiler, F., Barnes, J., and Prsa, A. (2010). Kepler Planet-Detection Mission: Introduction and First Results. *Science*, 327:977.

Brogi, M., de Kok, R. J., Albrecht, S., Snellen, I. A. G., Birkby, J. L., and Schwarz, H. (2016). Rotation and Winds of Exoplanet HD 189733 b Measured with High-dispersion Transmission Spectroscopy. *ApJ*, 817:106.

Claret, A. and Bloemen, S. (2011). Gravity and limb-darkening coefficients for the Kepler, CoRoT, Spitzer, uvby, UBVRIJHK, and Sloan photometric systems. *A&A*, 529:A75.

Collier Cameron, A., Guenther, E., Smalley, B., McDonald, I., Hebb, L., Andersen, J., Augusteijn, T., Barros, S. C. C., Brown, D. J. A., Cochran, W. D., Endl, M., Fossey, S. J., Hartmann, M., Maxted, P. F. L., Pollacco, D., Skillen, I., Telting, J., Waldmann, I. P., and West, R. G. (2010). Line-profile tomography of exoplanet transits - II. A gas-giant planet transiting a rapidly rotating A5 star. *MNRAS*, 407:507–514.

Craig, M. W., Crawford, S. M., Deil, C., Gomez, C., Günther, H. M., Heidt, N., Horton, A., Karr, J., Nelson, S., Ninan, J. P., Pattnaik, P., Rol, E., Schoenell, W., Seifert, M., Singh, S., Sipocz, B., Stotts, C., Streicher, O., Tollerud, E., Walker, N., and ccdproc Contributors (2015). ccdproc: CCD data reduction software. Astrophysics Source Code Library.

Dressing, C. D. and Charbonneau, D. (2015). The Occurrence of Potentially Habitable Planets Orbiting M Dwarfs Estimated from the Full Kepler Dataset and an Empirical Measurement of the Detection Sensitivity. *ApJ*, 807:45.

Fabrycky, D. and Tremaine, S. (2007). Shrinking Binary and Planetary Orbits by Kozai Cycles with Tidal Friction. *ApJ*, 669:1298–1315.

Foreman-Mackey, D., Hogg, D. W., Lang, D., and Goodman, J. (2013). emcee: The MCMC Hammer. *PASP*, 125:306.

Fressin, F., Torres, G., Charbonneau, D., Bryson, S. T., Christiansen, J., Dressing, C. D., Jenkins, J. M., Walkowicz, L. M., and Batalha, N. M. (2013). The False Positive Rate of Kepler and the Occurrence of Planets. *ApJ*, 766:81.

Gaudi, B. S., Stassun, K. G., Collins, K. A., Beatty, T. G., Zhou, G., Latham, D. W., Bieryla, A., Eastman, J. D., Siverd, R. J., Crepp, J. R., Gonzales, E. J., Stevens, D. J., Buchhave, L. A., Pepper, J., Johnson, M. C., Colon, K. D., Jensen, E. L. N., Rodriguez, J. E., Bozza,

V., Novati, S. C., D'Ago, G., Dumont, M. T., Ellis, T., Gaillard, C., Jang-Condell, H., Kasper, D. H., Fukui, A., Gregorio, J., Ito, A., Kielkopf, J. F., Manner, M., Matt, K., Narita, N., Oberst, T. E., Reed, P. A., Scarpetta, G., Stephens, D. C., Yeigh, R. R., Zambelli, R., Fulton, B. J., Howard, A. W., James, D. J., Penny, M., Bayliss, D., Curtis, I. A., Depoy, D. L., Esquerdo, G. A., Gould, A., Joner, M. D., Kuhn, R. B., Labadie-Bartz, J., Lund, M. B., Marshall, J. L., McLeod, K. K., Pogge, R. W., Relles, H., Stockdale, C., Tan, T. G., Trueblood, M., and Trueblood, P. (2017). A giant planet undergoing extreme-ultraviolet irradiation by its hot massive-star host. *Nature* , 546:514–518.

Grundahl, F., Fredslund Andersen, M., Christensen-Dalsgaard, J., Antoci, V., Kjeldsen, H., Handberg, R., Houdek, G., Bedding, T. R., Pallé, P. L., Jessen-Hansen, J., Silva Aguirre, V., White, T. R., Frandsen, S., Albrecht, S., Andersen, M. I., Arentoft, T., Brogaard, K., Chaplin, W. J., Harpsøe, K., Jørgensen, U. G., Karovicova, I., Karoff, C., Kjærgaard Rasmussen, P., Lund, M. N., Sloth Lundkvist, M., Skottfelt, J., Norup Sørensen, A., Tronsgaard, R., and Weiss, E. (2017). First Results from the Hertzsprung SONG Telescope: Asteroseismology of the G5 Subgiant Star μ Herculis. *ApJ*, 836:142.

Hartman, J. D., Bakos, G. Á., Buchhave, L. A., Torres, G., Latham, D. W., Kovács, G., Bhatti, W., Csubry, Z., de Val-Borro, M., Penev, K., Huang, C. X., Béky, B., Bieryla, A., Quinn, S. N., Howard, A. W., Marcy, G. W., Johnson, J. A., Isaacson, H., Fischer, D. A., Noyes, R. W., Falco, E., Esquerdo, G. A., Knox, R. P., Hinz, P., Lázár, J., Papp, I., and Sári, P. (2015). HAT-P-57b: A Short-period Giant Planet Transiting a Bright Rapidly Rotating A8V Star Confirmed Via Doppler Tomography. *AJ*, 150:197.

Howell, S. B., Sobeck, C., Haas, M., Still, M., Barclay, T., Mullally, F., Troeltzsch, J., Aigrain, S., Bryson, S. T., Caldwell, D., Chaplin, W. J., Cochran, W. D., Huber, D., Marcy, G. W., Miglio, A., Najita, J. R., Smith, M., Twicken, J. D., and Fortney, J. J. (2014). The K2 Mission: Characterization and Early Results. *PASP*, 126:398.

Ida, S. and Lin, D. N. C. (2005). Toward a Deterministic Model of Planetary Formation. III. Mass Distribution of Short-Period Planets around Stars of Various Masses. *ApJ*, 626:1045–1060.

Kennedy, G. M. and Kenyon, S. J. (2008). Planet Formation around Stars of Various Masses: The Snow Line and the Frequency of Giant Planets. *ApJ*, 673:502–512.

Kirby, E. N. (2011). Grids of ATLAS9 Model Atmospheres and MOOG Synthetic Spectra. *PASP*, 123:531.

Kovács, G., Zucker, S., and Mazeh, T. (2002). A box-fitting algorithm in the search for periodic transits. *A&A*, 391:369–377.

Kreidberg, L. (2015). batman: BAsic Transit Model cAlculatioN in Python. *PASP*, 127:1161.

Lin, D. N. C., Bodenheimer, P., and Richardson, D. C. (1996). Orbital migration of the planetary companion of 51 Pegasi to its present location. *Nature* , 380:606–607.

Lindegren, L., Lammers, U., Bastian, U., Hernández, J., Klioner, S., Hobbs, D., Bombrun, A., Michalik, D., Ramos-Lerate, M., Butkevich, A., Comoretto, G., Joliet, E., Holl, B., Hutton, A., Parsons, P., Steidelmüller, H., Abbas, U., Altmann, M., Andrei, A., Anton,

S., Bach, N., Barache, C., Becciani, U., Berthier, J., Bianchi, L., Biermann, M., Bouquillon, S., Bourda, G., Brüsemeister, T., Bucciarelli, B., Busonero, D., Carlucci, T., Castañeda, J., Charlot, P., Clotet, M., Crosta, M., Davidson, M., de Felice, F., Drimmel, R., Fabricius, C., Fienga, A., Figueras, F., Fraile, E., Gai, M., Garralda, N., Geyer, R., González-Vidal, J. J., Guerra, R., Hambly, N. C., Hauser, M., Jordan, S., Lattanzi, M. G., Lenhardt, H., Liao, S., Löffler, W., McMillan, P. J., Mignard, F., Mora, A., Morbidelli, R., Portell, J., Riva, A., Sarasso, M., Serraller, I., Siddiqui, H., Smart, R., Spagna, A., Stampa, U., Steele, I., Taris, F., Torra, J., van Reeven, W., Vecchiato, A., Zschocke, S., de Bruijne, J., Gracia, G., Raison, F., Lister, T., Marchant, J., Messineo, R., Soffel, M., Osorio, J., de Torres, A., and O'Mullane, W. (2016). Gaia Data Release 1. Astrometry: one billion positions, two million proper motions and parallaxes. *A&A*, 595:A4.

Lund, M. B., Rodriguez, J. E., Zhou, G., Gaudi, B. S., Stassun, K. G., Johnson, M. C., Bieryla, A., Oelkers, R. J., Stevens, D. J., Collins, K. A., Penev, K., Quinn, S. N., Latham, D. W., Villanueva, Jr., S., Eastman, J. D., Kielkopf, J. F., Oberst, T. E., Jensen, E. L. N., Cohen, D. H., Joner, M. D., Stephens, D. C., Relles, H., Corfini, G., Gregorio, J., Zambelli, R., Esquerdo, G. A., Calkins, M. L., Berlind, P., Ciardi, D. R., Dressing, C., Patel, R., Gagnon, P., Gonzales, E., Beatty, T. G., Siverd, R. J., Labadie-Bartz, J., Kuhn, R. B., Colón, K. D., James, D., Pepper, J., Fulton, B. J., McLeod, K. K., Stockdale, C., Calchi Novati, S., DePoy, D. L., Gould, A., Marshall, J. L., Trueblood, M., Trueblood, P., Johnson, J. A., Wright, J., McCrady, N., Wittenmyer, R. A., Johnson, S. A., Sergi, A., Wilson, M., and Sliski, D. H. (2017). KELT-20b: A Giant Planet with a Period of $P \sim 3.5$ days Transiting the $V \sim 7.6$ Early A Star HD 185603. *AJ*, 154:194.

Mandel, K. and Agol, E. (2002). Analytic Light Curves for Planetary Transit Searches. *ApJ*, 580:L171–L175.

Mazeh, T., Nachmani, G., Sokol, G., Faigler, S., and Zucker, S. (2012). Kepler KOI-13.01 - Detection of beaming and ellipsoidal modulations pointing to a massive hot Jupiter. *A&A*, 541:A56.

McCormac, J., Pollacco, D., Skillen, I., Faedi, F., Todd, I., and Watson, C. A. (2013). DONUTS: A Science Frame Autoguiding Algorithm with Sub-Pixel Precision, Capable of Guiding on Defocused Stars. *PASP*, 125:548.

McCormac, J., Skillen, I., Pollacco, D., Faedi, F., Ramsay, G., Dhillon, V. S., Todd, I., and Gonzalez, A. (2014). A search for photometric variability towards M71 with the Near-Infrared Transiting ExoplanetS Telescope. *MNRAS*, 438:3383–3398.

McDonald, I., Zijlstra, A. A., and Boyer, M. L. (2012). Fundamental parameters and infrared excesses of Hipparcos stars. *MNRAS*, 427:343–357.

Morton, T. D., Bryson, S. T., Coughlin, J. L., Rowe, J. F., Ravichandran, G., Petigura, E. A., Haas, M. R., and Batalha, N. M. (2016). False Positive Probabilities for all Kepler Objects of Interest: 1284 Newly Validated Planets and 428 Likely False Positives. *ApJ*, 822:86.

Nagasawa, M., Ida, S., and Bessho, T. (2008). Formation of Hot Planets by a Combination of Planet Scattering, Tidal Circularization, and the Kozai Mechanism. *ApJ*, 678:498–508.

Nugroho, S. K., Kawahara, H., Masuda, K., Hirano, T., Kotani, T., and Tajitsu, A. (2017). High-resolution Spectroscopic Detection of TiO and a Stratosphere in the Day-side of WASP-33b. *AJ*, 154:221.

Pepper, J., Pogge, R. W., DePoy, D. L., Marshall, J. L., Stanek, K. Z., Stutz, A. M., Poindexter, S., Siverd, R., O'Brien, T. P., Trueblood, M., and Trueblood, P. (2007). The Kilodegree Extremely Little Telescope (KELT): A Small Robotic Telescope for Large-Area Synoptic Surveys. *PASP*, 119:923–935.

Pietrinferni, A., Cassisi, S., Salaris, M., and Castelli, F. (2004). A Large Stellar Evolution Database for Population Synthesis Studies. I. Scaled Solar Models and Isochrones. *ApJ*, 612:168–190.

Pollacco, D. L., Skillen, I., Collier Cameron, A., Christian, D. J., Hellier, C., Irwin, J., Lister, T. A., Street, R. A., West, R. G., Anderson, D. R., Clarkson, W. I., Deeg, H., Enoch, B., Evans, A., Fitzsimmons, A., Haswell, C. A., Hodgkin, S., Horne, K., Kane, S. R., Keenan, F. P., Maxted, P. F. L., Norton, A. J., Osborne, J., Parley, N. R., Ryans, R. S. I., Smalley, B., Wheatley, P. J., and Wilson, D. M. (2006). The WASP Project and the SuperWASP Cameras. *PASP*, 118:1407–1418.

Reffert, S., Bergmann, C., Quirrenbach, A., Trifonov, T., and Künstler, A. (2015). Precise radial velocities of giant stars. VII. Occurrence rate of giant extrasolar planets as a function of mass and metallicity. *A&A*, 574:A116.

Ricker, G. R., Winn, J. N., Vanderspek, R., Latham, D. W., Bakos, G. Á., Bean, J. L., Berta-Thompson, Z. K., Brown, T. M., Buchhave, L., Butler, N. R., Butler, R. P., Chaplin, W. J., Charbonneau, D., Christensen-Dalsgaard, J., Clampin, M., Deming, D., Doty, J., De Lee, N., Dressing, C., Dunham, E. W., Endl, M., Fressin, F., Ge, J., Henning, T., Holman, M. J., Howard, A. W., Ida, S., Jenkins, J. M., Jernigan, G., Johnson, J. A., Kaltenegger, L., Kawai, N., Kjeldsen, H., Laughlin, G., Levine, A. M., Lin, D., Lissauer, J. J., MacQueen, P., Marcy, G., McCullough, P. R., Morton, T. D., Narita, N., Paegert, M., Palle, E., Pepe, F., Pepper, J., Quirrenbach, A., Rinehart, S. A., Sasselov, D., Sato, B., Seager, S., Sozzetti, A., Stassun, K. G., Sullivan, P., Szentgyorgyi, A., Torres, G., Udry, S., and Villasenor, J. (2015). Transiting Exoplanet Survey Satellite (TESS). *Journal of Astronomical Telescopes, Instruments, and Systems*, 1(1):014003.

Schlaufman, K. C. (2010). Evidence of Possible Spin-orbit Misalignment Along the Line of Sight in Transiting Exoplanet Systems. *ApJ*, 719:602–611.

Sedaghati, E., Boffin, H. M. J., MacDonald, R. J., Gandhi, S., Madhusudhan, N., Gibson, N. P., Oshagh, M., Claret, A., and Rauer, H. (2017). Detection of titanium oxide in the atmosphere of a hot Jupiter. *Nature* , 549:238–241.

Silva Aguirre, V., Davies, G. R., Basu, S., Christensen-Dalsgaard, J., Creevey, O., Metcalfe, T. S., Bedding, T. R., Casagrande, L., Handberg, R., Lund, M. N., Nissen, P. E., Chaplin, W. J., Huber, D., Serenelli, A. M., Stello, D., Van Eylen, V., Campante, T. L., Elsworth, Y., Gilliland, R. L., Hekker, S., Karoff, C., Kawaler, S. D., Kjeldsen, H., and Lundkvist, M. S. (2015). Ages and fundamental properties of Kepler exoplanet host stars from asteroseismology. *MNRAS*, 452:2127–2148.

Siverd, R. J., Collins, K. A., Zhou, G., Gaudi, B. S., Stassun, K. G., Johnson, M. C., Quinn, S. N., Bieryla, A., Latham, D. W., Ciardi, D. R., Rodriguez, J. E., Penev, K., Pinsonneault, M., Pepper, J., Eastman, J. D., Relles, H., Kielkopf, J. F., Gregorio, J., Oberst, T. E., Aldi, G. F., Esquerdo, G. A., Calkins, M. L., Berlind, P., Dressing, C., Patel, R., Stevens, D. J., Beatty, T. G., Lund, M. B., Labadie-Bartz, J., Kuhn, R. B., Colon, K. D., James, D., Yao, X., Jensen, E. L. N., Cohen, D. H., McLeod, K. K., Penny, M. T., Joner, M. D., Stephens, D. C., Villanueva, Jr., S., Zambelli, R., Stockdale, C., Evans, P., Tan, T.-G., Curtis, I. A., Reed, P. A., Trueblood, M., and Trueblood, P. (2017). KELT-19Ab: A P˜4.6 Day Hot Jupiter Transiting a Likely Am Star with a Distant Stellar Companion. *ArXiv e-prints*.

Snellen, I. A. G., de Kok, R. J., de Mooij, E. J. W., and Albrecht, S. (2010). The orbital motion, absolute mass and high-altitude winds of exoplanet HD209458b. *Nature* , 465:1049–1051.

Talens, G. J. J., Albrecht, S., Spronck, J. F. P., Lesage, A.-L., Otten, G. P. P. L., Stuik, R., Van Eylen, V., Van Winckel, H., Pollacco, D., McCormac, J., Grundahl, F., Fredslund Andersen, M., Antoci, V., and Snellen, I. A. G. (2017a). MASCARA-1 b. A hot Jupiter transiting a bright $m_V = 8.3$ A-star in a misaligned orbit. *A&A*, 606:A73.

Talens, G. J. J. et al. (2018). *in prep.*

Talens, G. J. J., Spronck, J. F. P., Lesage, A.-L., Otten, G. P. P. L., Stuik, R., Pollacco, D., and Snellen, I. A. G. (2017b). The Multi-site All-Sky CAmeRA (MASCARA). Finding transiting exoplanets around bright ($m_V < 8$) stars. *A&A*, 601:A11.

Temple, L. Y., Hellier, C., Albrow, M. D., Anderson, D. R., Bayliss, D., Beatty, T. G., Bieryla, A., Brown, D. J. A., Cargile, P. A., Collier Cameron, A., Collins, K. A., Colón, K. D., Curtis, I. A., D'Ago, G., Delrez, L., Eastman, J., Gaudi, B. S., Gillon, M., Gregorio, J., James, D., Jehin, E., Joner, M. D., Kielkopf, J. F., Kuhn, R. B., Labadie-Bartz, J., Latham, D. W., Lendl, M., Lund, M. B., Malpas, A. L., Maxted, P. F. L., Myers, G., Oberst, T. E., Pepe, F., Pepper, J., Pollacco, D., Queloz, D., Rodriguez, J. E., Ségransan, D., Siverd, R. J., Smalley, B., Stassun, K. G., Stevens, D. J., Stockdale, C., Tan, T. G., Triaud, A. H. M. J., Udry, S., Villanueva, S., West, R. G., and Zhou, G. (2017). WASP-167b/KELT-13b: joint discovery of a hot Jupiter transiting a rapidly rotating F1V star. *MNRAS*, 471:2743–2752.

Valenti, J. A. and Fischer, D. A. (2005). Spectroscopic Properties of Cool Stars (SPOCS). I. 1040 F, G, and K Dwarfs from Keck, Lick, and AAT Planet Search Programs. *ApJS*, 159:141–166.

van Leeuwen, F. (2007). Validation of the new Hipparcos reduction. *A&A*, 474:653–664.

Vogt, S. S., Marcy, G. W., Butler, R. P., and Apps, K. (2000). Six New Planets from the Keck Precision Velocity Survey. *ApJ*, 536:902–914.

Winn, J. N., Fabrycky, D., Albrecht, S., and Johnson, J. A. (2010). Hot Stars with Hot Jupiters Have High Obliquities. *ApJ*, 718:L145–L149.

Zhou, G., Rodriguez, J. E., Collins, K. A., Beatty, T., Oberst, T., Heintz, T. M., Stassun, K. G., Latham, D. W., Kuhn, R. B., Bieryla, A., Lund, M. B., Labadie-Bartz, J.,

Siverd, R. J., Stevens, D. J., Gaudi, B. S., Pepper, J., Buchhave, L. A., Eastman, J., Colón, K., Cargile, P., James, D., Gregorio, J., Reed, P. A., Jensen, E. L. N., Cohen, D. H., McLeod, K. K., Tan, T. G., Zambelli, R., Bayliss, D., Bento, J., Esquerdo, G. A., Berlind, P., Calkins, M. L., Blancato, K., Manner, M., Samulski, C., Stockdale, C., Nelson, P., Stephens, D., Curtis, I., Kielkopf, J., Fulton, B. J., DePoy, D. L., Marshall, J. L., Pogge, R., Gould, A., Trueblood, M., and Trueblood, P. (2016). KELT-17b: A Hot-Jupiter Transiting an A-star in a Misaligned Orbit Detected with Doppler Tomography. *AJ*, 152:136.

Related Publications

1. Stuik, R., Bailey, J. I., Dorval, P., Talens, G. J. J., Laginja, I., Mellon, S. N., Lomberg, B. B. D., Crawford, S. M., Ireland, M. J., Mamajek, E. E., and Kenworthy, M. A. (2017). bRing: An observatory dedicated to monitoring the β Pictoris b Hill sphere transit. *A&A*, 607:A45

2. Burggraaff, O., Talens, G. J. J., Spronck, J., Lesage, A.-L., Stuik, R., Otten, G. P. P. L., Van Eylen, V., Pollacco, D., and Snellen, I. A. G. (2018). Studying bright variable stars with the Multi-site All-Sky CAmeRA (MASCARA). *ArXiv e-prints*

3. Casasayas-Barris, N., Palle, E., Yan, F., Chen, G., Albrecht, S., Nortmann, L., Van Eylen, V., Snellen, I., Talens, G. J. J., Gonzalez Hernandez, J. I., Rebolo, R., and Otten, G. P. P. L. (2018). Na I and Hα absorption features in the atmosphere of MASCARA-2b/KELT-20b. *ArXiv e-prints*

Nederlandse Samenvatting

Aan het begin van de jaren negentig van de vorige eeuw was de vraag: "Zijn er planeten buiten ons zonnestelsel?", nog niet beantwoord. De eerste exoplaneten werden in 1992 ontdekt door Wolcszan & Frail. De ontdekte planeten waren iets zwaarder dan de Aarde, maar het was lastig om deze planeten te vergelijken met planeten in ons eigen zonnestelsel omdat de ster waarom ze draaiden, PSR B1257+12, een zogeheten pulsar was, een neutronenster die niet vergelijkbaar is met de zon. In 1995 werd de eerste planeet ontdekt rondom een ster van hetzelfde type als onze zon, 51 Pegasi, maar wederom bleek het moeilijk om de planeet te vergelijken met planeten in ons eigen zonnestelsel. De planeet 51 Pegasi b is namelijk in massa vergelijkbaar met Jupiter maar draait in slechts vier dagen om zijn ster heen. Ter vergelijking, Jupiter doet daar elf jaar over, en geen enkele planeet in ons zonnestelsel doet dat in minder dan 88 dagen. Een snelle omlooptijd betekent ook een korte afstand tot de ster, hierdoor is 51 Pegasi b ook heel heet, wel 1000 graden. In de ruim twintig jaar sinds deze eerste planeten werden ontdekt zijn er veel meer planeten rond andere sterren gevonden, en daarmee is de vraag "Zijn er planeten buiten ons zonnestelsel?" definitief beantwoord. Er zijn nu nieuwe vragen:, "Hoe vormen deze planeten?", "Hoe ontwikkelen ze zich verder?" en misschien wel de belangrijkste "Is er leven mogelijk, en zo ja, is dat er dan ook?". Dat zijn de vragen die sterrenkundigen proberen te beantwoorden door de eigenschappen van deze planeten in kaart te brengen.

De transit methode

De planeet rond 51 Pegasi werd ontdekt met de radiële snelheidsmethode. Bij deze methode wordt de beweging van de ster als gevolg van de planeet gemeten aan de hand van het Doppler effect – net zoals de toon van een ambulance verandert als deze je passeert, veroorzaakt het Doppler effect ook veranderingen in licht, waardoor licht blauwer lijkt als de lichtbron naar ons toe beweegt en roder als deze van ons af beweegt. Echter, voor deze methode zijn grote telescopen en dure spectrografen nodig, en meestal kan maar naar 1 ster tegelijk gekeken worden.

Een andere manier om planeten rond andere sterren te ontdekken is de transit methode. Als een planeet, gezien vanaf aarde, voor een ster langs beweegt zal deze tijdelijk iets minder helder lijken omdat de planeet een klein deel van het sterlicht verduistert, typisch niet meer dan 2%. Met de transit methode houden we de hoeveelheid licht die van een ster komt in de gaten, en als we dan met een regelmatig interval een kleine verandering in de helderheid waarnemen is dat een indicatie dat er misschien een planeet om de ster draait. Voor deze methode kunnen veel kleinere telescopen gebruikt worden en is een normale fotocamera genoeg als detector, ook kunnen meerdere sterren tegelijk worden waargenomen. Om deze redenen is de transit methode op dit moment de meest gebruikte methode om naar planeten

te zoeken, er zijn tientallen telescopen die deze methode gebruiken. Een van deze telescopen is de *Kepler* satelliet, die duizenden planeten ontdekte in een relatief klein stukje van de hemel.

Hete Jupiters

51 Pegasi b is een planeet die in massa het best te vergelijken is met Jupiter in ons zonnestelsel, tegelijk staat hij veel dichter bij zijn ster dan de planeten rond de zon, en heeft daardoor een hoge temperatuur. Sinds de ontdekking van 51 Pegasi b zijn er honderden vergelijkbare planeten ontdekt, en we noemen deze planeten 'hete Jupiters'. De hoge temperaturen en de korte omlooptijden maken hete Jupiters zeer geschikt voor het bestuderen van hun atmosferen.

Waarnemingen van de atmosferen van exoplaneten vallen in het algemeen in een van drie categorieën: transmissie spectroscopie, eclips waarnemingen, en fase waarnemingen. Bij transmissie spectroscopie wordt tijdens de planetaire transit waargenomen, omdat tijdens de transit een deel van het sterlicht door de planeet atmosfeer gefilterd wordt. Dit filteren laat een signaal achter dat informatie bevat over welke atomen en moleculen er in de atmosfeer aanwezig zijn. Planeten met een hoge temperatuur hebben een grotere atmosferische schaalhoogte, wat betekent dat de atmosfeer verder van het planeetoppervlak komt, er wordt dan dus meer sterlicht door de planeet atmosfeer gefilterd en het signaal van de atmosfeer is groter. Bij eclips waarnemingen, wanneer de planeet achter de ster langsgaat, meten we het licht voor, na, en tijdens de eclips. Tijdens de eclips word licht dat van de planeet komt verduisterd, en door dit te vergelijken met de hoeveelheid licht die we voor en na de eclips zien kunnen we onder andere de warmtestraling van de planeet meten. Metingen van de warmtestraling bevatten informatie over de temperatuur en ook weer over de atomen en moleculen in de planeet atmosfeer. Bij fase metingen meten we het licht gedurende de hele omloop van de planeet. Tijdens de omloop is steeds een ander deel van de planeet zichtbaar, net zoals het verlichte deel van de maan verandert. De variatie in de hoeveelheid licht gedurende de omloop van de planeet bevat informatie over het temperatuur verschil tussen de dag- en nacht-zijdes van de planeet. Voor hete Jupiters vertelt dit ons ook iets over luchtstromingen op de planeet, omdat voor deze planeten steeds dezelfde zijde naar de ster staat. Als ondanks deze permanente dagzijde het temperatuur verschil tussen de dag- en nachtzijdes klein is, betekent dat dat er een sterke wind van de dag naar de nachtzijde moet zijn die de hitte transporteert. Voor al deze waarnemingen is de korte omlooptijd een voordeel omdat de transit en eclips vaak voorkomen en het waarnemen van een gehele omloop slechts enkele dagen duurt.

Hete Jupiters zijn ook interessant vanwege de waargenomen hoeken tussen het baanvlak van de planeet en rotatie-as van de ster. De verwachting is dat het baanvlak loodrecht op deze as staat en voor hete Jupiters rond relatief koudere sterren zoals onze zon is dat inderdaad het geval. Voor hetere sterren, type A, lijkt het er op dat er veel variatie zit in hoek tussen het baanvlak en de rotatie-as. Er zijn een aantal theorieën over hoe dit zo komt, echter zijn er nog maar weinig hete Jupiters rond type A sterren bekend, wat het lastig maakt om hier een definitief antwoord op te vinden.

Dit proefschrift

In dit proefschrift beschrijf ik de Multi-Site All-Sky CAmeRA, ofwel MASCARA. MASCARA is een kleine robotische telescoop die specifiek bedoelt is om hete Jupiters rond de helderste sterren in de hemel te vinden. Deze heldere sterren waren om een aantal redenen nog niet eerder onderzocht. Ten eerste, verwachtte men dat er met de transit methode niet veel planeten te vinden zouden zijn rond deze sterren. Ten tweede zijn moderne astronomische camera's zo goed in het waarnemen van zwakke sterren dat deze heldere sterren de camera's zouden verzadigen en goede metingen dus lastig kunnen worden gedaan. Daarnaast zijn er ook relatief weinig van deze sterren, in een oppervlak ter grote van de maan staat gemiddeld minder dan 1 heldere ster, tegenover enkele tientallen zwakkere sterren. Het is dus veel efficiënter om naar de zwakkere sterren te kijken als je veel planeten wil vinden. Echter, als je geïnteresseerd bent in de atmosfeer van planeten moet je ze met een spectrograaf waarnemen, in zo'n instrument word het licht in vele kleine stukjes verdeelt en om dan per stukje genoeg licht te vangen moet je of heel lang, of een heldere ster waarnemen. En dus zoekt MASCARA naar hete Jupiters rond de helderste sterren, zodat we de atmosfeer van de ontdekte planeten in detail kunnen bestuderen.

Hoofdstuk 2

In het tweede hoofdstuk beschrijf ik hoe MASCARA werkt. Een MASCARA station bestaat uit een simpele behuizing met een bewegend dak. Aan de bovenkant, in een besloten ruimte, bevinden zich vijf camera's van elk 11 megapixels. Op elke camera zit een groothoeklens waardoor die bijna een-vijfde van de zichtbare hemel kan waarnemen, en de vijf camera's samen kunnen dus bijna de hele zichtbare hemel in een keer zien. Deze camera's maken elke 6.4 seconden een afbeelding van de hemel en produceren zo per nacht bijna 100 GB aan foto's per camera. Computers die zich in of nabij MASCARA bevinden verwerken deze plaatjes, ze meten waar de sterren staan en hoe helder ze in elk plaatje zijn. Deze metingen zijn met 6 GB per camera per nacht aanzienlijk behapbaarder en worden naar Leiden verstuurd voor verdere analyse. Omdat niet de gehele hemel vanaf een locatie bestudeerd kan worden zijn er twee MASCARA stations gebouwd: een in het noordelijk halfrond bij de sterrenwacht 'Observatorio del Roque de los Muchachos' op het Canarische eiland La Palma, en een in het zuidelijk halfrond bij de sterrenwacht 'La Silla' in Chili.

Hoofdstuk 3

De helderheidsmetingen van de sterren bevatten nog effecten die van de camera's of van de aarde komen, en die gecorrigeerd moeten worden voor de kleine signalen van planeten gedetecteerd kunnen worden. In het derde hoofdstuk beschrijf ik hoe we deze effecten uit de data halen met behulp van een computerprogramma geschreven in de programmeertaal PYTHON, en demonstreer ik met een aantal tests hoe goed MASCARA planeet signalen kan vinden. De drie sterkste effecten zijn: 1) de atmosfeer van de aarde, wolken en stof in de atmosfeer kunnen het sterlicht dimmen of zelfs helemaal blokkeren; 2) de transmissie van de camera lenzen, deze word minder naar de randen van de plaatjes toe waardoor sterren

daar zwakker lijken; en 3) de intra-pixel variaties, deze zijn het gevolg van het type camera's dat wordt gebruikt en veroorzaken een golfpatroon in het licht van de sterren. Deze effecten zijn gelukkig niet uniek per ster. Sterren die dicht bij elkaar staan aan de hemel worden op dezelfde manier beïnvloedt door de atmosfeer, en sterren die op dezelfde positie op de detector staan ondervinden dezelfde transmissie en intra-pixel variaties. Na het corrigeren van de sterkste effecten blijven er nog andere effecten te zien die de helderheid van individuele sterren op een unieke manier veranderen. Deze effecten hangen bijvoorbeeld samen met de naburige sterren en de helderheid van de maan. Deze effecten worden voor elke ster afzonderlijk gecorrigeerd, waarna we zover zijn om naar het repeterende signaal van planeten te zoeken. We zoeken deze signalen met de standaard methodes, en ik laat zien dat MASCARA met drie jaar data 93% van de signalen met omlooptijden tussen de een en vijf dagen en dieptes groter dan 1% kan vinden.

Hoofdstuk 4

De eerste hete Jupiter die we met MASCARA hebben ontdekt draait rond de ster HD 201585. Dit vierde hoofdstuk beschrijft de ontdekking van deze planeet, van de detectie met MASCARA tot de observaties met de Mercator, NITES en SONG telescopen die bevestigden dat het inderdaad om een planeet gaat en waarmee de massa, straal en baan van de planeet is bepaald. De planeet, MASCARA-1 b, draait in 2,15 dagen rond zijn ster en heeft een straal die 1,5 keer zo groot is als die van Jupiter, en een massa 3,7 keer zo groot. De ster is type A, en zoals de meeste hete Jupiters rond zulke sterren maakt het baanvlak van de planeet een grote hoek met de rotatie-as van de ster. Verder heeft de planeet een hoge temperatuur van bijna 2300 graden, wat het een van de heetste planeten maakt. Deze hoge temperatuur zorgt er ook voor dat MASCARA-1 b zeer geschikt is voor waarnemingen van zijn atmosfeer.

Hoofdstuk 5

De tweede hete Jupiter met MASCARA is ontdekt draait rond de ster HD 185603. Dit laatste hoofdstuk beschrijft de ontdekking van deze planeet, van de detectie met MASCARA tot de observaties met de NITES, SONG en IAC80 telescopen die ook hier bevestigden dat het inderdaad om een planeet gaat en waarmee de massa, straal en baan van de planeet werden bepaalt. De planeet, MASCARA-2 b, draait in 3,47 dagen rond zijn ster en heeft een straal die 1,8 keer zo groot is als die van Jupiter. De massa bleek in dit geval lastig te bepalen, maar is in elk geval kleiner dan 17 keer de massa van Jupiter. De ster is type A, en het baanvlak van de planeet staat loodrecht op de rotatie-as van de ster, hetzelfde als voor planeten rond zon-achtige sterren. De planeet heeft een temperatuur van 2000 graden, en is daarmee wat koeler dan MASCARA-1 b, maar nog steeds zeer geschikt voor waarnemingen van de atmosfeer.

Curriculum Vitae

I was born on 9 September 1991 in Alkmaar, the Netherlands. As a child I was interested in minerals and gems, but as time passed this interest did not grow into something more. Starting in 2003 I attended high school at the CSG Jan Arentsz, first in Noord-Scharwoude and later in Alkmaar. During my time there two of my teachers showed me how much fun physics could be, so that when the time came to choose my field of study for university, physics was high on my list of possibilities. However, when I visited the Leiden University open day with this in mind, I was surprised to learn of another possibility: astronomy. After joining the astronomy tour that day, I quickly made up my mind to study astronomy instead, a decision I have not regretted since.

During my Bachelor research project I worked with Michiel Hogerheijde, applying models to ALMA observations of CO and HCO^+ line emission in the protoplanetary disk TW Hya. During my master I first worked with Ignas Snellen on the H-band secondary eclipse of TrES-3 b and later with Joop Schaye and Rob Crain on galaxy morphology in the EAGLE cosmological hydrodynamical simulations. It was during the former project that my growing interest in the field of exoplanets was fully realized. I obtained my Master degree in October 2014.

Following my bachelor and master I decided to stay in Leiden and study exoplanets under the supervision Ignas Snellen, aiming to detect transiting hot Jupiters around the brightest stars in the sky with MASCARA. When I started my PhD in September 2014 the first MASCARA station, which had just been completed by Julien Spronck and Anna-Lea Lesage, was being tested at ASTRON in Dwingeloo. When testing was complete, I visited ASTRON to help pack up MASCARA for shipment to the Observatorio del Roque de los Muchachos on La Palma. Following this, the first few months of my PhD were spent helping Anna-Lea to finish the on-site reduction and verifying its results, and visiting La Palma with Julien to remedy some of the initial issues with the first MASCARA station. The next two years were filled mostly with the development of the post-processing pipeline, needed to calibrate the MASCARA data and detect the potential planet candidates, which finally resulted in the discovery of MASCARA-1 b. Following the discovery of MASCARA-1 b development on the pipeline wound down and I took the lead on follow-up efforts for further MASCARA candidates; became involved in the construction of the second MASCARA station; and the development of the on-site reduction for the bRing project, a sister survey to MASCARA. This all culminated in June 2017 when I travelled for four weeks, first to La Silla observatory in Chile in order to construct the second MASCARA station and then to Prague to present my work at a conference. Simultaneously, I wrote the publication on the second MASCARA planet and provided remote support for the commissioning of the bRing station at Siding Spring observatory in Australia. I finished my PhD by writing a detailed description of the post-processing pipeline and characterizing the performance of MASCARA.

I presented my work at conferences in Nunspeet, Prague and Keele and at a meeting in Amsterdam. I further attended conferences and workshops in Dwingeloo, Vietri sul Mare, Davos, Leiden (twice) and London. For my teaching duties I assisted Jarle Brinchmann with 'Sterrenkundig Practicum 2' for one year, and Martin van Exter with 'Optica' for two years. Starting in November 2018 I will work as a Postdoc at the iREx institute in Montrèal, Canada as part of the team working on the NIRISS instrument for the James Webb Space Telescope.

Acknowledgements

During my studies at Leiden I have had the professional and emotional support of a great many people. I've been lucky to get to know these people, and if I forget anyone here that reflects more on me than on them.

First I want to thank the support staff of the observatories where the MASCARA stations are located, the Observatorio del Roque de los Muchachos and La Silla observatory. Their support during preparation, construction and operation of the stations made this thesis possible. Of course, I extend the same thanks to the staff at the bRing sites, Sutherland observing station and Siding Spring observatory.

Then those I worked most closely with as part of the MASCARA and bRing teams and without whom this thesis would not be of the same quality. Julien, Anna-Lea and Remko, they were the ones to put the pieces in place for this PhD thesis. Gilles, for building and testing the second station and with whom I spent two weeks as a construction worker and electrician rather than an astronomer. Jeb, who helped me become a better programmer as we worked on the bRing software. Patrick, who has the dubious honour of having to keep MASCARA and bRing running from now on, I wish him the best of luck! (He'll need it.)

All the PhDs and Postdocs whom I shared group meetings with as part of Ignas' group, Matteo, Jayne, Remco, Jens, Henriette, Emanuele, Vincent, Sebastiaan, Javi, Alex, Paul, Paul, Dilovan and Aurélien. I don't know half of you half as well as I should like; and I like less than half of you half as well as you deserve (that's a joke, of course). Thank you for always creating a pleasant atmosphere in the group and interesting discussions.

My fellow students during my bachelor and master, Arthur, Steven, Leandra, Tom, Martin and Joris. We shared two offices during our research projects and many coffee breaks. I'd like to thank you for being my friends and showing me some of the more fun sides of student life, such as the parties organized by the Leidsche Flesch.

I also need to thank my fellow PhDs and friends of the last four years. Jorryt, we shared an office and had many discussions about the structure of academia. I hope I can be the one to win that bet for you. Chris and his one in particular Zoe, for the movie nights. I will forever hold you responsible for showing me many great movies, and 'The Room'. Mike and his one in particular Charlotte, for the game nights and delicious cakes. And of course Andrew, Ann-Sofie and Eva for brightening my days at the observatory and without whom the aforementioned movie and game nights would have been dull indeed. Thank you all for a great four years!

Most importantly, my mother and my brother for always supporting me. They keep the world turning.